Earthquakes and Active Faults in Central Asia

Eleanor Ainscoe

Thesis submitted to the University of Oxford

for the degree of Doctor of Philosophy

in

Earth Sciences



Department of Earth Sciences,

University of Oxford

Trinity, 2018

Supervised by Prof. Richard Walker, Prof. Barry Parsons and Dr. John Elliott

Citation: Ainscoe, E. A. (2019), Earthquakes and Active Faults in Central Asia, D.Phil. thesis, University of Oxford, Department of Earth Sciences, Oxford, UK.

Keywords: continental earthquakes, reverse faults, active tectonics, Central Asia, Suusamyr, Wuqia, Pishan.

This thesis has been typeset using LaTeX 2$_\varepsilon$, released under the LaTeX Project Public License (LPPL), and references were compiled using BibTeX. Many of the figures were produced using the open source Generic Mapping Tools (GMT) software, released under the GNU General Public License.

This work is licensed under the Creative Commons Attribution-NonCommercial-ShareAlike 4.0 International License. To view a copy of this license, visit the Creative Commons website.



Printed in the United Kingdom.

Declaration

The contents of this thesis are all my own work, except where otherwise stated. The views and opinions expressed herein are mine and not necessarily those of any other person or body unless so attributed.

Abstract

Earthquakes and active faults in Central Asia

Eleanor Ainscoe
Oriel College, Oxford

Trinity Term, 2018

This thesis presents the results of research centred on three large Central Asian earthquakes from recent decades: the 1985 Wuqia (China), 1992 Suusamyr (Kyrgyzstan) and 2015 Pishan (China) earthquakes. For the Pishan earthquake I construct a fault slip model based on coseismic interferograms. It shows that the earthquake took place on a well-established fault that is visible in a seismic reflection profile. However, the coseismic and early postseismic deformations are misaligned with the longer-term topographic uplift pattern. Therefore, other mechanisms must be considered to explain the growth of topography. In a reinvestigation of the Wuqia earthquake, I combine data from several techniques to show that although surface ruptures were produced along a well-known fault, the existing models of that fault are not compatible with the earthquake's focal mechanism or depth. Instead, most of the earthquake's moment was released below a detachment. The detachment acts as a barrier to geomorphic expression of the basement fault, even though the observations require slip to have taken place both above and below the detachment within a month or less. In a study on the 1992 Suusamyr earthquake, I examine the significance of surface ruptures more closely. I use remote sensing and field observations to measure the extent and scarp height of the fresh ruptures, and to construct a paleoseismic record for the fault. The results reveal significant variability in the surface rupture pattern between successive earthquakes on the fault. Finally, I use those results to inform a broader study on the Suusamyr Basin. I map the tectonic structures across the entire basin and provide a slip rate estimate for the Suusamyr Fault. Overall this thesis extends the body of knowledge on continental reverse faulting earthquakes, and demonstrates the challenges and complexities of interpreting the fault structure and seismic hazard of an area based on surface observations.

Extended Abstract

Earthquakes and active faulting in Central Asia

Eleanor Ainscoe

Oriel College, Oxford

Trinity Term, 2018

In order to understand the tectonics and seismic hazard of a region it is necessary to form an understanding of the active faults within it. This thesis is concerned with the active faults of Central Asia, their earthquakes, and what can be learned from them that might guide assessments of faults elsewhere in the world. In Chapter 1 I briefly introduce the topic of characterisation of continental faults, and the overall tectonics of Central Asia. In the following four chapters I present the results of research centred on three large Central Asian earthquakes from recent decades: the 2015 Pishan (China), 1985 Wuqia (China), and 1992 Suusamyr (Kyrgyzstan) earthquakes. Each chapter has its own goals and conclusions but, in general, for each earthquake I first establish what took place during the earthquake as far as is possible given the available data, then investigate how it can inform our understanding of the faults and geological structures that are present in that area.

Chapter 2 is focussed on the 2015 M_w6.3 Pishan (China) earthquake, which took place at an active fold-and-thrust belt on the southwest margin of the Tarim Basin. I use interferometric synthetic aperture radar (InSAR) to determine the fault parameters and slip distribution of the 2015 earthquake — a blind, reverse-faulting event with a fault

plane dipping southwards towards the Tibetan Plateau. The earthquake mechanism and location correspond closely to a fault mapped independently by seismic reflection, indicating that the earthquake's slip was on a pre-existing ramp fault over a depth range of ∼9–13 km. However, the geometry of folding in the overlying fluvial terraces cannot be fully explained by repeated coseismic slip in events such as the 2015 earthquake, nor by the early postseismic motion shown in my interferograms. A key role in growth of the topography must therefore be played by other mechanisms.

Chapter 3 deals with another earthquake at the edge of the Tarim Basin: the 1985 M_w6.9 Wuqia earthquake, which took place in the Pamir and Tien Shan forelands in the northwest corner of the Tarim Basin. By comparing pre-earthquake satellite images from the CORONA program to post-earthquake images from modern satellites I georeference surface rupture maps that were made in the months following the earthquake and add new observations showing that the ruptures are likely to have spanned ∼25 km in total —12 km further than previously thought. I correlate pre- and post-earthquake optical images and show that the total coseismic and postseismic (17 yrs) horizontal displacements were smaller than ∼2 m. This indicates that the surface ruptures, which reached up to ∼1.5 m horizontal displacement, were representative of the slip that reached the surface and there was no major blind component. The ruptures are consistent with slip on a south-dipping reverse fault, and are indeed located along and slightly in front of a stretch of the well-established Pamir Frontal Thrust. However, these observations are at odds with the focal mechanisms derived from seismology, which have one nodal plane dipping steeply to the southeast and another dipping at a moderate angle to the northeast. The depth of the mainshock shows that most of the seismic moment was released below a detachment. Drawing the observations together shows that slip must have taken place both above and below the detachment depth within 3 weeks at most, but the detachment nonetheless acts as an effective barrier to surface expression of the basement fault.

In Chapter 4 I begin by reinvestigating the surface ruptures from the M_w7.2 1992

Suusamyr (Kyrgyzstan) earthquake — a reverse faulting earthquake in the northern Tien Shan. The Suusamyr earthquake is a valuable opportunity to study a surface-rupturing earthquake in the Tien Shan whose fault plane parameters are independently known from seismology. It is also an apparently problematic case for the conventional methods of estimating earthquake magnitudes from their surface ruptures because its ruptures show significant displacement but are only mapped as having broken the surface along small, disparate portions of the fault. Here I present the results of surveys conducted along the Suusamyr Fault to establish whether that is the case. Two short sets of ruptures were identified following the earthquake. They are unusually short for their displacement and are separated by a 25 km gap. Using satellite imagery, high-resolution digital elevation models, and palaeoseismic trenching I first reassess the distribution of the 1992 ruptures and then reconstruct the Holocene earthquake record to establish the extent to which the 1992 earthquake is representative of the rupture behaviour of this fault. At one site I find evidence for at least two prehistoric surface rupturing earthquakes in the Holocene: one ∼3 ka and one >8 ka that, along with the modern event, gives recurrence intervals of ∼3 kyr and ∼5 kyr. At a second site I find evidence for one earthquake that probably took place before ∼4.4 ka. Within spatial gaps between segments of the 1992 ruptures there are clear prehistoric surface ruptures and the ruptures in each prehistoric earthquake were discontinuous. I conclude that there is significant variability in the surface rupture pattern of successive earthquakes on the Suusamyr Fault, with implications for the completeness of palaeoseismic records obtained from thrust scarps.

In Chapter 5 I build on the results in Chapter 4 to form an improved description of the faults in the Suusamyr Basin. Although part of the Suusamyr Fault ruptured in the western half of the basin in the 1992 earthquake, faults elsewhere in the basin did not and could also be seismic hazards. I use field observations and high-resolution satellite imagery and digital elevation models to compile a fault map for the Suusamyr Basin. It shows that the south-vergent Talas-Boundary Fault has relatively long, continuous

sections of rangefront scarps, but the surface expression of the north-vergent faults is highly segmented. There is no clear continuous fault or fold at the surface but instead there are multiple short sections where evidence of shortening is visible. In places the north-vergent fault is several kilometres in front of the rangefront and very close to the south-vergent fault, suggesting that the basin is in the process of closure. I use age and offset estimates from an uplifted terrace surface, a moraine, and a paleoseismic trench described in Chapter 4 to estimate a slip rate of at least 0.5 mm/yr for the Suusamyr Fault. Although there is no single-stranded Suusamyr Fault visible at the surface, evidence from the 1992 earthquake and a fault scarp in the neighbouring upper Toktogul Basin shows that the faults in the Suusamyr Basin are likely to still be capable of slipping in major earthquakes.

Finally, in Chapter 6 I briefly discuss some conclusions that can be drawn from the thesis as a whole and suggest some directions for future work.

Acknowledgements

I thank my supervisors, Richard Walker, Barry Parsons, and John Elliott for all their help and guidance during the past four years. I am particularly grateful to Richard and Barry for cultivating the fantastic group atmosphere here at Oxford, which has made it such a lively and interesting place to work even in the weeks when my DPhil itself wasn't going so well. Richard's patient, repeated reviews of draft manuscripts have made all the difference to the standard of writing in this thesis, and he must also take credit for being a major driving force in helping me to develop the ideas and their presentation in the later chapters. Barry pushed me to improve my work and how I communicated it on the Pishan project, and that has undoubtedly improved my work since then. I must thank John for his help on Pishan, and for all his very practical advice and encouragement throughout.

Everyone who has passed through the COMET group or our office during the time that I have been here has taught me something. Special thanks must go to Dave, Austin, Christoph, Tim and Yu who showed me the ropes during the first half of my DPhil, and Qi, Nick and JD who reminded me to chill out during the second half. They helped me with everything from my very first software instructions to the practicalities of fieldwork, to demonstrating how to be a good collaborator, and were generous with sharing examples of their work and putting up with my naivety and grumpiness respectively. The field trips that I was so lucky to be a part of would not have been possible, let alone as useful, educational and fun as they were without Kanatbek, Aidyn, Ainagul, Sagan, Sultan, Azat and Ramon Arrowsmith. Closer to

home, Andy Carr, Tim Craig and Stacy Carolin have all been great to work with, as has Alex Copley, whose intriguingly titled papers and later excellent project supervision were a big part of what made me think that maybe this tectonics business could be interesting.

Oriel College has been nothing but supportive to me as one of its students. There's nothing like trying to complain about your DPhil troubles to a group of people who don't know a thing about geology to make you realise how little your troubles really matter, and having somewhere to balance out my social environment away from Earth Sciences has been a huge help. Thank you to my teammates at OCBC for all the times I cycled through deserted Oxford streets, sleep-deprived and cold, but grinning because I was on my way to see you. Likewise, the various residents of East Avenue provided much-needed camaraderie, entertainment and wisdom. I am still dreading the day when we have to break up the fridge magnet collection.

I have to credit Tamsin for pointing out to me that thinking I would enjoy doing something was a good enough reason to do it. I thank my parents for accepting that decision not to get a traditional, stable job in good grace, and for not only letting me bring home all those rocks as a kid but buying me a display case for them and books about them too.

Lastly, I must acknowledge the funding from NERC that made it all possible, and the various Oxbridge grants and subsidies that I have benefited from over the years. I sometimes find it difficult to justify why I have been given the many amazing opportunities that I have been with so few strings attached, but I will always be grateful that I was.

Contents

Declaration ii

Abstract v

Extended Abstract vii

Acknowledgements xi

Contents xvi

List of Figures xx

List of Tables xxi

1 Introduction **1**

1.1 Characterisation of Continental Faults 1

1.2 Central Asian Tectonics and Cenozoic History 6

1.3 Overview of this Thesis 12

1.4 Publications arising from this thesis 14

2 The Development of Geological Structure and Surface Folding at a Rangefront Thrust: The M_w 6.3 2015 Pishan (China) Earthquake **15**

2.1 Introduction 15

2.2 Tectonic setting 18

2.3 3 July Pishan Earthquake fault geometry and coseismic slip distribution 19

2.3.1 InSAR 19

2.4 Comparison of fault positions derived from InSAR and seismic reflection 30

2.4.1 Are half-space elastic models for the surface displacements appropriate? . . . 33
2.5 Folding in the geomorphology . . . 35
2.5.1 Fluvial terrace deformation . . . 35
2.5.2 Abandonment age of the terraces in the Hotan Fold and Thrust Belt . . . 39
2.6 Postseismic deformation . . . 40
2.6.1 Postseismic interferograms from Sentinel-1 . . . 40
2.6.2 Causative mechanisms of the postseismic displacements . . . 42
2.6.3 An afterslip model for the postseismic interferograms . . . 43
2.7 Discussion . . . 47
2.7.1 Timing of topographic growth . . . 47
2.7.2 Change in fold shape from Pliocene to Late Quaternary . . . 53
2.8 Conclusions . . . 53

3 The 1985 Wuqia (China) Earthquake: Thin-Skinned Expression of a Basement Fault 55

3.1 Introduction . . . 55
3.2 Tectonic setting . . . 58
3.2.1 Stratigraphy . . . 58
3.2.2 Structures and cross-sections . . . 60
3.2.3 Shortening rates . . . 64
3.3 The Wuqia Earthquake and its seismology . . . 65
3.4 Surface ruptures . . . 71
3.5 Horizontal displacements from geodesy . . . 80
3.5.1 Image matching results . . . 82
3.6 Discussion . . . 85
3.7 Conclusions . . . 93

4 Variability in Surface Rupture Between Successive Earthquakes on the Suusamyr Fault, Kyrgyzstan **95**

4.1 Introduction . . . 95

4.2 The 1992 Suusamyr earthquake . . . 99

4.3 Methods . . . 101

4.3.1 Remote sensing and field methods . . . 101

4.3.2 Quaternary dating procedure . . . 103

4.3.3 Measurement of scarp heights and conversion to slip . . . 104

4.4 Surface ruptures from the 1992 earthquake . . . 105

4.4.1 M41 highway: the eastern ruptures . . . 107

4.4.2 Dzhalpaksu: the western ruptures . . . 109

4.4.3 Cholgondysai . . . 113

4.5 Prehistoric ruptures . . . 116

4.5.1 Chet-Korumdy Ridge . . . 116

4.5.2 Turabulak . . . 127

4.6 Discussion . . . 129

4.7 Conclusions . . . 134

5 Active Shortening in the Suusamyr Basin, Kyrgyzstan **135**

5.1 Introduction . . . 135

5.2 Methods . . . 140

5.3 Segmented expression of the south-dipping fault . . . 143

5.3.1 The far western part of the Suusamyr Basin . . . 143

5.3.2 Turabulak . . . 148

5.3.3 The Chet Korumdy Ridge . . . 151

5.3.4 The Aramsu East section . . . 151

5.3.5 The Aigyrjal section . . . 154

5.3.6 The Ak-Suu section . . . 159

5.4 The north-dipping fault (Talas-Boundary Fault) . . . 162

5.5 The ends of the basin . . . 165
5.6 Slip rates and shortening rates . . . 170
5.6.1 Dating offset Quaternary surfaces . . . 170
5.6.2 Slip rate estimate from the earthquake recurrence rate . . . 176
5.6.3 GPS velocities . . . 177
5.7 An active fault in the upper Toktogul Valley . . . 180
5.8 Discussion . . . 183
5.8.1 Clustering relationships between faults . . . 185
5.9 Summary . . . 188

6 Concluding remarks **191**
6.1 Suggestions for future work . . . 193

Bibliography **195**

Appendices **229**

A DEM Differencing for the Suusamyr Earthquake **229**
A.1 Introduction . . . 229
A.2 Aerial photographs and processing . . . 230
A.2.1 Airphoto processing workflow . . . 233
A.2.2 DEM differencing . . . 236
A.3 Differencing results . . . 238
A.4 Conclusions . . . 241

B Further details on the luminescence dating methodology **243**

List of Figures

1.1 Map of global seismicity 2
1.2 Example cross-sections through thrust belts 4
1.3 Diagrams showing geometric models for blind reverse faults 5
1.4 Summary of the Van Fault and Earthquake 6
1.5 Topography and velocity field of the India-Euarasia collision 8
1.6 Topography, earthquakes and velocity field of Central Asia 10
1.7 Map of locations studied in this thesis 12

2.1 Pishan overview maps 17
2.2 Coseismic interferograms 21
2.3 Uniform slip model results 24
2.4 Tradeoff plots 25
2.5 Pishan focal mechanism 27
2.6 Smoothing factor influence on coseismic slip distribution 28
2.7 Coseismic slip distribution 29
2.8 Seismic reflection profile 31
2.9 A test of layered elastic models 34
2.10 Terrace geomophology maps 36
2.11 Topographic profiles across the fold 38
2.12 Postseismic interferograms before correction 41
2.13 Postseismic interferograms after correction 42
2.14 Influence of smoothing on postseismic slip model 44

2.15 Postseismic slip model . . . 45
2.16 Slip distribution recovery tests 1 . . . 46
2.17 Slip distribution recovery tests 2 . . . 47
2.18 Comparison of datasets . . . 49
2.19 Forward models for faults mapped in the reflection profile . . . 51

3.1 Overview . . . 57
3.2 Stratigraphic columns for the northwest Tarim Basin . . . 59
3.3 Cross-sections through the Tian Shan and Pamir forelands around Kashi 61
3.4 Cross-sections through the Mushi and Mingyaole Anticlines . . . 62
3.5 Satellite image overview of the study area . . . 64
3.6 Locations for the Wuqia earthquake and 11th September aftershock . . 71
3.7 Map of the main section of the ruptures . . . 72
3.8 Ruptures in the river bed . . . 75
3.9 Newly mapped rupture . . . 78
3.10 Images of the splay fault . . . 79
3.11 Displacement map — South–North . . . 83
3.12 Displacement map — West–East . . . 84
3.13 Sketch cross-section . . . 88
3.14 Coulomb stress change models . . . 89
3.15 Map showing the broader context of the Wuqia earthquakes . . . 92

4.1 Overview map . . . 97
4.2 The eastern 1992 ruptures . . . 106
4.3 The eastern 1992 ruptures (part 2) . . . 108
4.4 Overview of the ruptures around the Dzhalpaksu River . . . 109
4.5 Two segments of the western 1992 ruptures . . . 111
4.6 Segment of the western 1992 ruptures . . . 112
4.7 Newly identified ruptures east of the Dzhalpaksu River . . . 113

4.8 The Cholgondysai fault segment 114
4.9 Cholgondysai — field photographs 115
4.10 DEM and interpretation of the western end of the CKR 117
4.11 Scarp above the western end of the CKR 118
4.12 CKR scarp trench log 122
4.13 Trench log close-up 124
4.14 Turabulak site and trench 128
4.15 Summary of the Suusamyr Fault surface ruptures 132

5.1 Overview of the northwestern Tien Shan 136
5.2 Overview of the Suusamyr Basin 138
5.3 Overview of the western half of the Suusamyr Basin 139
5.4 Overview of the eastern half of the Suusamyr Basin 140
5.5 Fault map of the western part of the basin 144
5.6 Images and profiles of Korumdy River area 147
5.7 The Turabulak site 149
5.8 The Turabulak site - profiles 150
5.9 The Chet-Korumdy Ridge 151
5.10 Aramsu East 152
5.11 The Aigyrjal segment of the Suusamyr fault 154
5.12 The Aigyrjal wind gap 156
5.13 Aigyrjal photographs 157
5.14 Aigyrjal profiles 158
5.15 The Ak-Suu fault segment 160
5.16 Perspective view of the Ak-Suu scarp and sampling pits 162
5.17 Mapping along the Talas-Boundary Fault 164
5.18 Field photographs of the south-facing scarp 165
5.19 Mapping along the Talas-Boundary Fault - 2 167
5.20 The western end of the basin 168

5.21 The eastern end of the basin. 169
5.22 The ^{230}Th/U dating sampling site 172
5.23 Constraints on shortening rate from GPS 178
5.24 Forward models of horizontal velocity around dip-slip faults 179
5.25 Map of the rupture in the upper Toktogul Basin 182
5.26 Relative timing of earthquakes 186

A.1 A typical aerial photo 231
A.2 Aerial survey layout and ground control points 232
A.3 The airphoto to DEM workflow 234
A.4 Camera calibration residuals 235
A.5 The DEM difference result 237
A.6 DEM difference at an excavation 239
A.7 DEM difference across the M41 Highway rupture 240
A.8 Swath profile through the DEM difference 241

B.1 Equivalent dose distributions 245

List of Tables

2.1 Sentinel-1 interferogram details for Pishan 19

2.2 Pishan earthquake fault parameters from various publications 23

2.3 Model-interferogram misfits 29

2.4 Dating results from the terraces at Pishan 39

3.1 Published parameters for Wuqia mainshock 67

3.2 Published parameters for Wuqia aftershock 68

3.3 Details of declassified imagery 73

3.4 Details of post-earthquake imagery 74

3.5 1985 offsets of the Wuqia earthquake 76

3.6 Cumulative offset measurements for scarps in the study area 77

4.1 Descriptions of the sedimentary units identified in the CKR trench . . . 123

4.2 ^{14}C dating results 125

4.3 Luminescence dating results 126

5.1 ^{230}Th/U age data for pedogenic carbonate samples 174

B.1 Details of the sample dose rate determinations 244

Chapter 1

Introduction

1.1 Characterisation of Continental Faults

Knowledge of the location, geometry, slip rate and seismic histories of active faults is a prerequisite for understanding the active tectonics of a region. Tectonically active regions are, in general, more complex in continental crust than in oceanic crust. In the continents, rather than being concentrated in narrow zones between rigid plates as in the plate tectonic model, deformation is distributed over many faults in extensive zones that can be hundreds of kilometres wide (Figure 1.1) (*Thatcher*, 2009). It is also not necessarily possible to determine the faulting style of a continental region from the plate motions of its surroundings (*Jackson and McKenzie*, 1988). To compound the problem, the continental crust has a long history and is compositionally, structurally and thermally heterogeneous. This means that it has pre-existing faults and rheological variations, and active faults in the real crust therefore often do not have the same configuration as idealised faults in a homogeneous crust would have under the same boundary stresses (e.g. *Bott*, 1959; *Sykes*, 1978; *Sibson*, 1985; *Roering et al.*, 1997).

Numerous methods exist to estimate the geometry, slip rate and seismic histories of active faults from observations. At the largest scale, the moment release rate of large volumes can be measured from seismic catalogues which have been compiled

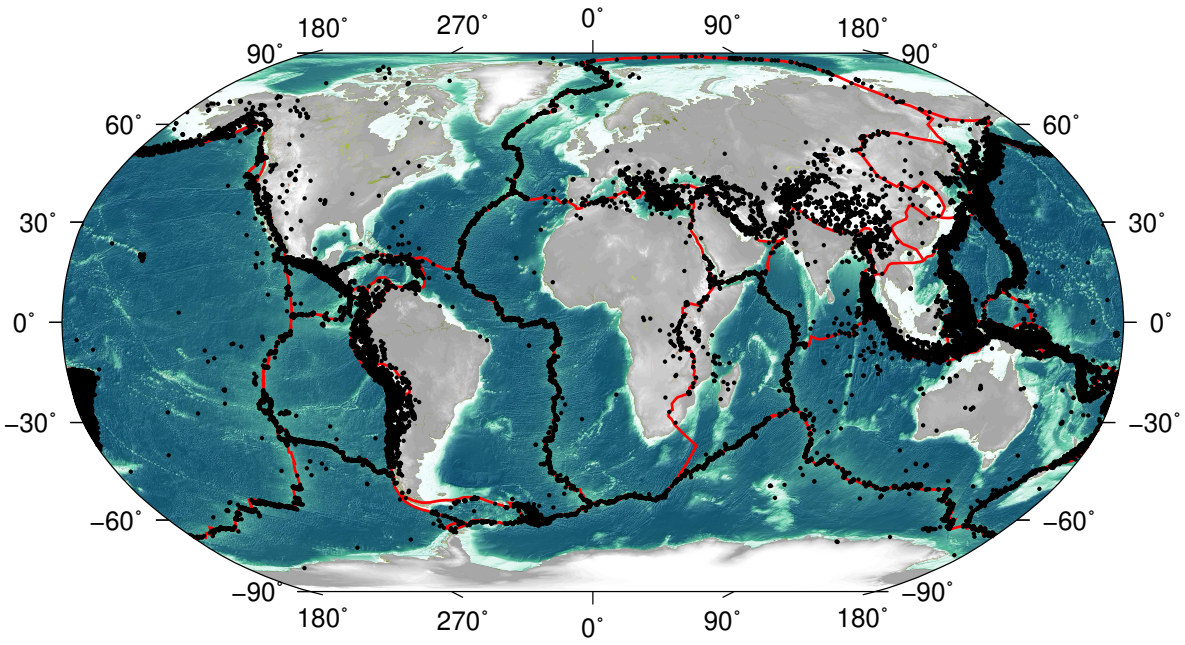


Figure 1.1: Map of global seismicity showing black dots for $M_w \geq 5$ earthquakes (January 1976–March 2018) from the GCMT catalogue (*Ekström et al.*, 2012) and red lines for the plate boundaries as defined by *Bird* (2003).

within the past century, and this gives an impression of the relative tectonic activities of different regions (see, for example, Figure 1.1). The seismic moment tensors of the earthquakes within a volume can further be used to obtain the overall strain rate tensor for that volume (*Kostrov*, 1974). However, seismic catalogues become less useful when considering smaller regions. Although a few select regions, such as parts of Italy (*Guidoboni et al.*, 2012), the Middle East (*Ambraseys*, 2009; *Zohar et al.*, 2016) and China (*Lee et al.*, 1976, 1978; *Wang*, 2004), have outstanding historical records of earthquakes, in most parts of the world the historical catalogues are not sufficiently long or detailed to be used as the basis of a full appraisal of fault slip rates and seismic capability (e.g. *Molnar*, 1979; *Goldfinger et al.*, 2013; *Stein and Friedrich*, 2014). This is in part due to our short observation duration compared to the rate at which each fault experiences its 'maximum magnitude' earthquakes, which is exacerbated because it is now recognised that a single recurrence interval can not adequately describe the time series of earthquakes on a fault (*Grant and Sieh*, 1994; *Weldon et al.*, 2004; *Goldfinger*

et al., 2013; *Gold et al.*, 2017), meaning that even longer observation durations would be needed for earthquake catalogues to be representative of a fault's seismic behaviour. Even when good records of earthquake dates and magnitudes do exist, the recorded location information is usually not good enough to identify the causative faults for earthquakes before the twentieth century.

To supplement the historical catalogues geologists use other methods to estimate the slip rates and earthquake histories of faults. Among these methods are geodetic measurements of interseismic strain or of creep (*Savage and Burford*, 1973; *Rosen et al.*, 1998; *Wright et al.*, 2001; *Jolivet et al.*, 2012; *Zheng et al.*, 2017), dating displaced geological units or geomorphological features to estimate slip rates (e.g. *Phillips et al.*, 2004; *Cowgill et al.*, 2009; *Burbank and Anderson*, 2011), paleoseismology (*McCalpin*, 2009) and indirect methods such as the interpretation of lake sediments (e.g. *Sims*, 1973; *Avşar et al.*, 2014; *Howarth et al.*, 2016). A complementary suite of methods has been used to map the location and orientation of faults. They include geological mapping, structural geology, seismic reflection, earthquake seismology, microseismology and various geodetic techniques.

Characterisation of reverse faults presents a particular challenge. Upon meeting a weak layer reverse faults have often been observed to change dip and follow the weak layer (then known as a detachment or décollement), forming a ramp-flat geometry, with some faults having several ramps and flats along their length (*Scholz*, 2002). The result is that reverse fault can be highly non-planar in the down-dip direction. Additionally, unlike strike-slip or normal faults, many reverse faults do not reach the surface, but instead terminate at depth beneath a fold (so-called "blind thrusts"). Thus, reverse faults show a great variety of styles in vertical cross-section (e.g. Figure 1.2).

Numerous different models have been required to represent reverse faults in various possible configurations and their relationship to cumulative changes in geological structure (e.g. *Suppe*, 1983; *Jamison*, 1987; *Suppe and Medwedeff*, 1990; *Chester and Chester*, 1990; *Erslev*, 1991; *Homza and Wallace*, 1995; *Wickham*, 1995; *Allmendinger*,

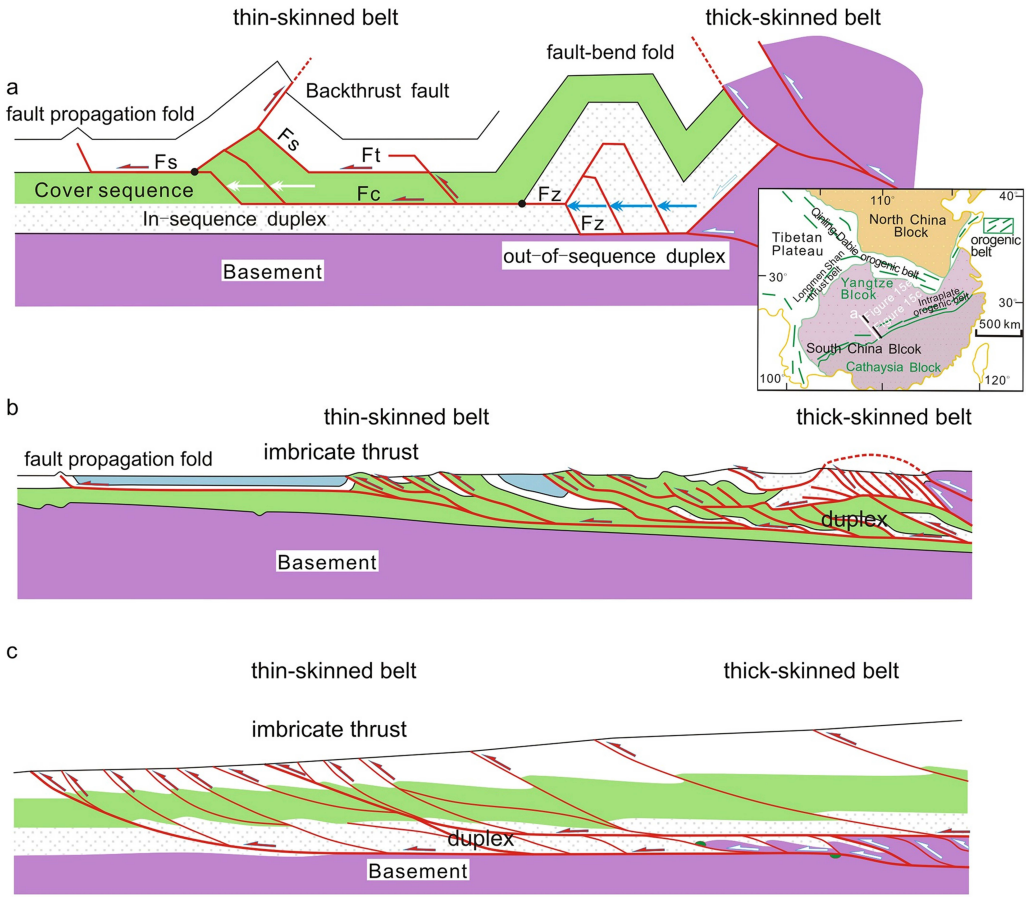


Figure 1.2: Three cross-sections through thrust belts showing a variety of possible structural styles. Modified from *Yan et al.* (2016). a) Cross-section through part of the South China Block. b) A cross-section from the Southern Appalachians. c) Idealized sketch of a thrust belt synthesized from the Moine thrust zone, Appalachian, and Alps orogenic belts. See *Yan et al.* (2016) for further details and references.

1998; *Amos et al.*, 2007; *Brandenburg*, 2013) (Figure 1.3). Despite these developments in describing the long-term geological development of individual fault systems, it is becoming apparent that some other aspects of reverse fault behaviour remain troublesome. For example, slip in the 2011 M_w 7.1 Van, Turkey earthquake, predominantly took place below ~6–8 km depth on faults that were previously unmapped (*Elliott et al.*, 2013; *Fielding et al.*, 2013; *Akoğlu et al.*, 2018). *Mackenzie et al.* (2016) showed that the topography above those faults is not representative of them but is instead controlled by differently oriented shallower faults that did not rupture in the 2011 earthquake (Figure 1.4). The results of *Mackenzie et al.* (2016) and others (*Falcon*, 1969; *Landgraf et al.*, 2013; *Copley and Reynolds*, 2014; *Copley and Jolivet*, 2016; *Melnick*, 2016)

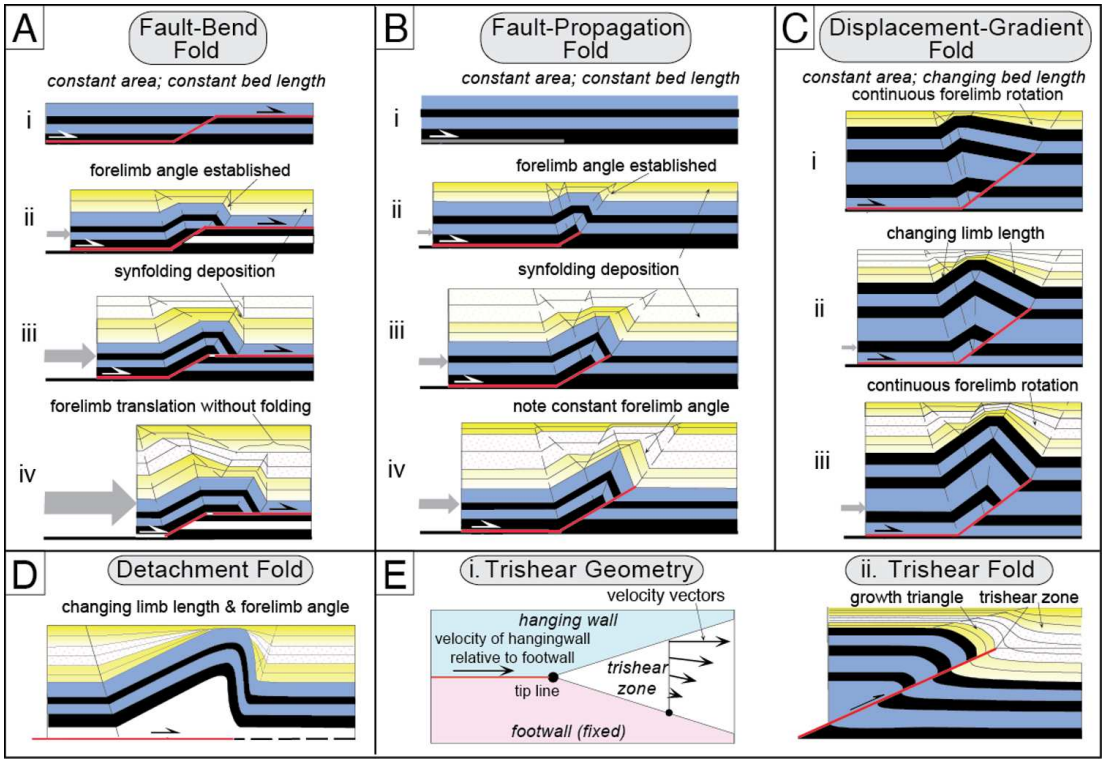


Figure 1.3: Diagrams showing five of the most commonly used and adapted geometric models for folds associated with a blind reverse fault. Reproduced from *Burbank and Anderson* (2011).

suggest that although observations of surface geomorphology and geology have been widely (and often successfully) used to aid characterisation of reverse faults, there may be limitations on what current methods can tell us about active reverse faults, and particularly their seismicity, based on surface observations.

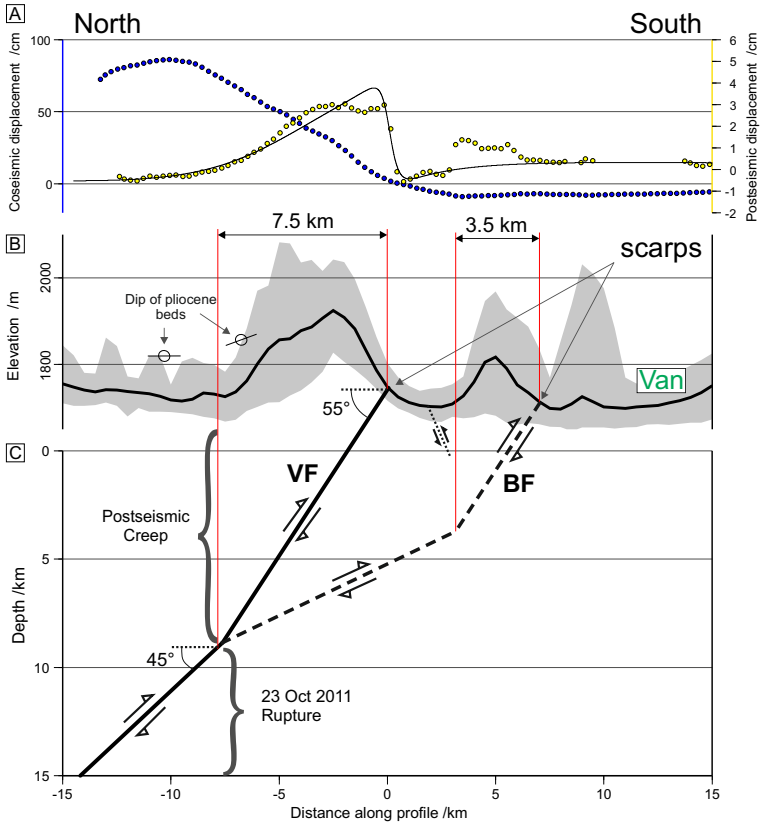


Figure 1.4: Cross-section through the western part of the Van Fault, reproduced from *Mackenzie et al.* (2016). The M_w 7.1 earthquake occurred at depth, whereas the topography and early postseismic deformation respond to shallower faults. a) Profiles through the line-of-site coseismic (blue) and early postseismic (yellow) displacements from the 23rd October 2011 earthquake. b) SRTM topography along the same profile (average in black, full range in grey). c) Structural cross-section.

1.2 Central Asian Tectonics and Cenozoic History

Around fifty million years ago the Indian continent collided with Eurasia (*Dupont-Nivet et al.*, 2010; *Najman et al.*, 2010; *Bouilhol et al.*, 2013; *DeCelles et al.*, 2014; *Hu et al.*, 2015). The collision zone became the largest active continental collision on earth and convergence continues to this day at a rate of ~35 mm/yr (*Kreemer et al.*, 2014). The most prominent consequence of the collision is the uplift and crustal thickening of the Tibetan Plateau (*Dewey and Burke*, 1973; *Chen et al.*, 1993) (Figure 1.5), but a much larger surrounding area has also been affected. That surrounding area plays an important role in the accommodation of the motion of India today (*Molnar and Tapponnier*, 1975; *Tapponnier and Molnar*, 1976), and it is the area northwest of the

Tibetan Plateau that is the focus of this thesis.

Immediately north of much of the Tibetan Plateau sits the Tarim Basin. Because of its strength (*Molnar and Tapponnier*, 1981; *Vilotte et al.*, 1984; *England and Houseman*, 1985; *Neil and Houseman*, 1997), the Tarim Basin undergoes very little internal deformation (*Reigber et al.*, 2001; *Shen et al.*, 2001; *England and Molnar*, 2005) and instead comprises a large, rigid, low elevation region within the collision zone. Active shortening resumes on the far side of the basin in the Tien Shan mountain range (Figure 1.5). The Tien Shan experienced a period of tectonic quiescence in the Mesozoic and early Cenozoic, causing much of the region to be peneplained (*Makarov*, 1977; *Chediya*, 1986; *Abdrakhmatov et al.*, 2001) but ∼20-25 Ma it began to undergo north-south shortening and topographic growth as a result of the India-Eurasia collision (*Hendrix et al.*, 1994; *Sobel and Dumitru*, 1997; *Yin et al.*, 1998; *Bande et al.*, 2017a). Shortening is now taking place throughout the range on reverse faults and some strike-slip faults (*Ghose et al.*, 1998; *Abdrakhmatov et al.*, 2001; *Thompson et al.*, 2002). The rate of shortening has varied through time (*Burbank et al.*, 1999; *Bullen et al.*, 2003; *Bande et al.*, 2017a) but currently it reaches ∼22 mm/yr in the western part of the Tien Shan (up to two thirds of the total India-Eurasia convergence rate) (*Abdrakhmatov et al.*, 1996; *Reigber et al.*, 2001; *Zubovich et al.*, 2010) and slows eastwards (Figure 1.6).

To the west of the Tarim Basin lie the Pamir Mountains (Figure 1.5). Topographically the Pamirs are a slightly lower extension of the Tibetan Plateau. They have indented some 300 km northwards into Eurasia, separating the once-connected Tajik and Tarim Basins (*Burtman and Molnar*, 1993), and continue to indent northwards, subducting Eurasian lithosphere southwards beneath them (*Burtman and Molnar*, 1993; *Fan et al.*, 1994; *Sobel et al.*, 2013). This rapid, localised shortening between the Pamirs and the Tien Shan is evident at the surface across the Alai Valley (*Arrowsmith and Strecker*, 1999; *Zubovich et al.*, 2016) (Figure 1.6). The crustal earthquakes in the interior of the Pamirs have strike-slip and normal focal mechanisms (Figure 1.6). This indicates, and GPS data confirm, that the interior of the Pamirs is still shortening

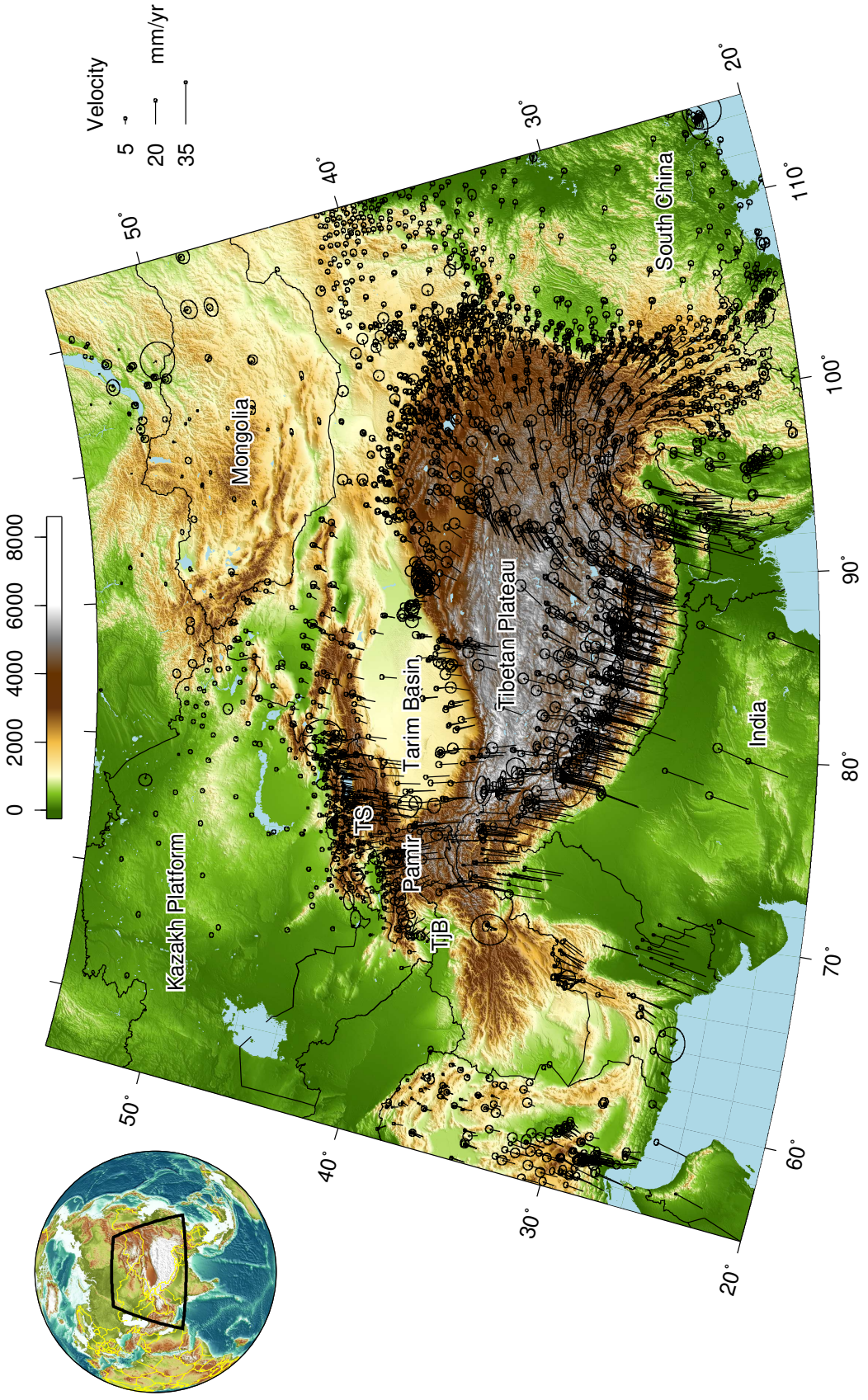


Figure 1.5: Topography and velocity field (*Kreemer et al.*, 2014) of the India-Euarasia collision. TjB: Tajik Basin, TS: Tien Shan.

but, like the Tibetan Plateau, the Pamirs are now also undergoing lateral extension (*Ischuk et al.*, 2013; *Zubovich et al.*, 2016). The rate of extension is around 2.5 times the NNE–SSW shortening rate (*Ischuk et al.*, 2013; *Zubovich et al.*, 2016) and has been interpreted to be the result of gravitational collapse (*Strecker et al.*, 1995; *Burtman*, 2013; *Schurr et al.*, 2014; *Zubovich et al.*, 2016; *Jay et al.*, 2017).

The Tien Shan and Pamir ranges are often described as archetypes of intracontinental mountain belt and intracontinental subduction respectively (e.g. *Ghose et al.*, 1998; *Bullen et al.*, 2001; *Blayney et al.*, 2016; *Landgraf et al.*, 2016; *Bande et al.*, 2017b). This is due to their large size, high deformation rates, relatively straightforward settings and the paucity of other active examples, but they are nonetheless relatively under-studied compared to other regions of active continental tectonics around the world. Although there is a sizeable body of literature in the Russian and Chinese languages (some of which I have found and cited for this thesis but which I acknowledge I have not been able to do full justice to), access to the region and to the literature was difficult for western scientists for most of the second half of the twentieth century. In the past two and a half decades, access to Central Asia has become considerably easier and a great deal of important research has been done. However, practical deterrents to study, summarised by *Brunet et al.* (2017) as "the remote, mountainous topography, the vast desert basins and the inconveniently placed, uncrossable borders", still remain and have left many questions still to be answered.

Remoteness aside, much of Central Asia is currently well-suited to study of the surface expression of active faults. Most importantly, it contains numerous active faults, some of which have slipped in earthquakes during the instrumental era (e.g. *Abdrakhmatov et al.*, 2001; *Thompson et al.*, 2002; *Ghose et al.*, 1998; *Burtman and Molnar*, 1993). Although there is some snow and ice coverage, vegetation rarely obscures the geomorphology, meaning that the surface geomorphology is clear both in the field and in satellite images. Fault slip rates are high enough and erosion rates low enough for the tectonic influence on geomorphology to be visible (if not always easily recognised and

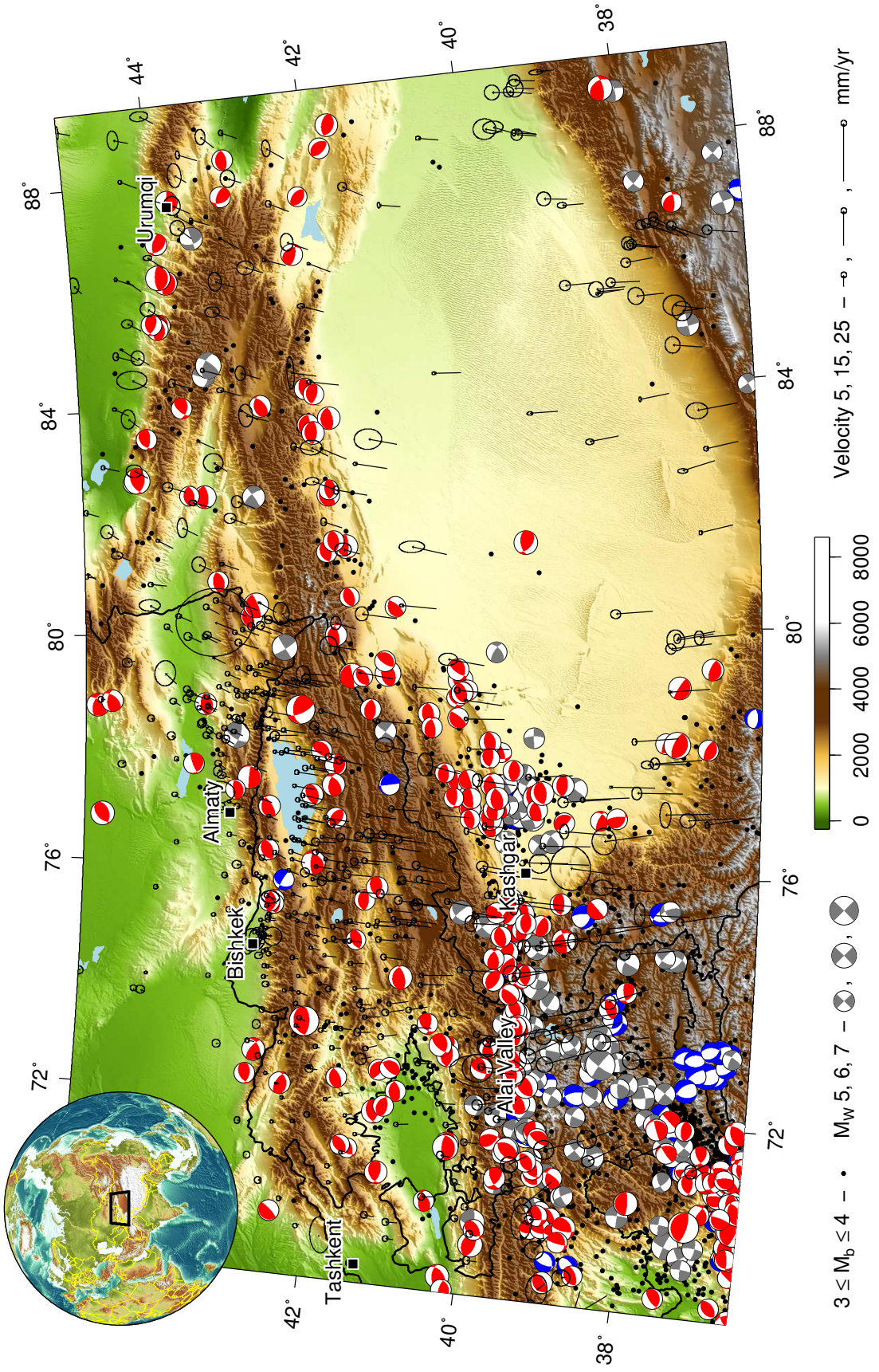


Figure 1.6: Topography, earthquakes (mechanisms from the GCMT catalogue (*Ekström et al.*, 2012), black dots from the USGS catalogue) and velocity field (*Zheng et al.*, 2017) of the Tarim Basin, Tien Shan and Pamir.

interpreted), with the result that Central Asia has been the setting of several studies that have made important contributions to the field of active faulting more generally (*Burbank and Anderson*, 2011). Finally, the political situation (in Kyrgyzstan for the purposes of this thesis) permits good access for fieldwork, enabling samples to be collected for Quaternary dating and more detailed analyses to be done.

The high rates of deformation in Central Asia indicate that it is likely to be liable to earthquakes, but historical records reinforce that message. Central Asia has a history of damaging earthquakes. The cities of Almaty and Tashkent illustrate this problem well. Almaty, the former capital of Kazakhstan (Figure 1.6) was destroyed or damaged three times around the turn of the 20th century, by the 1887 M7.3 Verny (*Hay*, 1888; *Mushketov*, 1890; *Kondorskaya et al.*, 1982), 1889 M8 Chilik (*Mushketov*, 1891; *Krüger et al.*, 2015; *Abdrakhmatov et al.*, 2016) and 1911 M8.0 Chon-Kemin (*Bogdanovich et al.*, 1914; *Delvaux et al.*, 2001; *Kulikova and Krüger*, 2015) earthquakes. In contrast, the 1966 M5.1 Tashkent, Uzbekistan earthquake (Figure 1.6, *Kondorskaya et al.* (1982)) shows the damage that can be done by even a moderate magnitude earthquake in unfavourable conditions. It had a shallow hypocentre directly beneath the city of Tahkent and reportedly left 200,000–300,000 people homeless although there were few fatalities (*RIA Novosti*, 2011). Seismic catalogues list many more strong and major earthquakes that have hit Central Asia (e.g. *Kondorskaya et al.*, 1982; *Kalmetieva et al.*, 2009), but the slip rates, earthquake histories and geometries of its faults are still far from fully understood, showing that there is a practical as well as academic need for research on Central Asian tectonics. Overall, Central Asia is a highly suitable focus region for a study on reverse faults and their surface expression because the tectonic situation of the region is of academic interest, amenable to study and creates seismic hazard.

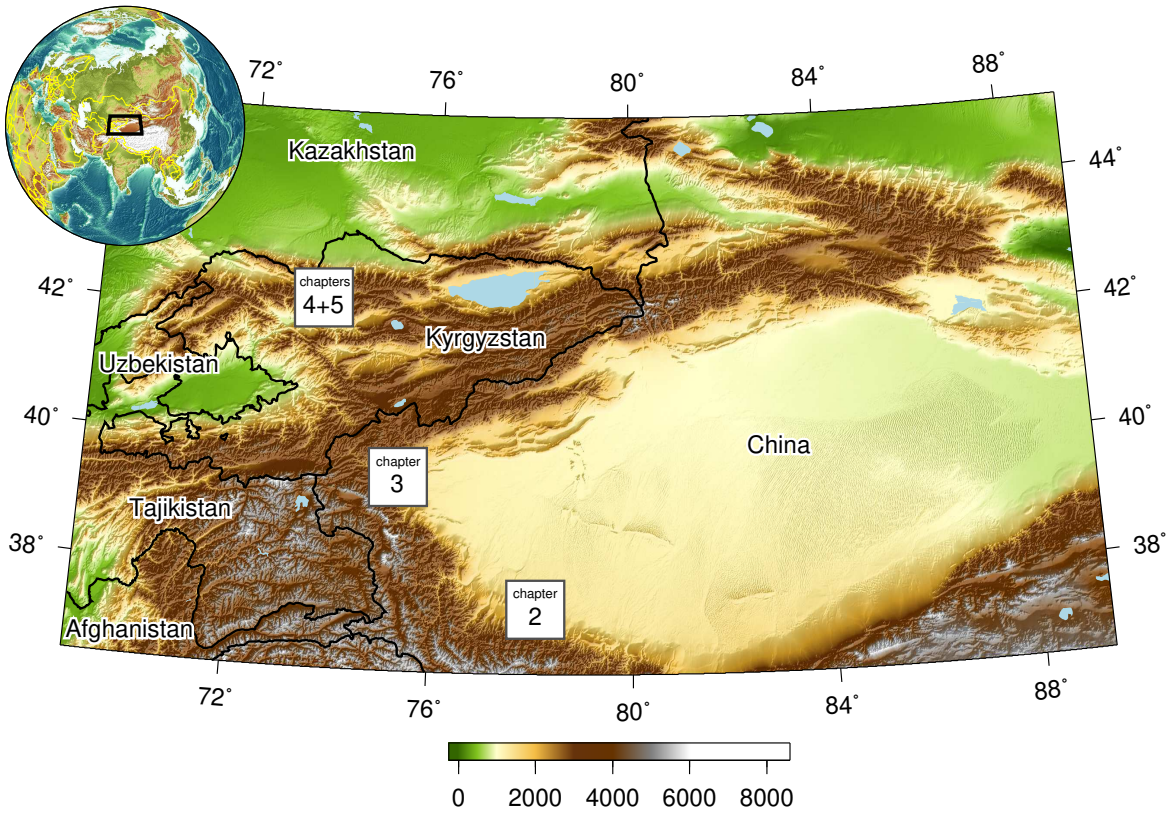


Figure 1.7: Map showing the locations studied in this thesis. They are marked by white boxes and the corresponding chapter numbers.

1.3 Overview of this Thesis

This thesis describes the results of research on the active faults and folds in three locations in Central Asia, which are shown in Figure 1.7. A general goal of the thesis is to add to the much-needed body of knowledge on the characteristics of active faults. My more specific focus is on our understanding of the surface expression of reverse faults. I aim to contribute to extending what is understood about reverse faults and earthquakes from surface observations, and to identifying the limitations of this endeavour.

In **Chapter 2** I address the question of how and when shallow folds grow by investigating the 2015 Pishan, China earthquake. Pishan is well suited to studies of deformation through the earthquake cycle because its tectonic situation is relatively straightforward and there is an excellent variety of datasets available for it. These datasets allow me to compare the deformation that takes place during different phases

of the earthquake cycle and at different timescales.

In **Chapter 3** I look at the effect that a detachment may have in masking the effects of a basement fault by reinvestigating the 1985 Wuqia, China earthquake. Previous studies on the Wuqia earthquake have each focussed on only one aspect of the earthquake. In this chapter I synthesise those data, add to them with new analysis of 20th century archive imagery, and interpret them in the context of the regional stratigraphy and structural geology.

In **Chapter 4** I ask how reliable surface scarps are for determining earthquake history in the Tien Shan by conducting a detailed study of surface ruptures from the 1992 Suusamyr, Kyrgyzstan earthquake and prehistoric earthquakes along the same fault.

In **Chapter 5** I take a broader perspective on the Suusamyr Basin, Kyrgyzstan and its surroundings. Only the south-dipping fault in the western half of the basin ruptured in 1992. In this chapter I map the surface expression of shortening in the entire Suusamyr Basin and estimate the slip rate of the Suusamyr Fault.

In **Chapter 6** I briefly reflect on the overall findings of the thesis and on some promising directions for future research that are suggested by this work.

Full introductions to the particular location and scientific question that each chapter addresses, and the methods used, are given within the chapters.

1.4 Publications arising from this thesis

The material of Chapter 2 is published in *Ainscoe et al.* (2017):

> Ainscoe, E. A., J. R. Elliott, A. Copley, T. J. Craig, T. Li, B. E. Parsons, R. T. Walker, Blind Thrusting, Surface Folding, and the Development of Geological Structure in the M_w 6.3 2015 Pishan (China) Earthquake, 2017, *Journal of Geophysical Research: Solid Earth*, 122, 11, 9359–9382, doi:10.1002/2017JB014268

The material of Chapter 4 is published in *Ainscoe et al.* (2019):

> Ainscoe, E. A., K. E. Abdrakhmatov, S. Baikulov, A. S. Carr, A. J. Elliott, C. Grützner, R. T. Walker, Variability in Surface Rupture Between Successive Earthquakes on the Suusamyr Fault, Kyrgyz Tien Shan: Implications for Palaeoseismology, 2019, *Geophysical Journal International*, 216, 1, 703–725, doi:10.1093/gji/ggy457

Chapter 2

The Development of Geological Structure and Surface Folding at a Rangefront Thrust: The M_w 6.3 2015 Pishan (China) Earthquake

2.1 Introduction

The relationship between individual earthquake cycles and the long-term development of fold and thrust structures is not fully understood. Theoretical geometrical models have been proposed to describe how folds form and grow over time above thrust faults with various geometries (e.g. *Suppe*, 1983; *Suppe and Medwedeff*, 1990; *Erslev*, 1991; *Homza and Wallace*, 1995) and the development of thrust-related folds in nature over tens of thousands to millions of years has been studied by analysis of drainage, topography and structural geology (e.g. *Burbank et al.*, 1999; *Daëron et al.*, 2007). However, it is not clear how complex fault and fold structures develop through repeated earthquake cycles, nor how these longer term structures may or may not correlate with the surface deformation measured today (e.g. *Nissen et al.*, 2007). The relative importance

of interseismic, coseismic and postseismic deformation to the development of geological structures and topography in regions of continental shortening is not known. Given that historical records of earthquakes are often much shorter than the recurrence times for each fault, data sources with longer temporal coverage and global spatial coverage, such as digital elevation models and geomorphology, combined with dating, provide a valuable opportunity to augment assessments of seismic hazard (*Stein and King*, 1984; *Taylor and Yin*, 2009; *Zhou et al.*, 2015a; *Talebian et al.*, 2016). Making use of this opportunity depends on developing an ability to interpret the spatial and temporal relationship between long-term structures and individual earthquakes. To address this issue, here I investigate structural growth at a blind rangefront thrust where we can directly compare surface motion observations from InSAR, sub-surface seismic reflection data, and surface geomorphology.

On 3 July 2015 an M_w6.3 earthquake hit Pishan county in Xinjiang, China at 01:07:47 UTC (09:07 local time). Local media reported three deaths and damage to several thousand buildings. The epicenter was located approximately 20 km southwest of the historic Silk Road town of Pishan (also known as Guma), an oasis town on the edge of the Taklamakan Desert. Thirty aftershocks with magnitude $m_b \geq 4.0$ were reported by the United States Geological Survey (USGS) in the seven months following the earthquake and form a distributed pattern roughly trending northwest-southeast, approximately 100 km in extent (Figure 2.1).

I present a source model for the Pishan earthquake based on Sentinel-1 interferometric synthetic aperture radar (InSAR) and teleseismic body wave modelling. I subsequently identify postseismic motion in interferograms covering the first seven months following the event. I correlate the relative locations and magnitudes of coseismic and postseismic displacements to the tectonic geomorphology of the area in order to constrain the mechanism by which the current topography has formed over the late Quaternary. I compare my results to a seismic reflection survey across the same location to investigate the full history of the underlying folds and thrusts in the Pliocene.

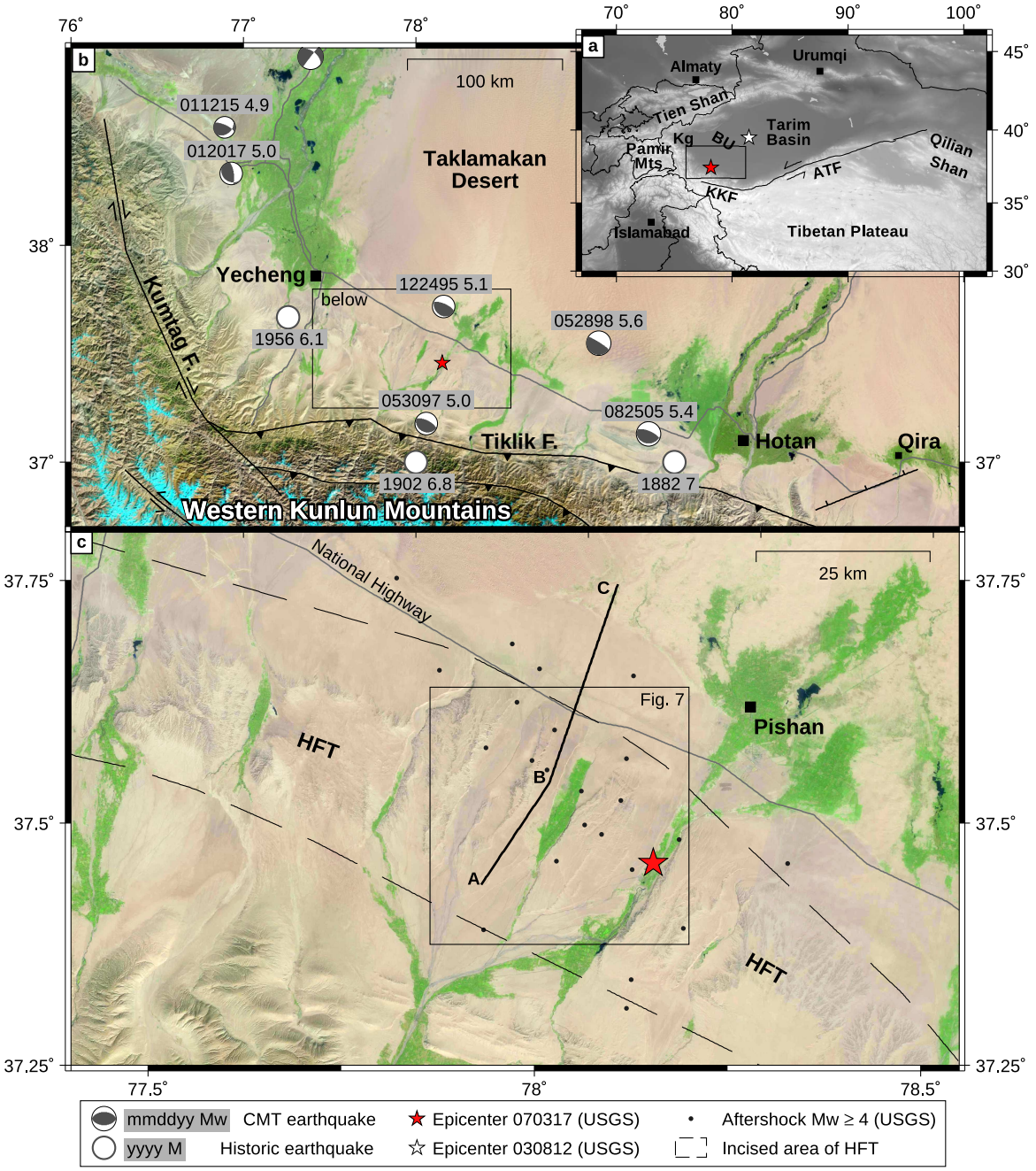


Figure 2.1: a) Overview map of the Tarim Basin and its surroundings. ATF: Altyn Tagh Fault. KKF: Karakax Fault. BU: Bachu Uplift. Kg: Kashgar city. Black rectangle shows the area of panel b. b) Landsat 8 imagery (RGB 654) of the southwest Tarim Basin region. Faults after (*Wei et al.*, 2013) and (*Avouac and Peltzer*, 1993). c) Landsat imagery around the epicenter of the 2015 Pishan earthquake (red star) and showing the incised area above the Hotan Fold and Thrust Belt (HFT). Line A-B-C shows the location of the seismic reflection profile (Section 2.4).

2.2 Tectonic setting

Pishan is situated at the margin between the Tibetan Plateau and the southwestern corner of the Tarim Basin, 800 km north of the Himalayan front (Figure 2.1). The Tarim Basin acts as a rigid block within the India-Eurasia collision; although it is surrounded by mountain ranges undergoing active shortening - the Tien Shan to the north, the Pamir mountains to the west and the Tibetan Plateau to the south - the Tarim Basin has low seismicity, flat topography and GPS measurements show little internal deformation (*Molnar and Tapponnier*, 1978; *England and Molnar*, 2005). At the south-west corner of the Tarim Basin, where I focus my attention in this chapter, gravity anomalies (*Lyon-Caen and Molnar*, 1984), receiver functions (*Kao et al.*, 2001; *Wittlinger et al.*, 2004), seismic refraction (*Qiusheng et al.*, 2002), and geological mapping (*Matte et al.*, 1996) show that the Tarim Basin is underthrusting the Western Kunlun Mountains, which form the edge of the Tibetan Plateau. GPS stations are relatively sparse, but 0–3 mm/yr of N-S convergence is possible within the uncertainties of the measurements (*Ge et al.*, 2015), and the region has hosted M_s 7.0 and 6.8 earthquakes in 1882 and 1902 respectively and an M_w 6.1 event in 1956 (*Lee et al.*, 1978; *Avouac and Peltzer*, 1993; *Li et al.*, 2012a; *USGS*, 2017) (Figure 2.1).

Across the northern rangefront of the Western Kunlun Mountains the elevation changes rapidly from 5000 m to 2100 m within a horizontal distance of just 50 km and post-Mesozoic basin sediments have a thickness of around 10 km (*Wei et al.*, 2013; *Jiang and Li*, 2014). The most basinward active shortening visible at the surface is in the low-lying, gently northward-sloping piedmont. The structures here are known as the Hotan Fold and Thrust Belt and are expressed around Pishan as a belt of exposed and folded bedrock and terraces crossing from 77.0°E, 37.75°N to 78.75°E, 37.2°N (Figure 2.1). The total upper crustal shortening across the Hotan Fold and Thrust Belt has been of the order of several tens of kilometres (*Jiang et al.*, 2013) and occurred in two stages: the first ∼23–10 Ma, and the present stage, into which the 2015 Pishan earthquake falls and which began ∼5 Ma (*Wei et al.*, 2013; *Jiang and Li*, 2014).

Table 2.1: Details of the Sentinel-1A interferograms used in this study.

Track	Direction asc/dsc	Date 1 yymmdd	Date 2 yymmdd	⊥ B [a] m	ΔT [b] days	ΔPT [c] days	Gradient removed [d] cm/km
			Coseismic interferograms				
129	asc	150611	150705	-39	24	2	-
056	asc	150630	150724	53	24	21	-
136	dsc	150624	150718	-26	24	15	-
			Postseismic interferograms				
129	asc	150705	160113	-46	192	-	2.43
056	asc	150724	160201	-133	192	-	4.19
136	dsc	150718	160102	19	168	-	2.72

[a] Perpendicular baseline at scene centre.
[b] Timespan.
[c] Postseismic interval.
[d] Topographically-correlated phase gradient removed from the interferogram.

2.3 3 July Pishan Earthquake fault geometry and coseismic slip distribution

2.3.1 InSAR

Coseismic Sentinel-1 interferograms

I used InSAR data showing ground displacements to obtain the focal parameters of the Pishan mainshock and made use of the interferograms' dense near-field spatial coverage to constrain the fault location, slip extent and slip distribution. The coseismic ground deformation was measured by constructing interferograms using data from the European Space Agency's (ESA) Sentinel-1A satellite, which carries a C-band synthetic aperture radar (SAR). I made interferograms from three tracks: two ascending and one descending (Figure 2.2, Table 2.1), each had a timespan of 24 days.

In interferometric wideswath mode, as used in this study, Sentinel-1 uses the Terrain Observation with Progressive Scans (TOPS) acquisition method (*De Zan and Monti Guarnieri*, 2006). This produces a swath with a total width of 250 km, acquired in three sub-swaths. Each sub-swath is acquired as a series of individual bursts

of ∼19 km length in which the beam is steered in the azimuth direction from backwards to forwards. Each full interferogram therefore contains multiple burst and sub-swath boundaries. Across each burst boundary there is a significant change in viewing geometry and Doppler centroid, so highly accurate coregistration is required to avoid phase jumps at the burst boundaries.

I processed the radar data using the GAMMA software to coregister single look complex (SLC) images to within <0.0005 SLC pixel in azimuth (less than 1 cm). An initial coregistration lookup table was made taking into account precise orbit state vectors and elevation using the 30 m SRTM1 DEM from the USGS. I then determined a uniform offset in range and azimuth to apply to the entire slave SLC. This was initially done using intensity cross-correlation of a number of patches, iterated until the azimuth offset was <0.01 SLC pixel. I then refined the offset using a spectral diversity method (*Scheiber and Moreira*, 2000) and iterated until the azimuth offset was <0.0005 SLC pixel.

After coregistration I constructed the differential interferogram and filtered it three times using an adaptive spectral filter (*Goldstein and Werner*, 1998). This emphasises the dominant wavelengths in the signal, preserving high phase gradients and minimizing the extent of incoherent areas affecting unwrapping. The initial coherence was generally high and interferograms were inspected visually after each step of filtering to ensure that there were no modifications during filtering which would bias my following analysis. I masked the interferograms to 95% coherence and unwrapped them using a Minimum Cost Flow algorithm. The final interferograms were geocoded and downsampled to 100 m. Where available I used the 30 m STRM1 dataset for topographic correction. I found that the voids in the SRTM data had been imperfectly filled in the 90 m SRTM Plus dataset. At void boundaries there is a step change in elevation that led to phase errors in the interferograms. I therefore used the non-void filled SRTM1 DEM and did not retrieve the phase within the void areas. These regions are situated predominantly in the mountains to the south, well away from the tectonic deformation. The perpendicular

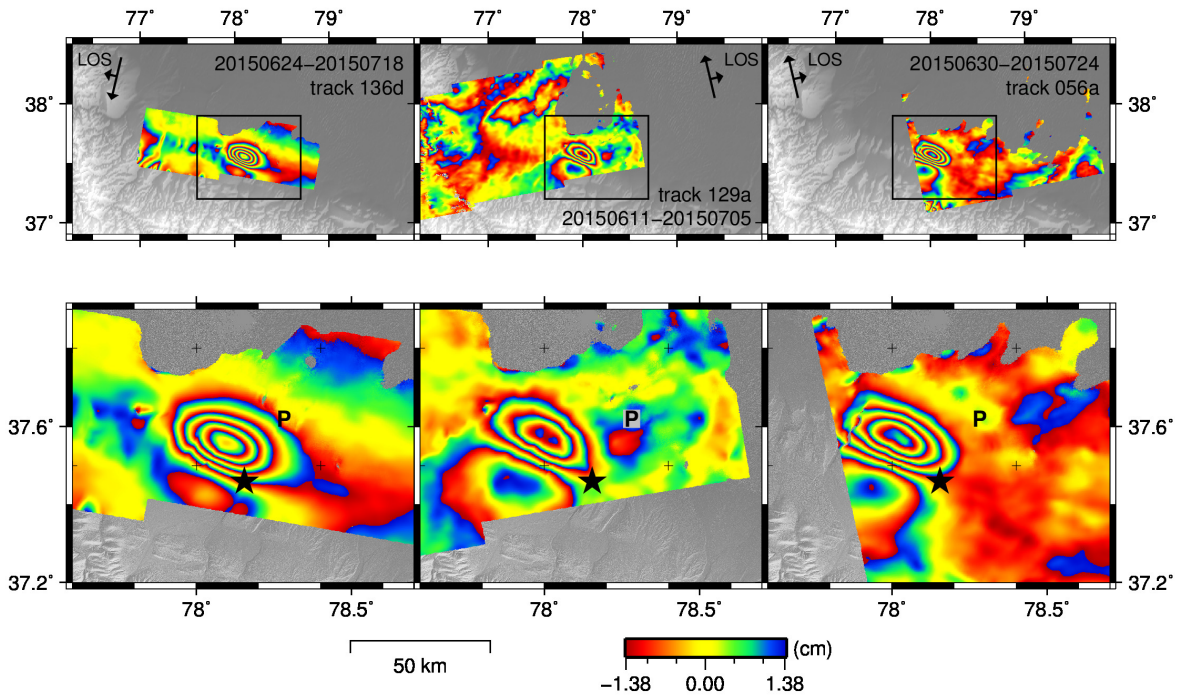


Figure 2.2: Coseismic interferograms from three Sentinel-1 tracks. Top row shows the full extent of each interferogram used in this study, overlaid on a hillshaded topographic map. The lobe with the greatest change shows decreased range, i.e. displacement towards the satellite. The timespan of each interferogram is printed on the right, format yyyymmdd. Black box shows the area enlarged in the lower panel. Black stars show epicenter (USGS), P marks Pishan town.

baselines for all interferograms used in this study are <150 m.

The final interferograms were geocoded and downsampled to 100 m. They show a simple two-lobed signal that varies smoothly over ∼45 km, consistent with a blind event associated with buried faulting (Figure 2.2). The northern lobe indicates motion towards the satellite, with a peak line-of-sight (LOS) displacement of 11.8 cm for track 056a. The southern lobe represents motion away from the satellite, with peak LOS motion of 5.9 cm for the same track. The three tracks cover the spatial extent of the entire deformation zone, although coherence is lost in some areas of the desert 50 km to the north of Pishan. Whilst the two ascending interferograms covering the earthquake have the same look geometry, the different locations of the peak displacement of the earthquake relative to the SAR scene extents provides differing sensitivities to the ground deformation: the earthquake lies in the near-range portion of track 056a, with

incidence angles ∼30°, indicating a greater sensitivity to vertical motion than east-west; for track 129a the incidence angle is nearer 45° in the far range, resulting in an equal sensitivity to vertical and east-west ground displacement.

Uniform-slip model

By fitting the ground displacements measured by InSAR with an elastic dislocation model (*Okada*, 1985; *Wright et al.*, 1999) I obtained an independent estimate of the fault parameters. The model comprises uniformly distributed slip on a rectangular dislocation in an elastic half-space and I inverted for strike, dip, rake, location in x and y, top depth, bottom depth, length and slip.

Elastic constants of the half-space were set by selecting Lamé parameters: $\lambda = \mu = 3.23 \times 10^{10}$ Pa. To reduce computation times, and to give greater weight to the observations closer to the fault, I used a median filter to downsample the 100 m resolution interferograms to a 2 km grid in the near-field and a 10 km grid in the far-field. The interferograms do not contain any discontinuities as are seen in surface-rupturing earthquakes and, given the smooth deformation signal, a 2 km spacing gives high enough resolution to represent the full displacement signal given the spatial wavelength of correlated atmospheric noise. After downsampling I have 2654 data points in total across the three tracks. The method used a nonlinear downhill Powell's algorithm with multiple Monte Carlo restarts (*Wright et al.*, 1999) to find the best-fitting model to my downsampled interferograms. Orbital errors and choice of unwrapping point were accounted for by solving for the nuisance parameters of linear gradients in phase across the interferograms (flattening) and a uniform phase shift.

I estimated uncertainties in my solution by making 250 perturbed interferograms, which had noise added to them based on a characterisation of the noise in a far-field, minimally deformed, portion of each interferogram away from the earthquake (*Wright et al.*, 2003; *Funning et al.*, 2005). The fault parameters found by inverting these perturbed datasets are fitted with normal distributions (Figure 2.4) and give some

Table 2.2: Pishan mainshock fault parameters from catalogues, body wave modelling and uniform slip inversion of InSAR.

Model	Long. (deg)	Lat. (deg)	Strike (deg)	Dip (deg)	Rake (deg)	Centroid depth (km)	Length (km)	Width (km)	Slip (m)	M_o (10^{18} Nm)	M_w
GCMT	78.14[b]	37.58[b]	109	22	85	15.6	-	-	-	5.3	6.4
auxiliary plane			294	68	92						
USGS NEIC	78.154[c]	37.459[c]	105	24	60	15.5	-	-	-	5.3	6.4
auxiliary plane			317	69	102						
He et al. (2016)[a]	78.1390[b] ±0.0004	37.7157[b] ±0.0005	113.8 ±0.2	27.2 ±0.2	93.7 ±0.6	10.98 ±0.05	22.18 ±0.05	8	0.6	4.12	6.33
Wen et al. (2016)[a]	78.057[d] ±0.4km	37.571[d] ±0.3km	114.0 ±1.6	23.6 ±1.5	92.6 ±3.2	8.8 ±0.4	22.1 ±0.5	10.1 ±1.0	0.59 ±0.06	-	6.4
Body wave (this study)	78.14[e]	37.58[e]	102	23	73	16.5	-	-	-	2.5	6.2
auxiliary plane			300	68	97						
InSAR (this study)[a]	78.140[f] ±1.7km	37.777[f] ± 2.7km	112 ±2.4	21 ±2.5	83 ±4.9	11.0 ±0.8	21.5 ±1.1	9.3 ±2.1	0.6 ±0.2	4.0 ±0.2	6.3

[a] Uniform slip model.
[b] Centroid.
[c] Epicenter. Focal depth 20.0 km.
[d] Not specified.
[e] Fixed at GCMT location.
[f] Up-dip projection of center.
[g] Fixed.

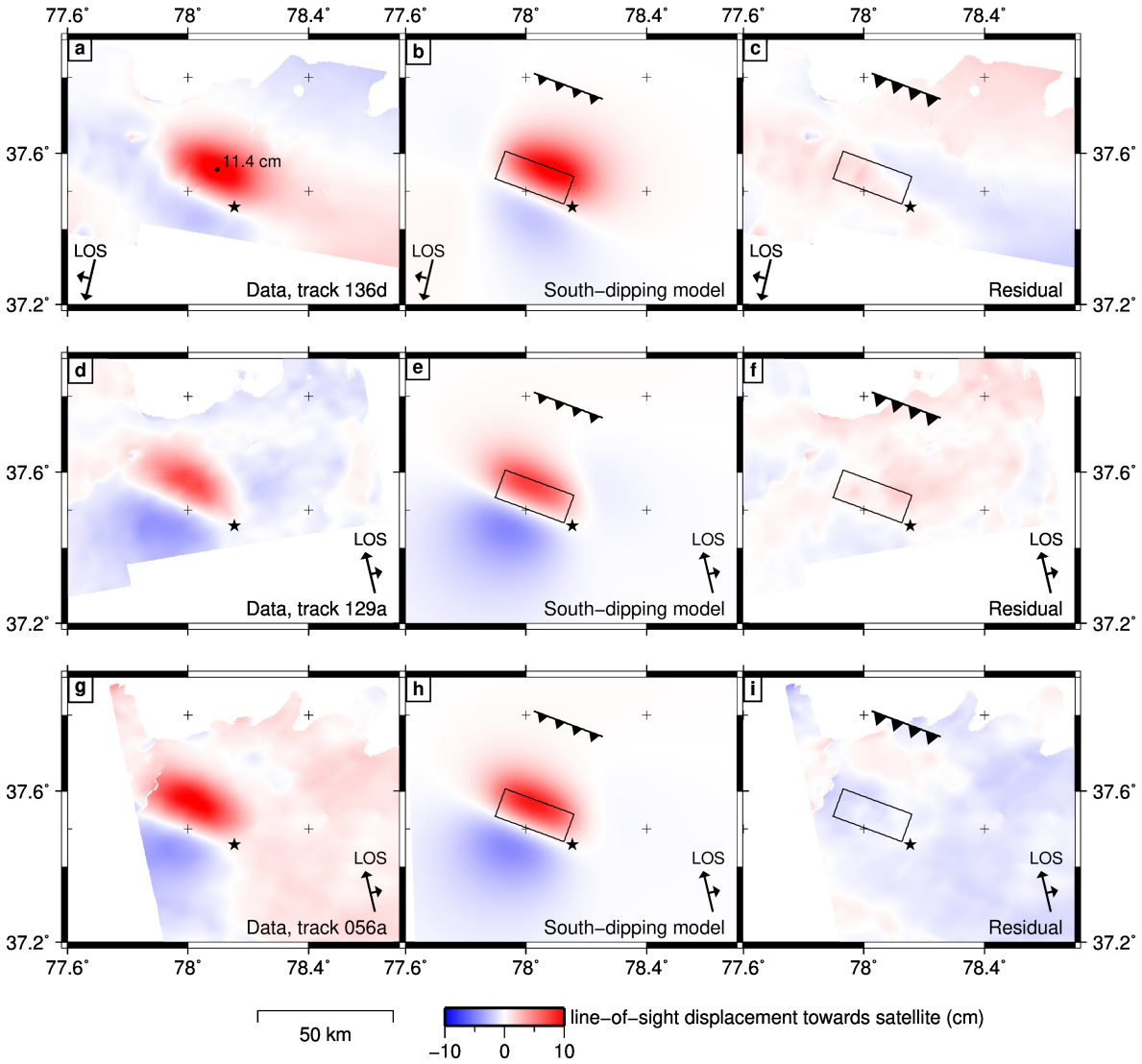


Figure 2.3: Results of uniform-slip models for the coseismic interferograms. a) Unwrapped interferogram for track 136, location of maximum line-of-sight displacement towards the satellite of 11.4 cm is marked by the black dot. b-c) Model and residual line-of-sight displacement for a south-dipping fault model. Blacked ticked lines:up-dip projection of the fault plane to the surface. Black boxes: location of the uniform slip patch at depth. Black stars: epicenter (USGS). d-f) and g-i) show the equivalent figures for tracks 129 and 056.

indication of the influence of noise, mostly expected to be from the atmosphere (*Scott and Lohman*, 2016), on my results. This provides a more complete assessment of the uncertainties than those of *He et al.* (2016) and *Wen et al.* (2016). The standard deviation for each parameter is listed in Table 2.2.

The result is shown in Figure 2.3 and Tables 2.2 and 2.3. It shows a single reverse faulting earthquake on a fault striking WNW-ESE, parallel to the distribution of

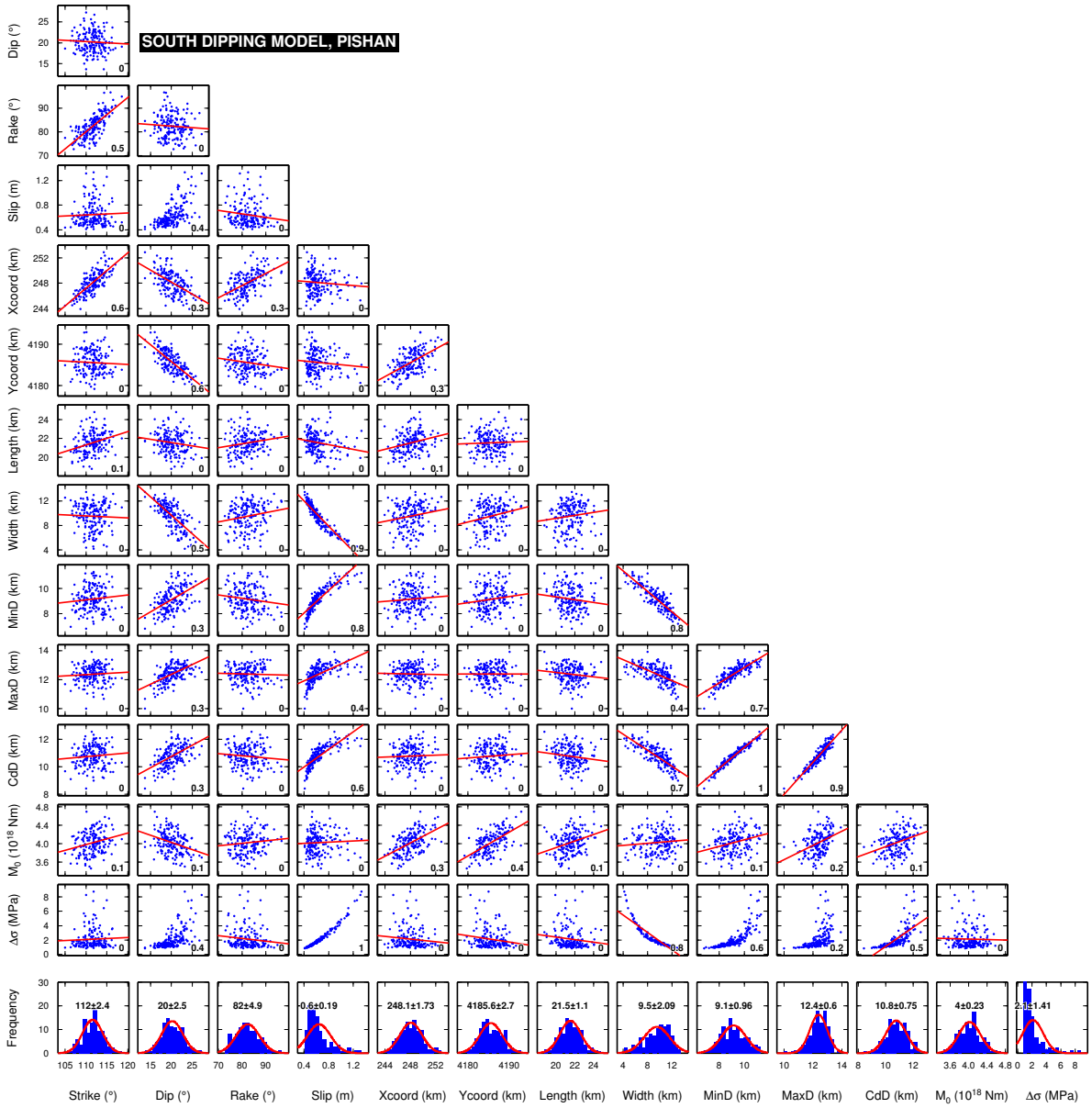


Figure 2.4: Tradeoff plots for the uniform slip model inversion described in Section 2.3.1.

aftershocks and dippping shallowly to the south. The focal mechanism derived from InSAR agrees well with the mechanism obtained by a joint inversion of teleseismic P and SH waveforms performed by Dr T. J. Craig (Figure 2.5) (*Ainscoe et al.*, 2017) and with the GCMT catalogue (Table 2.2). I believe the south-dipping nodal plane is the fault plane because it agrees with the seismic reflection profile presented in *Li et al.* (2016) and Section 2.4, whereas the north-dipping plane would cross unbroken reflectors on the reflection profile and would give a poor fit to the postseismic displacements in

Section 2.6.

Distribution of coseismic slip

To enable a more detailed comparison between coseismic slip and the long-term geological structure visible in seismic reflection profiles (Section 2.4), I invert for the distribution of slip on the fault plane based upon the geometry found in Section 2.3.1.

Taking the location, strike, dip and rake from the uniform slip inversion, I extended the fault plane laterally, to 20 km depth and to the surface. The fault was split into patches of size 2 km in length and ∼2 km in down-dip width, and I carried out a non-negative least-squares inversion to solve for slip on each patch and for the interferogram nuisance parameters (*Wright et al.*, 2004; *Funning et al.*, 2005). In order to find a physically realistic solution the method imposes a positivity constraint and Laplacian smoothing (Figure 2.6). The multiplying factor of the Laplacian (i.e. the strength of the smoothing) determines the balance between roughness and root mean squared (RMS) misfit to the downsampled InSAR data. I chose a smoothing factor in the apex of the RMS misfit vs roughness curve, aiming to give the highest resolution possible without introducing spurious slip patches (Figure 2.6). By inspection of the results from a variety of smoothing factors, I see that my main conclusions are not strongly influenced by the choice of smoothing factor from within a reasonable range.

My preferred slip distribution is shown in Figure 2.7. It shows a single slip patch with a peak slip of 1.1 m, length ∼20 km and down-dip width ∼10 km. This model corresponds to the majority of the slip being at 9.5–13 km depth. I found no substantial slip above 8 km depth. My interferograms have good coverage above the surface projection of the fault planes and I can be confident in my conclusion that the earthquake was blind. My results are consistent with field observations that found no evidence of surface ruptures (*Lu et al.*, 2016) and are also consistent with my interpretation of local geomorphology (Section 2.5), with seismic reflection profiles (*Li et al.*, 2016) and the slip distributions of *Zhang et al.* (2016) and *Sun et al.* (2016) but contradict earlier

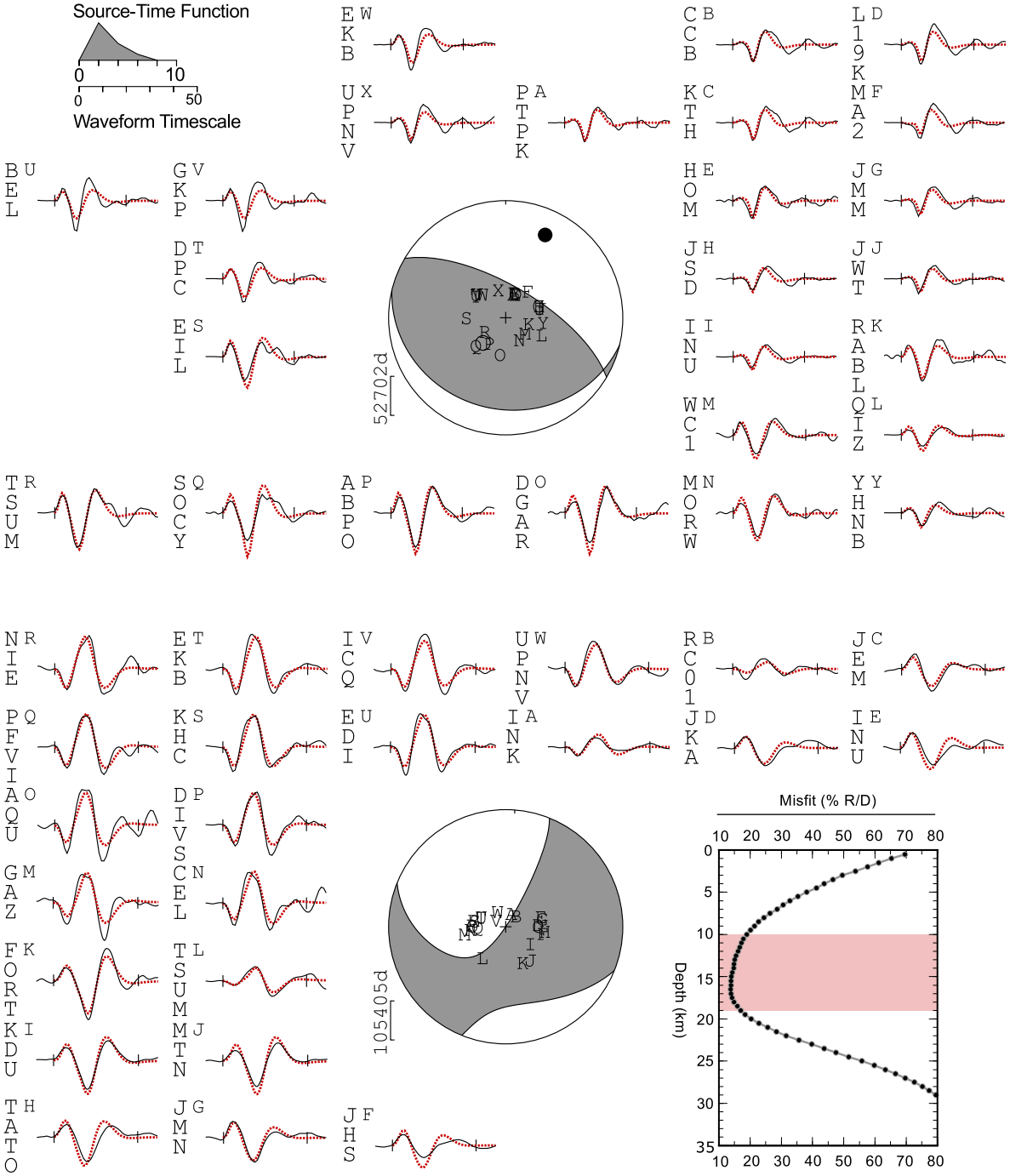


Figure 2.5: Focal mechanisms and source-time function obtained from teleseismic body waveform modelling of P (top) and SH (bottom) waves performed by Dr T.J. Craig (*Ainscoe et al.*, 2017). Mechanisms are shown as lower hemisphere projections with compressional quadrants shaded in gray. Seismograms are shown in black next to their station code, synthetic seismograms from the model solution are shown as dashed red lines. Bottom right: misfits for solutions with depth fixed at a range of values, plotted as a percentage fraction of residual divided by data (% R/D). Pink band shows the acceptable range of depths. Numerical values for this solution are listed in Table 2.2.

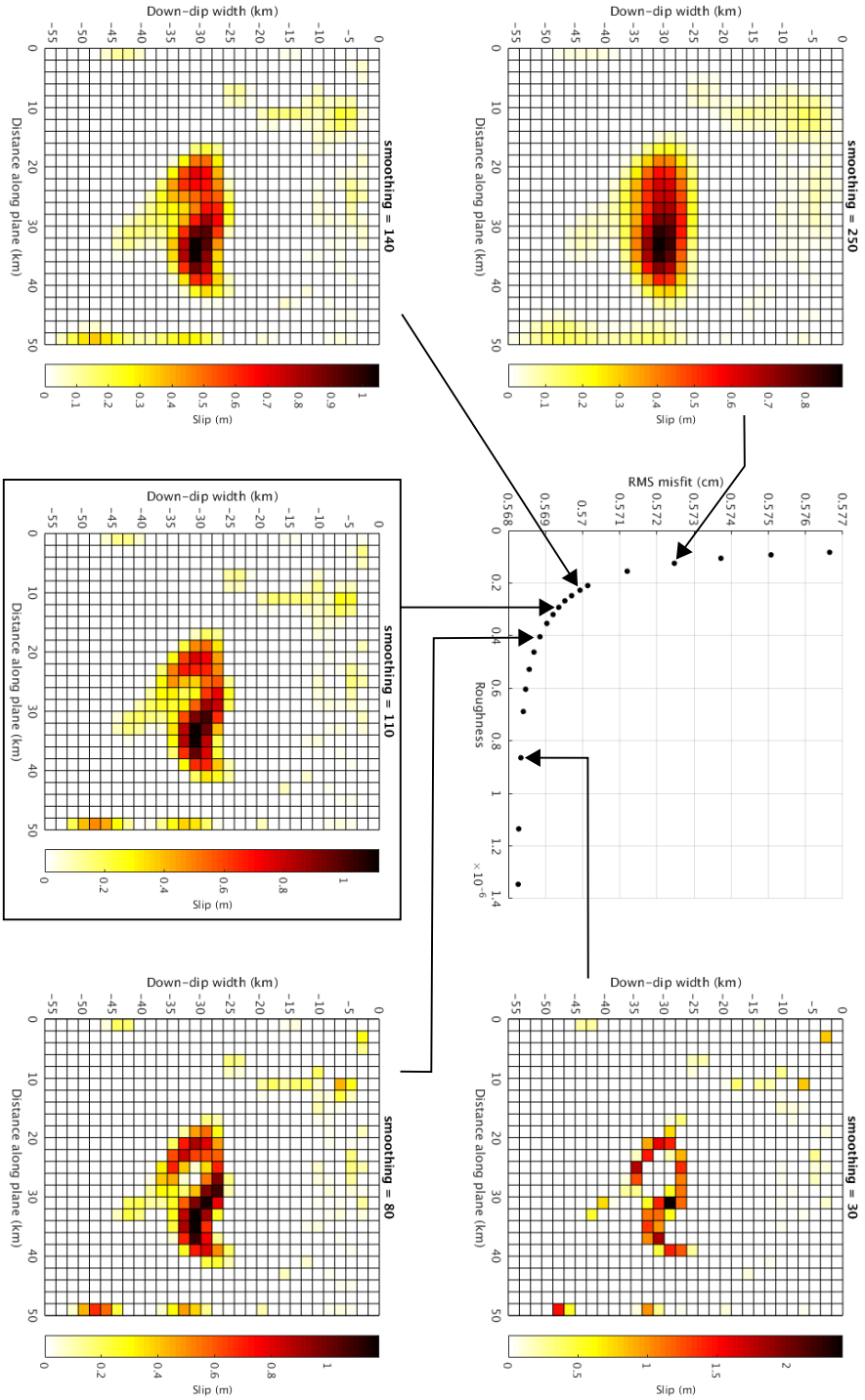


Figure 2.6: The results of applying a variety of smoothing values in the inversion for coseismic slip distribution. The selected smoothing value is 110.

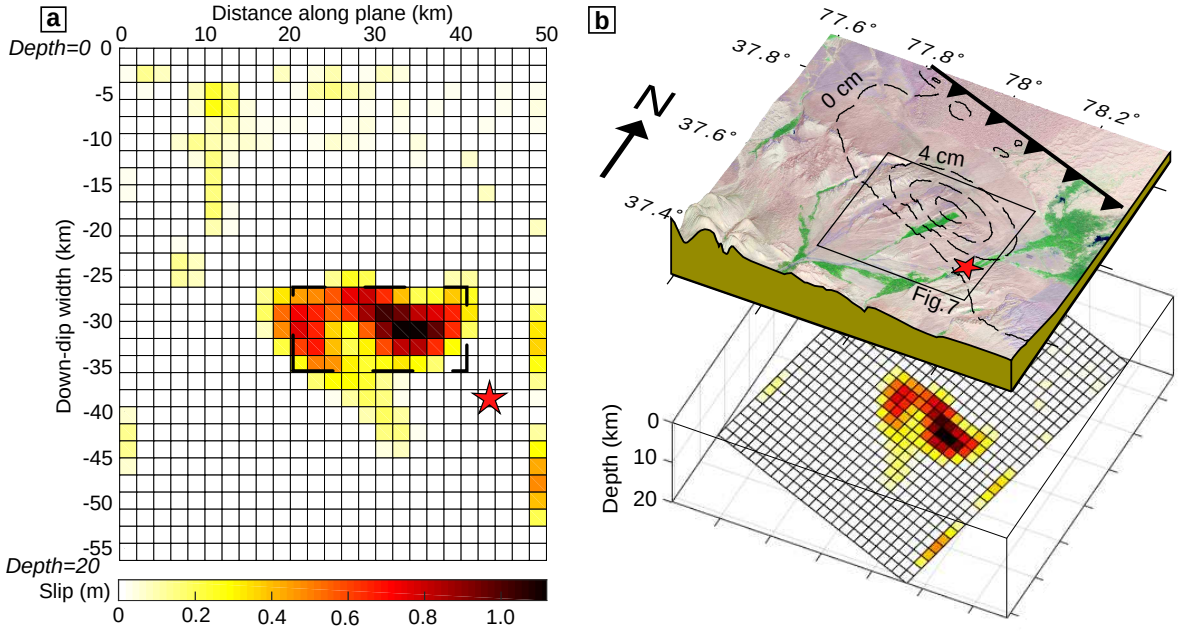


Figure 2.7: a) Coseismic slip distribution. Black dashed lines show the extent of the fault plane from uniform slip model. Red star: hypocenter (USGS), projected onto the fault plane. b) 3D perspective view of the slip distributions and the fault's surface projection. Black dashed lines: contours of the models' vertical ground displacements plotted in 4 cm increments from zero. Black box: location of Figure 2.10. Red star: epicenter (USGS).

Table 2.3: Misfits between the models and interferograms.

Period	Dip direction	Uniform/ Distributed	Track RMS (cm) 129	056	136	Overall RMS (cm)
coseismic	South	distributed	0.58	0.61	0.52	0.57
	South	uniform	0.59	0.66	0.53	0.60
postseismic	South	distributed	0.38	0.30	0.37	0.36

InSAR-derived slip distributions by *Wen et al.* (2016) and *He et al.* (2016). The latter slip distributions each show ~20 cm of slip in the shallow portion of the fault plane, including at the surface. My interferograms show that there is no discontinuity at the surface projection of the fault and I suggest that the shallow slip suggested by other studies (*He et al.*, 2016; *Wen et al.*, 2016) is an artefact as a consequence of their incomplete data coverage in the Taklamakan Desert (Figure 2.1) above the surface projection of the fault plane - the area most sensitive to shallow slip.

2.4 Comparison of fault positions derived from InSAR and seismic reflection

A high-resolution seismic reflection profile that crosses the coseismic slip patch has been published and described by *Li et al.* (2016). Their profile D-D' is a combination of two individual profiles which overlap. Here, in Figure 2.8, I show a slightly modified version (see below) of the more northerly of the two, which crosses the whole of the coseismic fault and was taken along line A-B-C (Figure 2.1). The profile shows a stacked series of northward-vergent thrusts forming a wedge between a basal detachment at the Paleozoic-Pre-Paleozoic boundary and a roofing detachment at the Cenozoic-Mesozoic boundary. Above this wedge lie ∼7.5 km of Cenozoic sediments which are folded into a monocline above the wedge tip and are not offset by any significant faults (Figure 2.8). The wedge is thickened by up to a factor of two compared to the undeformed Paleo-Mesozoic unit north of the thrust tip. This thickening, the sub-horizontal dip of reflectors within most parts of the wedge and the smooth, simple folding of the roofing detachment suggests that, instead of forming by rotation of coherent blocks, internal deformation of the wedge has played a part in its development in addition to slip on the bounding faults. I have added a small backthrust to the interpretation by (*Li et al.*, 2016). The backthrust is the most prominent sign of internal deformation within the wedge and offsets a prominent horizon at 10 km horizontal distance. It is not enough alone to account for the wedge thickening but it could contribute to keeping the reflectors above it sub-horizontal; if the backthrust slipped 1 m for every 2.2 m of slip on the frontal ramp then the two faults would have equal throw. The backthrust is in the hanging wall of the ramp and presumably is transported by it. Due to the constant thickness of the Pliocene unit (N2 on Figure 2.8), *Li et al.* (2016) label it as pre-growth strata and conclude that the initiation age of the deformation of the wedge is ≤3.6 Ma.

I note a very good agreement in location but a difference in dip and depth between my InSAR-derived fault plane estimate and the frontal wedge thrust in *Li et al.* (2016)'s

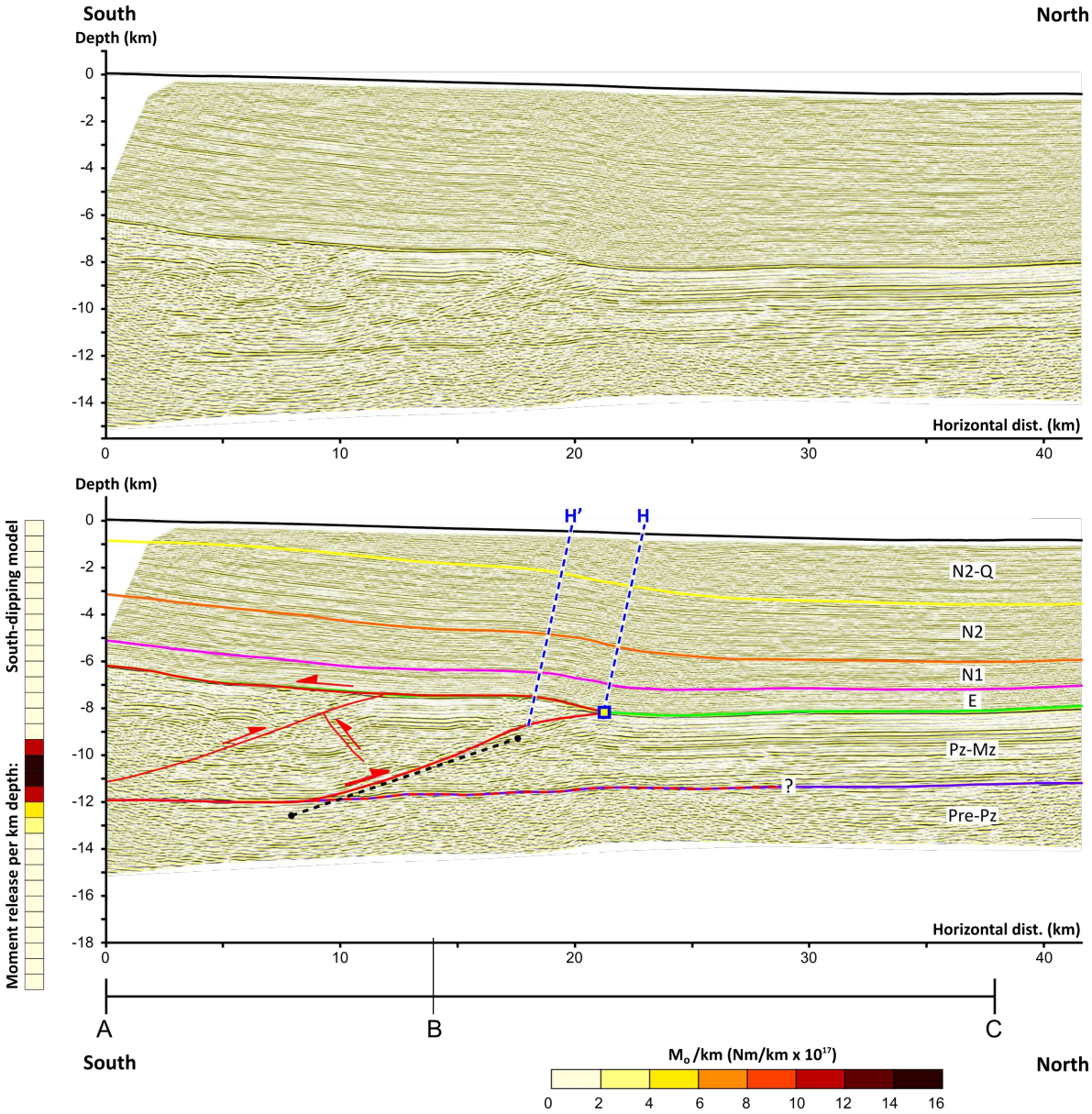


Figure 2.8: Seismic reflection profile along the line A-B-C (Figure 2.1) (adapted from *Li et al.* (2016) and with my modified velocity model). Top panel - uninterpreted. Lower panel - with interpretation. The backthrust at 10 km horizontal distance is my interpretation, all other interpretation is taken from *Li et al.* (2016). Dashed black lines: fault planes found by my uniform slip models. H' and H: fold axes. N2-Q: Pliocene-Quaternary 3.6 Ma - present (*Zheng et al.*, 2000). N2: Pliocene. N1: Miocene. E: Paleogene. Pz-Mz: Paleozoic-Mesozoic. Pre-Pz: Precambrian. Left - coloured squares show the depth distribution of moment release per unit depth in my finite slip model.

reflection profile interpretation. However, *Li et al.* (2016) used a first-approximation velocity model: a uniform velocity of 3000 m/s. Whilst 3000 m/s is appropriate for the Cenozoic section it is likely to be an under-estimate for the deeper units. The Paleozoic and Mesozoic units are predominantly sediments, such as limestones, dolomite and gypsiferous mudstone, whereas the pre-Paleozoic units consist of metamorphic and volcanic rocks (*Lu et al.*, 2016). Data from Kashgar, where the lithologies are thought to be similar to the Pishan area, indicate that the velocity of the pre-Cenozoic units is commonly in the range ∼4500–5500 m/s, whereas the Cenozoic unit is usually ∼2800–3200 m/s (*Heermance et al.*, 2008). I therefore requested an updated version of the seismic reflection profile from Tao Li (the first authour of *Li et al.* (2016) and our collaborator), changing the time-depth conversion to incorporate a velocity model of 3000 m/s for the Cenozoic sediments and 5000 m/s for earlier units. The result is shown in Figure 2.8, and the location of the profile is shown in Figure 2.10. The top four units (N2-Q to E) of the newly converted profile are unchanged from the original but below that the effect is that reflections have been deepened, with the greatest effect on the deepest parts of the profile. The Precambrian-Paleozoic unit boundary level with the zero kilometre horizontal distance marker on Figure 2.8 has increased in depth from 10.5 km to 12 km and the dip of the front ramp fault has increased from 10–14° (*Li et al.*, 2016) to 16–20°, bringing the dip into line with teleseismic and InSAR estimates for the 2015 earthquake (Table 2.2).

The southward-dipping InSAR solution matches the independently-constructed updated seismic reflection profile closely in depth, location and dip. I note that, as always, both the InSAR fault location and geometry and the reflection profile have uncertainties associated with them and it would be unwise to rely on interpreting the fine details of the comparison. However, the excellent match is strong evidence that the causative fault of the Pishan earthquake was the frontal wedge thrust that is visible in the reflection profile (*Li et al.*, 2016). This consistency indicates that InSAR solutions of active faulting could provide useful constraints on the velocity migration of seismic reflection

profiles, particularly in areas of thick sedimentary cover lacking bore-hole constraints on seismic velocities.

2.4.1 Are half-space elastic models for the surface displacements appropriate?

Although I have argued in Section 2.4 that a layered velocity model is most appropriate for the Pishan region, the elastic dislocation models I have used to model the surface displacements shown in the interferograms use a uniform half-space elastic model. The issue of whether a layered elastic model significantly alters the surface deformation due to slip on a buried fault has been addressed by *Cattin et al.* (1999) and *Honda and Yomogida* (2003). Their papers investigated a suite of situations where a fault is covered by a low-rigidity top-layer. *Honda and Yomogida* (2003)'s scenarios are more applicable to Pishan - most of their scenarios use a Young's modulus ratio of 0.35 which is very similar to the ∼0.3–0.36 that we expect at Pishan. Both papers found that the greatest impact of using a half-space model rather than a layered model is on amplitude of the signal and that the amplitude change is largest for the horizontal components of displacement rather than the vertical which we focus on in this chapter. Based on the results in *Cattin et al.* (1999) and *Honda and Yomogida* (2003), my half-space assumption could mean that I have overestimated the amount of slip by approximately 10% and that my models show the top depth as being shallower than the true depth by approximately 1 km. These changes are of similar magnitude to the model uncertainties and do not change my main conclusions. A layered elastic model did not change the wavelength or location of surface displacements by any amount that would be significant for my conclusions.

The published studies cover a range of fault geometry-elastic model scenarios and discuss the impact of varying each parameter but did not include any scenarios that exactly matched the fault dip, length, depth and elastic model that we expect at Pishan. I have therefore tested the impact of elastic model choice for the fault geometry and

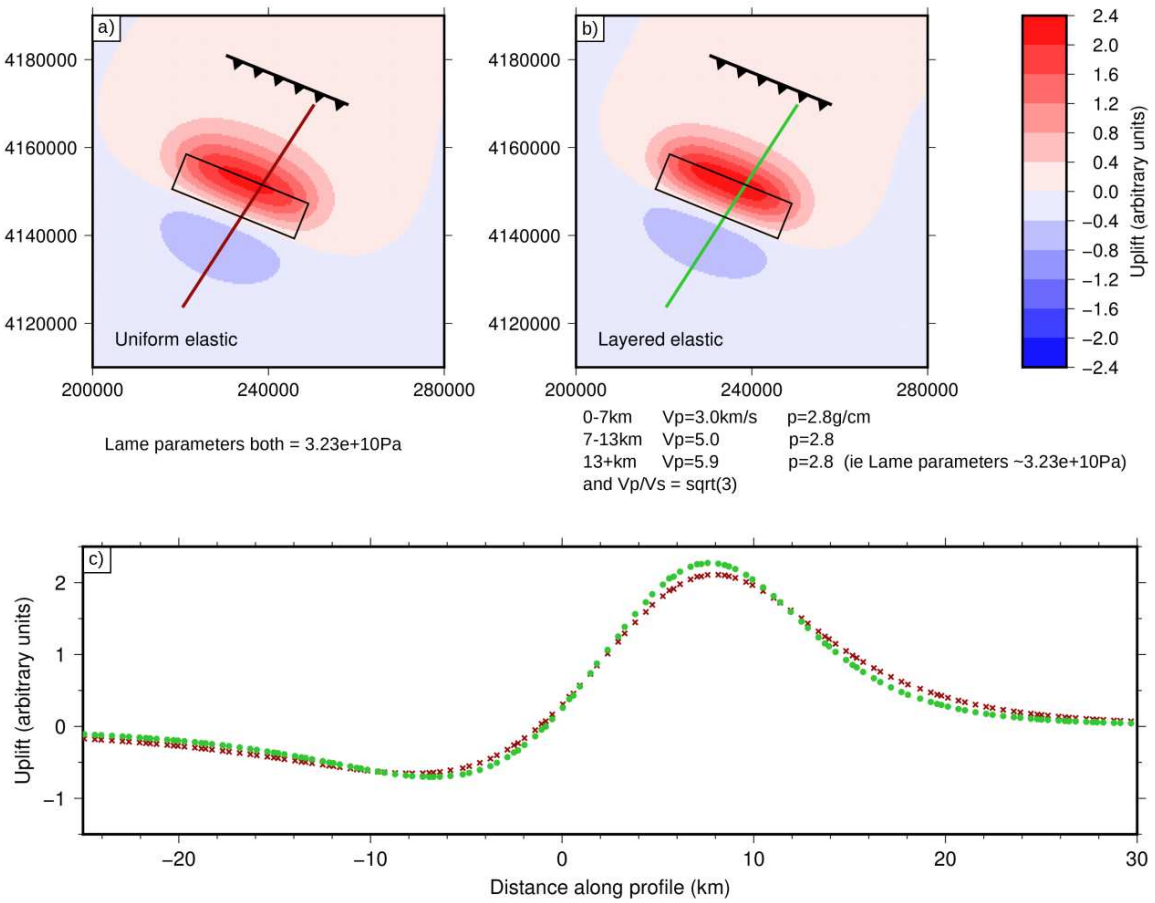


Figure 2.9: A test of the impact of using a layered elastic model on suface displacements. a) Vertical displacements of forward model for the fault shown as a medium-dashed line in Figure 2.19 and for the uniform elastic model that I used. b) Vertical displacements for a forward model of the same fault but in a layered elastic model which matches the seismic velocities at Pishan. c) Profiles through the two vertical displacement maps (uniform in red crosses, layered in green dots). Coordinates are in UTM 43N.

elastic structure of the Pishan earthquake using the fault location shown by the medium-dashed line in Figure 2.19, this is a forward model representing the coseismic fault. I used the EDGRN/EDCMP programs (*Wang et al.*, 2003) to create forward models for uniform and layered cases and the results are shown in Figure 2.9. The shear wave velocities (V_s) and relative densities of the layers are unknown at Pishan so the layered model case assumes $V_p/V_s = \sqrt{3}$ and that density = 2.8 g/cm^3 for all layers. I found that neither peak location or wavelength was significantly changed, although the layered velocity model did give a slightly shorter wavelength and higher amplitude, in agreement with the results from *Cattin et al.* (1999) and *Honda and Yomogida* (2003).

2.5 Folding in the geomorphology

2.5.1 Fluvial terrace deformation

The Pishan earthquake occurred under the alluvial apron that skirts the southern edge of the Taklamakan Desert. Drainage runs to the north-northeast from the Western Kunlun Mountains. A belt of incision ~25 km wide crosses from northwest to southeast parallel to the strike of the fault (Figure 2.1, Section 3.2). In some places it exposes pre-Quaternary sediments (*Matte et al.*, 1996; *Li et al.*, 2016) and in the Pishan area it preserves a sequence of folded fluvial terraces. The mainshock epicenter and the surface-projected fault plane lie in this terraced area (Figures 2.1 and 2.7b).

I mapped the terraces adjacent to the Kuoshtagh and Pinxinaxiang town rivers using 1.5 m resolution SPOT7 optical imagery (pansharpened), the 30 m SRTM1 DEM, GoogleEarth and Bing Maps (Figure 2.10). I inferred relative age from mapping, surface preservation and height and labelled the terraces in order of increasing age but were not able to correlate terraces between the two catchments (i.e. Te1 does not necessarily correlate with Tw1). Topographic profiles projected onto lines Y-Y' and Z-Z' are shown in Figure 2.11. In order to isolate the tectonic contribution to topography, it is necessary to remove the depositional slope. I have assumed and removed a linear depositional gradient of 0.92° as described in the next paragraph. After the removal of this depositional gradient I assume any remaining elevation changes on individual terraces are due to post-depositional tectonic deformation (e.g. *Molnar et al.*, 1994; *Poisson and Avouac*, 2004; *Walker et al.*, 2015).

Quantification of the original depositional gradient is not straightforward. Upstream, a single river forms one broad fan as it leaves the mountains (UF on Figure 2.10a) but through the incised belt drainage has been split into four channels, each of which has formed its own small fan downstream of the terraces (DF on Figure 2.10a). This prevents us from following coeval depositional surfaces upstream and downstream of the deformed terraces with confidence. I have therefore taken the depositional gradi-

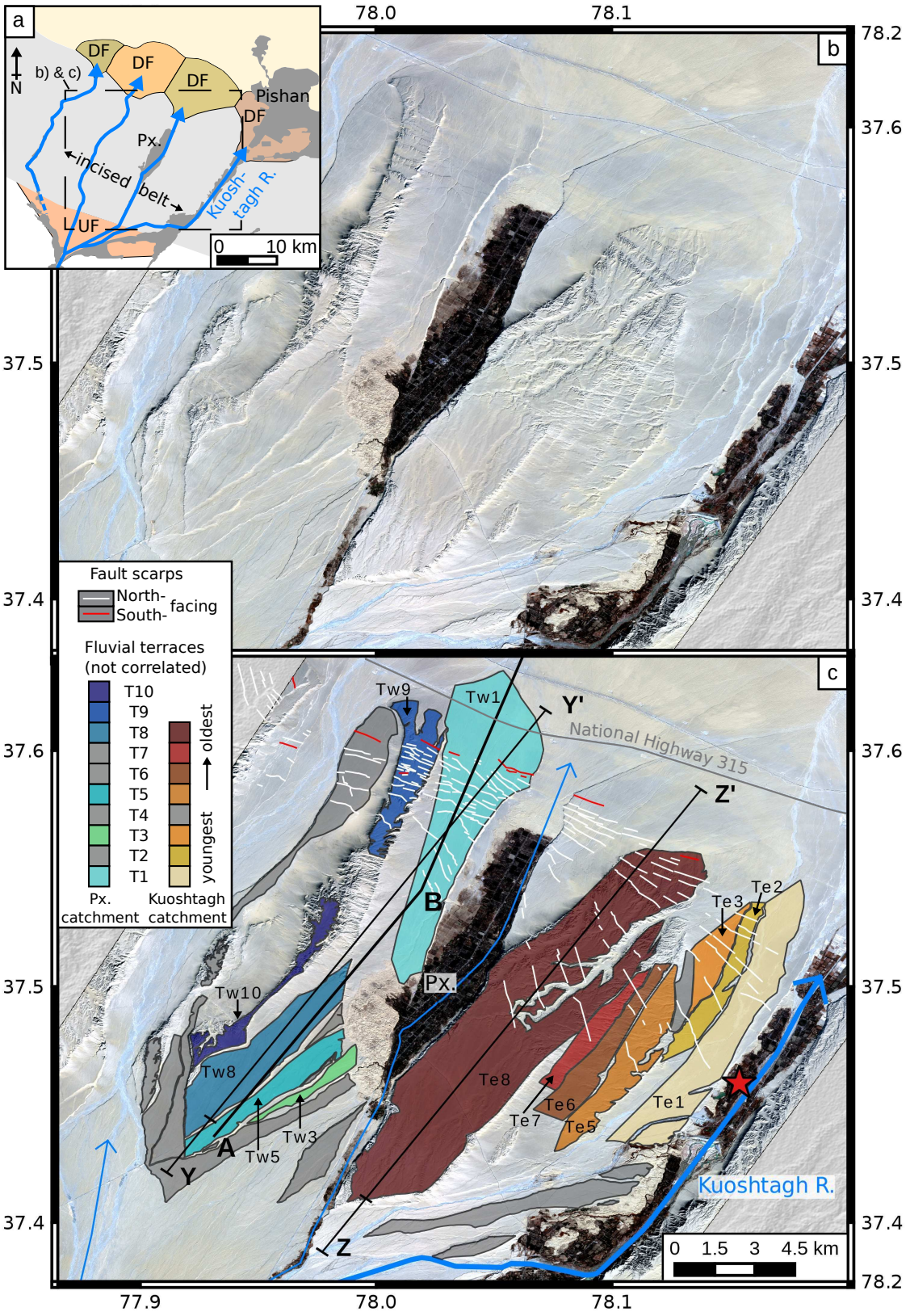


Figure 2.10: a) Simplified sketch map of the geomorphology around the Pishan terraces. UF: fan upstream of the fold. DF: downstream fans. b) Uninterpreted SPOT7 imagery of the Pishan terraces and surface scarps. c) Interpreted version of the same area. Coloured polygons: terraces with profiles in Figure 2.11. Solid black lines: profiles Y-Y' and Z-Z', distance markers at 0 km. Red star: epicenter (USGS). Px: Pinxinaxiang town. Thick blue arrow: active river. Thin blue arrows: inactive drainage routes. Line A-B: part of the seismic reflection line shown in Figure 2.1. Grayed-out terraces were not used in Figure 2.11.

ent from only the upstream fan and have removed it from all my profiles in Figures 2.11c and 2.11d. I note that alternative options, such as using the gradients of the channels or of the downstream fans, lead to different assumed depositional gradients in the range ∼0.70–0.95°, but each of these gradients are potentially contaminated by later sediment deposition or by slopes perpendicular to the profile lines. My conclusions would be unchanged by using a depositional gradient from anywhere within the ∼0.70–0.95° range.

The profiles in Figures 2.11c and 2.11d show an anticline with a width of 15–20 km. Higher, older terraces show greater magnitudes of folding than the lower, more recently abandoned ones, showing that the fold growth has been ongoing over the period during which the terraces were formed. The main fold crest is at 11–14 km horizontal distance on my profiles but the lowest terraces (Tw1 and Te1-3) have a slightly more northerly crest at around 16 km, suggesting basinward hinge migration may have taken place.

My remote mapping found no single primary surface scarp or rupture and no surface evidence for a major fault reaching the surface. This is consistent with the seismic reflection profile (Section 2.4, *Li et al.* (2016)) which shows continuous, unbroken, reflectors above and up-dip of the coseismic fault. There is, however, a series of surface scarps distributed over 5–10 km across the steep northern limb of the fold (Figures 2.10, 2.11). The scarps cut across fluvial terrace risers, strike roughly parallel to the fold axis and are larger on older terraces. This shows that the scarps are tectonic in origin and, like the fold, their growth has been ongoing for some time. I find local instances where the scarps are non-parallel, bend and truncate each-other. This pattern is not compatible with being bedding-plane slip. Unlike conventional bending moment faults, the scarps are asymmetrical. The great majority are south-up, although I do find a small number which are north-up (Figure 2.10). The scarps are not spread across the fold crest and there are none on the southern limb. By summing the scarp height measurements made by *Li et al.* (2016) (T3 on their Figure 2b) I estimate that one half to one third of the height change on Tw9 is provided by the scarps, which are each 1–20 m high.

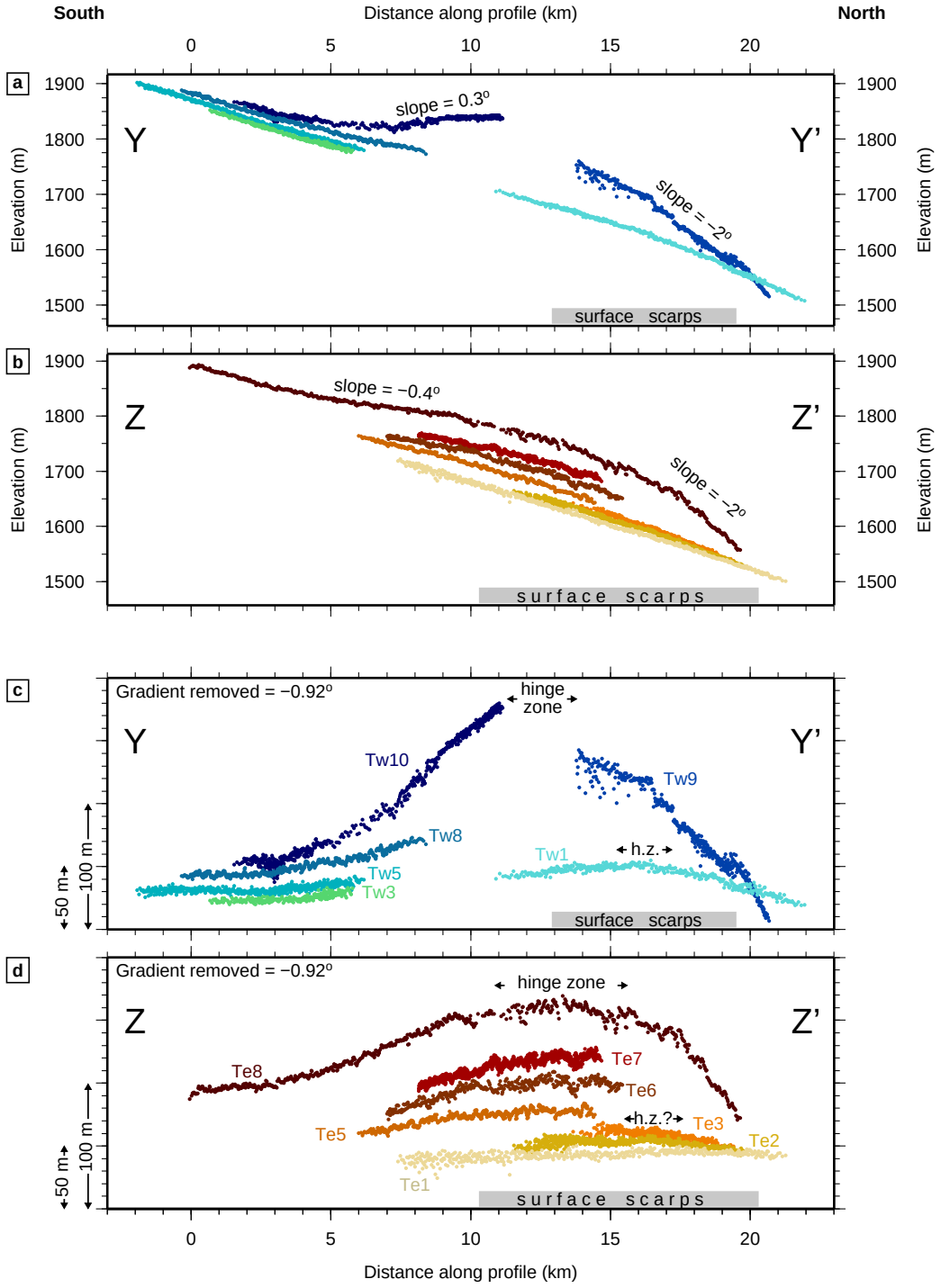


Figure 2.11: SRTM1 profiles of the coloured terraces in Figure 2.10. a) Profiles from the western terraces showing true elevations and vertically exaggerated true slopes. b) Profiles from the eastern terraces, true elevations, vertically exaggerated true slopes. c) and d) Show the profiles from a) and b) after the removal of the gradient of the fan upstream.

2.5.2 Abandonment age of the terraces in the Hotan Fold and Thrust Belt

In Section 2.5.1 I showed that uplift has been ongoing with a consistent pattern since at least the formation of the oldest terraces in Figure 2.10 and it is useful for the following discussion to place bounds on that duration. Dating on the terraces has been conducted by *Guilbaud et al.* (2017) (Table 2.4). They dated the deposition of one terrace using optically-stimulated luminescence (OSL) dating, and dated the abandonment of three other terraces by cosmogenic nuclide dating using ^{10}Be. They found that the two highest terraces that were sampled — Tw8 and Tw10 — are both old enough to have reached secular equilibrium for ^{10}Be, meaning that their ages are more than 1.5 Ma. An intermediate terrace — Tw1, which they interpret to as correlated with Te3 — has an age of 220±30 ka, and the lowest terrace that they sampled has an age of 40±3 ka (Table 2.4). These age results, morphological analysis led *Guilbaud et al.* (2017) to estimate a slip rate of 0.5–2.5 mm/yr over the whole fold system, with their prefered range based on their interpretation of the seismic reflection data being 2.0–2.5 mm/yr.

Table 2.4: Dating results from the terraces at Pishan. Data taken from *Guilbaud et al.* (2017).

Terrace level	Terrace level in *Guilbaud et al.* (2017)	Dating method	Age (ka)
unnamed[a]	T2	OSL	40±3
Tw1	T4	cosmogenic isotopes	220±30[b]
Tw8	T7	cosmogenic isotopes	>1500
Tw10	T9	cosmogenic isotopes	>1500

[a] Unnamed level below Te1. Approx. location: 78.072°E, 37.559°N.

[b] Age without surface erosion (their favoured interpretation). If the erosion rate is assumed to match the rate deduced from older terraces, then this age is 250±35 ka (*Guilbaud et al.*, 2017).

2.6 Postseismic deformation

2.6.1 Postseismic interferograms from Sentinel-1

I constructed three postseismic interferograms covering the time from two days to seven months after the earthquake (Table 2.1) using the same three tracks as used in Section 2.3.1, including both ascending and descending viewing geometries. I processed the interferograms using the methods described in Section 2.3.1 and found that coherence is similar to that of the coseismic interferograms.

Topographically correlated signals in the interferograms partially obscure the tectonic signal (Figure 2.12). This made it necessary to add the additional processing step of atmospheric correction for the postseismic interferograms. After unwrapping I made an empirical linear correction, which is a widely used and tested method for atmospheric correction (e.g *Elliott et al.*, 2008; *Bekaert et al.*, 2015a; *Copley et al.*, 2015). After unwrapping I worked only on a subset region of interest from the large Sentinel-1A TOPS mode interferograms. I used cropped areas (displayed in Figures 2.13a, b and c), that are nonetheless larger than a scene from traditional earlier SAR instruments, to avoid any chance of incorporating areas with substantially different atmospheric conditions into my single empirical fit of elevation versus phase (a topic discussed by *Barnhart and Lohman* (2013) and *Bekaert et al.* (2015b)). There are no topographic barriers or bodies of water in the region that would make it particularly susceptible to spatially variable atmospheric conditions and a spatially invariant linear correction is sufficient for my purposes. The elevation-phase correlation coefficients for tracks 056, 136 and 129 were 0.9, 0.8 and 0.4 respectively (Figure 2.12). I then proceeded to the flattening step. There is some coregistration error in t129a which causes apparent motion away from the satellite at burst boundaries (regularly spaced lines parallel to LOS on Figure 2.13b) but my conclusions are the same if t129a is excluded.

Figure 2.13 shows the postseismic displacement signal. Like the coseismic signal it consists of two lobes with the same sign of displacement as for the earthquake deforma-

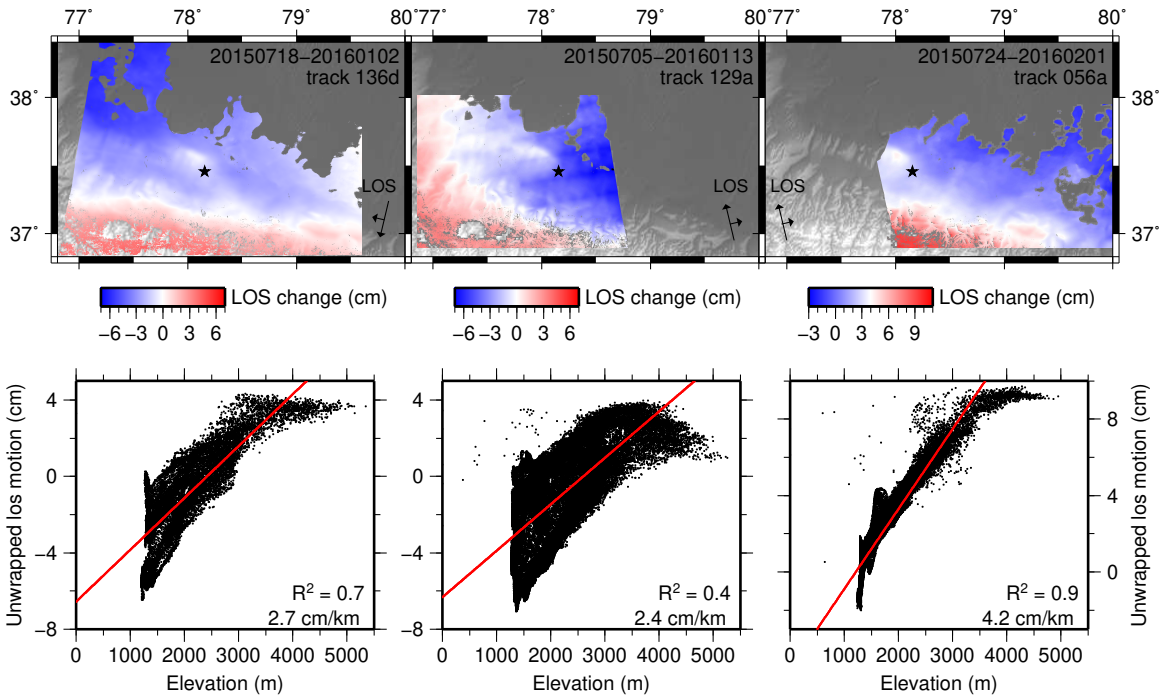


Figure 2.12: Top row: the three postseismic interferograms before a topographic correction was applied. Bottom row: LOS displacement vs elevation plots for each interferogram showing the trends which were removed.

tion but about one fifth of the magnitude. The northern, more prominent lobe indicates motion towards the satellite, with a peak LOS displacement of 2.7cm in track 056a. A small-displacement lobe of motion away from the satellite is present further south but is less well resolved above the noise. The signal is asymmetrical for all three tracks: profiles through the unwrapped interferograms show it has a steep northern (updip) side and a broader southern limb that is punctuated by a change in gradient (at ∼12 km in Figures 2.13d, e and f), south of which the displacement gradient is decreased. The axis of peak postseismic displacement is shifted approximately 1 km NNE (in the updip direction) from the coseismic peak axis. The peak motion away from the satellite is shifted by ∼7 km in the downdip direction from the coseismic peak and the transition from uplift to subsidence is also shifted southwards in the postseismic interferograms.

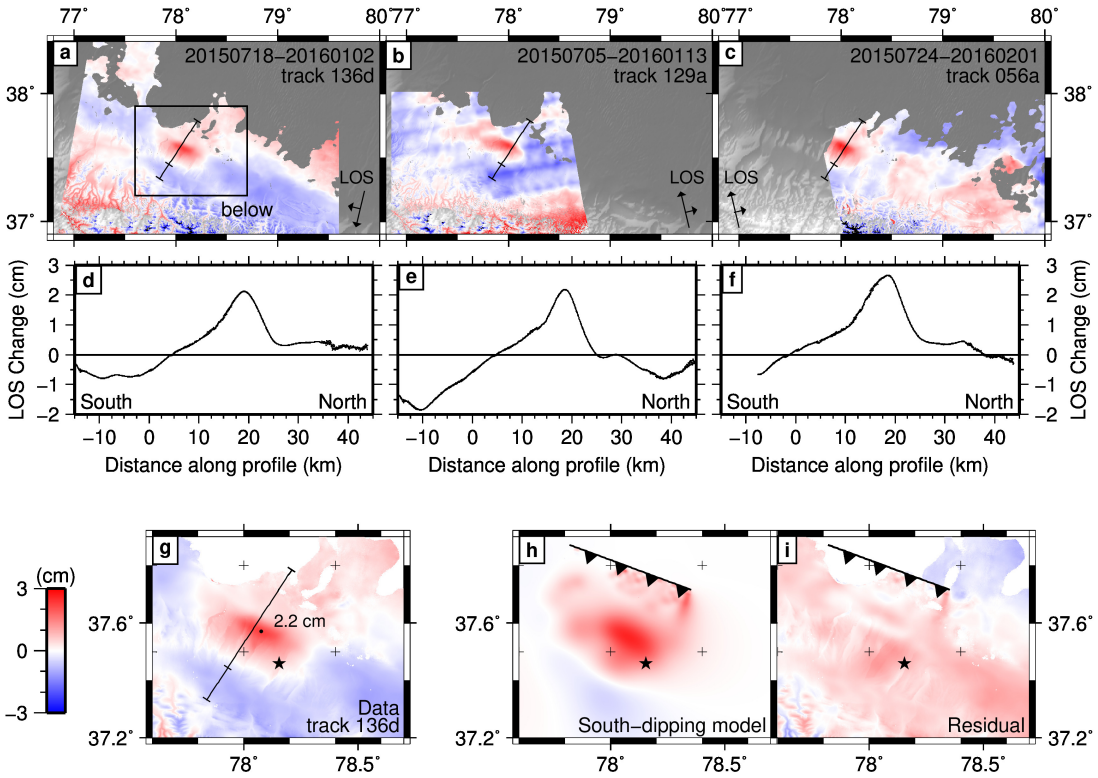


Figure 2.13: a-c) Unwrapped postseismic interferograms as detailed in Table 2.1. Timespan is shown in the top right of each panel, format yyyymmdd. d-f) Profile along the line marked on panels a-c. g), h), i) Data, distributed slip models, and residuals for the postseismic deformation signal for track 136d. Black, ticked lines show surface projection of the fault planes shown in Figure 2.15, with ticks pointing down-dip. Black star shows epicenter (USGS).

2.6.2 Causative mechanisms of the postseismic displacements

Postseismic surface displacement can be caused by a number of mechanisms. In this case, the earthquake's moderate magnitude, midcrustal slip depth and the short timescale and lengthscale of the observed signals rule out mantle relaxation as a cause of the signal, which is typically observed for much larger events (*Wright et al.*, 2013). The polarity of the postseismic and coseismic displacement patterns is the same. This is not consistent with poroelastic rebound being the dominant postseismic deformation mechanism (*Jónsson et al.*, 2003), although I cannot discount it playing a minor role. In situations such as this, where an unfaulted pile of sediments overlies a blind thrust fault (Section 2.4), *Lyzenga et al.* (2000) identified anelastic relaxation of the sediments as another potential mechanism for postseismic relaxation. This would not explain the

change in gradient in the southern limb in the profiles (Section 2.6.1 and Figure 2.13) but could be acting in combination with another mechanism. Afterslip is the final candidate for the cause of the postseismic displacements. I can not rule out a combination of mechanisms and, given the asymmetrical and kinked profile discussed in Section 2.6.1, a combination may be likely.

2.6.3 An afterslip model for the postseismic interferograms

Using the fault plane extent, rake, slip patch size and smoothing factor taken from my models of coseismic slip distribution (Section 2.3.1) I applied the same method to model the distribution of afterslip, assuming for now that afterslip is the sole tectonic cause of the postseismic displacements in Figure 2.13. The resulting slip distribution has the shape of a ring that sits around the base and sides of the coseismic slip patch and partially overlaps with it at the top (Figures 2.14 and 2.15). The ring shape arises from the short wavelength peak in the displacements superimposed on a longer wavelength which was discussed in Section 2.6.1 and Figure 2.13. Slip at two distinct depths is required to match the kink (Section 2.6.1) and is seen across a range of different model smoothing factors (Figure 2.14). This distribution is resolvable above the noise level: Figure 2.15b shows the standard deviation from 100 interferograms that were perturbed (as in Section 2.3.1) and then modelled using my prefered smoothing value. It is also not an artefact of the inversion: in tests where the LOS ground displacements produced by synthetic filled or ring-shaped slip patches were downsampled to the same resolution as used in the slip inversion and then modelled, the ring and filled shapes were recovered (Figures 2.16 and 2.17).

Afterslip distributed around and slightly overlapping the coseismic slip patch is in line with theoretical models including but not limited to the case where a velocity-weakening patch is surrounded by velocity-strengthening fault plane (*Marone et al.*, 1991; *Helmstetter and Shaw*, 2009; *Avouac*, 2015) and has already been observed in some cases (e.g. *Miyazaki et al.*, 2004; *Thomas et al.*, 2014; *Liu et al.*, 2016). In this case

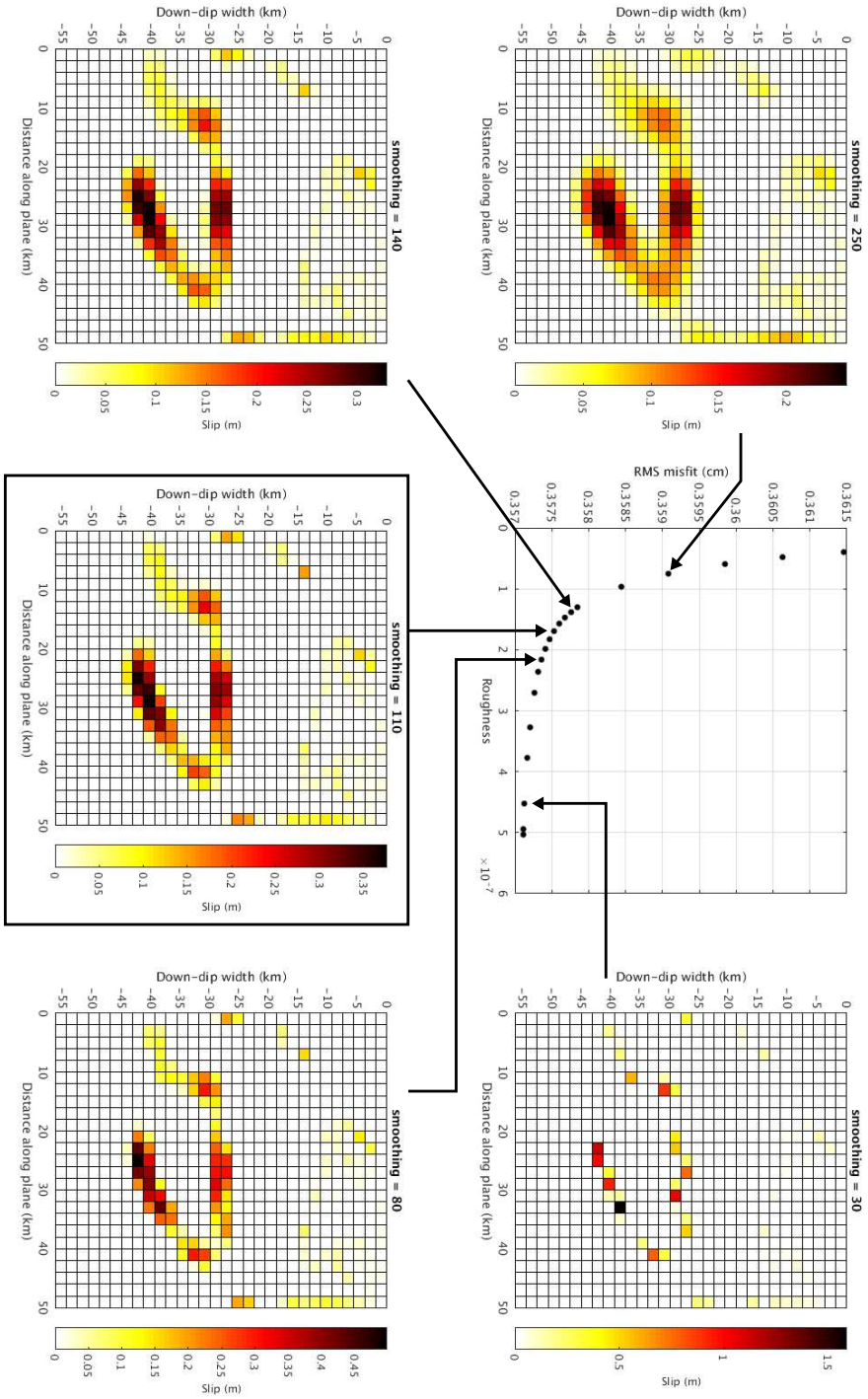


Figure 2.14: The results of applying a variety of smoothing values in the inversion for postseismic slip distribution. The selected smoothing value is 110.

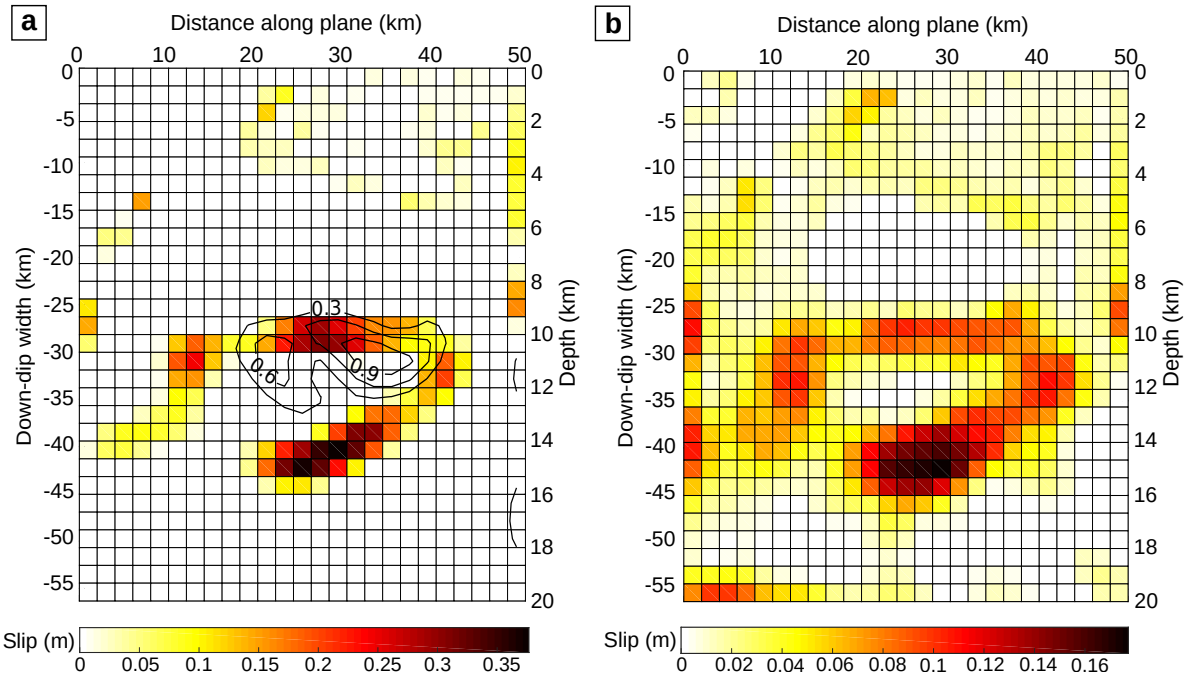


Figure 2.15: a) Slip distribution for an afterslip model on a planar, south-dipping fault showing contours of coseismic slip in units of metres. b) Standard deviation of the slip distribution at my preferred smoothing value.

my interpretation is limited by the similarity of surface displacement patterns produced by different models. *Lyzenga et al.* (2000) showed that the surface displacement due to anelastic deformation of overlying sediments can be well fit by a model of slip on a discontinuity close to the top half of the coseismic slip plane. Although the plane is predicted to be slightly above and steeper than the coseismic plane, these differences are too small and my ability to isolate the shallow part of the signal is insufficient for us to confidently attribute the signal to one cause or the other. Similarly, I was not able to distinguish between a planar fault geometry and a fault that flattens to a dip of one degree below 12 or 12.7 km depth at the base of the coseismic slip patch. They fit the data equally well, and although the non-planar slip models are more disjointed than the planar model, they are more consistent with the thrust system interpreted from the seismic reflection profile discussed in Section 2.4, which shows the fault shallowing into a flat at a depth of around 12 km (depending on the seismic velocity assumptions). The twelve geometries tested all showed afterslip at at least two distinct depths, as in

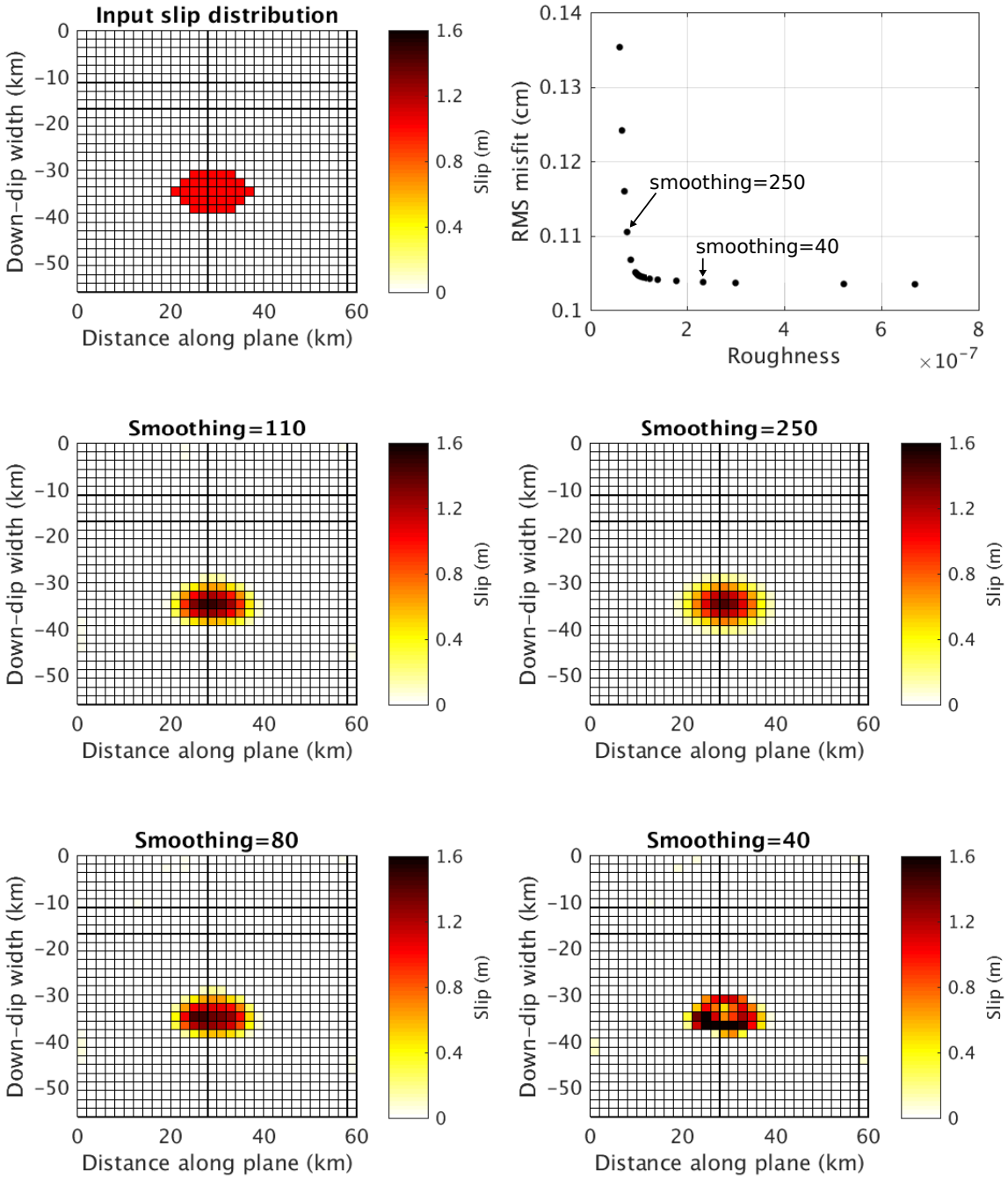


Figure 2.16: The results of the tests described in Section 2.6.3. The displacement field due to the input slip distribution (in this case a filled slip patch) shown in the top left was downsampled using the same method I applied to the postseismic interferograms and the downsampled datasets were then inverted to test how well the origunal slip distribution would be recovered. The lower four panels show the results of that inversion for four different smoothing values.

Figure 2.15.

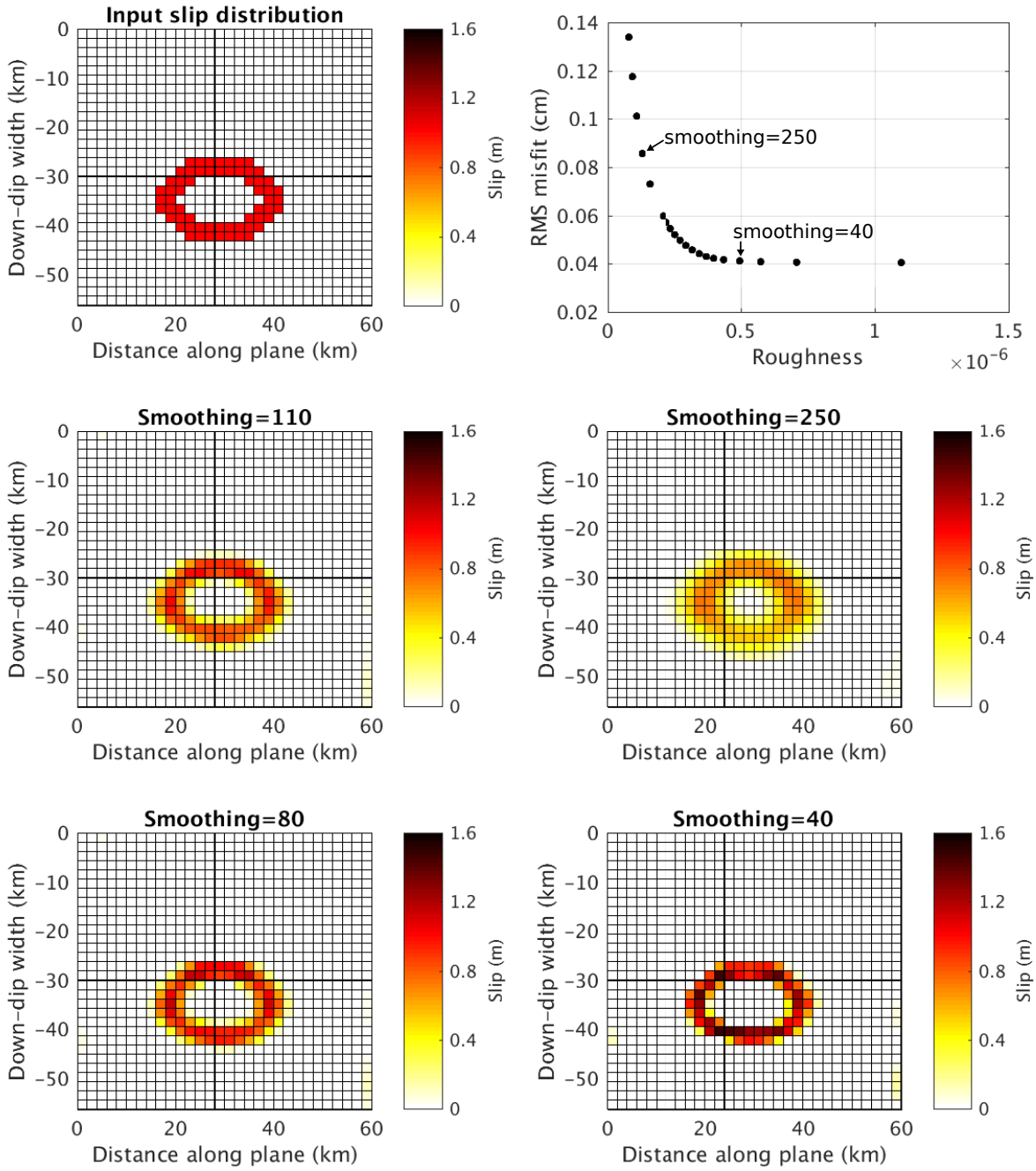


Figure 2.17: As Figure 2.16 but for a ring-shaped input slip distribution.

2.7 Discussion

2.7.1 Timing of topographic growth

The observations presented above allow us to place some constraints on the mechanisms controlling topographic growth at the northern Tibetan rangefront and its timing within

the seismic cycle. Recent work on reverse faults has attributed topographic growth to various mechanisms depending on setting, including: coseismic slip (*Stein and Ekström*, 1992; *Le Béon et al.*, 2014), postseismic afterslip on a single fault (*Stein and Ekström*, 1992; *Copley*, 2014; *Elliott et al.*, 2015; *Zhou et al.*, 2016; *Elliott et al.*, 2016), afterslip on multiple faults (*Copley and Reynolds*, 2014; *Mackenzie et al.*, 2016) and slip on faults or sections of fault that play an apparently minor part in the region's seismic activity (*Whipple et al.*, 2016; *Melnick*, 2016; *Saillard et al.*, 2017).

I have shown that the Pishan earthquake took place on one of the main faults within the Hotan Fold and Thrust Belt and is the most basinward of a set of stacked thrusts. The lack of any major fault trace at the surface, the unbroken Cenozoic reflectors in the reflection profiles and my findings that slip in the Pishan earthquake stopped at depth and there was no shallow (<9 km) afterslip, show that the Cenozoic sediments accommodate permanent strain in a distributed manner by folding. My results allow us to discuss the deeper driving processes and show that deformation in the time between significant earthquakes is likely to contribute significantly to building topography. Despite its location on a prominent fault, the coseismic ground displacements from the earthquake do not align with the anticline in Quaternary fluvial terraces (Figure 2.18). The peak coseismic uplift is offset approximately 5 km into the foreland from the topographic fold axis of the higher terraces and approximately 2 km from the axis of the lower, younger terraces. Although the northern part of the anticline was uplifted, the southern part subsided during the earthquake. The peak ground uplift in the first seven months of postseismic motion is a further kilometre offset from the topographic fold axis compared to the coseismic uplift (Figure 2.18).

My results show that distributed postseismic relaxation of the Cenozoic sediments after the coseismic stress change also cannot explain the anticline growth. *Lyzenga et al.* (2000) showed that the displacement signal caused by sediment relaxation after an earthquake would appear similar to afterslip close to the upper half of the coseismic fault plane, as I have in my afterslip-only postseismic models (Figure 2.15 and Section 2.6).

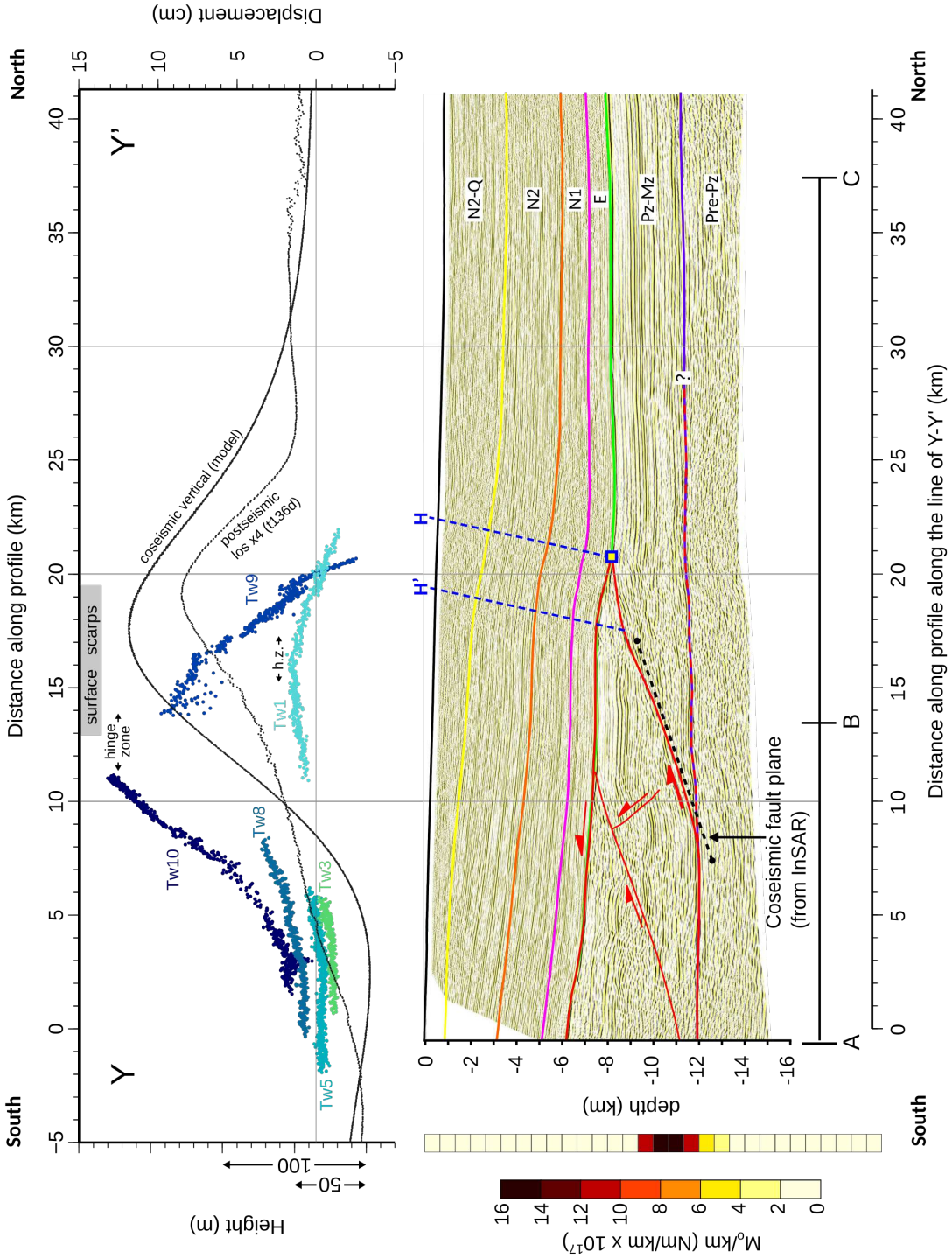


Figure 2.18: Aligned profiles along an extended Y-Y' line. Topographic profiles taken from Figure 2.11c are overlain on the vertical displacements from my coseismic model and a four-times vertically exaggerated profile through the postseismic interferogram. Below: seismic reflection profile duplicated from Figure 2.8. Black dashed line shows fault plane from uniform slip model. Coloured sidebar with key shows coseismic moment release with depth in my distributed slip model. Note no modification of the seismic reflection data was made to account for the 15° change in azimuth at B. There is no misalignment along A-B, where the profiles are parallel, but along B-C the seismic profile is stretched in comparison to the topography and InSAR. This results in ∼230 m misalignment at 20 km horizontal distance and < 1km at 40 km.*(bottom)*

This would produce an uplift peak several kilometres to the north of the fold crest. I can therefore conclude that the anticline and minor scarps described in Section 2.5 did not form coseismically by repetitions of the July 2015 earthquake.

The geometry shown in Figure 2.18 suggests the nature of the deformation in the time between 2015-like earthquakes. It shows a flat detachment leading to a ramp, which has little or no offset at its tip. In this configuration northward horizontal flux of material decreases from south to north, leading to material being forced upwards into an anticline (e.g. *Suppe and Medwedeff*, 1990; *Wickham*, 1995; *Burbank and Anderson*, 2011). I have seen the effects of slip on the ramp in the 2015 earthquake. The remaining mechanisms are therefore slip on different parts of the ramp-and-flat (particularly interseismic transport on the detachment) and internal deformation of the wedge. Although only a few key faults have been interpreted in Figure 2.8, both the wedge geometry and the reflections show that it has undergone internal thickening in the past and may still be doing so.

The long wavelength part of the postseismic signal did uplift the anticline in the months following the earthquake. This signal is due to the afterslip below the coseismic slip patch which I discussed in Section 2.6 and could be an important part of the ramp and flat slip. However, with $<$8 mm uplift of the fold crest during the earliest, fastest phase of postseismic motion, future studies will need to find a strongly sustained signal for it to have been a major contributor to the $\geq$120 m anticline. Brief inspection of interferograms from early 2016 to early 2017 shows that the rate of postseismic displacement for that period was less than half of the rate for the earlier postseismic period shown in Figure 2.13, and that the peak signal continued to be north of the fold crest.

Figure 2.19 shows ground displacements from elastic forward models of earthquakes on the detachment, on the more loosely interpreted $\sim$21°-dipping thrust fault 10 km behind the 2015 earthquake, and on the small backthrust. It is important to note that these models do not include the interseismic strain which loads the faults and therefore

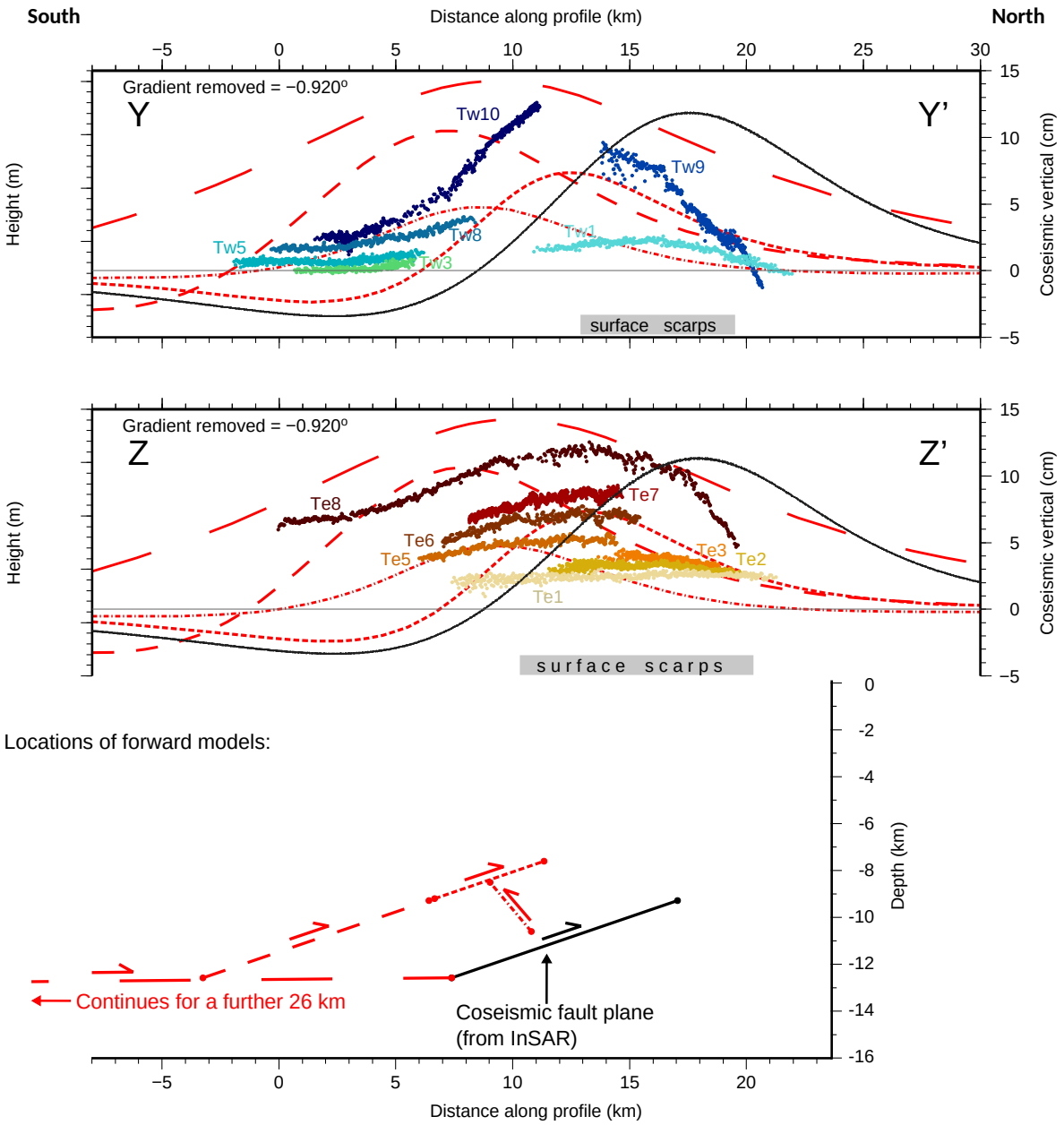


Figure 2.19: Profiles through coseismic uplift pattern and terraces as in Figure 2.18. Red dashed lines show the results of a suite of forward models, assuming rake 90, magnitude arbitrary. Long dashes: detachment,dip 0.5°, down-dip length 46 km. Medium dashes: ramp to south of 2015 earthquake's fault, dip 21°, depth range same as coseismic. Short dashes: ramp to south, dip 21°, depth 7.6–9.2 km. Dot-and-dash: backthrust, dip 50°, depth 8.5–10.6 km.

Figure 2.19 does not show the total ground deformation resulting from transport on these faults over the >100 ka timescale recorded by the fluvial terraces. The uplift patterns differ from the terrace folding and I am not able to account for the anticline

by coseismic slip alone on any of these other mapped faults. This is not surprising because as I have stated, over the timescale of multiple earthquake cycles, interseismic and additional aseismic deformation must be invoked in order to avoid space problems. The models do illustrate that deformation (either localized or continuous and spatially-distributed) to the south of the coseismic fault plane would produce uplift in a location to match the long-term uplift shown by the fluvial terraces.

My study, along with the results of *Copley and Reynolds* (2014); *Copley* (2014); *Mackenzie et al.* (2016), shows that it is not always valid to assume that fold growth above blind reverse faults is coseismic or that it is appropriate to model it as an elastic dislocation. Even in cases where folds and coseismic uplift have been seen to match topography, such as at the Coalinga anticline, *Stein and Ekström* (1992) reported that a modest fraction of the folding was postseismic, so at best modelling all fold growth as coseismic is likely to over-estimate the coseismic moment release rate. One approach to extracting quantitative information from fold growth is to fit elastic dislocation models to terrace anticlines in an attempt to locate faults and estimate their slip rates (e.g. *Benedetti et al.*, 2000). My observational work, along with an earlier sandbox model by *Bernard et al.* (2007), suggests that this may not always be appropriate.

Many studies adopt a different approach to the analysis of folds above blind reverse faults by assuming a kinematic model and using that as the basis to derive slip rates (e.g. *Rockwell et al.*, 1988; *Shaw et al.*, 2002; *Amos et al.*, 2007; *Daëron et al.*, 2007; *Le Béon et al.*, 2014). In subsequently estimating earthquake recurrence rates, the assumption is made that all the slip occurs in earthquakes, which as I have seen may not always be valid. The models are purely geometrical and do not need to specify physical mechanisms for the deformation, but the geometries implicitly require that not all of the fold growth occurs through coseismic slip in an elastic medium. This approach relies on a good choice of kinematic model which, as *Hubbard et al.* (2014) discuss, is not straightforward even at a location with a wealth of supplementary borehole and seismic reflection data. There is a need, therefore, to develop further physical models

relating driving stresses to fold growth above blind faults.

2.7.2 Change in fold shape from Pliocene to Late Quaternary

The high-quality strike-perpendicular seismic reflection profile that directly crosses the coseismic slip patch allows us to study the long-term development of the fold and thrust structures at Pishan (Section 2.4). The constant thickness of the Paleogene to early Pliocene sediments overlying the fault indicates that they pre-date the onset of folding at $\leq$3.6 Ma, and therefore show the full cumulative displacement since that time (*Jiang and Li*, 2014; *Li et al.*, 2016). They form a monocline with the southern limb dipping to the north slightly more steeply than the northern limb (Figure 2.8) and with a wavelength noticeably shorter than the topographic anticline - its two hinge axes are only 3 km apart (Figure 2.18). The anticline, though prominent in the surface geomorphology, is not visible in the long-term geological structure. This suggests that there was a change in shortening style before the formation and abandonment of the oldest terraces and recently enough for its effects to be below the detection level of the seismic reflection profile. The change in style is reminiscent of the northward shift of the topographic fold hinge from the older to younger terraces in Figure 2.11 and both stages of fold style development are likely to be related to the immaturity of the Hotan Fold and Thrust Belt. This highlights the importance of the balance of the shortening mechanisms behind the frontal thrust - the fault which broke in 2015 has accumulated significant offset and appears to have played an important role in the development of sub-surface structure and to still play an important role in the present day, yet the style and location of folding above it have changed over time.

2.8 Conclusions

In summary, my seismic and geodetic results show that the Pishan earthquake occurred on the frontmost of a well established stacked series (*Li et al.*, 2016) of thrusts which

does not reach the surface and had been independently mapped on seismic reflection data. The ability of InSAR to constrain the depth extent of faulting has proven to be useful affirmation of a velocity model in the depth migration of the seismic reflection survey and may be applicable elsewhere for the accurate imaging of thick sedimentary piles and structures with few or no prior velocity constraints. The first six months of postseismic deformation saw displacements of one fifth the magnitude of the coseismic static displacements, with the locations broadly similar but the spatial patterns differing slightly. I attribute the postseismic signal to afterslip below the coseismic slip patch and either afterslip at the top of the coseismic patch or distributed deformation in the unbroken overlying sediments.

The axis of the anticline in Quaternary terraces above the fault is offset by ∼5 km back from the coseismic peak and ∼6 km from the postseismic peak, confirming that the coseismic and early postseismic deformations are not sufficient to describe the growth of geological structures. Down to a depth of 6–8 km the topographic growth is accommodated by distributed deformation. I suggest that this deformation is influenced from below by aseismic deformation within or bounding the wedge or by the sum of further earthquakes around the 2015 slip patch. The difference in fold shape between the full cumulative record given by seismic reflection and Quaternary geomorphology shows that the style of shortening has changed recently in the lifetime of this rangefront.

Chapter 3

The 1985 Wuqia (China) Earthquake: Thin-Skinned Expression of a Basement Fault

3.1 Introduction

The 1985 Wuqia earthquake is the largest earthquake to have hit the Pamir–Tarim Basin–Tien Shan junction since the invention of modern seismology and it occurred at a recognised major and fast-slipping fault — the Pamir Frontal Thrust (PFT) (Figure 3.1). Seismic reflection and geological cross-sections indicate that the region is underlain by a detachment that separates Cenozoic cover from the basement at ∼6–10 km depth and that the PFT is a gently dipping, east-southeast-striking fault that reaches the surface along this detachment. The surface ruptures were consistent with a north-vergent reverse fault striking east to south-east. However, results from earthquake seismology list the centroid depth as ∼10–25 km and the mechanism as oblique, with nodal planes dipping gently to the NNE or steeply to the SE, at odds with the expected gently SW dip of the PFT and with a centroid depth below the detachment. No geodetic estimates of the fault parameters are available for the earthquake.

My goals are to reconcile these apparently contradictory observations and to compare the surface expression of shortening on this major fault to the expression of faults involved in other continental reverse earthquakes of Central Asia. There is no easily accessible summary for the Wuqia earthquake and its context. Information on the earthquake is spread across several publications and their appendices in two languages. In this study I provide a synthesis and, by doing so, show that the earthquake sequence involved slip on both basement and shallow faults. By comparing pre- and post-earthquake imagery, I show that the ruptures are likely to have extended $\sim$12 km further in length than previously thought. Finally, I attempt to use image correlation to derive a geodetic coseismic displacement map in order to compare field measurements of displacements at the scarp with the total displacement field.

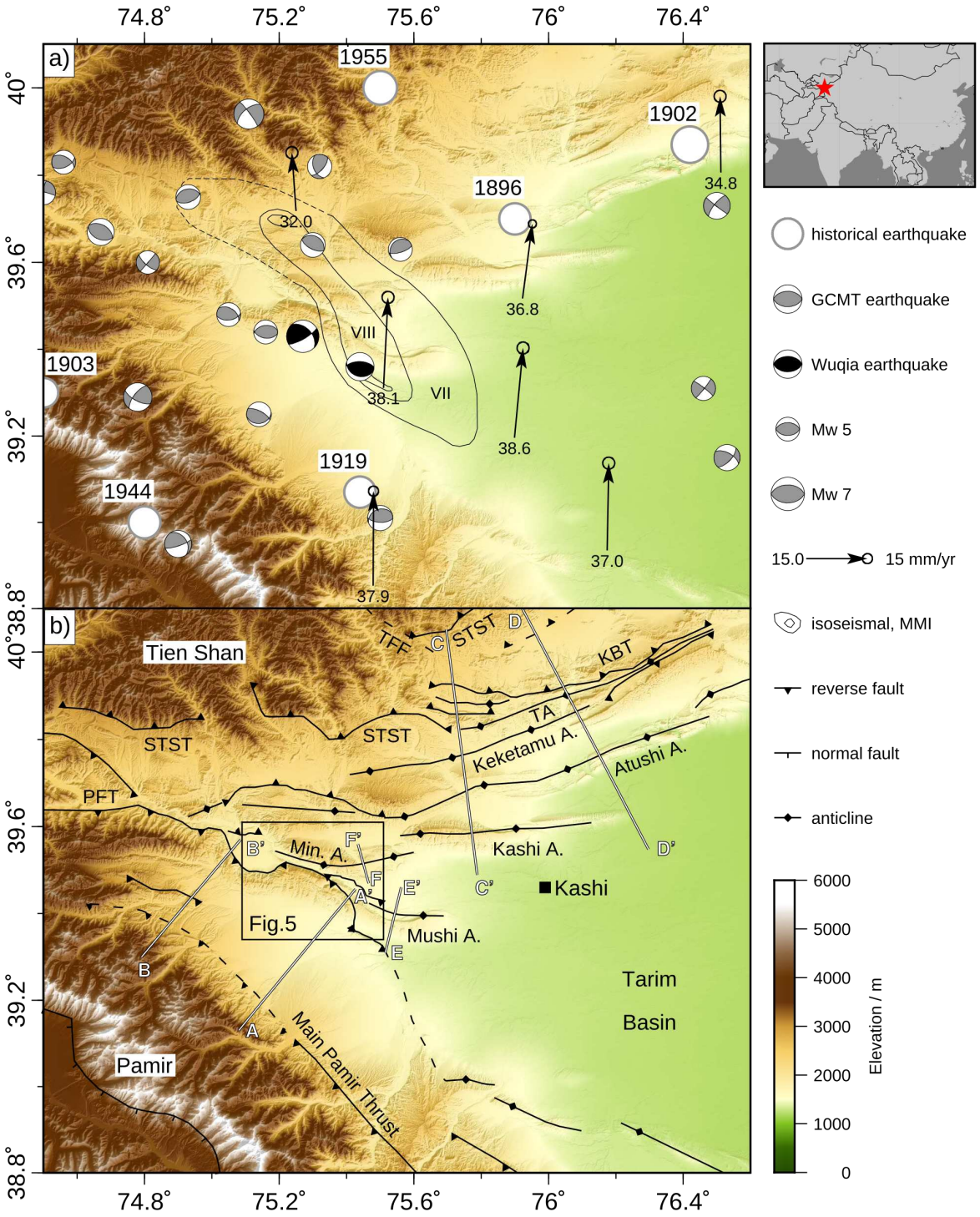


Figure 3.1: a) Seismicity and GPS vectors for the Pamir–Tarim Basin–Tien Shan junction region, scaled by magnitude. Focal mechanisms are from the GCMT catalogue, except for the Wuqia earthquake and its largest aftershock (both black) which are from *Burtman and Molnar* (1993). The mainshock is the larger of the two black mechanisms. White circles show historic earthquakes, their years and approximate locations (*Kondorskaya et al.*, 1982; *Storchak et al.*, 2013; *Kulikova and Krüger*, 2017). GPS velocities relative to Eurasia are from *Zubovich et al.* (2010). Isoseismals for the Wuqia earthquake are from *Feng et al.* (1986). MMI = Modified Mercali Intensity b) Major faults and folds. After *Li et al.* (2013b) and *Heermance et al.* (2008). A. = Anticline, KBT = Kashi Basin Thrust, Min. A. = Mingyaole Anticline, PFT = Pamir Frontal Thrust, STST = Southern Tien Shan Thrust, TA = Tashipishake Anticline, TFF = Talas–Fergana Fault.

3.2 Tectonic setting

The Wuqia earthquake took place at the Pamir–Tarim Basin–Tien Shan junction, in far western China — a zone of north-south convergence (*Zubovich et al.*, 2010) (Figure 3.1a). In this section I will first review the stratigraphy of the region, then describe its tectonic structures and the structural style of the shortening before summarising the published Holocene shortening rates to show how strain accommodation is distributed across the various structures.

3.2.1 Stratigraphy

The stratigraphy and depositional history of the western Tarim Basin have been thoroughly studied (e.g. *Bally et al.*, 1986; *Hu*, 1992; *Heermance et al.*, 2007, 2008; *Bosboom et al.*, 2011; *Wei et al.*, 2013). The formations present and their thicknesses vary spatially and, reflecting this, Figure 3.2 shows two slightly different stratigraphic columns for the Pamir and Tien Shan sides of the foreland around Kashi (also known as Kashgar). On the Pamir foreland side of the basin, the Paleozoic rocks are overlain unconformably by <1 km each (*Hu*, 1992) of Jurassic and Cretaceous strata, while to the north, at the Tien Shan foreland side, the Jurassic is absent and ∼200 m of Cretaceous strata directly overlie the Paleozoic (*Heermance et al.*, 2007).

Cenozoic sediments that are 6–10 km thick cover the Cretaceous. In the Pamir side of the foreland the stratigraphy is similar to that of much of the rest of the western Tarim Basin (*Bosboom et al.*, 2011; *Wei et al.*, 2013; *Cheng et al.*, 2016). There, the Paleogene Kashi Group sits conformably over the Cretaceous strata. It and the late Cretaceous strata are the product of five marine transgressions and regressions into the Tarim Basin and include facies ranging from shallow marine to evaporative tidal flats, with the result that they include massive gypsum beds and gypsiferous lithologies at several levels (*Bosboom et al.*, 2011; *Wei et al.*, 2013, and references therein). Based on published stratigraphic columns and isopachs, the Kashi Group's thickness is <1500 m (*Hu*, 1992; *Bosboom et al.*, 2011; *Wei et al.*, 2013), but some interpretations of seismic

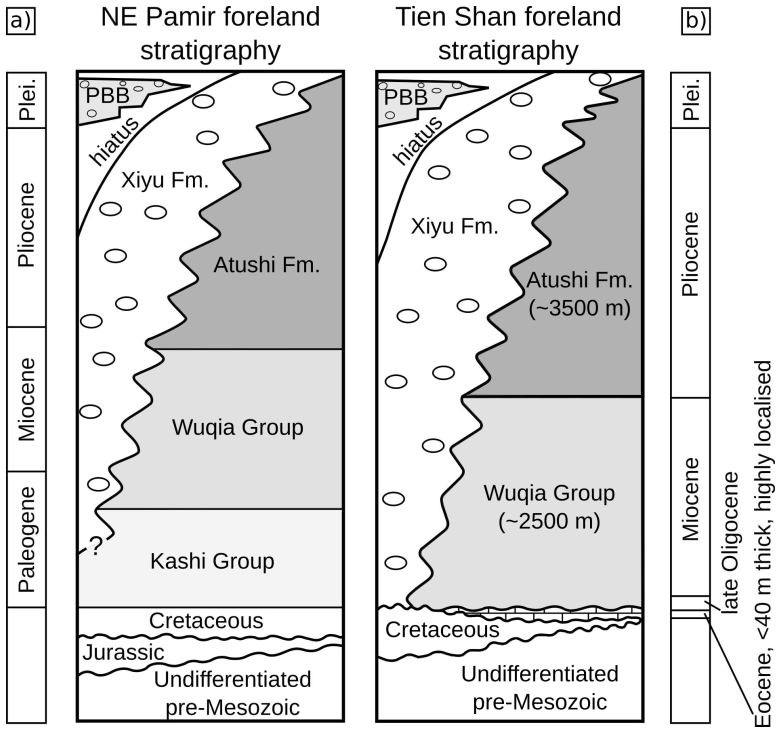


Figure 3.2: Stratigraphic columns for the northwest Tarim Basin. a) Stratigraphic column for the NE Pamir foreland around the epicentral area of the Wuqia earthquake. Based on *Scharer et al.* (2004); *Bosboom et al.* (2011); *Wei et al.* (2013); *Li et al.* (2015) and references therein. b) Stratigraphic column for the Kashi foreland of the Tien Shan, modified from *Heermance et al.* (2007). Both columns are amalgamated from partial sections at multiple sites. Horizontal wavy lines represent disconformities, sloping wavy lines represent angular unconformities. PBB: Piggyback Basin sediments, $<$ 300 m thickness and localised.

reflection and resistivity profiles across the Pamir foreland west of Kashi show the Kashi Group as thick as $\geq$3 km (*Chen et al.* (2010); *Thompson Jobe et al.* (2017), Figure 3.3b). In the Tien Shan foreland around Kashi the Kashi Group is absent and is replaced by a sub-parallel unconformity — the result of peneplantion from the late Cretaceous to Oligocene (*Abdrakhmatov et al.*, 2001; *Heermance et al.*, 2007). From the late Oligocene onwards, the main features of the stratigraphic history are shared across both the Pamir and Tien Shan sides of the Kashi foreland.

The late Oligocene marks the final transition from marine to continental formations. The Kashi Group is superseded by the Wuqia Group, which dates from the late Oligocene through Miocene (*Hu* (1982), cited in *Scharer et al.* (2004)). The Wuqia Group is predominantly made up of fine-grained lithologies: mudstone, shale, siltstone

and fine-grained sandstone, and the units near its base contain some gypsiferous beds (*Heermance et al.*, 2007; *Wei et al.*, 2013). The Plio-Pleistocene Atushi (or Artux) Formation follows, which is 1.5–4 km thick and, in general, slightly coarser than the Wuqia Group (*Heermance et al.*, 2007; *Wei et al.*, 2013). The uppermost major formation is the Xiyu Formation — a highly time-transgressive wedge-shaped conglomerate which thickens from south to north and whose basal contact is an angular unconformity (*Scharer et al.*, 2004; *Heermance et al.*, 2007).

On the basis of geological mapping, structural geology and seismic reflection profiles, several levels within the Kashi and Wuqia Groups have been identified as being capable of acting as detachments (e.g. *Scharer et al.*, 2004; *Heermance et al.*, 2008; *Wang et al.*, 2016). The gypsiferous strata in the Kashi Group, and particularly a massive gypsum bed at its base, have been identified as detachment horizons (*Scharer et al.*, 2004; *Wang et al.*, 2016), and in the lower Wuqia Group well-bedded gypsiferous shales have been interpreted as playing the same role (*Heermance et al.*, 2008). Overall, the weak Kashi and Wuqia Groups behave as a ductile detachment zone beneath the more competent Atushi and Xiyu Formations (e.g. *Scharer et al.*, 2004; *Heermance et al.*, 2008). The most structurally significant detachment level is at the base of the Cenozoic (i.e. at the base of either the Kashi or Wuqia Group, depending on location), which is seen on seismic reflection profiles as a widespread strong, flat-lying reflector at ∼6–10 km depth (e.g. *Scharer et al.*, 2004; *Chen et al.*, 2007; *Heermance et al.*, 2008; *Li et al.*, 2013b). The basal-Tertiary detachment divides the Cenozoic 'cover' from the Mesozoic and Paleozoic 'basement' below.

3.2.2 Structures and cross-sections

The surface geology reveals an array of faults and folds within the Pamir–Tarim Basin–Tien Shan junction zone; they fan in strike from NW–SE in the south at the Main Pamir Thrust (MPT), to E–W in the north at the Southern Tien Shan Thrust (STST) (Figure 3.1b). Four cross-sections through the forelands are shown in Figure 3.3; they

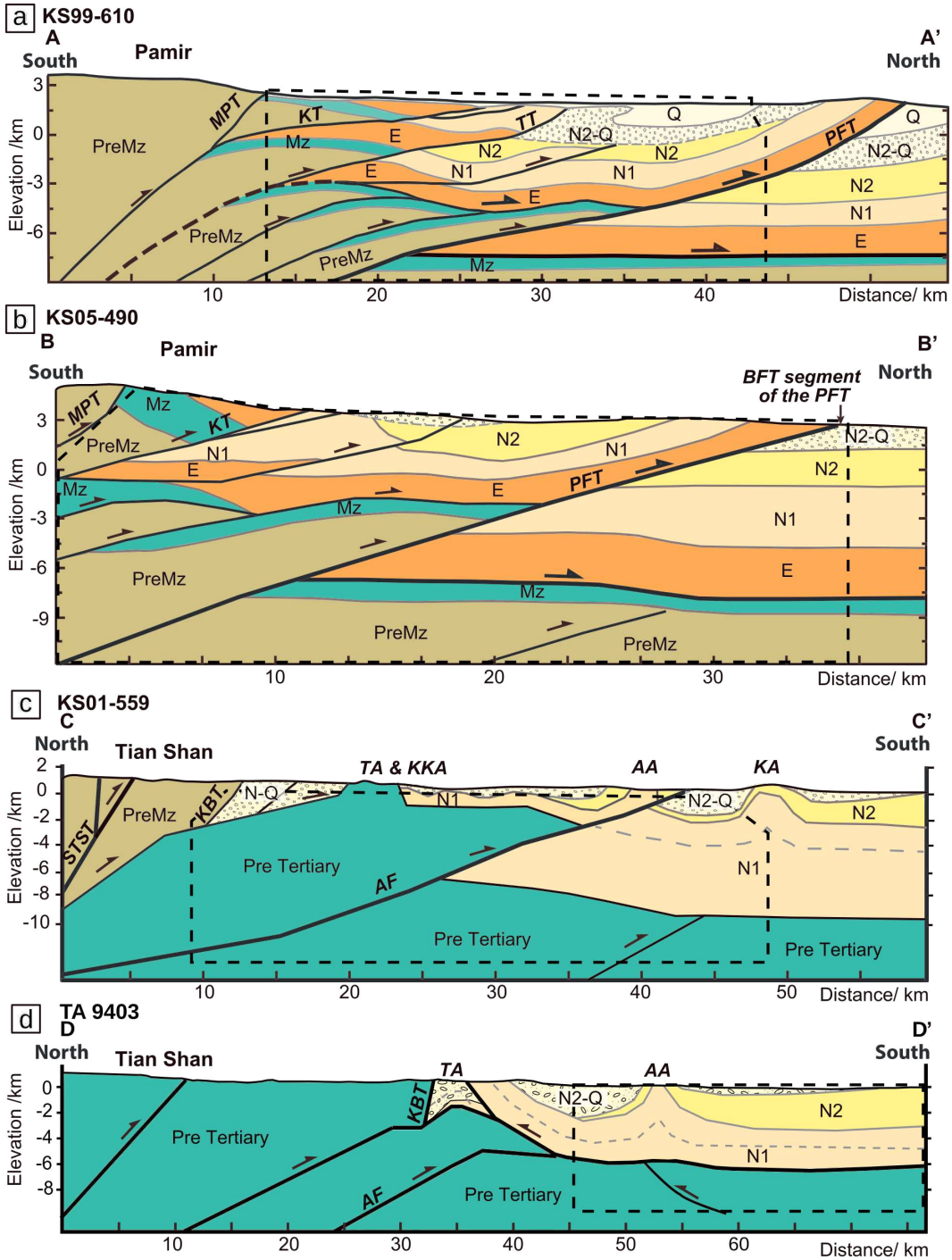


Figure 3.3: Cross-sections through the Tian Shan and Pamir forelands around Kashi. Locations shown in Figure 3.1. a)-c) are modified from *Thompson Jobe et al.* (2017), who modified them from *Chen et al.* (2010), *Cheng et al.* (2016) and *Heermance et al.* (2008) respectively. d) modified from *Heermance et al.* (2008). Note that the details of interpreted fault locations, fault dips and unit thicknesses for profiles a) and b) vary between different publications. Dashed black boxes show the extent of the seismic reflection profiles. AA = Atushi Anticline, AF = Atushi Fault, BFT = Bieertuokuoyi segment of the PFT, KA = Kashi Anticline, KBT = Kashi Basin Thrust, KKA = Keketamu Anticline, KT = Kenenbierte Thrust, MPT = Main Pamir Thrust, PFT = Pamir Frontal Thrust, STST = Southern Tien Shan Thrust and TA = Tashipishake Anticline. Q = Quaternary, N2-Q = Plio-Pleistocene conglomerates, N2 = Pliocene, N1 = Miocene, E = Paleogene, Mz = Mesozoic.

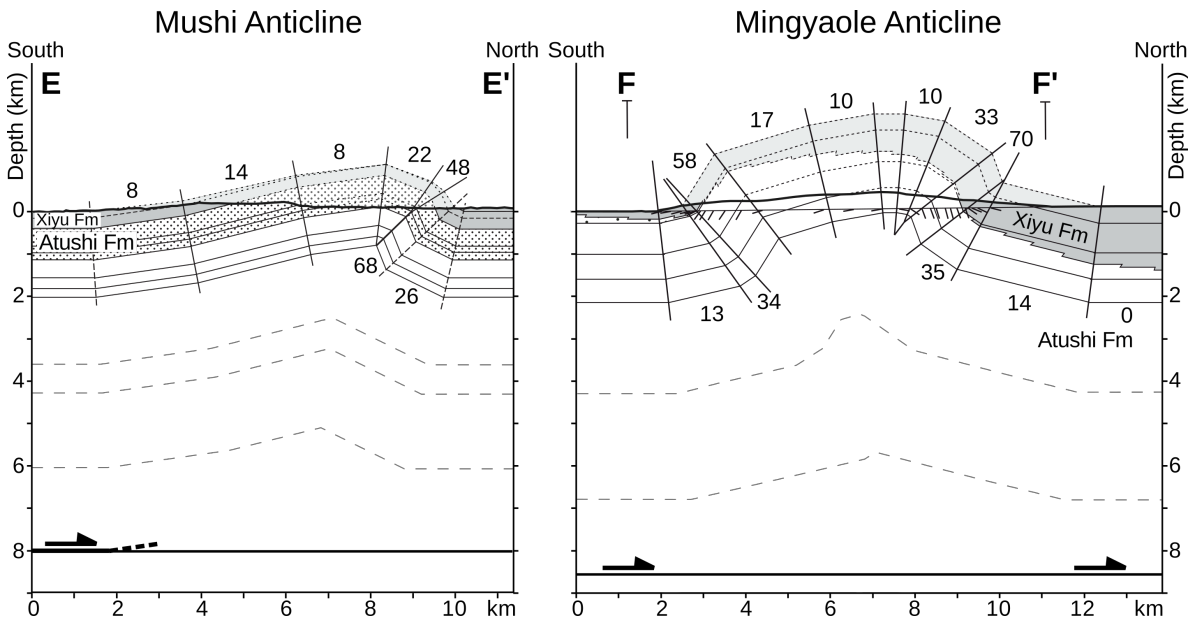


Figure 3.4: Geological cross-sections through the Mushi and Mingyaole Anticlines, modified from *Li et al.* (2013b) and (*Scharer et al.*, 2004) respectively. Locations shown on Figure 3.1. Deeper horizons are dashed because the deformation style at those levels is speculative (*Li et al.*, 2013b). The detachment depth below the Mushi Anticline is based on comparison to other publications (*Li et al.*, 2013b). Numbers show dip angles. Both folds exhibit north vergence in cross-section (*Scharer et al.*, 2004; *Li et al.*, 2013b).

are based on interpretation of seismic reflection profiles and on surface observations. In the foreland away from the Pamir and Tien Shan rangefronts the detachment dominates the shortening style: the deformation is thin-skinned (*Scharer et al.*, 2004; *Heermance et al.*, 2008), taking place on folds interpreted as detachment folds or fault tip folds (from north to south: the Atushi, Kashi, Mingyaole and Mushi Anticlines, Figures 3.1b, 3.4) (e.g. *Chen et al.*, 2005; *Scharer et al.*, 2006; *Li et al.*, 2013b).

In the foreland immediately adjacent to the Tien Shan, thrusts do cut through the Paleozoic basement to the surface but are thought to have only modest modern slip rates (*Heermance et al.*, 2008). Any shortening in the basement is generally supposed to take place predominantly beneath the Pamir and Tien Shan rangefronts rather than within the foreland (e.g. *Scharer et al.*, 2004; *Heermance et al.*, 2008; *Chen et al.*, 2010; *Wang et al.*, 2016; *Cheng et al.*, 2016; *Thompson Jobe et al.*, 2017). On the Pamir side of the foreland, the slip on several imbricate reverse faults in the basement is believed to focus on the basal Cenozoic detachment. This fault in the base of the Cenozoic is

named the Pamir Frontal Thrust (PFT), is north-vergent and meets the surface (*Chen et al.*, 2010; *Cheng et al.*, 2012; *Wang et al.*, 2016). The extent to which shortening above and below the detachment are decoupled in the region between the PFT and the Pamir is under debate. Cross-sections by *Chen et al.* (2010) and *Cheng et al.* (2012) both included faults that cut through the basement and foreland sediments, but a reinterpretation by *Wang et al.* (2016) based on analogue models argued that the detachment divides the stratigraphy into two separate structural levels.

The Pamir Frontal Thrust is in the centre of my study area (Figures 3.1 and 3.5). It is known by different names along strike: in the western part of our region of interest the fault steps southwards, forming an embayment and is known as the Biertuokuoyi Frontal Thrust (BFT)(Figure 3.5) The basin within the embayment is named the Mayikake Basin and on its opposite side the Mayikake Thrust (MT), a south-vergent thrust, takes up part of the slip at this longitude. To the east of the Mayikake Basin the bedrock fault is known as the Tuomuluoan Thrust (TT). It overrides the Mingyaole Anticline, with the Kezilesu River running between them in a narrow valley. At the eastern end of the TT the Quaternary fault scarps separate from the bedrock fault. The Quaternary scarps, which I will discuss in detail in this study, continue along-strike and have been named the Mingyaole South Thrust (MST) (Figure 3.5). The bedrock fault (TT) bends to the south and is replaced by the Mushi Anticline (Figures 3.4 and 3.5).

On the basis of a seismic reflection profile published by *Chen et al.* (2010), and the surface outcrop of Paleogene strata overthrusting Plio-Pleistocene Xiyu conglomerates (*Li et al.*, 2012b), the Tuomuluoan Thrust has been interpreted as being subparallel to bedding and having a shallow dip (<20° but non-planar). However, it is not completely proven that the active fault has shallow dip: the Holocene fault scarps are north of the geological fault outcrop and the seismic reflection profile is not clear or extensive enough to exclude a different dip for the TT or to exclude the existence of a second fault with a different dip.

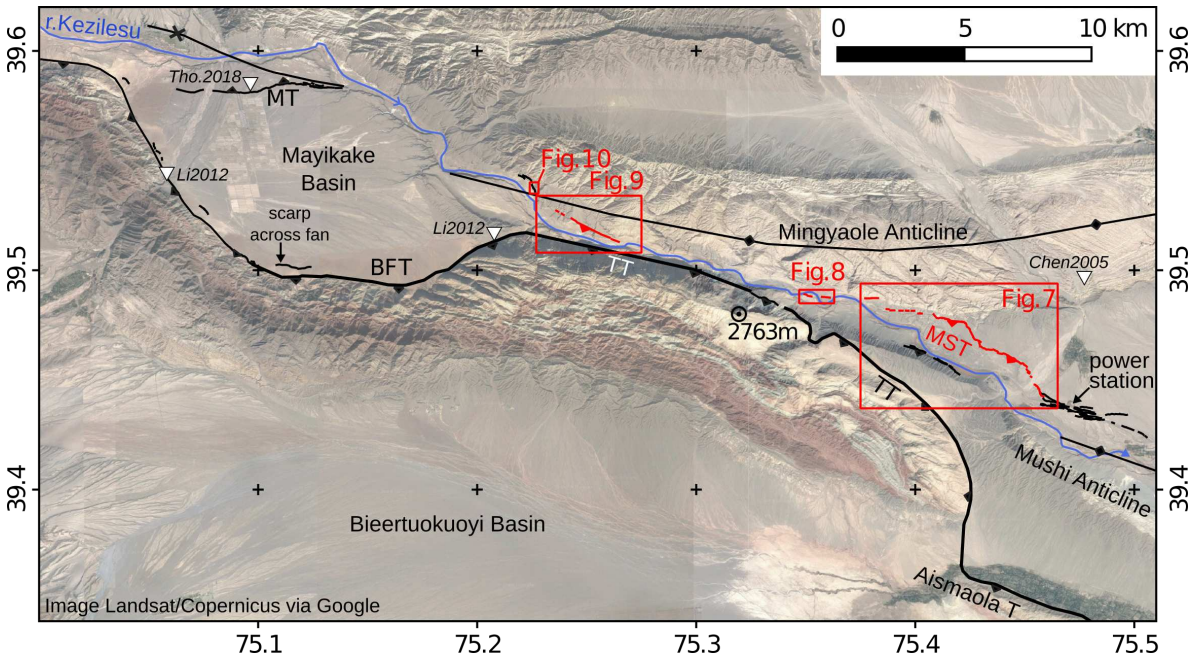


Figure 3.5: Overview of the study area. Red sections are believed to have ruptured in 1985. Inverted white triangles show sample sites that were used to estimate published shortening rates and are labelled with the first paper to describe that sample, some sites have been revisited in later studies (Section 5.6). A. = Anticline, BFT = Bieertuokuoyi Frontal Thrust, MT = Mayikake Thrust, TT = Tuomuluoan Thrust.

3.2.3 Shortening rates

Since the late-Miocene or Pliocene, the faults and folds within the foreland have taken up the majority of the shortening in the region (*Heermance et al.*, 2008; *Thompson et al.*, 2015). This is partly at the expense of the STST and northern Tien Shan foreland structures (*Heermance et al.*, 2008), and partly at the expense of the MPT, which now has very low activity at this longitude (*Sobel et al.*, 2011; *Li et al.*, 2012b; *Thompson Jobe et al.*, 2017; *Bufe et al.*, 2017).

The Pamir Frontal Thrust is the fastest-slipping fault in this part of the convergence zone and based on GPS velocities and Quaternary slip estimates, it and its immediate neighbours accommodate ~6–9 mm/yr of convergence (*Zubovich et al.*, 2010; *Li et al.*, 2012b). Based on magnetostratigraphy, its Tuomuluoan Thrust section has a shortening rate of ≥6.4 mm/yr over the past ~0.35 Ma (*Li et al.* (2012b), Figure 3.5). The Mingyaole Anticline next to it has a shortening rate of ~2.4 mm/yr (*Chen et al.*, 2005;

Thompson et al., 2018). Directly along-strike to the west, the Bieertuokuoyi Frontal Thrust and Mayikake Thrust accommodate shortening with slightly different proportions. *Li et al.* (2012b) measured a terrace tread that has been vertically offset across the BFT by 38 m at a site where the fault dip is 75±5°SW and striae on the hanging wall fault surface are inclined at 34° from the horizontal (a rake of 146° according to the conventional definition). Using *Thompson et al.* (2018)'s revised date of 12–14 ka for this terrace, this corresponds to a shortening rate of ∼4.6 mm/yr. Opposite it the Mayikake Thrust offsets the ∼12–14 ka terrace by 15 m vertically; given the dip at that site of 16±3°, this corresponds to a shortening rate of ∼3.7 mm/yr (*Thompson et al.*, 2018). As the TT bends in the east, the Mushi Anticline takes up just $1.5^{+1.3}_{-0.5}$ mm/yr of shortening (*Li et al.*, 2013b). This reduced value is presumably accounted for by shortening on the Aismaola Thrust (Figure 3.5) and by an overall eastwards decrease of shortening rates at the transition to the stable Tarim Basin (Figure 3.1a).

3.3 The Wuqia Earthquake and its seismology

The Wuqia earthquake struck Wuqia County on 23rd August 1985 at 20:41.56 local time (12:41.56 UTC). The earthquake sequence killed 64 people in total (*Fan et al.*, 1994); the shaking reached intensity IX in places and caused considerable damage to buildings, including a middle school in Wuqia county and the Kashi Power Station dam (*Feng et al.*, 1986).

Burtman and Molnar (1993) and *Fan et al.* (1994) both studied the earthquake's focal mechanism, moment and depth as part of regional studies and *Wang et al.* (1987) studied its mechanism and moment in a short, specifically targeted study. *Burtman and Molnar* (1993) used *McCaffrey and Abers* (1988)'s waveform inversion program to find the set of parameter values that gave the minimum misfit between synthetic waveforms and teleseismic body waves recorded at analogue Worldwide Standardised Seismograph Network (WWSSN) stations. They used a half-space velocity model (V_p = 6.2 km/s,

$V_s = 3.6$ km/s) and a source time function made up of a series of overlapping triangular pulses. *Fan et al.* (1994) also used the teleseismic P and SH waveforms recorded at WWSSN stations and also aimed to minimise the misfit between them and synthetic waveforms but they did so using a slightly different inversion method developed by *Holt and Wallace* (1987). They used a trapezoid-shaped source time function and a near-source velocity structure of a 4 km-thick lower velocity layer ($V_p = 4$ km/s, $V_s = 2.3$ km/s) overlying a halfspace ($V_p = 6$ km/s, $V_s = 3.5$ km/s). *Wang et al.* (1987) took a different approach and looked at long-period surface waves recorded at the 15 very long period digital stations of the IDA network and performed an inversion using the spectral amplitude method to estimate components of the earthquake's moment tensor. All three studies and the GCMT catalogue treat the earthquake as a point source (unless it is explicitly split into sub-events) and the depths they find correspond to the centroid of the earthquake moment release. None of the three inverted for horizontal location.

Table 3.1: Published earthquake parameters for the 23rd August 1985 Wuqia mainshock. SV az. = slip vector azimuth. B+M93 = *Burtman and Molnar* (1993). F94 = *Fan et al.* (1994). W87 = *Wang et al.* (1987). Values in italics show the alternative nodal plane and ranges show the uncertainty of the solution in the row above. Of these, all but the GCMT used fixed latitude and longitude taken from catalogues at the time.

Model	Method	M_o (N m)	M_w	Strike (°)	Dip (°)	Rake (°)	SV az. (°)	Centroid Depth (km)	Longitude °E	Latitude °N
B+M93	single event with directivity	2.22×10^{19}	6.8	60	76	47	45	18	75.27	39.43
				35–85	58–78	32–57		<25		
				316	*46*	*160*	*150*			
	three sub-events	3.6×10^{18}	(6.3)	45	70	62	12	18	75.27	39.43
		7.9×10^{18}	(6.6)	68	71	34	56	19	75.27	39.43
		9.9×10^{18}	(6.6)	61	72	52	39	18	75.27	39.43
				282	*34*	*142*	*135*			
				326	*58*	*158*	*158*			
				309	*41*	*152*	*151*			
F94		2.79×10^{19}	6.9	66	59	56	29	16	75.27	39.49
				56–76	49–69	46–66				
				299	*45*	*133*	*155*			
				289–309	*35–55*	*123-143*				
W87		5.7×10^{19}	7.1	60	80	50	48	-	75.2	39.4
				310	*40*	*160*	*146*			
GCMT		3.29×10^{19}	6.9	63	80	62	45	15	75.09	39.54
				315	*29*	*159*	*154*			

Table 3.2: Published earthquake parameters for the 11th September 1985 aftershock. SV az. = slip vector azimuth. B+M93 = *Burtman and Molnar* (1993). F94 = *Fan et al.* (1994). Values in italics show the alternative nodal plane and ranges show the uncertainty of the solution in the row above. Of these, all but the GCMT used fixed latitude and longitude taken from catalogues at the time.

Model	Method		M_o (N m)	M_w	Strike (°)	Dip (°)	Rake (°)	SV az. (°)	Centroid Depth (km)	Longitude °E	Latitude °N
B+M93	single event		8.1×10^{17}	5.9	108	31	104	2	7	75.44	39.36
					48–138	21–38	44–129		4–10		
					272	*60*	*82*	*198*			
F94	two sub-events		1.19×10^{18}	6.0	118	39	112	1	6	75.44	39.36
					88–148		82–142				
					271	*54*	*173*	*208*			
					241–301		*178–238*				
GCMT			1.82×10^{19}	6.1	90	44	68	29	10	75.32	39.50
					299	*50*	*110*	*179*			

Although the earthquake is typically referred to with a magnitude of M7.4 (e.g. *Feng et al.*, 1986, 1988; *Li et al.*, 2012b; *Bufe et al.*, 2017), seismological studies have found that its moment magnitude was M_w6.8–7.1 (Table 3.1). The focal mechanism is intriguing, given the geological setting. *Wang et al.* (1987), *Burtman and Molnar* (1993), *Fan et al.* (1994) and the GCMT catalogue all favour either a fault striking ENE dipping steeply to the south with an oblique left-lateral reverse sense of slip (slip vector towards the northeast) or a fault on the alternative nodal plane, striking NW, dipping at approximately 45° to the NE, and a right-lateral sense of slip with small reverse component (slip vector to the south-southeast) (Table 3.1). Their best-fit depths are 15–19 km (Table 3.1). *Burtman and Molnar* (1993) remarked that the signals were complicated and required a model including either directivity (towards the NW) or three sub-events to fit the waveforms well. That study gave the most complete discussion of the uncertainty in the solution and found that the strike, dip and rake are correct to within 25° or less (see Table 3.1 for full details). The centroid depth is relatively poorly constrained — *Burtman and Molnar* (1993) concluded that the depth is less than 25 km but "probably not confined to the upper 10 km".

An aftershock on 11th September 1985 had a moment magnitude of 5.9–6.1 and a shallower depth of 4–10 km. Both *Burtman and Molnar* (1993) and *Fan et al.* (1994) note that their solutions for the 11th September event are poorly constrained, but they gave a strike that is roughly east, a dip of ∼21–39° to the south and a reverse sense of slip (see Table 3.2 for details).

Although *Wang et al.* (1987), *Burtman and Molnar* (1993) and *Fan et al.* (1994) did not solve for the location of the earthquakes, global catalogues do provide location estimates, which are shown in Figure 3.6 along with isoseismals from *Feng et al.* (1986). The Global Centroid Moment Tensor (GCMT) project provides an estimate of the centroid location (centre of the earthquake's moment distribution) (*Ekström et al.*, 2012). The National Earthquake Information Center (NEIC) catalogue and the International Seismological Information Centre's recalculated EHB catalogue (*Weston*

et al., 2018), which uses the method of the *Engdahl et al.* (1998) bulletin, each provide an estimate of the epicentre location. Although catalogue locations for earthquakes from the 1980's often have errors of ≥15 km (e.g. *Berberian*, 1979; *Ambraseys*, 2001), the locations nevertheless do confirm that the earthquakes both took place within the foreland and not beneath the Pamir rangefront, which is ∼30 km away from both the seismically-estimated locations and the main axis of the isoseismals.

Although published studies on this earthquake have concluded that the partially reverse sense of slip and broadly east-west strike of the mainshock focal mechanism are in keeping with the regional setting (*Fan et al.*, 1994), it is not easily matched with the reported surface ruptures, which were south-up reverse-right-lateral ruptures, arcing in strike from east-west to southeast-northwest (*Feng et al.*, 1988) (Figure 3.5). In the following sections I will first review the surface ruptures from the Wuqia earthquake, then attempt to derive an independent estimate of the focal mechanism from geodetic measurements.

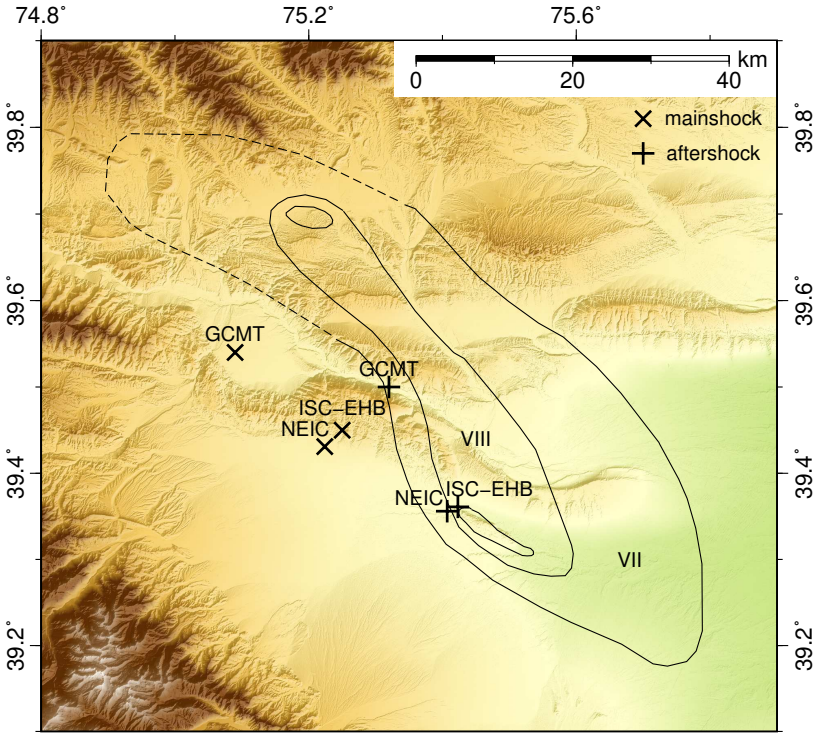


Figure 3.6: Locations for the Wuqia earthquake and 11th September 1985 aftershock. x's mark locations for the mainshock, +'s show aftershock locations. Contour lines show isoseismals and their Modified Mercali Intensity (*Feng et al.*, 1986). See Section 3.3 for explanation of acronyms. All data were accessed on 15th June 2018.

3.4 Surface ruptures

Surface rupture maps and measurements were published by *Feng et al.* (1986, 1988), but are only available in non-digital form, without location coordinates and in Chinese journals, so are not readily accessible for English-speaking readers. Therefore, in order to assess the surface expression of the Wuqia earthquake it was necessary to compile and update the reports. In this section I present a comprehensive compilation of Holocene surface rupture mapping, drawn from *Feng et al.* (1986, 1988) and from my own mapping using sub-metre modern imagery and pre-earthquake declassified spy satellite imagery. The modern imagery was taken from GoogleEarth, which provides coverage of the entire region at sub-metre (50–60 cm) resolution with data from Pléiades, GeoEye-1, WorldView-2 and QuickBird-2 (Table 3.4). The details of the pre-earthquake imagery are given in Table 3.3. I georeferenced the offset measurements that I digitised from

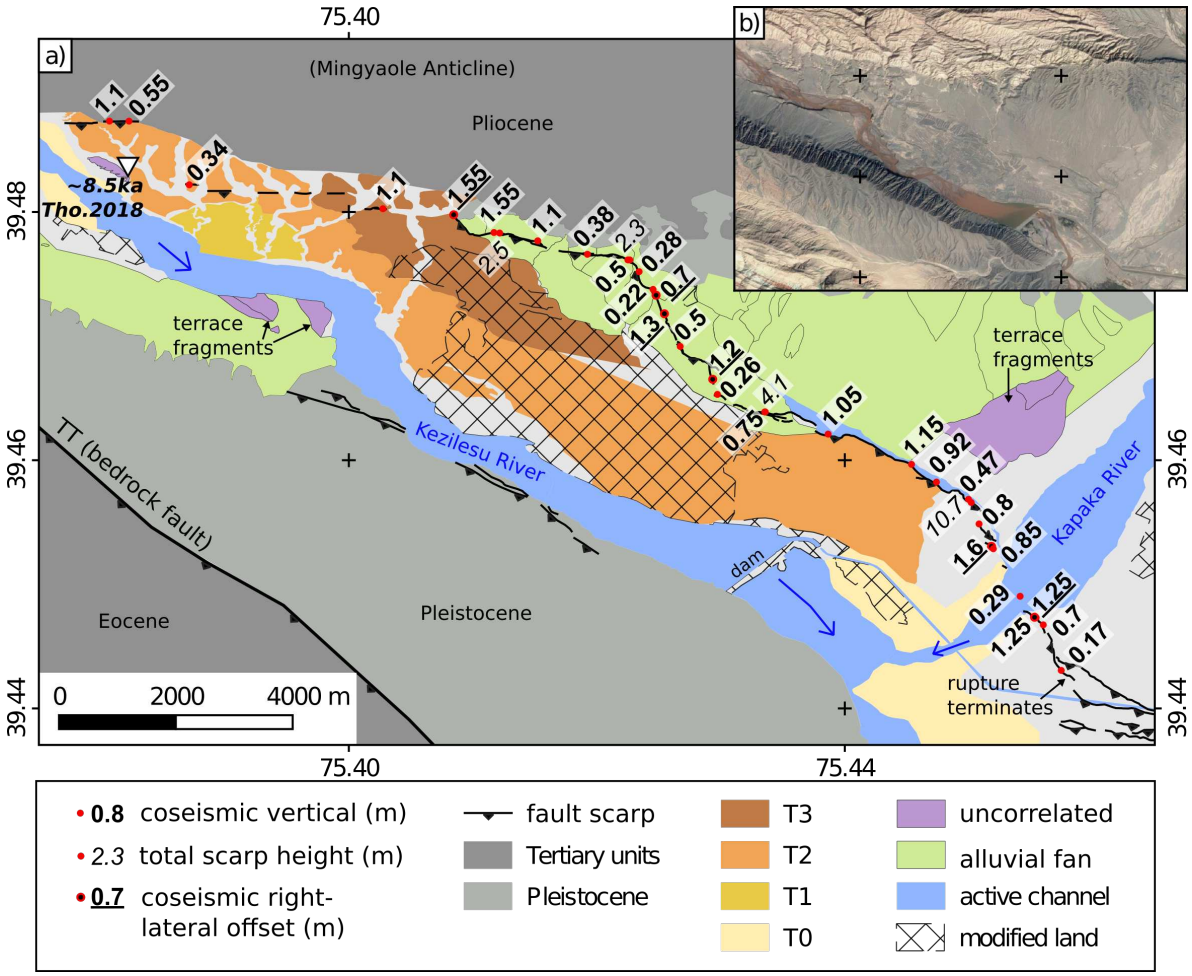


Figure 3.7: The main section of the 1985 surface ruptures. See Figure 3.5 for location. a) Geomorphic map and compiled offset measurements (see Table 3.5 for details). Inverted white triangle marks the site where *Thompson et al.* (2018) collected samples for optically stimulated luminescence and cosmogenic radionuclide dating, yielding a terrace abandonment age of ~8.5 ka for T2 (a 95% confidence interval of 3.5–12.8 ka for the cosmogenic radionuclide age). Terraces in this figure have not been correlated with the terraces in Figure 3.9a. 'Modified land' marks surfaces that have been disturbed by mining, agriculture, construction, etc. b) the same area in GoogleEarth imagery.

Feng et al. (1986) and *Feng et al.* (1988) by comparing the shapes and relative locations of the ruptures, terrace risers and rivers in the *Feng et al.* (1986, 1988) maps with the same features in modern georeferenced imagery and using the scale bars and north arrows that are provided on the *Feng et al.* (1986, 1988) figures for guidance. I estimate that this method results in locations that are accurate to within ~150 m (often better) for most of the *Feng et al.* (1988) measurements and approximately 500 m for the measurements from *Feng et al.* (1986) (Figure 3.7).

Table 3.3: Details of the declassified satellite imagery used in this study. Note that KH-1 to KH-4B satellites are also known by the codename "Corona" and the KH-9 satellites are also known by the codename "Hexagon". Courtesy of the USGS.

Id	Acquisition date	Mission designator	Mision No.	Ground resolution
DS1010-2086DF133	1964/09/20	KH-4A	1010-2	≥2.8 m
DS1010-2086DF134	1964/09/20	KH-4A	1010-2	≥2.8 m
DS1010-2086DA138	1964/09/20	KH-4A	1010-2	≥2.8 m
DS1010-2086DA139	1964/09/20	KH-4A	1010-2	≥2.8 m
DS1043-1039DF063	1967/08/10	KH-4A	1043-1	≥2.8 m
DS1104-2185DA083	1968/08/19	KH-4B	1104-2	≥1.8 m
DZB1206-500082L016001	1973/08/04	KH-9	1206-5	6–9 m
DZB1216-500324L007001	1980/09/07	KH-9	1216-5	6–9 m

Table 3.4: Details of the post-earthquake satellite imagery used in this study. The images were accessed using GoogleEarth. Each scene provides partial covereage of the study area and together they have complete, overlapping coverage.

Id	Acquisition date	Satellite	Best ground resolution*
1010010004E00A03	2006/03/20	QuickBird-2	60 cm
1050410002196C00	2009/10/18	GeoEye-1	46 cm
103001001E06F000	2013/01/26	WorldView-2	49 cm
DS_PHR1B_20131... 0010558539_SE1_PX... _E075N39_0507_04826	2013/10/01	Pléiades	50 cm

* The images are pansharpened from panchromatic images whose nominal ground resolution is listed here. Post-processing seems to result in slightly lower resolution in the image viewer.

The surface ruptures are located close to where the TT and Mushi Anticline meet. Around 13 km of ruptures begin in the east at the end of a series of thrust scarps in the limb of the Mushi Anticline and trend northwest before they change in strike and run east-west along the southern edge of the Mingyaole Anticline (Figure 3.7). In this area, the locations of ruptures that can be mapped remotely today agree well with the mapping in *Feng et al.* (1988). The east-west trending sections of the ruptures were primarily compressional and south-up, with vertical displacements of up to 1.55 m. The northwest trending sections had right-lateral displacements of up to 1.55 m and smaller vertical displacements that were also south-up (*Feng et al.*, 1988) (Figure 3.7). This suggests that the slip vector pointed to the north or north-northeast. Except where it crossed the youngest surfaces, the 1985 displacement added to a pre-existing scarp that now has a height of ∼2–10 m (Table 3.5). The ruptures end in the west with scarps that cross low terraces within meanders of the Kezilesu river (Figure 3.8).

I have mapped an additional scarp 7.5 km to the west of that site which also appears to have ruptured in 1985. On both modern and 1964 imagery there is a well-established 12–30 m high scarp (Table 3.6) offsetting terraces north of the Kezilesu River at the point where the TT bends southwards into the embayment and the fault becomes known as the BFT (Figures 3.5 and 3.9). On the post-earthquake imagery, the same scarp continues onto the lowest surface and runs into the active river channel. That

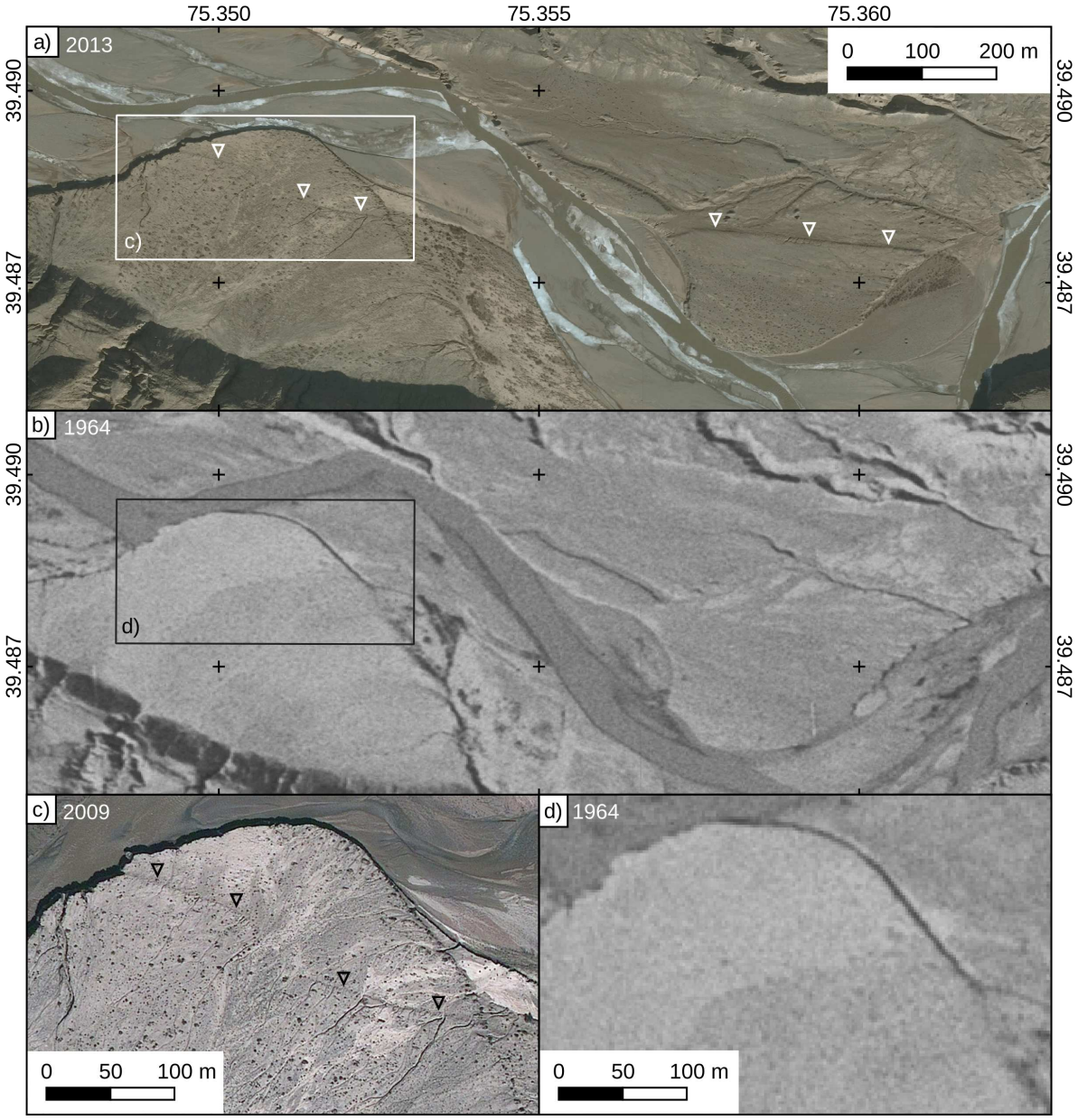


Figure 3.8: The 1985 ruptures as they crossed the low terraces by the Kezilesu River. a) 2013 image of the scarps from GoogleEarth, copyright CNES/Airbus. b) Pre-earthquake 1964 Corona image of the same area, showing no scarps (ID: DS1010–2086DA139). c) Zoomed-in post-earthquake image of the western scarps. GoogleEarth/DigitalGlobe. d) The same location in 1964.

section of the scarp is not visible in the 1964 images (three different images cover this location), suggesting that this section of the fault was reactivated in 1985 and broke a fresh scarp in the lowest, youngest surface. If this scarp did rupture in 1985 it would bring the total length spanned by the ruptures up to 25 km, including a 7.5 km gap in the

Table 3.5: Offset measurements for the 1985 Wuqia earthquake. Orientations are V: vertical, or RL: right-lateral. F88: *Feng et al.* (1988), F86: *Feng et al.* (1986).

Long. °E	Lat. °N	Orientation	Offset (m)	Reference	Notes
75.3806	39.4873	V	1.10	F88	
75.3822	39.4873	V	0.55	F88	
75.3871	39.4821	V	0.34	F88	location approx.
75.4027	39.4802	V	1.10	F88	
75.4084	39.4797	RL	1.55	F88	
75.4117	39.4783	V	1.55	F88	
75.4152	39.4776	V	1.10	F88	
75.4192	39.4765	V	0.38	F88	
75.4226	39.4761	V	0.50	F88	
75.4234	39.4751	V	0.28	F88	
75.4245	39.4737	V	0.22	F88	
75.4247	39.4732	RL	0.70	F88	
75.4254	39.4718	RL	1.30	F88	
75.4267	39.4691	V	0.50	F88	
75.4293	39.4665	RL	1.20	F88	
75.4297	39.4653	V	0.26	F88	
75.4335	39.4638	V	0.75	F88	
75.4386	39.4621	V	1.05	F88	
75.4453	39.4596	V	1.15	F88	
75.4473	39.4582	V	0.92	F88	
75.4499	39.4568	V	0.47	F88	
75.4541	39.4490	V	0.29	F88	
75.4552	39.4473	RL	1.25	F88	
75.4554	39.4473	V	1.25	F88	
75.4574	39.4430	V	0.17	F88	
75.4508	39.4548	V	0.8	F86	location approx.
75.4518	39.4530	RL	1.6	F86	location approx.
75.4519	39.4528	V	0.85	F86	location approx.
75.4559	39.4467	V	0.7	F86	location approx.

narrowest part of the Kezilesu River valley. Although the Wuqia earthquake ruptures were surveyed in the 1980's and this section was not mapped, my interpretation that this section also broke in 1985 is the most compatible with the information we have. It is plausible that the surveys would not have visited this site: it is some distance from the other ruptures and, although there are now a few buildings ∼3 km from the site, in 1985 there were no roads providing access and no local residents. Although the quality of the Corona images means that small features can be invisible on them,

Table 3.6: Cumulative offset measurements for scarps in the study area. Orientations are V: vertical, or RL: right-lateral. T18: *Thompson et al.* (2018), no reference indicates a new measurement for this study was made using the AW3D30 DEM for vertical offsets or using modern imagery for lateral offsets.

Long. °E	Lat. °N	Orientation	Offset (m)	Uncertainty (m)	Reference	Notes
75.2262	39.5365	RL	1.4	±0.5	.	
75.2263	39.5365	RL	1.9	±0.5	.	
75.2263	39.5365	RL	1.8	±0.5	.	
75.2486	39.5203	V	12.9	±3.8	.	
75.2511	39.5190	V	34.3	±1.9	.	
75.2547	39.5172	V	19.6	±1.2	.	
75.2571	39.5160	V	21.9	±2.0	.	
75.2584	39.5156	V	30.3	±1.2	.	
75.2591	39.5153	V	26.5	±1.6	.	
75.4121	39.4783	V	2.5	±0.9	.	
75.4225	39.4761	V	2.3	±1.1	.	
75.4335	39.4638	V	4.1	±0.7	.	
75.4501	39.4566	V	10.7	±0.7	.	
75.0591	39.5408	V	38		T18	
75.1096	39.5843	V	15		T18	location approx.

that seems unlikely here - the sun in Figures 3.9c and 3.9e was oriented so it would have cast a shadow behind the scarp if any scarp had been there at the time, and the pre-earthquake imagery does show a small channel of similar size to the scarp, 200 m to the east. Overall, it seems probable that this section of scarp did rupture in 1985, but higher-quality pre-earthquake images or a field visit would be necessary to absolutely confirm this interpretation.

The scarp extends a further ∼3.2 km from the Kezilesu River bank in the east until it reaches the Mayikake Basin in the west (Figure 3.9). The scarp does not cross the basin but another scarp, also on the northern side of the Kezilesu River, does become evident (Figures 3.5 and 3.10). That scarp begins by trending northwards with a right-lateral displacement, then bends gently to trend westwards (Figure 3.5) with predominantly north-up displacements, suggesting that it too accommodates some of the north-south shortening but is south-vergent. The scarp offsets small channels by <2 m (Figure 3.10, Table 3.5). It is very fresh — similar to the scarps known to have ruptured in 1985

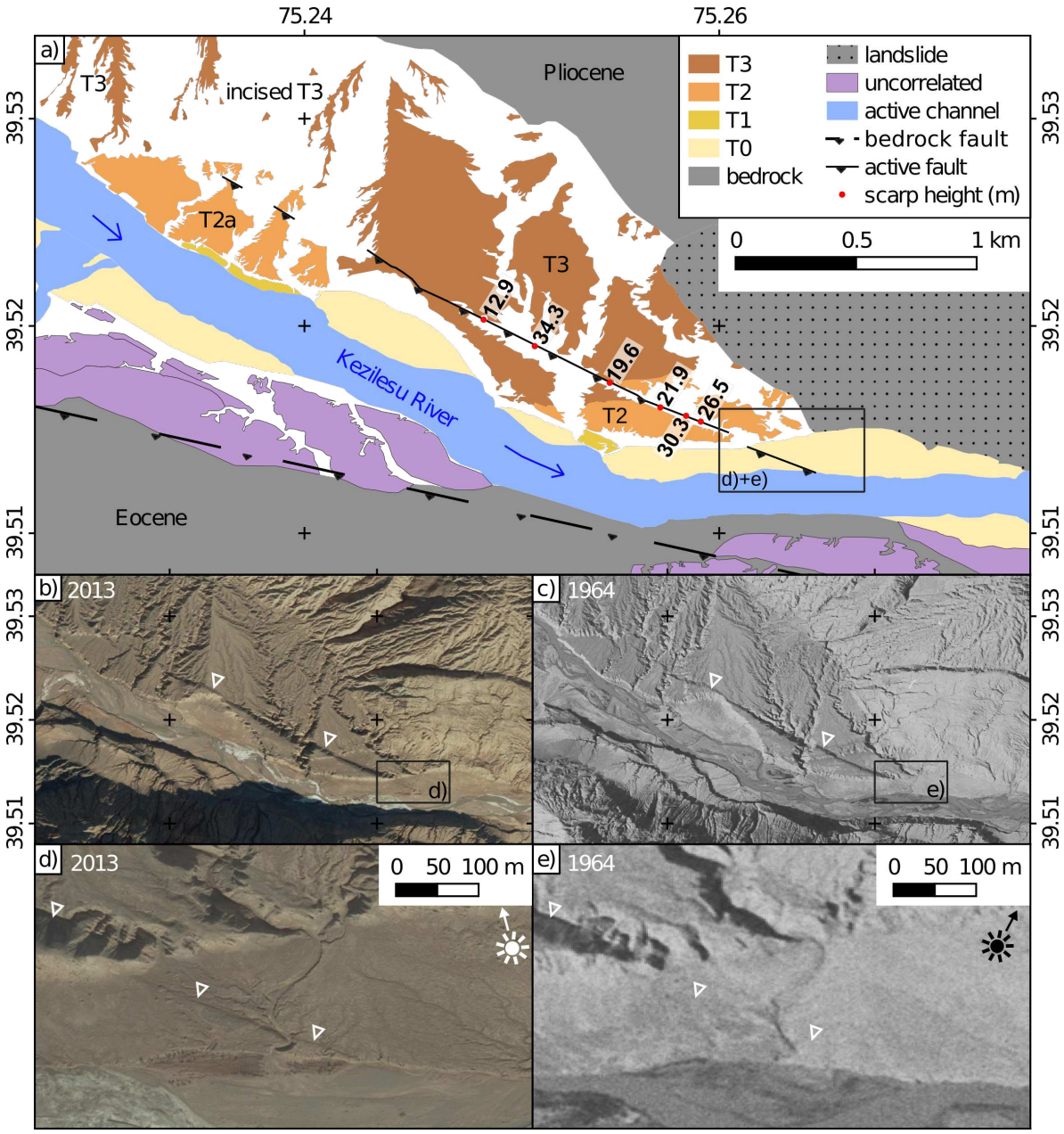


Figure 3.9: a) A geomorphic map of the western end of the Tuomuluoan Thrust, showing the active fault offsetting terraces by 12–30 m. Purple polygons show terrace levels of various heights south of the river which have not been correlated with the terraces north of the river because no ages are available and the fault between them makes correlation based on elevation unreliable (e.g. *Thompson et al.*, 2018). b) 2013 image of the same area. Copyright GoogleEarth/DigitalGlobe. c) 1964 image of the same area (ID: DS1010–2086DA139). d) and e) Zoomed-in images of the part of the scarp closest to the river. The scarp is visible in the post-1985 image but not in the pre-1985 image.

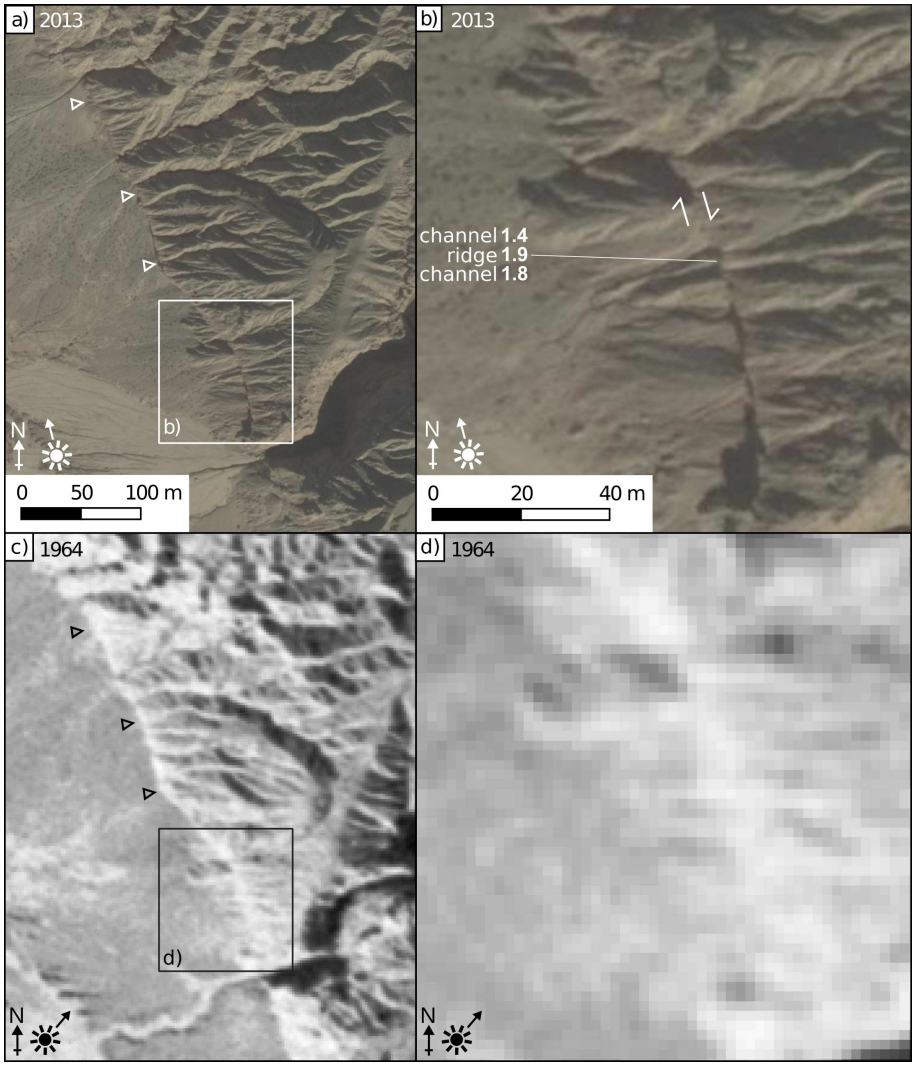


Figure 3.10: a) Part of the minor scarp on the northeastern edge of the Mayikake Basin. Location is shown in Figure 3.5 b) A close-up of the strike-slip section of the fault. Numbers show horizontal offset measurements in metres. c) and d) 1964 image of the same areas (ID: DS1010-2086DF133).

— but it is also faintly visible on pre-earthquake imagery (Figure 3.10) and it is not clear from the imagery whether the scarp had any displacement in 1985 so, taking the conservative approach, I have not marked it as a 1985 rupture in Figure 3.5 or included it in the discussions of rupture length. Along the southern side of the basin I did not find any scarps in the alluvial fans crossing the BFT until 8 km west of the start of the Mayikake Basin (beginning with the short section marked as "scarp across fan" on Figure 3.5c) and there is no suggestion that there were surface ruptures on the BFT in 1985. The 1985 surface ruptures therefore appear to have end at the edge of the

Mayikake Basin.

The exact timing of rupture formation is not clear. *Feng et al.* (1986) reported that a survey immediately after the 23rd August mainshock failed to find primary surface ruptures, but after the 11th September aftershock, 5 km of ruptures were found close to the Kashi power station (Figure 3.5), this is the eastern 5 km of the 13 km of mapped ruptures. That section then alerted the scientists to the rest of the ruptures, which were mapped in April–May and September 1986 (*Feng et al.*, 1988). In summary, although the eastern 5 km of ruptures have been attributed to the aftershock, and the rest have implicitly been attributed to the mainshock, it is not certain what portion of the ruptures each earthquake caused, or whether any aseismic deformation in the 7 months following the mainshock increased their size.

3.5 Horizontal displacements from geodesy

Several studies since the Wuqia earthquake have shown that postseismic deformation can have a large magnitude in proportion to the mainshock (*Freed*, 2007; *Zhou et al.*, 2016; *Floyd et al.*, 2016) and continue at measurable rates for long durations (*Gourmelen and Amelung*, 2005; *Copley*, 2014; *Copley and Reynolds*, 2014). It is also well known that for many continental reverse-faulting earthquakes a significant proportion of the slip is blind (e.g. *Yielding et al.*, 1981; *Berberian et al.*, 2000; *McAuliffe et al.*, 2015). This leads to the question of whether the 1986 scarp measurements accurately reflect the total tectonic displacement across the region up to the present day; to address the question I have turned to geodesy.

No published geodetic observations covering the Wuqia earthquake exist. It predates InSAR-capable satellites but the existence of pre-earthquake optical imagery allows me to create a horizontal displacement map. *Leprince et al.* (2007a); *Ayoub et al.* (2008, 2009) and *Hollingsworth et al.* (2012) developed and demonstrated techniques for determining horizontal displacements in the time between two images based on precise

coregistration of the two images, followed by correlation. The method has been successfully applied to several earthquakes worldwide using a variety of satellite systems and aerial photos (e.g. *Avouac et al.*, 2006; *Leprince et al.*, 2007a,b; *Milliner et al.*, 2016; *Zhou et al.*, 2016).

I have applied the method, which is implemented in COSI-Corr (*Leprince et al.*, 2007a), to measure horizontal displacements of the Wuqia earthquake. I used a 15 m resolution panchromatic Landsat 7 image, taken on 16th August 2002, and two KH-9 images for two separate correlations (Table 3.3). A 1973 KH-9 image provides full coverage of the area, while a 1980 image that covers part of the area was used because it gives an area of overlap between the two correlations, allowing me to confirm any results, and because the 1980 image is higher quality than the earlier image (the quality of the mapping program results generally improved over time). Although higher-resolution KH-4A and KH-4B imagery predating the earthquake is available, it is currently unsuitable for quantitative analysis due to its camera and acquisition method (e.g *Casana and Cothren*, 2008). The Landsat image was chosen to match the time of year of the KH-9 images and because it pre-dates open cast mining that is now close to some parts of the ruptures.

The processing involves determination of the exterior and interior orientations of the two images, orthorectification, coregistration and resampling onto a common grid, and finally, taking a set of correlation measurements in a sliding window across the images. Landsat images are already georeferenced and orthorectified, so only the KH-9 images required pre-processing. Tie points (which later were georeferenced and became GCPs) were picked between the Landsat and KH-9 images and placed according to the recommendations made by *Ayoub et al.* (2009). I used JAXA's 30 m AW3D30 DEM for GCP elevation and for orthorectification and resampled the KH-9 images onto the Landsat grid. I performed a two-stage frequency-based correlation with a window size dropping from 64 to 32 pixels and a step size of 16 pixels (240 m). These correlation parameters were found to give a good balance between resolution and noise,

but other parameter combinations gave similar results. The long-wavelength component of the signal is a consequence of sensor model errors, GCP distribution and any film or scanning distortion (*Ayoub et al.*, 2009; *Hollingsworth et al.*, 2012), and I therefore detrended the displacement maps by fitting and removing second-order polynomials.

3.5.1 Image matching results

The results are shown in Figures 3.11 and 3.12. There is no clear, consistent relationship between the results and topography, meaning that any change of topography between the acquisition dates is too small to cause an artefact and there is no need to apply any correction for using the same, imperfect DEM for both dates.

I delimited the area of interest into western, central and eastern regions as shown in Figures 3.11 and 3.12, and plotted the data from each region onto profiles perpendicular to the fault. In each profile the standard deviation of the raw data from a linear trendline is 3–11 m, and the standard deviation of the median-filtered values is 0.8–1.5 m, with the exception of the profile in Figure 3.12c, which has a standard deviation for the median-filtered values of 3.2 m. In keeping with the visual assessment of image quality, the 1980-2002 profiles generally showed smaller standard deviations than the 1973-2002 profiles. Three of the profiles show step changes across the fault: Figure 3.12c, Figure 3.11h and Figure 3.12h. Figure 3.12c shows a step corresponding to ∼10 m left-lateral slip, which is larger than would be expected for a $M_w \leq 7.1$ earthquake, the adjacent swath profile shows no step change and there is no data coverage for the 1980-2002 correlation so I believe the step to be an artefact. The profiles in Figures 3.11h and 3.12h each show a smoothed step close to the fault with a magnitude of ∼2 m, which would amount to the hanging wall (south of the fault) moving ∼2 m south and ∼2 m west with respect to the hanging wall. This differs from the north to north-northeast slip vector azimuth seen in the surface ruptures (Section 3.4). Neither of the corresponding profiles in the displacement map from the 1973-2002 image pairing ('e' panels) show the same signals, and nor do the profiles taken across the adjacent section

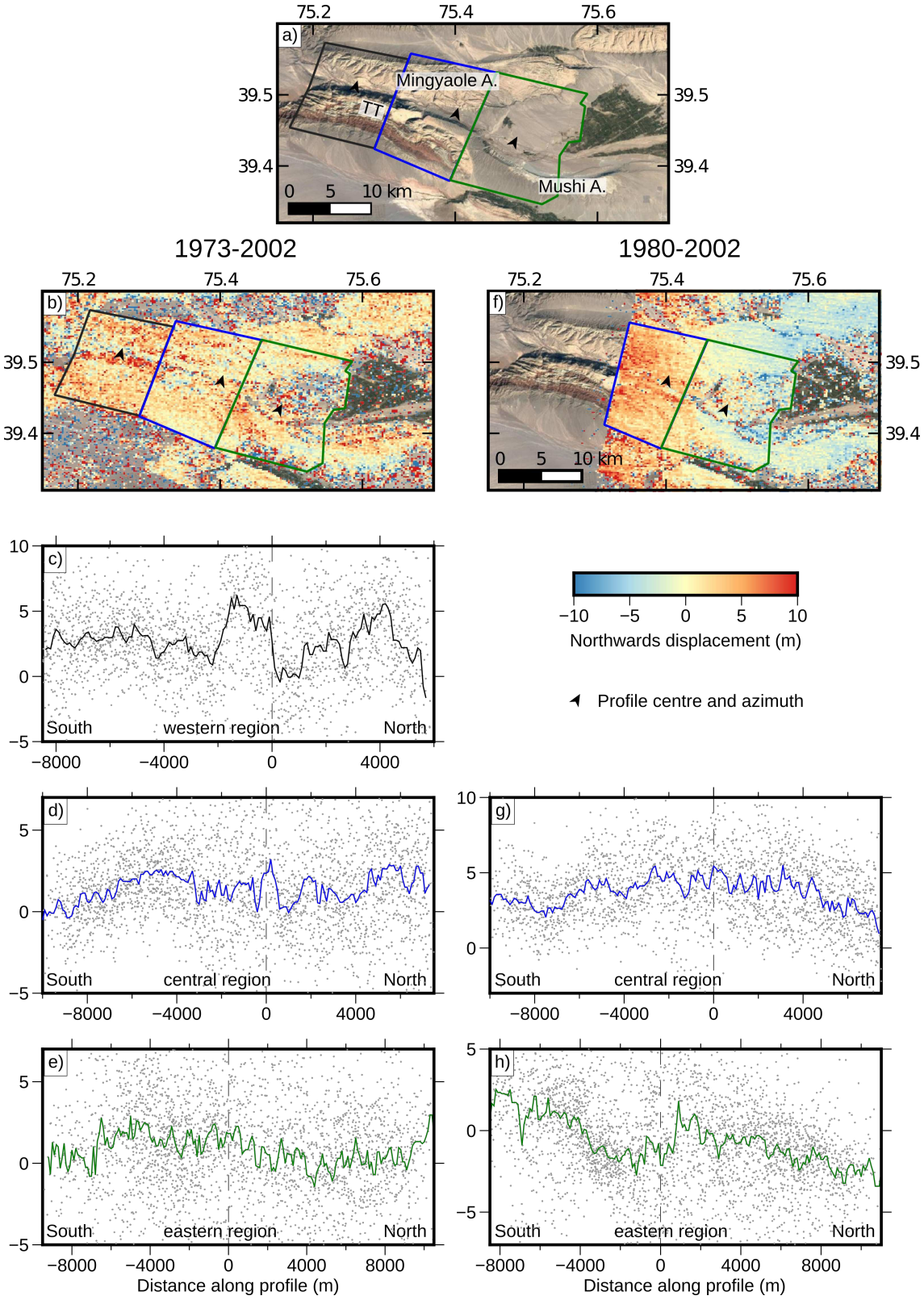


Figure 3.11: South to North displacement maps for the Wuqia earthquake made by correlating KH-9 and Landsat 7 images. a) GoogleEarth Image showing the same location as panels b) and f). b) Displacements over the Tuomuluoan Thrust (TT) and Mingyaole and Mushi anticlines from the 1973-2002 image pair. c)-e) Profiles through that displacement map. Solid lines show the median values (250 m filter width). f), g) and h) show the corresponding results for the 1980-2002 image pair.

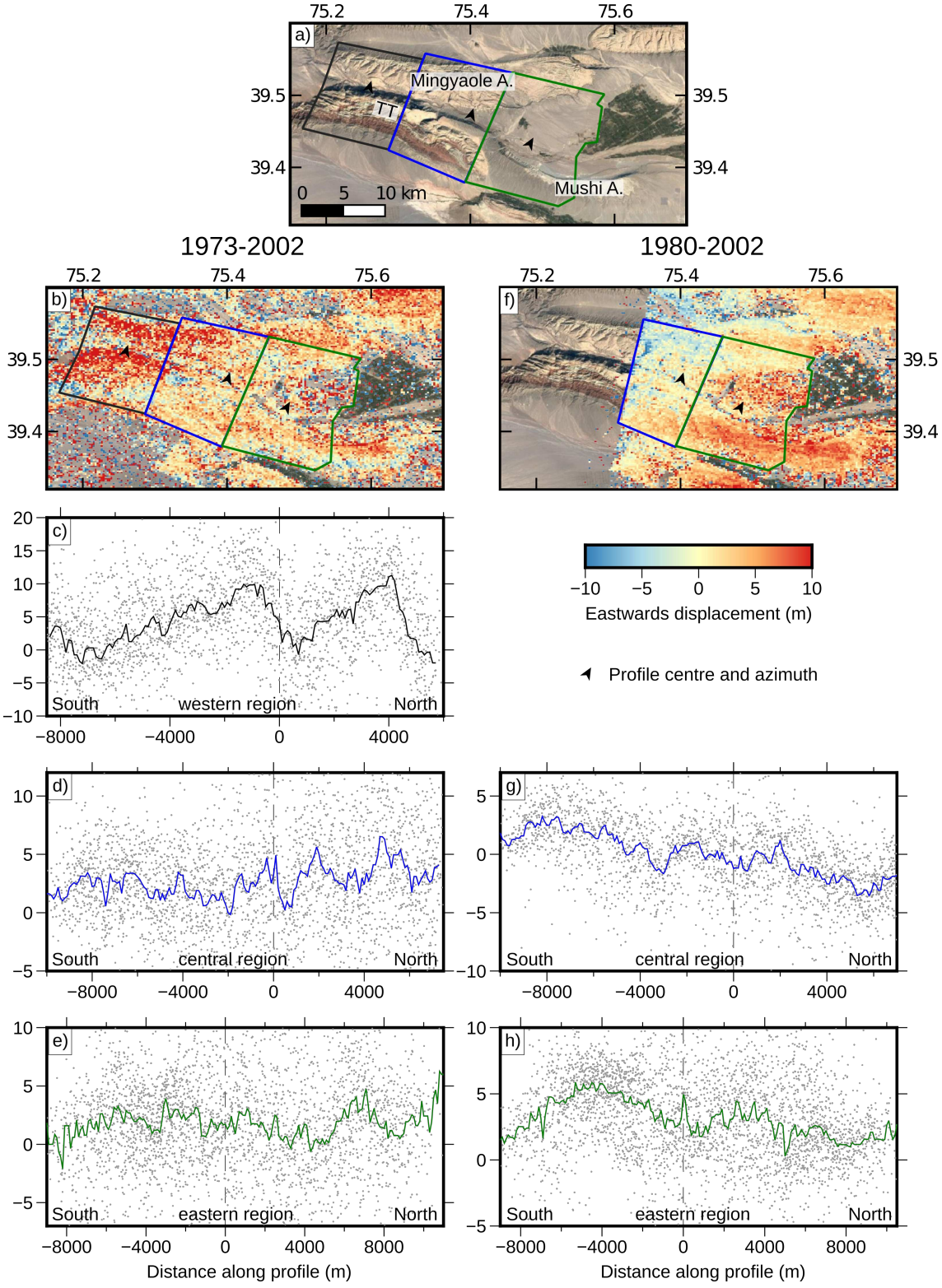


Figure 3.12: As Figure 3.12 but for West to East displacements.

of the fault along-strike ('g' panels). Therefore, although it is possible that one or both of these steps across the fault do represent true movement that the 1973-2002 optical image correlation has failed to capture, overall the results are inconclusive with respect to the possible displacements of ≤2 m. I conclude that there have been no laterally extensive horizontal displacements of more than 2 m during and since the earthquake. The field measurements are therefore representative of total slip at the surface since the earthquake.

3.6 Discussion

Investigating the Wuqia earthquake has yielded advancements to our understanding of both the surface expression of reverse faults and earthquake sequences in the presence of detachments. Upon first inspection the surface expression of the Wuqia earthquake is straightforward. I showed in Section 3.4 that there were at least 13 km, and probably up to 25 km of surface ruptures. The ruptures took place on pre-existing scarps, and the 1985 sequence did rupture all of the available palaeoscarps within the rupture area — that is, I found no palaeoscarps that did not rupture in 1985 alongside the 1985 ruptures or within spatial gaps of the 1985 ruptures. Using image correlation (Section 3.5) I showed that, unlike many other continental reverse earthquakes, there was not a large blind component or a large postseismic slip after the field survey. All or most of the displacement from the earthquake is shown in the surface ruptures, and amounts to ≤2 m.

However, the focal mechanism of the mainshock does not match the strike or sense of slip of the surface ruptures: the slip vector of the mainshock is to the northeast or south-southeast, rather than matching the surface ruptures' slip vector to the north or north-northeast. The fault that is dominant in terms of moment release either has a strike that is 25–75° different to the strike of the Tuomuluoan Thrust or, if we take the other nodal plane to be the fault plane, it would dip in the opposite direction,

with a strike difference to the TT of ∼160°. I can not distinguish between these two scenarios. The strike of the NE-dipping plane agrees with the long axis of the isoseismals (Figure 3.6, *Feng et al.* (1986)) so I consider it more likely to be the fault plane but, on the other hand, the SE-dipping plane is the only one of the two that would have caused the south-up surface ruptures that we observe, and the steeper dip of the SE-dipping plane means that it would reach up to shallower depths than the NE-dipping plane.

This comparison of the focal mechanism and surface ruptures shows, as has been shown for several reverse faults elsewhere (e.g. *Copley and Reynolds* (2014); *Mackenzie et al.* (2016); Chapter 2), that the surface ruptures and topography do not show a full picture of the faults at depth. Following earthquakes at Van, Turkey (2011) (*Mackenzie et al.*, 2016) and Sefidebeh, Iran (1994) (*Copley and Reynolds*, 2014) it has been suggested that earthquakes or postseismic slip on separate faults above the mainshock-generating fault generate topography. In the Wuqia case we are limited by our imperfect knowledge of the timing of rupture formation. There is an indication that at least part of the surface ruptures was caused by the 11th September aftershock, which was shallower than the mainshock and whose strike and rake are compatible with the ruptures (Sections 3.3 and 3.4). If the M_w 5.9–6.1 aftershock caused all 25 km in length and ≤1.5 m in displacement then it would have a greater length than is usually seen for earthquakes of its magnitude (*Wells and Coppersmith*, 1994). Because the aftershock could have been shallow and on a mature fault, I cannot rule out the possibility that it caused all of the ruptures, but based on scaling it is unlikely. Aseismic deformation could be appealed to as a contributor to the ruptures (e.g. *Johanson et al.*, 2006; *Copley and Reynolds*, 2014; *Copley*, 2014; *Elliott et al.*, 2015; *Floyd et al.*, 2016; *Wedmore et al.*, 2017) but to have caused as much as 1.5 m of displacement within the 7 months between the mainshock and *Feng et al.* (1986)'s survey, the rate of aseismic slip would need to have been high. The remaining option is that the mainshock caused all or part of the ruptures. Although the focal mechanism does not match the rupture pattern, it is possible that multiple planes were involved in the earthquake. Differently

oriented faults within the shallower Cenozoic sediments could have broken at the same time as the basement fault and caused the ruptures. Slip on multiple planes would explain why the seismic waveforms cannot be modelled well by a point source, although the three sub-event solution that *Burtman and Molnar* (1993) found did not include any shallower sub-events that would match the ruptures (Table 3.1). Without further data I cannot say to what extent the mainshock, aftershocks and aseismic slip each contributed to the surface ruptures. *Bufe et al.* (2017) and *Qiao et al.* (2017) both derived deformation rate maps from Envisat time series covering the years 2003–2010 that include some of the postseismic time period at Wuqia. They found uplift along the length of the Kashi Anticline and two patches of uplift along parts of the Mushi Anticline and TT (time-averaged uplift rate up to ∼4–6 mm/yr) but did not investigate which postseismic mechanisms operated during that time or their rates.

Figure 3.13 shows a rough sketch cross-section of the region with my interpretation. The tectonic setting of Wuqia is reminiscent of the Simply Folded Belt in Iran's Zagros Mountains, where there has been significant interest and debate concerning depth segmentation of faulting but progress has been limited by a lack of recent large earthquakes (e.g. *Falcon*, 1969; *Nissen et al.*, 2010; *Roustaei et al.*, 2010; *Nissen et al.*, 2014a; *Elliott et al.*, 2015; *Barnhart et al.*, 2018). The depth of the Wuqia mainshock is noteworthy. At ∼10–25 km centroid depth, slip in the earthquake was primarily below the basal-Tertiary detachment. Combined with the existence of surface ruptures, this depth estimate tells us that faults both above and below the detachment were active within a short time period, meaning that either the detachment is locally broken, or that there is a strong connection between the two sides of the detachment. This conclusion is unexpected because the extensive presence of detachment folds (including the anticlines adjacent to the PFT), the fanned trends of the tectonic structures within the Pamir–Tien Shan–Tarim Basin junction, and the absence of outcrops of pre-Tertiary rocks within the centre of the foreland suggest that the region shortens in a thin-skinned manner and that the topography and structural geology of the sedimentary cover re-

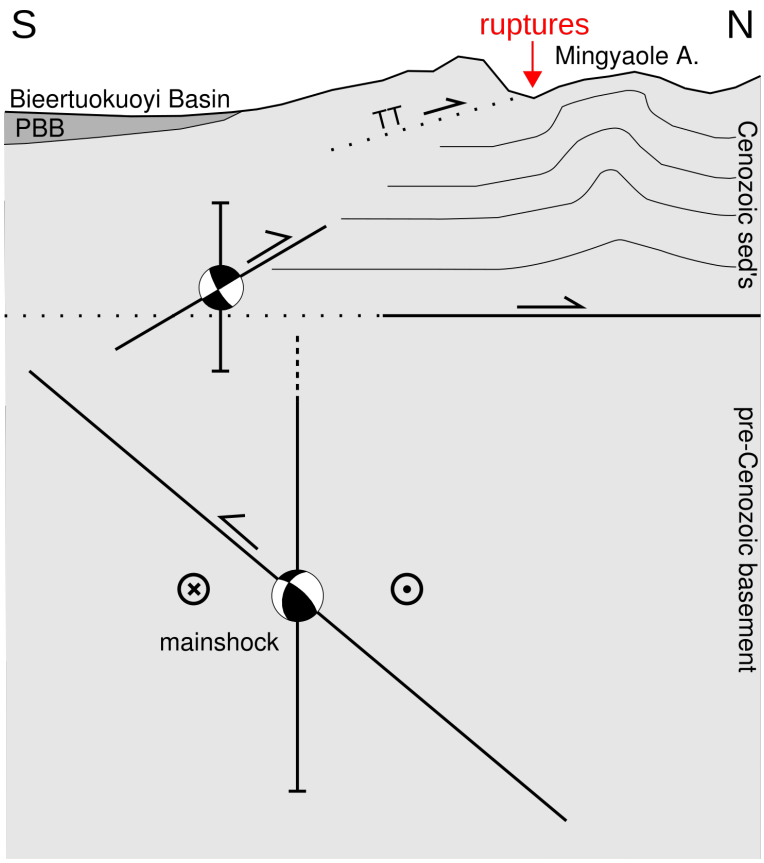


Figure 3.13: A rough sketch cross-section through the PFT and Mingyaole Anticline showing side-on focal mechanisms for the Wuqia earthquake and 11th September aftershock (*Burtman and Molnar*, 1993). Horizontal uncertainties in earthquake locations (not shown) are greater than the vertical uncertainties. No vertical exaggeration. Fault lengths are estimates based on the earthquakes' seismic moment, assuming a square, planar fault plane, a slip:length ratio of 5×10^{-5} and a shear modulus of 3×10^{10} GPa. TT = Tuomuluoan Thrust (dip of active fault uncertain). PBB = unbroken Quaternary piggyback basin sediments.

flect only the current phase of orogeny. My study of this earthquake has demonstrated that basement shortening does take place in the Pamir–Tien Shan foreland, rather than solely beneath the rangefronts and it has shown that, although there is a difference in fault geometry between the shallow and deeper levels, the two sides do interact.

I have investigated the nature of that interaction further using Coulomb stress change modelling. I calculated the Coulomb stress change that the Wuqia mainshock would cause on the fault plane of the 11th September aftershock using the Coulomb 3.3.01 software (*Lin and Stein*, 2004; *Toda et al.*, 2005) and the result is shown in Figure 3.14. The technique involves calculating the stress change that slip on a fault

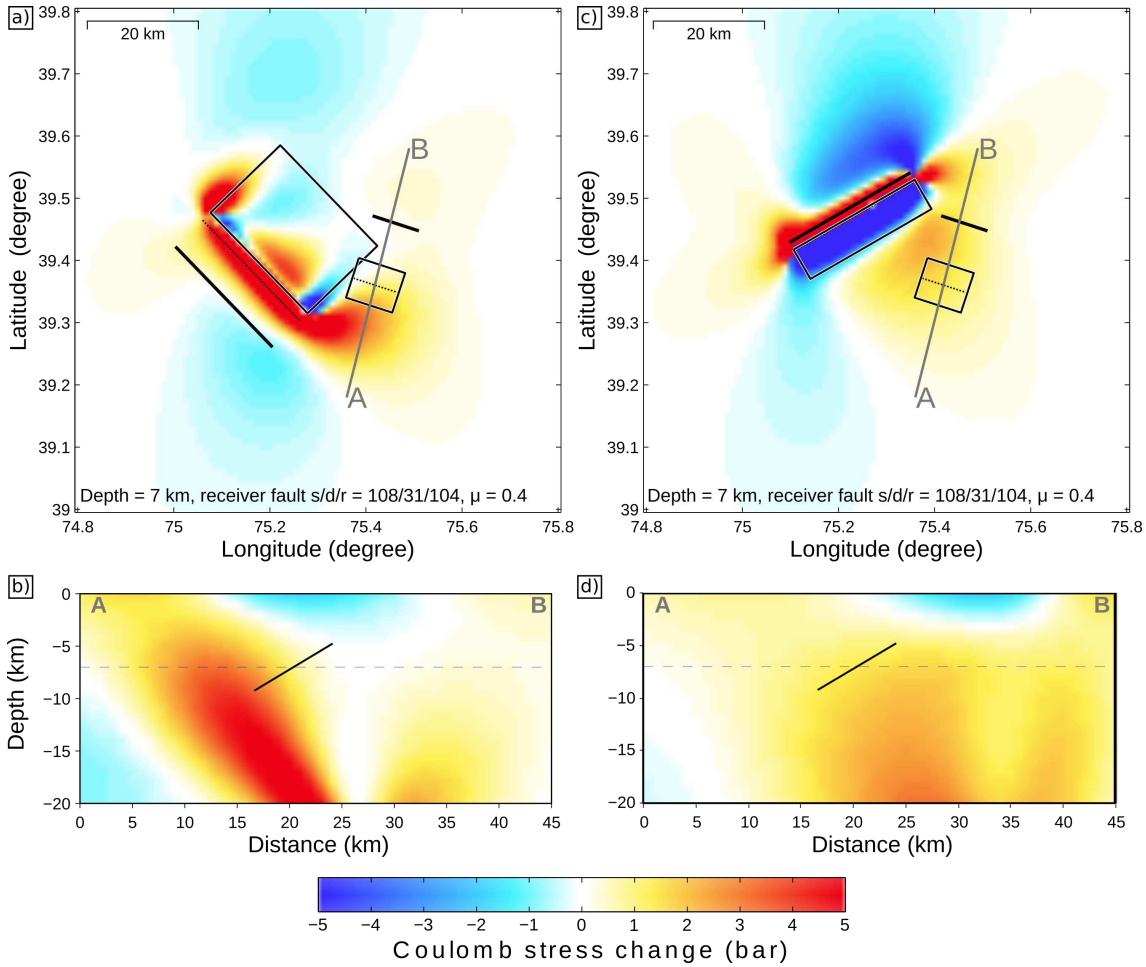


Figure 3.14: a) Map of the Coulomb stress change that a M_w 6.9 earthquake on a fault with strike 316, dip 46, rake 160 (as in the Wuqia mainshock) would cause at 7 km depth on receiver faults with the orientation of the 19th September aftershock. b) Cross-section through a), note there is a change in distance scale. c) and d) show the equivalent maps for a mainshock with strike 60, dip 76, rake 47 (i.e. the other nodal plane). Dotted black lines show the intersection of the fault plane projection with the maps' depth level of 7 km. 1 bar = 0.1 MPa.

would cause on the elastic half-space around it and then resolving that stress change into shear and normal components for a given orientation of 'receiver' fault (*King et al.*, 1994). The Coulomb stress change is a measure of whether the receiver fault has been pushed closer to or further from failure, and is defined as $\Delta\text{CFF} = \Delta\tau + \Delta\mu\sigma$, where τ is the shear stress, σ is the change in normal stress (positive for fault unclamping) and μ is the effective coefficient of friction on the fault plane (*Lin and Stein*, 2004).

The models in Figure 3.14 are based on the best available data but use simple

assumptions and are intended to show plausible scenarios rather than to replicate the 1985 conditions exactly. I assume planar, square faults; the lengths of 25×25 km and 8.7×8.7 km were estimated from their magnitudes and assuming a slip:length ratio of 5×10^{-5} and a shear modulus of 3×10^{10} GPa. The relative locations of the two faults are some of the most important parameters for the results. Here the longitude and latitude of the fault centres are assumed to be at the ISC-EHB epicentres, which are also close to the NEIC epicentres and to the centroid locations assumed by *Burtman and Molnar* (1993) (Section 3.3). The fault centre depths are 18 km and 7 km (*Burtman and Molnar*, 1993), but the cross-sections in Figure 3.14 show that the results have relatively low sensitivity to small depth errors. For the example shown the effective coefficient of friction (μ) is assumed to be 0.4 but a re-run of the calculations using μ = 0.1 gave similar results.

I find that an earthquake on either of the nodal planes determined by *Burtman and Molnar* (1993) would cause a moderate increase in Coulomb stress on the fault plane of the aftershock, pushing it closer to failure by around one bar (a tenth of a megapascal). It is possible therefore that the basement and cover are still mechanically separated by the detachment but influenced each other by static stress transfer and that that is what triggered this aftershock.

Participation of faults on both sides of or across the detachment during the Wuqia earthquake sequence shows that the decoupling is not complete. It is also possible that, unlike the superficial deposits, the geometry of faulting within the basement is influenced by inheritance: if the south-dipping, southeast-striking nodal plane of the focal mechanism were the fault plane then, as stated above, there would be a difference in strike between the mainshock fault plane and the surface structures. Activation of an inherited fault in the basement is one explanation for this difference. It is well documented that reactivation of basement weaknesses that pre-date the current orogeny can influence the present-day style of deformation (e.g. *Allen and Vincent*, 1997; *D'Lemos et al.*, 1997; *Webb and Johnson*, 2006; *Selander et al.*, 2012). Although basement faults have

not been mapped in the Kashi foreland beneath the earthquake, the Shache-Yangdaman Fault (SYF) does strike northwest-southeast across the Tarim Basin (Figure 3.15, *Wei et al.* (2013); *Bande et al.* (2017b)). The SYF is now buried but is interpreted as being a right-lateral fault that was involved in the northward indentation of the Pamir ∼25 Ma and may connect to the Tien Shan's Talas–Fergana Fault to its north (*Bande et al.*, 2017b). The existence of the SYF suggests that the western Tarim Basin may have some pre-existing susceptibility to deform by slip on southeast-striking faults and it is plausible that the Wuqia earthquakes focal mechanism is a reflection of that.

Wuqia's pattern of a deeper oblique or strike-slip earthquake beneath a shallower reverse earthquake matches the depth-distribution of seismicity that has generally been seen in the northwest of the Tarim Basin (*Xu et al.*, 2006; *Sloan et al.*, 2011). In a compilation of reliable earthquake depths and mechanisms *Sloan et al.* (2011) found that earthquakes with centroid depths <10 km all had reverse mechanisms, while events with depths of 10–20 km were generally strike-slip or normal (Figure 3.15). A further similarity is that the T-axes of the strike-slip and normal events were oriented WNW-ESE, the same orientation as for the Wuqia mainshock.

The setting of the earthquakes discussed by *Sloan et al.* (2011) is not identical; this section of their study was dominated by earthquakes in or geographically close to the 1997–8 Jiashi sequence in the Tien Shan foreland south of the Kepingtage fold-and-thrust belt (Figure 3.15), 150 km to the east of the Wuqia earthquakes. *Sloan et al.* (2011)'s favoured explanation for the normal and strike-slip earthquakes is that they are caused by extensional flexure due to the loading of the Tarim Basin crust by the Tien Shan and Pamir mountains. With this interpretation the shallower reverse earthquakes are taken to be part of a completely separate thin-skinned deformation and earthquakes of unknown mechanism that have been observed in that region at depths of 30–45 km would be expected to be reverse earthquakes due to compressional flexure. Wuqia is much closer to the Tien Shan and Pamir loads so it is not a given that the flexure patterns there and at Jiashi are the same; no normal faulting earthquakes have been

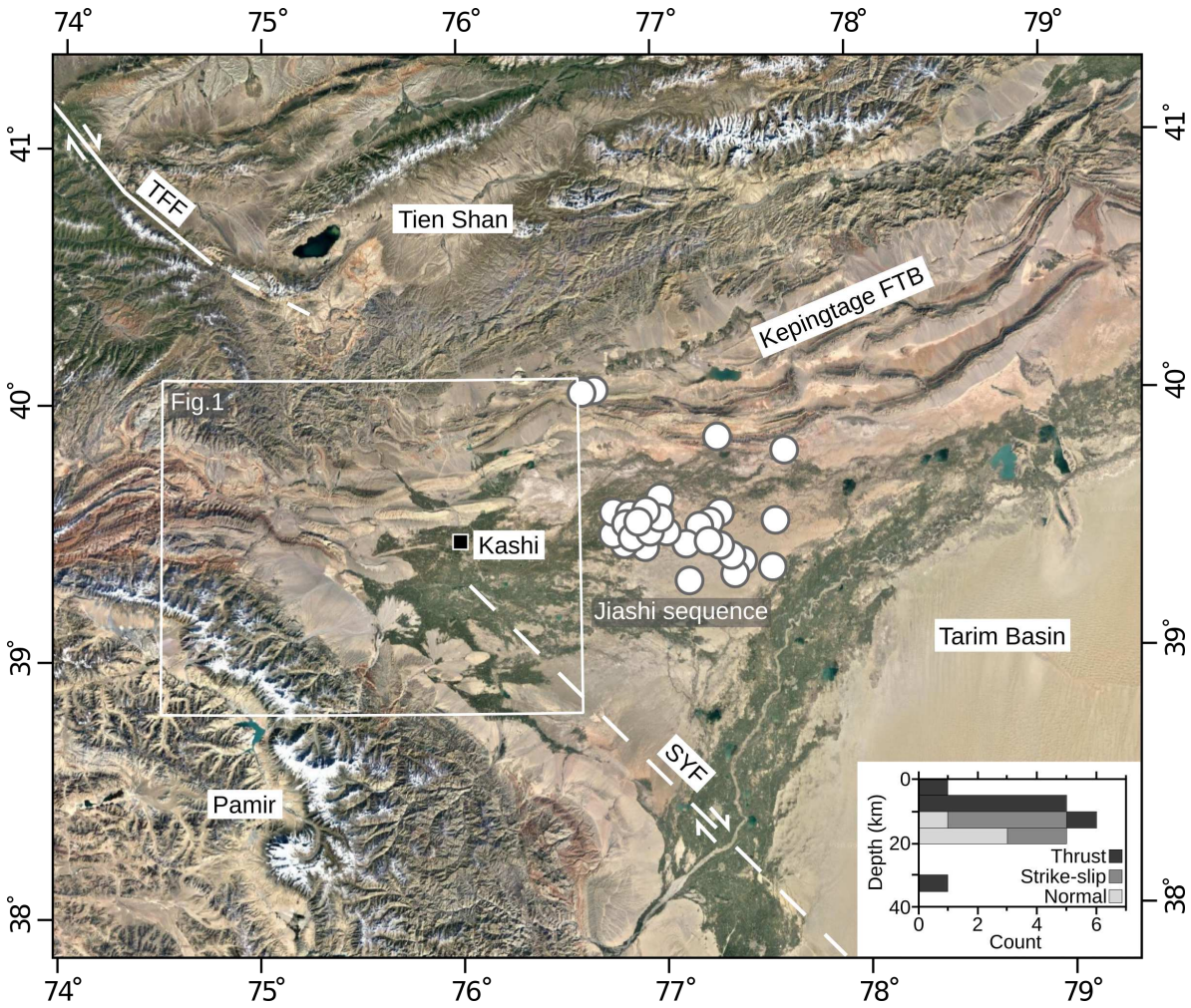


Figure 3.15: Map showing the locations of the earthquakes (white dots) used by *Sloan et al.* (2011) to study the depth distribution of focal mechanisms in the northwest Tarim Basin region. Most but not all of the earthquakes were part of the 1997–8 Jiashi sequence (*Xu et al.*, 2006; *Sloan et al.*, 2011). Inset: histogram of centroid depths by mechanism, reproduced from *Sloan et al.* (2011). SYF = Shache-Yangdaman Fault (*Wei et al.*, 2013). Kepingtage FTB = Kepingtage fold-and-thrust belt. TFF = Talas–Fergana Fault. Image Landsat/Copernicus via GoogleEarth.

seen alongside the strike-slip earthquakes around Wuqia. We can say that although the Wuqia and Jiashi parts of the northwest Tarim Basin could be under slightly different stress conditions, the outcome in terms of depth segmentation and orientation of focal mechanisms is similar.

3.7 Conclusions

I have provided a synthesis of what is known about the M_w6.9 1985 Wuqia earthquake and its largest aftershock. I have shown that the surface ruptures likely spanned ∼25 km — 12 km further than previously thought — that the earthquake broke pre-existing scarps and that the blind component of surface displacement, if there was one, was less than half of the total. By reviewing the published seismology alongside the surface ruptures and their setting shows that the Wuqia sequence involved faults both above and below a regionally significant detachment, but that the fault below the detachment does not dominate the deformation style of the sedimentary sequence above.

I conclude that the Wuqia earthquake surface ruptures are well-matched with the longer-term expression of the fault but, when all datasets are considered, the earthquake shows a complex relationship between the surface and the sub-surface fault structure and serves as a useful example in the study of active deformation in the presence of detachments. The study underlines the value of detailed investigation of historical earthquakes, but also shows uncertainties in what can be inferred about the event's source when making measurements restricted to the Earth's surface; as the fault scarps and topographic expression of faulting reflect deformation above the Tertiary detachment, and mask the effects of basement faulting.

Chapter 4

Variability in Surface Rupture Between Successive Earthquakes on the Suusamyr Fault, Kyrgyzstan

4.1 Introduction

Establishing the seismic history of a region is an important part of seismic hazard assessment. Specifically, information on the magnitudes, dates and locations of past earthquakes can contribute to assessments of the potential magnitude and recurrence frequency of earthquakes that threaten a location (e.g. *Youngs et al.*, 2003; *Field et al.*, 2014; *Petersen et al.*, 2015).

The most direct methods for extending our knowledge of the sizes and dates of past earthquakes are based on identification, measurement and dating of offset Quaternary landforms and sedimentary deposits. The length of an earthquake rupture can be measured directly if its surface rupture trace is sufficiently well preserved. The age and displacement of historic or prehistoric earthquakes can be found by palaeoseismic excavations that expose datable stratigraphic relationships between different faulting events. Conversions from the measured displacement and/or length of a rupture to the

corresponding earthquake magnitude rely on empirical scaling relationships that are derived from catalogues of well measured more recent earthquakes whose magnitude is known from seismology or geodesy (*Wells and Coppersmith*, 1994; *Mai and Beroza*, 2000; *Leonard*, 2010; *Stirling et al.*, 2013; *Anderson et al.*, 2017).

Uncertainties in the scaling relationships are caused by variability in slip, rupture length and surface rupture length among earthquakes of a given magnitude. Additionally, for the application of scaling relationships to determining the magnitudes of prehistoric earthquakes, a strategy for how to use measurements of surface ruptures must be chosen. For example, typically only a point measurement of displacement is available from palaeoseismic trenches, whereas scaling relationships between displacement and magnitude typically refer to the average or maximum displacement of an entire rupture. Statistical methods have been proposed to account for this limited sampling (*Hemphill-Haley and Weldon*, 1999; *Biasi and Weldon*, 2006). For studies relating rupture length to magnitude, care must be taken to use scaling relationships that specifically relate the parameters that are observable. While subsurface rupture length bears a more direct and meaningful relationship to earthquake magnitude, surface rupture length is the only proxy for this value available for prehistoric earthquakes. Thus, a proper understanding of the relationship between subsurface rupture length, surface rupture length and magnitude is crucial when interpreting the magnitude of past earthquakes from geomorphology.

Interpretation of prehistoric earthquake ruptures is particularly important for the Tien Shan mountain range in Central Asia (Figure 4.1) which was hit by magnitude >7 earthquakes in 1887, 1889 and 1911 (*Kondorskaya et al.*, 1982; *Kulikova and Krüger*, 2015; *Krüger et al.*, 2015). The region has the capacity for more major and damaging earthquakes, as it accommodates 20±2 mm/yr (*Zubovich et al.*, 2010) of the shortening between India and Eurasia across multiple faults (*Thompson et al.*, 2002). However, due to the recurrence interval on each individual fault typically being several thousand years (*Abdrakhmatov et al.*, 2016; *Deev et al.*, 2016; *Landgraf et al.*, 2016; *Grützner et al.*,

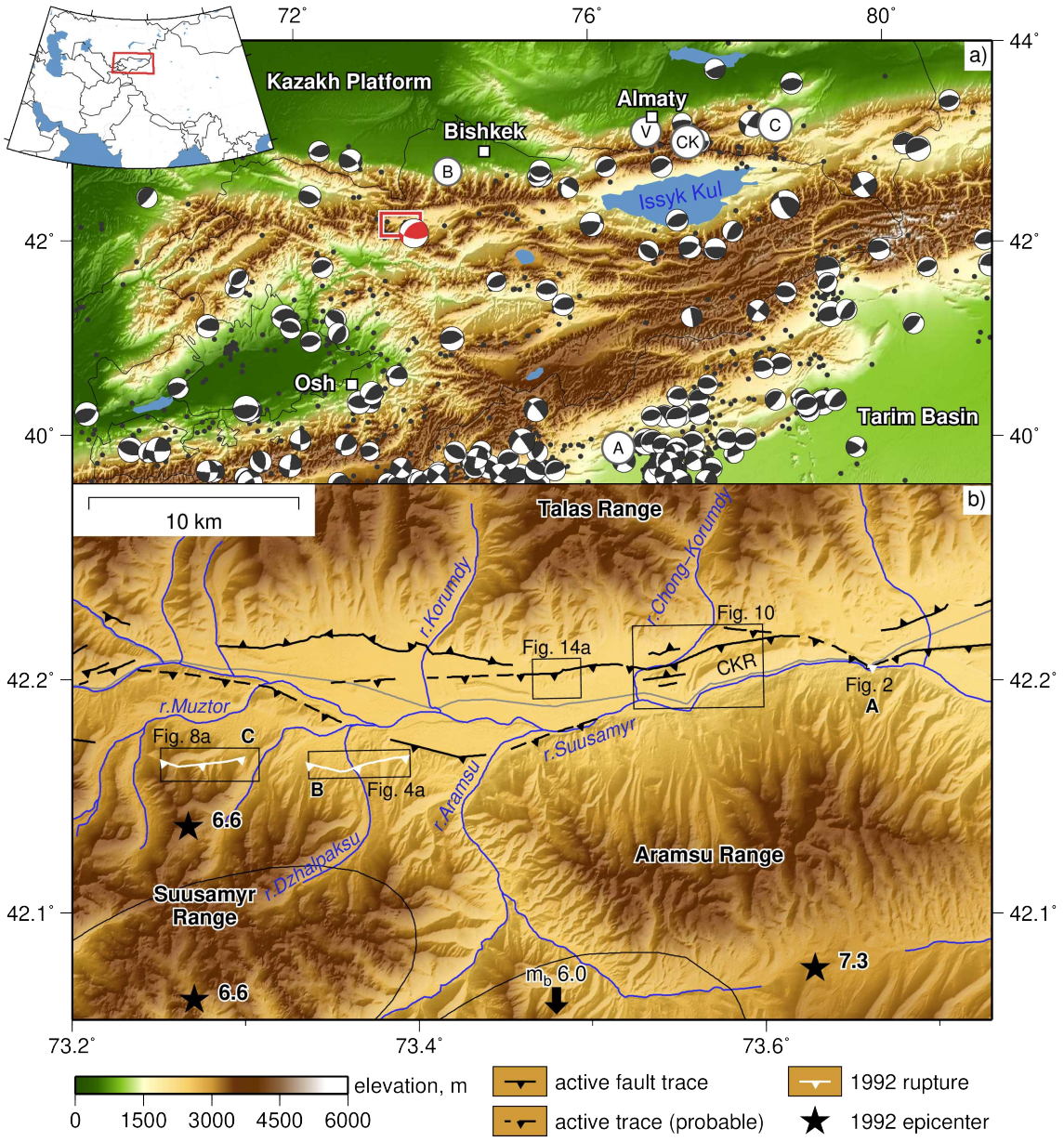


Figure 4.1: a) Overview map of the Suusamyr Basin and its situation within the Tien Shan. Red box shows the location of panel b). Red focal mechanism: 1992 Suusamyr earthquake (*Mellors et al.*, 1997). Black focal mechanism: CMT catalogue earthquakes. White dots: Chilik 1889, Chon-Kemin 1911, Verny 1887, Belovodskoe 1885 and Atushi 1902 epicentres (*Kondorskaya et al.*, 1982; *Krüger et al.*, 2015; *Kulikova and Krüger*, 2015, 2017). Small black dots: earthquakes from the EHB bulletin 1960–2008. b) Overview of the western Suusamyr basin. Black stars mark the epicentres of the Suusamyr earthquake and two largest aftershocks (*Mellors et al.*, 1997). Black, ticked lines mark the main active fault traces (from my own mapping). The 1992 earthquake ruptured sections in the east (labelled A and Fig. 2) and west (white lines with labels B and C).

2017; *Patyniak et al.*, 2017), much of what is known about the earthquake history and slip rate of Tien Shan faults comes from palaeoseismic and geomorphic studies (e.g. *Thompson et al.*, 2002).

The M_w7.2 19th August 1992 Suusamyr earthquake, Kyrgyzstan, is the largest earthquake to have hit the Tien Shan since the 1946 Chatkal earthquake (*Kalmetieva et al.*, 2009; *Bindi et al.*, 2012), and is the only surface rupturing earthquake to have occurred in the Tien Shan in recent decades. Its magnitude, location, and overall strike, dip and rake have been well established through modern seismology (*Mellors et al.*, 1997; *Gómez et al.*, 1997). The event is therefore a valuable opportunity to relate the seismological characteristics of earthquake size with their surface rupture characteristics in the Tien Shan. This earthquake rupture is also an illuminating exception to the expectation that earthquake ruptures reach the surface with continuous surface expression in that it showed an extremely discontinuous surface rupture with a total surface rupture length much shorter than the estimated subsurface rupture length, but with a substantial amount of slip reaching the surface at the parts that did break. Aftershocks define a fault plane 50±10 km long (*Mellors et al.*, 1997), consistent with the magnitude according to scaling relationships (*Thingbaijam et al.*, 2017), and yet only two short, isolated surface rupture sites were found. One showed ∼4 m of surface slip over a length of only 600 m (A in Figure 4.1) and the other was reported as showing up to 1.8 m vertical displacement over a total length of 3.4 km (B in Figure 4.1) (*Ghose et al.*, 1997).

These observations violate the standard approach used in relating palaeoseismological studies to seismic hazard, and illustrate a substantial challenge in using some of the few observations available to assess the magnitudes of past earthquakes. It is therefore critical to understand the nature of surface ruptures from this earthquake and their implications for the continuity of surface slip that would be found in paleoseismic investigations.

In this chapter I use high resolution satellite imagery and digital elevation models

(DEMs) to examine the distribution of surface ruptures from 1992 and to compare their distribution to older palaeo-earthquake scarps. I reconstruct the Holocene earthquake record from palaeoseismic trenching. Finally, I discuss the Suusamyr Fault in terms of its implications for palaeoseismic interpretations in general.

4.2 The 1992 Suusamyr earthquake

The 19th August 1992 earthquake caused major damage in the Suusamyr region and minor structural damage in Bishkek (Figure 4.1a). Shaking reached Modified Mercalli (MM) Intensity X in small areas and was VIII–IX around much of the western Suusamyr basin region (*Ghose et al.*, 1997). Approximately 50 deaths were reported, mostly as a consequence of landsliding, and there was considerable damage from shaking to buildings in the surrounding villages (*Ghose et al.*, 1997).

The mainshock was recorded by seismic stations globally and by an analogue regional network. A digital regional network and an additional six temporary local stations recorded aftershocks from 7 and 27 days after the mainshock respectively (*Mellors et al.*, 1997). *Mellors et al.* (1997) and *Gómez et al.* (1997) estimated the focal mechanism from body-wave and surface-wave inversions. The mechanism shows a fault striking east-west (088–100°) and dipping steeply to the south (49–60°), with a reverse sense of slip and a small right-lateral component (rake 105–127°). This corresponds to a slip vector pointing to the northwest and a P-axis azimuth of approximately 333–359° — a typical value for the Tien Shan (*Ghose et al.*, 1998). The centroid depth is poorly constrained as 12–17 km, the moment magnitude is listed as M_w7.0–7.3 and directivity studies found that the rupture propagated westward (*Gómez et al.*, 1997; *Mellors et al.*, 1997). *Mellors et al.* (1997) found that a single-event model fits the observed waveforms well, but that a complex source is possible. The aftershock locations formed a plane dipping to the south from the surface on the southern side of the Suusamyr valley to near the hypocentre at ∼18 km depth. Based on the aftershock zone *Mellors et al.*

(1997) estimated a total rupture length of 50±10 km, with the centre around ∼73.5–73.6°E. Three strong aftershocks (M_s6.6, M_s6.6 and m_b6.0) located progressively west of the mainshock occurred within the first two hours (*Mellors et al.*, 1997), (Figures 4.1 and 4.2). As two of the relocated aftershock epicentres are to the south of the zone of small aftershocks recorded by the local network, it is possible that the strong aftershock relocations based on teleseismic data may have a southward bias (*Mellors et al.*, 1997)). It was not possible to determine the aftershock focal mechanisms or depths due to sparse teleseismic coverage and interference from mainshock surface waves (*Mellors et al.*, 1997).

Field and helicopter surveys conducted within the year after the earthquake reported that surface ruptures were created at two distinct sites separated by 25 km (*Ghose et al.*, 1997; *Bogachkin et al.*, 1997). The eastern site is located close to the M41 highway at the eastern end of the Chet-Korumdy Ridge (CKR) — a prominent elongated hill in the valley between the Talas Range and the Aramsu Range (Figure 4.1). At this eastern site *Ghose et al.* (1997) reported a north-facing scarp 500 m in length, both ends of which displaced the Suusamyr River bed, causing rapids. They reported that the scarp had a "fold-scarp" morphology, with a maximum vertical displacement of 2.7 m. At a marker that shows convergence they estimated a net slip of 4.2 ±0.4 m. They also reported several shorter, smaller-offset scarps in the footwall of the main scarp; they attribute minor north-facing scarps to near-surface splays or to secondary deformation and the south-facing scarps breaking the highway itself as most likely to be on steeply-dipping conjugate fault planes (not shown on Figure 4.1 because the road has been rebuilt).

The second rupture site is 25 km to the west of the M41 site, along the northern range front of the Suusamyr Range. *Ghose et al.* (1997) report that the ruptures there are split into three segments that stretch for ∼3.4 km across the hillside west of the Dzhalpaksu River (Figure 4.1b). These segments are also interpreted to be north-facing reverse ruptures with, from east to west, lengths of 800 m, 1.2 km and 1 km and maximum vertical displacement of 1.8 m, 0.9 m and 0.8 m respectively, although these

measurements were taken on a reconnaissance visit, rather than as a detailed survey. *Bogachkin et al.* (1997) reported that the western ruptures spanned more than 6 km but did not give sufficient detail on the location or number of rupture segments for us to understand the discrepancy between their value and that of *Ghose et al.* (1997), as the two figures in *Bogachkin et al.* (1997) show rupture segments that were also described by *Ghose et al.* (1997).

Bogachkin et al. (1997) and *Ghose et al.* (1997) differ on whether the surface ruptures showed a strike-slip component. *Bogachkin et al.* (1997) reported up to 10–15 cm right-lateral component of slip at the western ruptures and 20–30 cm at the eastern site, in keeping with the right-lateral component of the seismic mechanism. *Ghose et al.* (1997) did not find evidence for lateral slip but the heavily broken soil and turf at the eastern site could have masked a small (e.g. 20–30 cm) lateral component, and a $\leq$10–15 cm lateral displacement could also have been missed on their visit to the western ruptures.

Secondary cracks and fissures were reported in several places along the valley, notably a series of grabens along the crest of the CKR and a series of cracks associated with landslides on the Aramsu Range south and southeast of the primary rupture by the M41 highway. Landslides on the south side of the CKR also broke the highway, large boulders adjacent to the ridge were displaced and overturned by strong acceleration, and numerous other landslides and rockfalls occurred in the region (*Ghose et al.*, 1997).

4.3 Methods

4.3.1 Remote sensing and field methods

I conducted reconnaissance and preparatory mapping using satellite imagery and digital elevation models. The imagery included post-earthquake Pléiades optical scenes and pre-earthquake declassified US Key Hole (KH) spy satellite images taken in 1968 and 1971 for the CORONA program, supplemented by sub-5-m resolution images from the

archived historical imagery available on GoogleEarth and Nokia Here. The DEMs came from Pléiades imagery, AW3D30 (*Takaku et al.*, 2014) and the Shuttle Radar Topography Mission (SRTM) (*Farr et al.*, 2007).

I constructed a high-resolution DEM of the area of interest from three stereo pairs of Pléiades imagery acquired on 9th and 21st September 2015, supplied as 0.5 m resolution panchromatic and 2 m resolution four-band multispectral versions. I extracted an elevation pointcloud from the panchromatic imagery using ERDAS Imagine's Leica Photogrammetry Suite (LPS) software. Detailed descriptions of my method can be found in *Middleton et al.* (2015) and *Zhou et al.* (2015b). Briefly, the method involves identifying a few tens of tie points that the images have in common and using those tie points to refine the rational polynomial function (RPF) model that describes the relationship between image coordinates and ground coordinates. Next, many more common points between the two images are identified using pixel-by-pixel matching with a 9x9 sized cross-correlation window. The locations of a point in the two images are triangulated based on the RPFs of those images in order to determine the three-dimensional position of that point. I gridded the resulting pointcloud at 2 m spacing to make a raster DEM. Finally, I used panchromatic images to pansharpen the multispectral images, and used the DEM to orthorectify them before they were used for mapping.

We conducted field surveys in June 2015 and June 2016 to ground-truth my remote mapping, conduct unmanned aerial vehicle (UAV) and differential GPS surveys, excavate trenches and sample for chronological controls. I took aerial photographs from a compact digital camera mounted slightly off-nadir on a UAV. The surveys were conducted using a DJI Phantom 2 quadcopter at a typical flying altitude of 50–110 m, and included some flight paths with convergent viewing directions in order to minimize doming error in the elevation models (*James and Robson*, 2014). I constructed dense pointclouds and orthophotos from the photographs using the structure-from-motion method with Agisoft's Photoscan Pro software (e.g. *Westoby et al.*, 2012). Ground

control point (GCP) markers were measured in the field using differential GPS and used to scale and orient the point cloud. Offset measurements were made from the dense point cloud.

To determine the history of surface rupturing earthquakes in the Suusamyr valley we excavated two palaeoseismic trenches and logged them in the field. We selected trench locations in small abandoned stream channels to maximise the chance of a continuous supply of fine sediment and we selected locations where the local strike is roughly parallel to the overall strike of the fault. I constructed trench photomosaics using Agisoft Photoscan Pro and used the photomosaics to guide the digitisation of my trench logs (Section 4.5).

4.3.2 Quaternary dating procedure

We obtained age constraints from sediments within the trenches from radiocarbon (^{14}C) and infrared stimulated luminescence (IRSL) dating. Note that, in keeping with convention, I have given 2-sigma uncertainties for the radiocarbon dates and 1-sigma uncertainties for the IRSL dates. ^{14}C samples were dated by BetaAnalytic and calibrated by me using OxCal4.3 (*Bronk Ramsey*, 2009) with the IntCal13 curve (*Reimer et al.*, 2013). I note that, as for all detrital samples, my samples are susceptible to inheritance because the event dated by charcoal ^{14}C dating is the fixation of the carbon in the living source plant rather than the sample's final deposition, which could have been some time later (*Blong and Gillespie*, 1978; *Schiffer*, 1986).

Luminescence samples were collected from freshly cleaned exposures by hammering 5 cm diameter steel tubes into the trench wall. When a tube was removed the exposed end was quickly sealed and packed solid. The luminescence dating was carried out by Andrew S. Carr at the University of Leicester. Sample preparation followed the protocols described in *Abdrakhmatov et al.* (2016). The details of the environmental dose rate determination are given in Appendix B. Coarse grain K feldspars were analysed using the post-IR IRSL single aliquot regeneration method (*Murray and Wintle*, 2000;

Thomsen et al., 2008; *Buylaert et al.*, 2009). This uses an initial low temperature (50°C) IR stimulation followed by a higher temperature (225°C) stimulation. Slight over-dispersion in the resulting equivalent doses was seen for all samples, i.e. there was a spread in equivalent dose (D_e) distributions for the individual aliquots beyond what is expected from individual measurement uncertainties alone (*Galbraith et al.*, 1999). The equivalent dose distributions for all samples are also positively skewed, consistent with some proportion of the grains being incompletely bleached on deposition (e.g. *Olley et al.*, 1998; *Arnold et al.*, 2007). This is manifested in several high outliers in the equivalent dose distributions (Appendix B). These were removed when outside 1.5 × the interquartile range (following *Medialdea et al.*, 2014), before averaging using the central age model (CAM; *Galbraith et al.* (1999)). The $pIRIR_{225}$ ages for samples KGZ15-L02 and KGZ15-L03 had fading rates above 2% (g-values 2.0±0.3% and 2.4±0.2% respectively), so an additional fading correction following *Huntley and Lamothe* (2001) was applied to their final ages.

4.3.3 Measurement of scarp heights and conversion to slip

The scarp heights presented in this study were measured using the following method. I took swath profiles with a width of 50 cm from the dense point cloud of the UAV DEM. Profiles were taken approximately perpendicular to the scarps but with the azimuth manually adjusted where necessary to ensure that profiles followed, rather than cross-cut, landforms. Matching sections on the hanging wall and footwall of each profile were marked out manually. Bushes, snow and excavations were either cropped or avoided and profiles were rejected if slope changes along the profile made it challenging to pick correlative sections. I fitted lines of equal slope to the two marked-out sections using a least-squares method and took the offset between the lines as the scarp height. For four exceptional profiles which I discuss in Section 4.5.1 it was necessary to fit unequal slopes to the two sections. Error bars show the RMS residual between the points and best fit lines. I found that, for my sites, fitting different slopes to the two sections usually gave

results that were within the range of uncertainty form the equal slope method, and I rejected profiles where the different methods gave dramatically different scarp heights (with my system, if the two slopes are unequal then the equal-sloped lines from my preferred method will have a worse fit and so the uncertainty will be reflected by bigger error bars).

Converting scarp heights to estimates of slip magnitude also needs some care. Non-horizontal ground surfaces and non-perpendicular angles between a scarp and the normal to the slope both cause scarp height to be unequal to throw (*Thompson et al.*, 2002; *Mackenzie and Elliott*, 2017). The site of the eastern 1992 ruptures (M41 site) has a slope of almost zero and the Turabulak site has a consistently shallow (4°) slope perpendicular to the scarp, such that scarp height is approximately equal to throw. The slope at the 1992 western ruptures (Dzhalpaksu site) often exceeds 10° and the aspect varies along strike. Therefore, to rule out geometry effects, I extended *Mackenzie and Elliott* (2017)'s method for throw estimation from profiles and added functionality to estimate the magnitude of slip and 68% probability error bars, as described in Section 4.4.

4.4 Surface ruptures from the 1992 earthquake

From satellite imagery verified with fieldwork I have identified ∼7.6 km of scarps which show signs of having ruptured in the 1992 Suusamyr earthquake — a 5.4 km addition to the 2.2 km of ruptures mapped by previous publications (*Ghose et al.*, 1997; *Bogachkin et al.*, 1997). The majority — around 6.9 km — are found within a 12 km stretch around the Dzhalpaksu and Cholgondysai streams, and a previously mapped 525–600 m long scarp is located 23 km east of there, close to the M41 highway (A, B and C in Figure 4.1). In this section I review and reassess the location and dimensions of the 1992 ruptures.

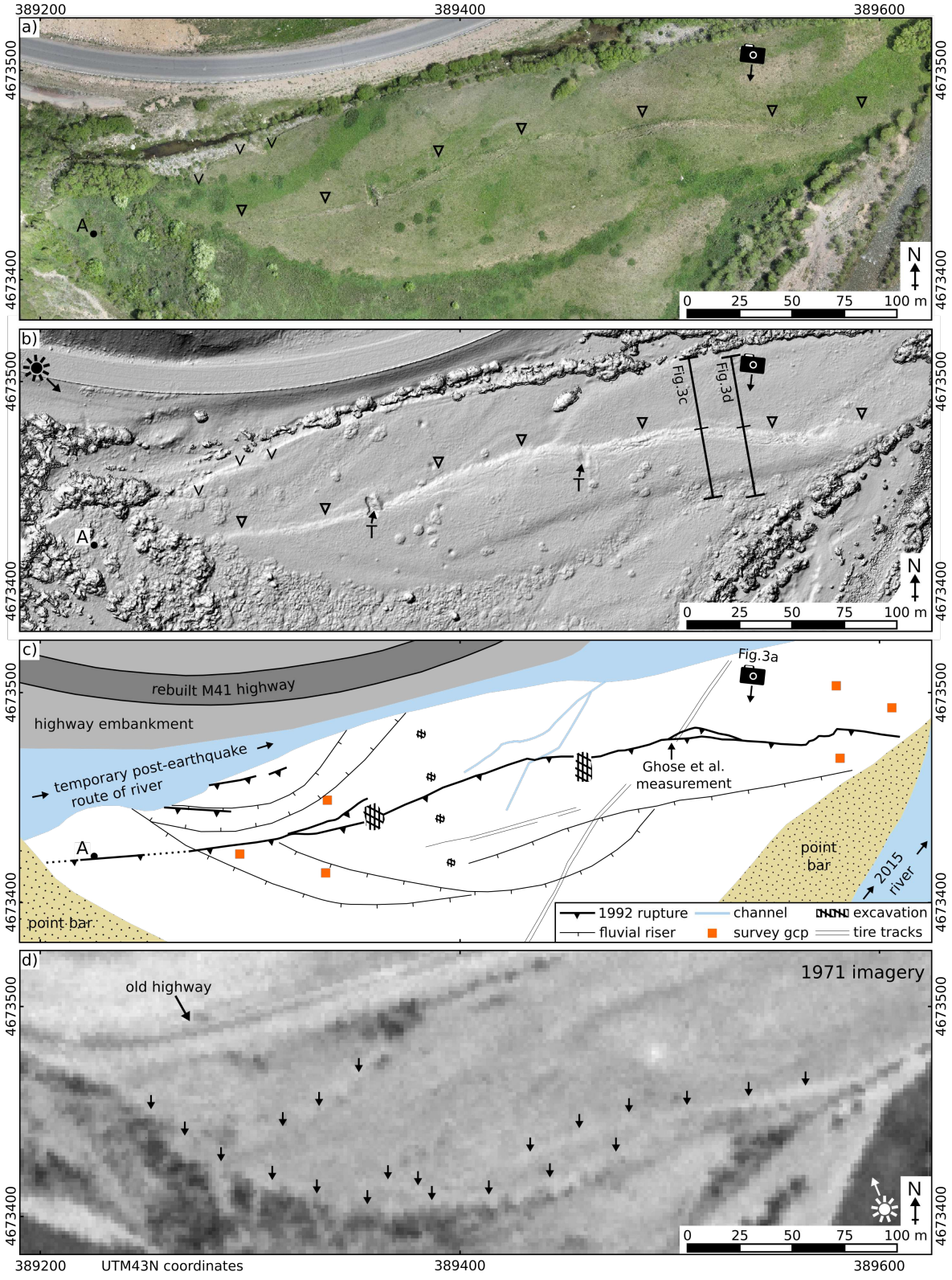


Figure 4.2: a) UAV orthophoto showing the eastern 1992 ruptures at the M41 highway. b) Hillshaded UAV-DEM of the same area. Triangles mark the main scarp, Vs mark minor scarps, T marks old trench sites. A marks the zero point of Figure 4.3b. c) Geomorphic map of the area shown in panels a) and b). d) KH-4B CORONA imagery acquired on 22nd September 1971 showing the same area before the earthquake. Arrows point to the fluvial risers marked in panel c).

4.4.1 M41 highway: the eastern ruptures

The largest-offset ruptures from the 1992 earthquake are developed in a low river terrace between the M41 highway and a bend in the Suusamyr River (A in Figure 4.1, Figure 4.2). The uplift of the southern side of the ruptures during the earthquake dammed the river and caused a short-lived partial diversion of the main river around the northern side of the fault (*Ghose et al.*, 1997) (Figure 4.2). The scarp is well preserved: cracks and rips in the grass are still obvious in the field (Figure 4.3a) and in my point cloud, so I am confident that there has been only minimal site modification since the river adopted its current course shortly after the earthquake. *Ghose et al.* (1997) interpreted the morphology as a fold-scarp with a gentle southern backlimb and a steeper frontal side. With the aid of declassified 1971 KH-4B imagery (Figure 4.2d) we see that the supposed backlimb escarpment predates the earthquake and I therefore interpret it instead as a fluvial riser. The hanging wall is slightly warped; for around half of my topographic profiles the hanging wall section slopes a few degrees more steeply to the north than the footwall (e.g. Figure 4.3d), but the impact of this on my offset measurements is small compared to the height of the scarp and is captured within the error bars. In its 200 metre-long highest section the scarp has a typical height of around 2.7 m and a maximum height of 3.1±0.1 m (Figure 4.3). The offset tails off quickly to either side, down to 0.5 m as it approaches the river to the west and 1.4±0.1 m to the east where it is truncated by a point bar. Two subsidiary scarps along the bank of the temporary river channel are still clearly visible and have heights up to 0.9 m (Figure 4.2), a third mapped by *Ghose et al.* (1997) is now overgrown. *Ghose et al.* (1997) used observations of an offset track oblique to the fault and assumed no lateral slip (which makes this an upper bound estimate) to measure cross-fault convergence and estimate a maximum slip of 4.2 ± 0.4 m (location marked on Figure 4.2). Their uncertainty value of ±0.4 m was assigned by allowing a 10% margin of error. My scarp height measurements agree with theirs used in this estimate. Using my maximum scarp height of 3.1 ± 0.1 m and assuming a maximum plausible dip of 60° (the steepest dip

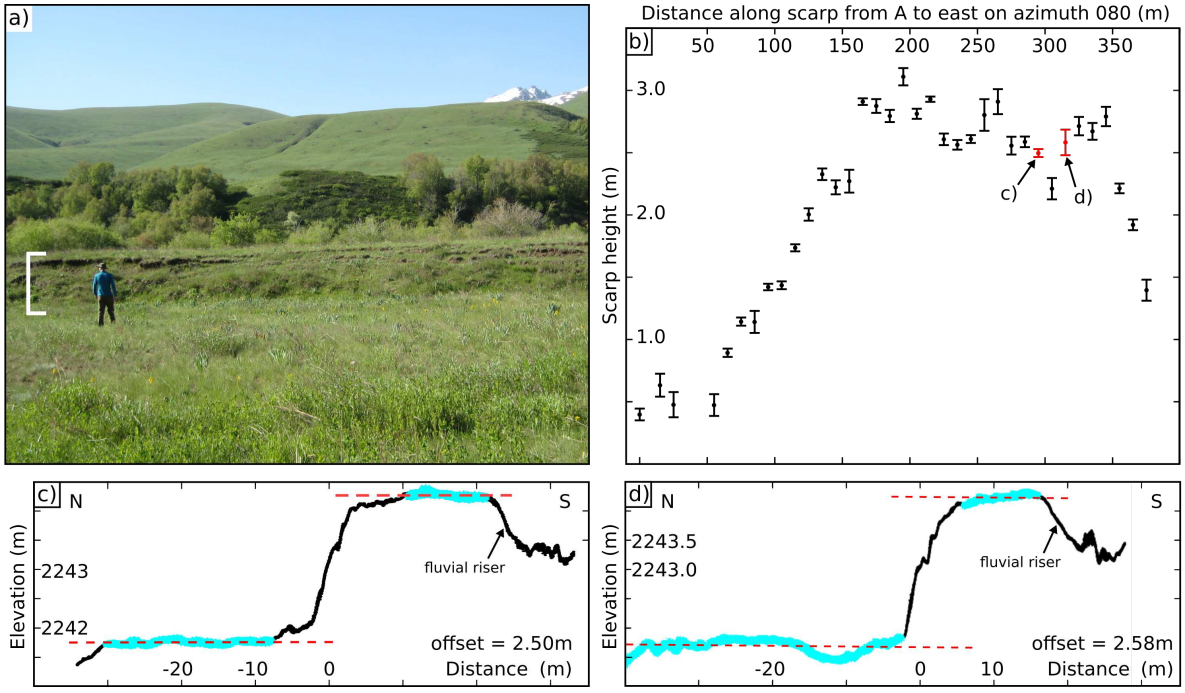


Figure 4.3: a) Field photograph of the eastern rupture from 1992, viewpoint marked on Figure 4.2. b) Scarp height distribution. c) & d) Examples of the profiles used to make the throw distribution.

estimate from the seismological studies (*Mellors et al.*, 1997; *Gómez et al.*, 1997)), I find that the maximum slip has a lower bound of 3.6 ± 0.1 m. I was unable to find any additional markers to measure horizontal displacements.

The most striking characteristic of the eastern rupture is its small length to height ratio. My elevation models and imagery suggest that the original mapping did not miss any extensions of the rupture. Across the river to the west the ground is only thinly vegetated and the only escarpments visible in satellite imagery or my Pléiades DEM appear to be fluvial and are also visible on pre-1992 CORONA imagery. On the eastern side of the rupture there is a 250 m wide area in which the river now makes a hairpin bend. The land within the hairpin is seasonally flooded so any scarps may have been quickly eroded but, as shown in Figure 4.3b, the scarp tapers quickly as it approaches the river on either side, suggesting that the scarp naturally ended within the river. *Ghose et al.* (1997) reported that the scarp created rapids in the river at both its ends and mapped the scarp as crossing the entire width of the river. Assuming that the scarp broke at least half way across the river on each side and at most broke the

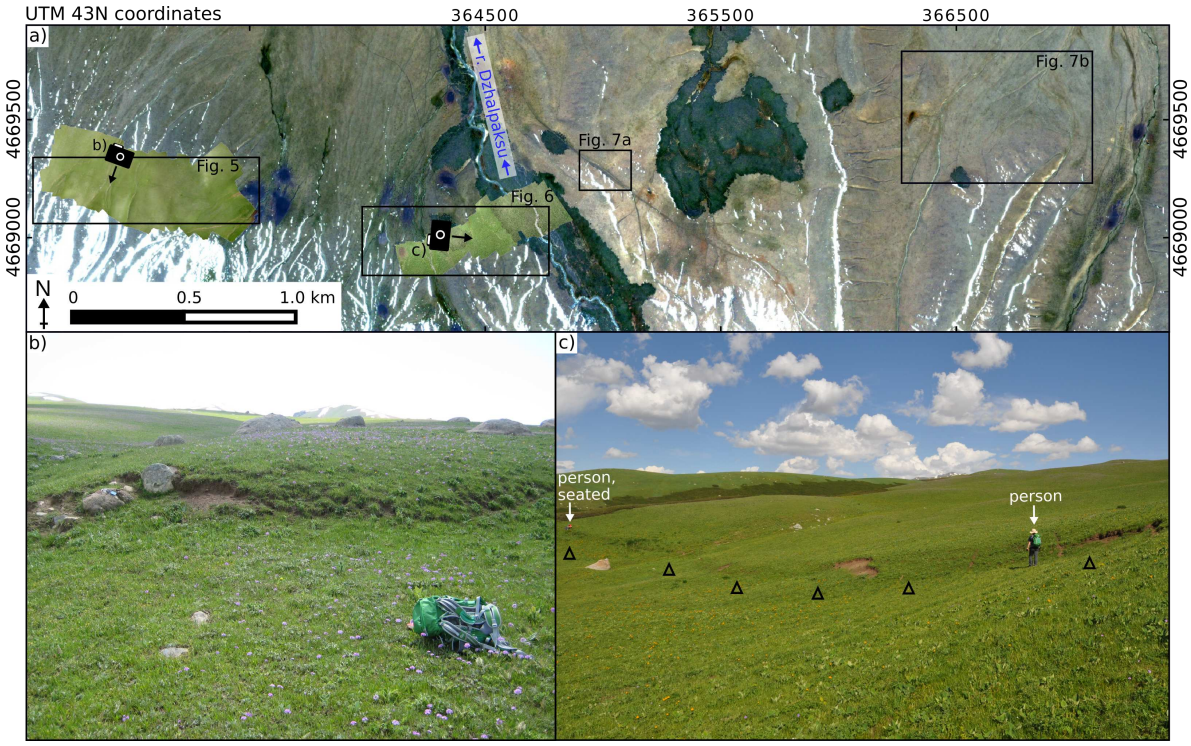


Figure 4.4: a) An overview of the 1992 ruptures around the Dzhalpaksu River showing orthophotos from the two UAV surveys. b) A close-up photograph of the scarp, day rucksack for scale. c) View along a section of the scarp.

whole width of the river, the total length of the eastern rupture is therefore 525–600 m.

4.4.2 Dzhalpaksu: the western ruptures

The second set of 1992 ruptures lie 25 km to the west of those described in Section 4.4.1 and track across the northern hillside of the Suusamyr Range (B in Figure 4.1, Figure 4.4). They comprise three segments to the west of the Dzhalpaksu River which were identified by *Ghose et al.* (1997) and *Bogachkin et al.* (1997), and two newly mapped segments east of the river. I find that the relative locations of the three previously identified segments are as described by *Ghose et al.* (1997), but the lengths are significantly shorter than the 3.4 km total length that they estimated. Including the hillside between segments, the previously identified ruptures span 2 km; the ruptures themselves total 1.5 km in length. *Ghose et al.* (1997) were unable to conduct a detailed survey of the three segments that they identified; I visited all three in the field and constructed DEMs and orthophotos derived from UAV survey photographs. The western and central seg-

ments of the three have lengths of 340 m and 550 m respectively (Figure 4.5). They strike ∼104° and overlap in a stepover zone, with the central segment 40–70 m downslope of the other. The third segment is located 600 m to the east and has an overall strike of ∼ 68° (Figures 1 and 6). It extends for 600 m to the west of the Dzhalpaksu River before being obscured by vegetation as it approaches the river itself (Figure 4.6).

Although the scarps are fresh and reports from the time confirm that they broke in the 1992 earthquake, 1968 KH-4A imagery shows scarps in the same location as the west and central segments which even match the bends of the 1992 ruptures (Figure 4.5a and 4.5b), showing that the 1992 earthquake re-ruptured a pre-existing scarp. My offset measurements in Figure 4.5 are therefore compound scarp offsets rather than single-event offsets. No pre-existing scarp is visible for the third segment closest to the Dzhalpaksu River and the scarps visible on the KH-4A imagery do not extend beyond the extent of the fresh 1992 rupture. Significantly, this suggests that the prehistoric earthquake or earthquakes also only ruptured short segments.

Figures 4.5d and 4.6b show scarp height distributions for the three segments which had been identified previously. The three have similar heights; exceptional profiles show offsets of 2 m or more but more typically the scarp height is around 0.7–1.2 m. At the stepover between the western and central segments the two scarps taper so that total offset remains roughly the same along strike until it dies out at the ends of the ruptures. To convert my scarp height measurements to slip estimates I have used an extended version of the profile method of *Mackenzie and Elliott* (2017), which takes into account fault dip, slope aspect, slope angle, the proportion of lateral slip and their uncertainties. Using a uniform probability density function of 15–45° for dip, lateral slip of ±10 % and appropriate slope and aspect for each profile, my profiles typically have a maximum-likelihood slip of 0.9–1.5 m with a large upper error bar due to the uncertainty in near-surface fault dip. The distribution of calculated slip along strike is not much changed in shape from the scarp height distribution, showing that the distribution in Figure 4.5d reflects real distribution of slip reaching the surface and is

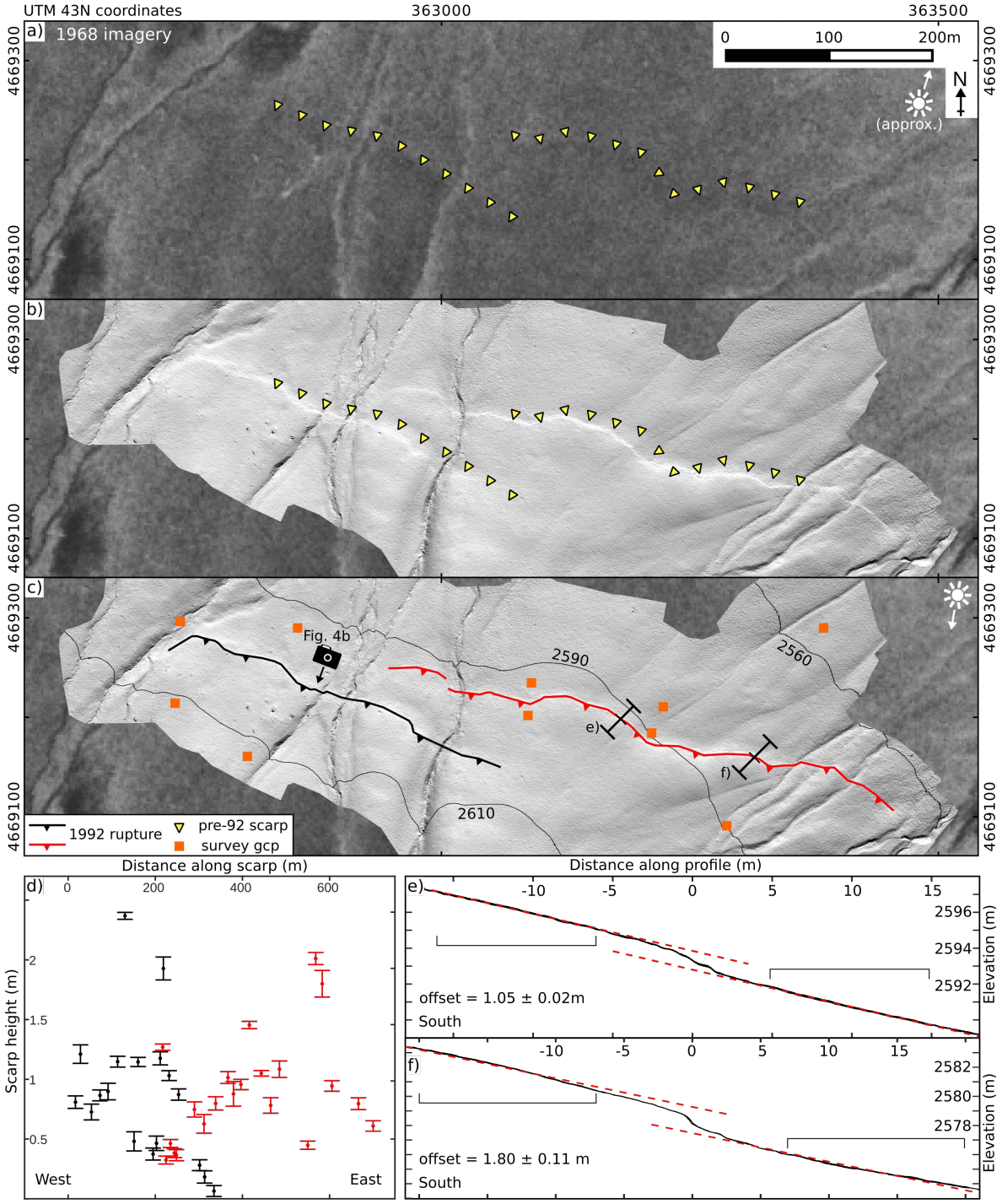


Figure 4.5: The site of two segments of the 1992 ruptures west of the Dzhalpaksu River (Figure 4.4). a) Pre-earthquake 21st September 1968 KH-4A imagery showing pre-existing scarps marked by yellow triangles. b) The same area, overlain with a hillshade of my 10 cm resolution DEM acquired in June 2016. c) Interpreted version of the hillshaded DEM showing the 1992 ruptures. d) Height distribution of the two rupture segments shown in c). Distance along scarp is a straight line distance along azimuth 104°. e) A typical example of the profiles used to measure scarp height. The best fit lines are shown in dashed red and the sections of the profile that they were fitted two are marked. f) Example of a profile with higher uncertainty. The hanging wall section (south) has non-uniform slope and is three degrees steeper than the footwall section.

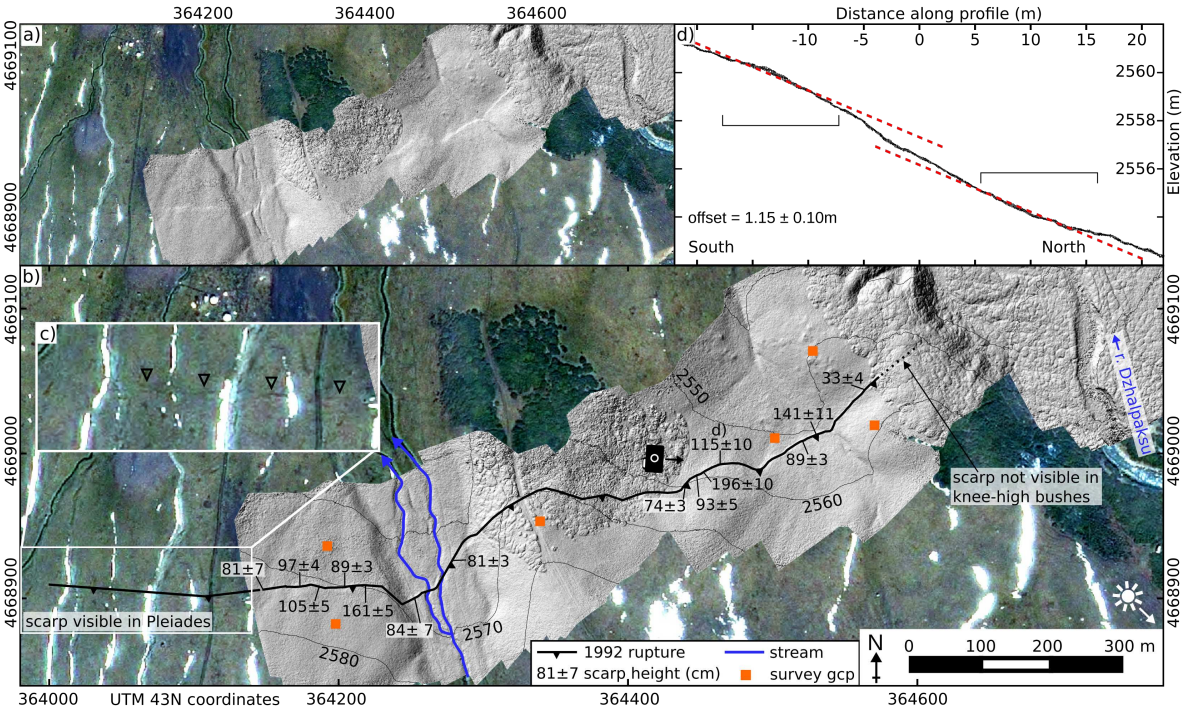


Figure 4.6: The easternmost of the three 1992 surface rupture segments west of the Dzhalpaksu River, described by *Ghose et al.* (1997). a) Hillshaded UAV DEM overlain on Pléiades imagery. b) Interpretation. c) Close-up of the Pléiades imagery. d) A typical topographic profile. The best fit lines are shown in dashed red and the sections of the profile that they were fitted to are marked.

not an illusion caused by the effects of geometry. We did not observe any lateral offsets here but note that extremely few good markers cross the scarps which would show lateral offsets, and some small-scale evidence could have been lost due to erosion.

Although *Ghose et al.* (1997) and *Bogachkin et al.* (1997) did not map any ruptures on the hillside to the east of the Dzhalpaksu River (Figure 4.1), I have mapped two fresh segments that I interpret from their morphology to have ruptured in 1992. The first lies 400 m along-strike to the east of the mapped segment, is 130 m long, and can be seen in Pléiades imagery (Figures 4.4 and 4.7a). The second rupture is 530 m in length and situated 1400 m east from the first on an azimuth of 082° (Figures 4.7b and 4.7c). Although I was unable to visit either of the newly mapped segments in the field, the 530 m segment has similar or slightly less shadowing in the imagery than the already-mapped scarps and the shorter segment does have less shadowing, suggesting that they have smaller heights than the already-mapped scarps. A GoogleEarth image

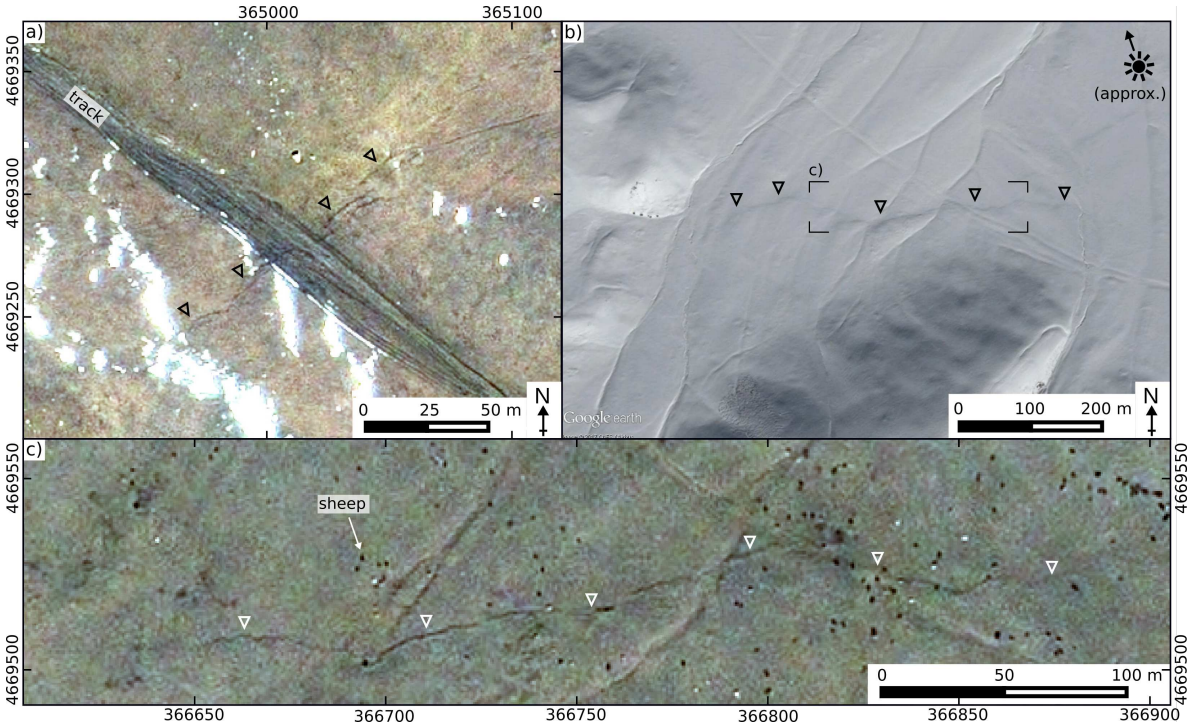


Figure 4.7: Newly identified surface ruptures, locations shown in Figure 4.4. a) Pléiades imagery of a small scarp east of the Dzhalpaksu River. Note that the scarp is fresh enough for parallel strands of fissures to be visible. b) Snow-covered 9th November 2016 scene showing the shadow of another scarp. Imagery from GoogleEarth, copyright CNES/Airbus. c) Pléiades imagery showing the same scarp cross-cutting small channels as shown in panel b).

with snow cover (Figure 4.7b), shows the scarps casting a shadow when illuminated from the south-southeast, meaning that, like the previously mapped ruptures, these scarps are north-facing. Their age is unknown but they are unvegetated and have thin parallel, black strands that I interpret as open fissures, both qualities that match the 1992 scarps rather than the prehistoric scarps I show in Section 4.5.

4.4.3 Cholgondysai

A 4 km-long fault scarp begins 6 km to the west of the western end of the Dzhalpaksu ruptures, along-strike (C in Figure 4.1, Figures 4.8 and 4.9). In its eastern half there is a significant change in slope and roughness across the scarp from steeper, rougher topography in the south to shallower, smoother topography downhill on the northern side. The scarp here has occasional fissures (Figure 4.8a). After a 180 m-wide stepover southwards the fault continues and crosses the Cholgondysai stream. In this section the

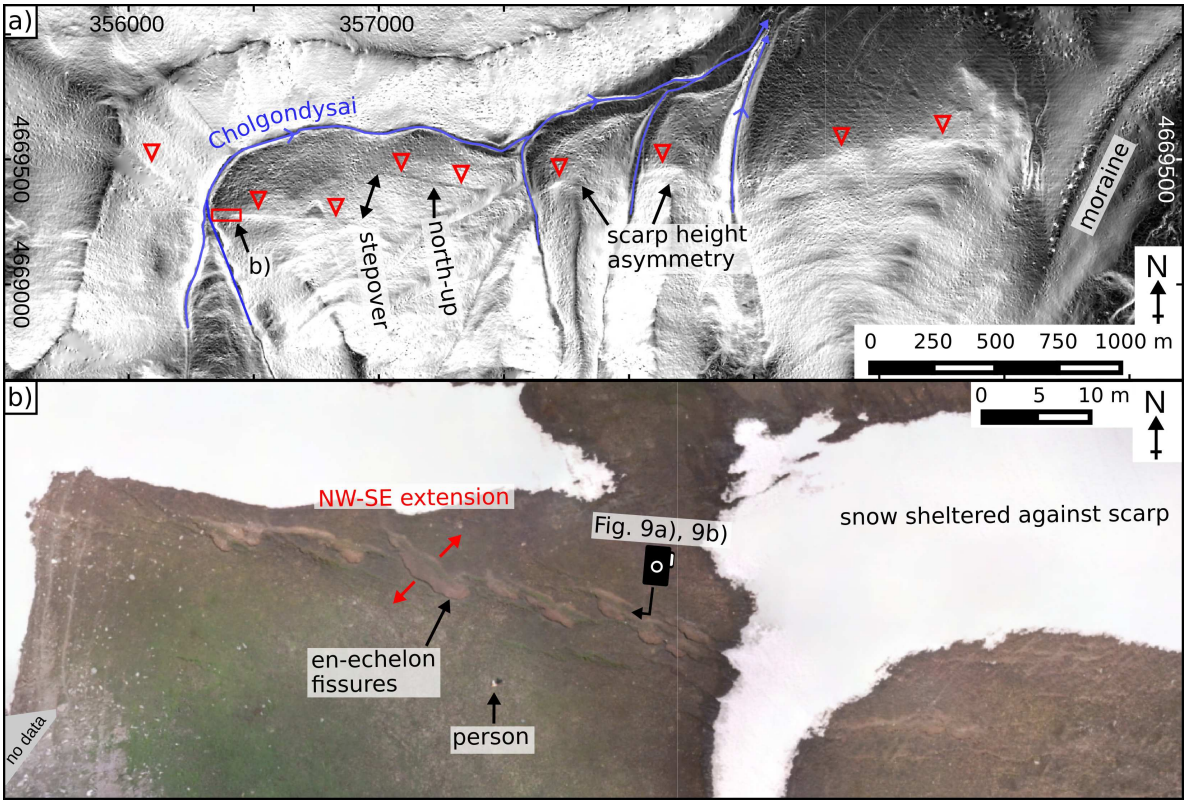


Figure 4.8: The Cholgondysai fault segment. a) Slope map of the Pléiades DEM. The scarp is marked by red triangles. b) UAV orthophoto of the fresh en-echelon fissures on the scarp close to the Cholgondysai stream. Location shown in a).

fault cuts across topography with a dip of $> 70°$S (as estimated in the field, Figure 4.9b) and there is a ∼1 km segment with abundant en-echelon open fissures indicating a right-lateral slip component (Figure 4.8b). The right-lateral component is also apparent in the larger-scale morphology — the offset is predominantly south-up but the vertical offsets are larger on west-facing ridge slopes than on east-facing slopes and on one east-facing slope the scarp appears to be north-up (Figure 4.8a). I conclude that the fault here is a right-lateral oblique thrust.

The entire length of the 4 km scarp is also visible on pre-1992 CORONA imagery and the changes of slope and roughness across it suggest that it has hosted multiple earthquakes. In June 2016 elongate patches of snow were present, sheltered against the north-facing scarp which has a smoothly curved cross-section and a height of 3–8 m. As can be seen in Figure 4.9a, the fissures in the soil on the scarp crest have some young vegetation within them but are generally still sharp-edged and unvegetated, similar

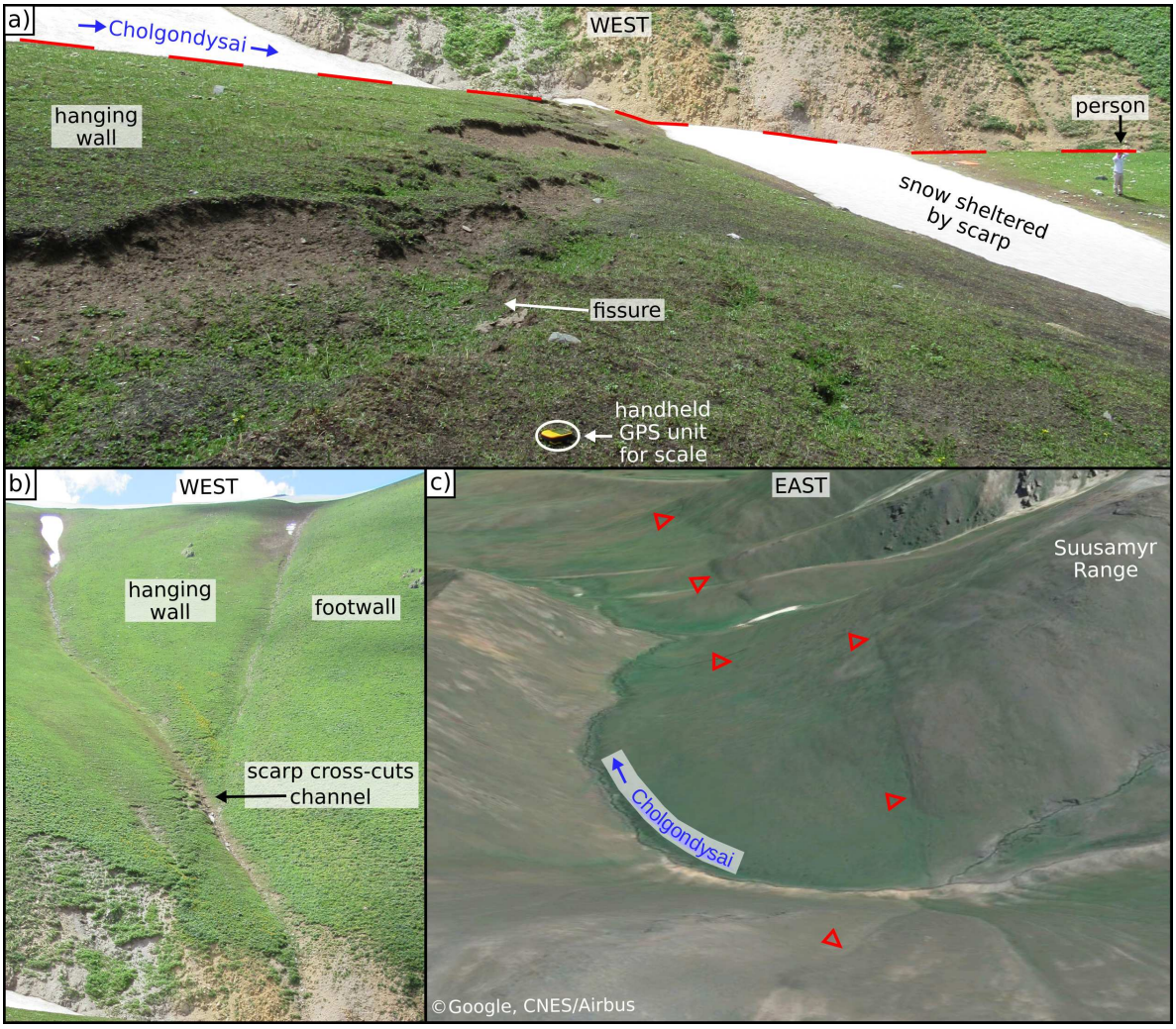


Figure 4.9: a) and b) Field photos of the Cholgondysai fault segment showing fresh fissures and the scarp crossing up the hillside steeply. c) GoogleEarth perspective view looking in the opposite direction along the fault. Our field site is in the foreground. Image acquisition date 16th August 2013.

to the fissures at the confirmed 1992 scarps (Section 4.4). There have been no other earthquakes greater than magnitude six in this region in the past century which could have formed the fissures so it is probable that the fissures do date from 1992 reactivation of this compound scarp. At least a 1 km stretch has abundant fresh fissures and the occasional fissures on the eastern 3 km of the scarp suggest that it too may have hosted some small displacements in 1992. I have found no evidence of scarps crossing the moraine and hillside between this Cholgondysai fault section and the Dzhalpaksu sections.

4.5 Prehistoric ruptures

I have already shown two sections of the 1992 earthquake ruptures that reactivated pre-existing scarps. In this section I will describe prehistoric ruptures that I have identified within the epicentral area but were not reactivated in 1992. Both scarps are situated alongside northern edges of anticlines that run through the valley and are within the 25 km gap between the eastern and western ruptures.

4.5.1 Chet-Korumdy Ridge

The Chet-Korumdy Ridge was the site of some of the most intense shaking and significant secondary effects during the 1992 earthquake (Section 4.2, *Ghose et al.* (1997)). The ridge is approximately 10 km long and reaches up to 300 m above the Suusamyr River (Figure 4.10). Outcrops in landslide scars on the southern flank of the CKR expose beds of poorly consolidated sediments ranging from coarse sand to 10 cm-long cobbles. Although these beds are to the south of the ridge crest, they dip to the north-west (strike 240°) at 25–40°, indicating that they are in the northern limb of an anticline and that the Suusamyr River has cut through the core of the fold. My interpretation of the ridge as a fragment of the northern limb of a fold leads to the conclusion that the grabens that opened along the crest of the ridge in 1992 are most probably related to gravitational collapse during shaking rather than being bending moment faults from fold-growth, which I would expect to find at the fold axis.

A moraine from the Talas Range to the north has been emplaced against the western end of the ridge (Figure 4.10). The edge of the moraine is truncated on its western side by an alluvial surface belonging to the Chong-Korumdy River, but since incising into the moraine the river has been diverted to the west leaving a wind gap through the CKR (*Chediya et al.*, 1997; *Korjenkov et al.*, 1999) and a suite of low alluvial terraces. A short south-facing scarp cuts the terraces and part of the lowest fan surface. It has greater offset where it crosses the older surfaces, showing that its activity has been ongoing through the period of formation of the different surfaces (Figure 4.10). I interpret it as

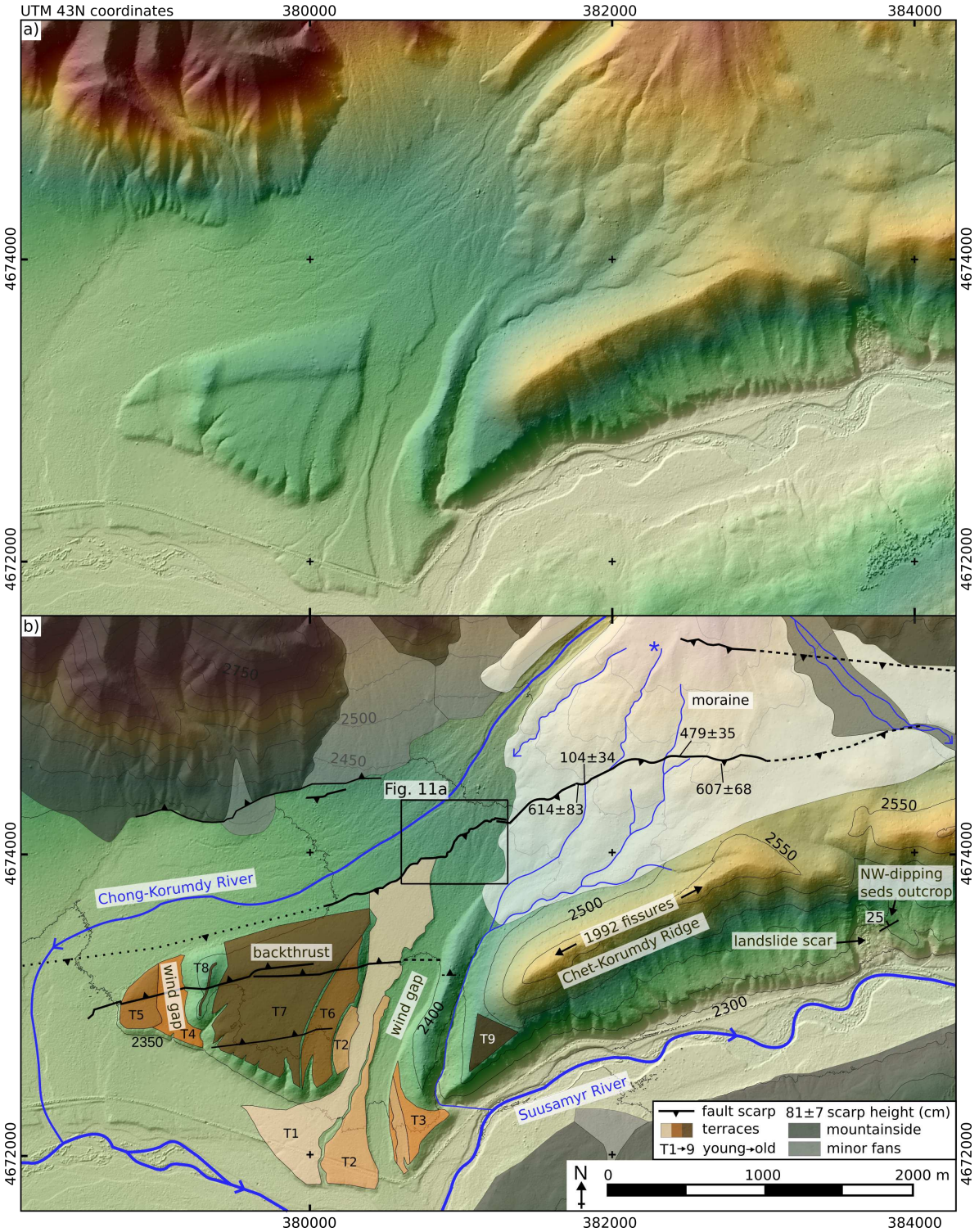


Figure 4.10: a) Hillshaded Pléiades DEM for the western end of the CKR (location shown in Figure 4.1). b) My interpretation of that area. See text for details.

a backthrust because the fault trace moves northward in lower topography.

A prominent north-facing scarp runs along the northern edge of the CKR (Fig-

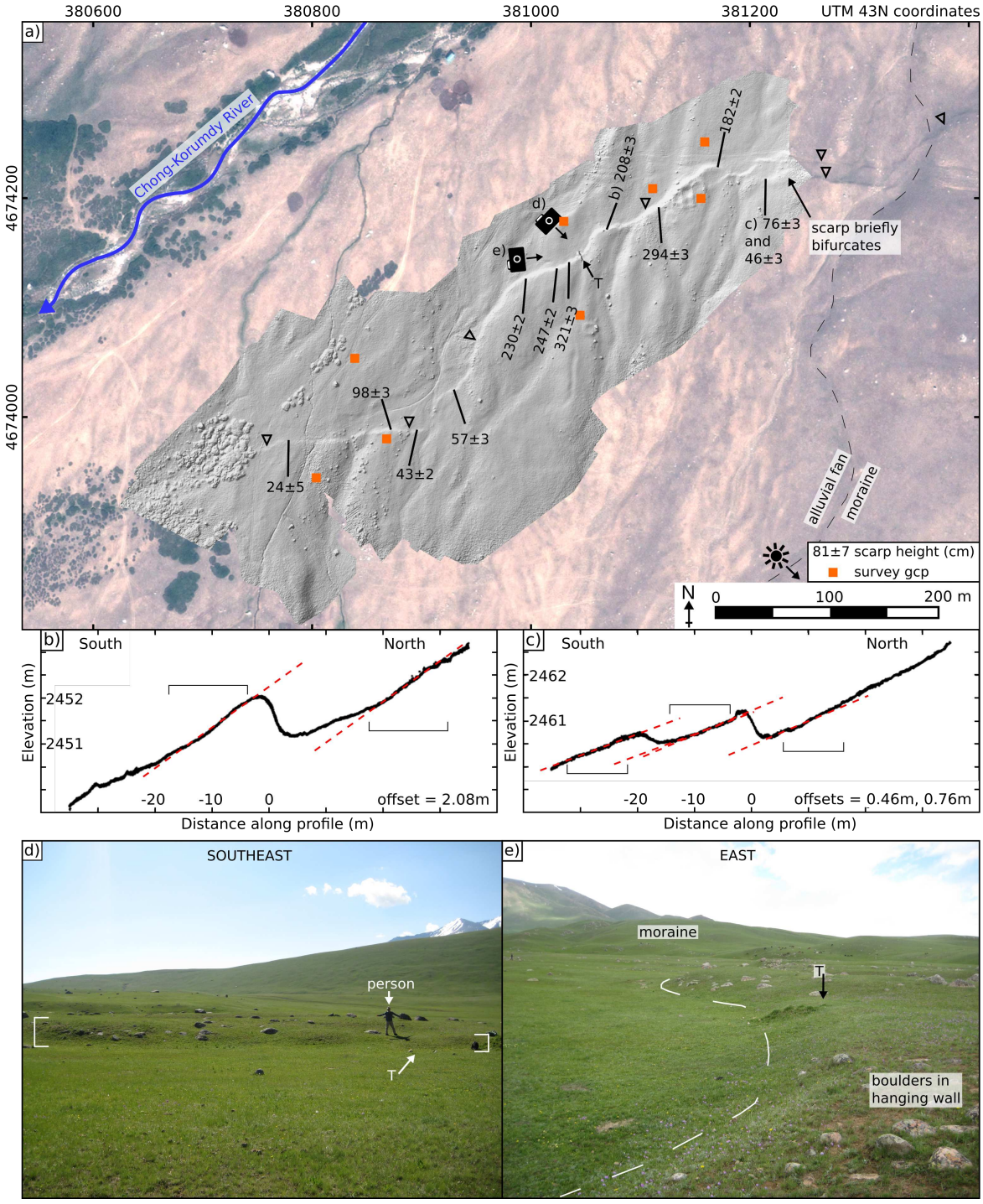


Figure 4.11: a) Hillshaded DEM of the uphill-facing scarp around my 2015 trench (T), annotated with scarp heights. b) & c) Topographic profiles. d) & e) Field photographs of the scarp, note that the trench is at a low point in a former channel and that elsewhere boulders are exposed in the hanging wall but buried in the footwall.

ure 4.10). In the moraine north of the CKR the scarp is manifested by change in drainage — one prominent stream (marked by a star in Figure 4.10) is diverted along the fault and the scarp forms a topographic low perpendicular to the drainage direction. There are few sites suitable for offset measurements in the moraine and for the sites I did select it was necessary to fit regression lines with unequal slopes to the two sides of the profiles so I am cautious about detailed interpretation of the results. However I find vertical displacements of 4.4–7 m in the moraine surface and for a stream channel I find 0–1.3 m vertical displacement (Figure 4.10). After it passes onto the alluvial surface west of the moraine the scarp offsets numerous small, anastomosing north-south channels. Its height is typically 2–3 m in the eastern part of this section (Figure 4.11) but after a left-stepping jog of 150 m the height decreases to <1 m. After ∼1.3 km across the fan, the scarp becomes difficult to map further westwards, if it is present at all, due to erosion by scarp-parallel channels. The height difference between the scarp in the moraine and the alluvial fan shows that the scarp ruptured in multiple prehistoric earthquakes, with the moraine showing the offsets from events that pre-date the fan. I can also infer that the fault hosted surface-rupturing earthquakes prior to the diversion of the Chong-Korumdy River and that folding and faulting have occurred contemporaneously.

In the field the scarp is smooth and without visible fissures in the hanging wall (Figure 4.11e). To assess the recent activity history of the scarp we dug a trench across it at 42.2104°N, 073.5589°E on an azimuth of 334° (Figures 4.11 and 4.12). This is at a point where one of the abandoned small channels crosses the scarp and the scarp height is a relatively low 1.1 m. The full trench log and unit descriptions are given in Figures 4.12 and 4.13 and Table 4.1. The northern side of the trench (footwall) exposed a sequence of sub-horizontal clays and sands down to a depth of 1.8 m, where it reached a densely packed conglomerate (unit 90). I interpret the conglomerate as the main fluvial/alluvial deposit which forms this surface, and the sand and clay to be ponded sediments dammed by the scarp. The hanging wall is made up of a hard

boulder conglomerate and a silty clay with gravel clasts, overlain by approximately 50 cm of poorly sorted soil. The hanging wall units are massive, with very different macrostructure to that of the footwall deposits, so I interpret all of the hanging wall units as being sub-units of unit 90 (the conglomerate), rather than being the result of over-topping of the scarp. In the central part of the trench, below the topographic scarp, the layered clay and sands have been offset and rotated by several strands of reverse faults, and show many plastic deformation structures (Figure 4.13). Clasts from the unconsolidated sand and gravel units are smeared out along the fault zone and in parts are aligned with it (unit 120). A thin sand layer (unit 20) caps the fault zone and has not been offset. Above it is poorly sorted soil which I interpret to be sourced from post-earthquake sediment influx, reworking of the unconsolidated fault zone material and erosion of the hanging wall.

I interpret the trench as showing evidence for at least two earthquakes. The first offset the gravel conglomerate (unit 90 and sub-units) and formed an uphill facing scarp. The layers of ponded clay and sand that I now see in the footwall (units 30–80) built up against this scarp and were then faulted in a second earthquake. Units 10 and 20 postdate the earthquakes; there is no displacement of these units and no disturbance at ground level.

Radiocarbon dates and ISRL ages from samples collected in the trench show increasing age with depth as expected (Figure 4.12). Full details of the results are listed in Tables 4.2 and 4.3. Sample KGZ15-C02 was collected from unit 20, which postdates the most recent event, and gave an age of 3166–3347 cal yr BP (full 2σ range). IRSL samples KGZ15-L01, KGZ15-L02 and KGZ15-L03 were taken from unit 40, which has been cut by a strand of the fault to give an apparent double thickness layer in the fault zone (see squares C4 and C5 on Figure 4.12), this is among the youngest layers to pre-date the most recent earthquake. The IRSL samples returned dates of 3.0±0.1 ka, 3.0±0.2 ka and 3.5±0.2 ka (Table 4.3). The pre-earthquake IRSL ages and the radiocarbon date of sample KGZ15-C02 are indistinguishable, given their uncertainties. My

radiocarbon samples from the oldest ponded sediments deeper in the trench give us a minimum estimate on the date of the penultimate earthquake, subject to the same inheritance caveat. The deepest sample taken from within unit 80 just above the boulder conglomerate gave an age of 7866–8001 cal yr BP and the next, 20 cm higher, gave 5935–6249 cal yr BP.

In summary, the CKR scarp has ruptured in multiple events; I identify two surface-rupturing events in a trench where the scarp crosses an abandoned fluvial surface. The first is likely to predate ∼8 ka and the second is at ∼3 ka which, given recurrence rates in the Tien Shan can be several thousand years (e.g. *Abdrakhmatov et al.*, 2016; *Deev et al.*, 2016; *Landgraf et al.*, 2016; *Grützner et al.*, 2017; *Patyniak et al.*, 2017) and I have no reason to think that this fault is exceptionally fast, might have been one of the most recent events in the basin. I do not observe any signs of coseismic or postseismic displacement from the 1992 earthquake.



Figure 4.12: a) Trench log for the 2015 CKR trench (location shown in Figure 4.10c, unit descriptions are given in Table 4.1). b) Photomosaic of the trench.

Table 4.1: Descriptions of the sedimentary units identified in the CKR trench (see Figure 4.12)

Unit number	Description
	POST-EARTHQUAKE UNITS
10	Brown silty soil with coarse sand throughout, poorly sorted. Occasional short (10 cm) lenses of medium red sand.
20	Coarse sand with fine sand matrix. Narrow layer lying unconformably above deformed units in the fault zone.
	UNITS PREDATING THE MOST RECENT EVENT
30	Medium to coarse red sand, poorly sorted and loose.
40	Medium brown silty clay, darkening with depth.
40b	Medium brown clay with gravel clasts. Interpreted as being correlative with unit 40.
41	Red, medium-fine sand lenses (interspersed throughout unit 40).
42	Fine gravel with fine sand matrix (in thick lenses within unit 40).
45	Folded lens of well sorted, medium-grained grey sand.
46	Folded lens of moderately well sorted fine gravel.
47	Medium to coarse gravel lens — channel deposit located at fault scarp. Unconformable lower contact with units 70 and 80; interfingered to the north with units 50 and 55.
49	Coarse gravels in a clay matrix. Not found elsewhere in trench, located only within fault zone; contact with unit 40b becomes gradational at the northern side.
50	Coarse to fine sand, fining upwards into the clay. Well sorted.
55	Brown clay layers, laterally extensive (>1m), interfingering with unit 50. Relatively rigid beds within deformable loose sands, thus contain important shortening structures near fault zone.
60	Discontinuous coarse sand layer found at base of unit 50, capping clay unit 65.
65	Dark (blue-purple-grey) clay.
67	Red, medium to coarse sand. Tapers out towards fault.
70	Pale, beige clay.
80	Dark brown clay, darkening downwards into nearly black organic-rich clay. Becomes more gravel-rich and paler close to the fault.
85	Layered channel deposit, fine sand to medium gravel. Much better sorting than in unit 90c.
90	Hard conglomerate of silt and cobbles.
90a	Brown silty soil with coarse sand throughout, poorly sorted.
90b	Very silty pale brown clay containing some gravel and sporadic <10 cm clasts. Distinct from hard gravel (unit 90c) below but uncertain, gradational upper contact.
90c	Hard conglomerate with clasts from boulders down to gravel in a densely packed finer matrix: oldest unit evident in trench.
	UNCORRELATED UNITS
100	Clayey coarse sand with roots. Mixed zone of units 10, 49 and 50?
110	Channel lens of coarse sand and fine gravel.
120	Gravels smeared out along fault zone; clasts aligned with fault plane. May be sourced from several different units.

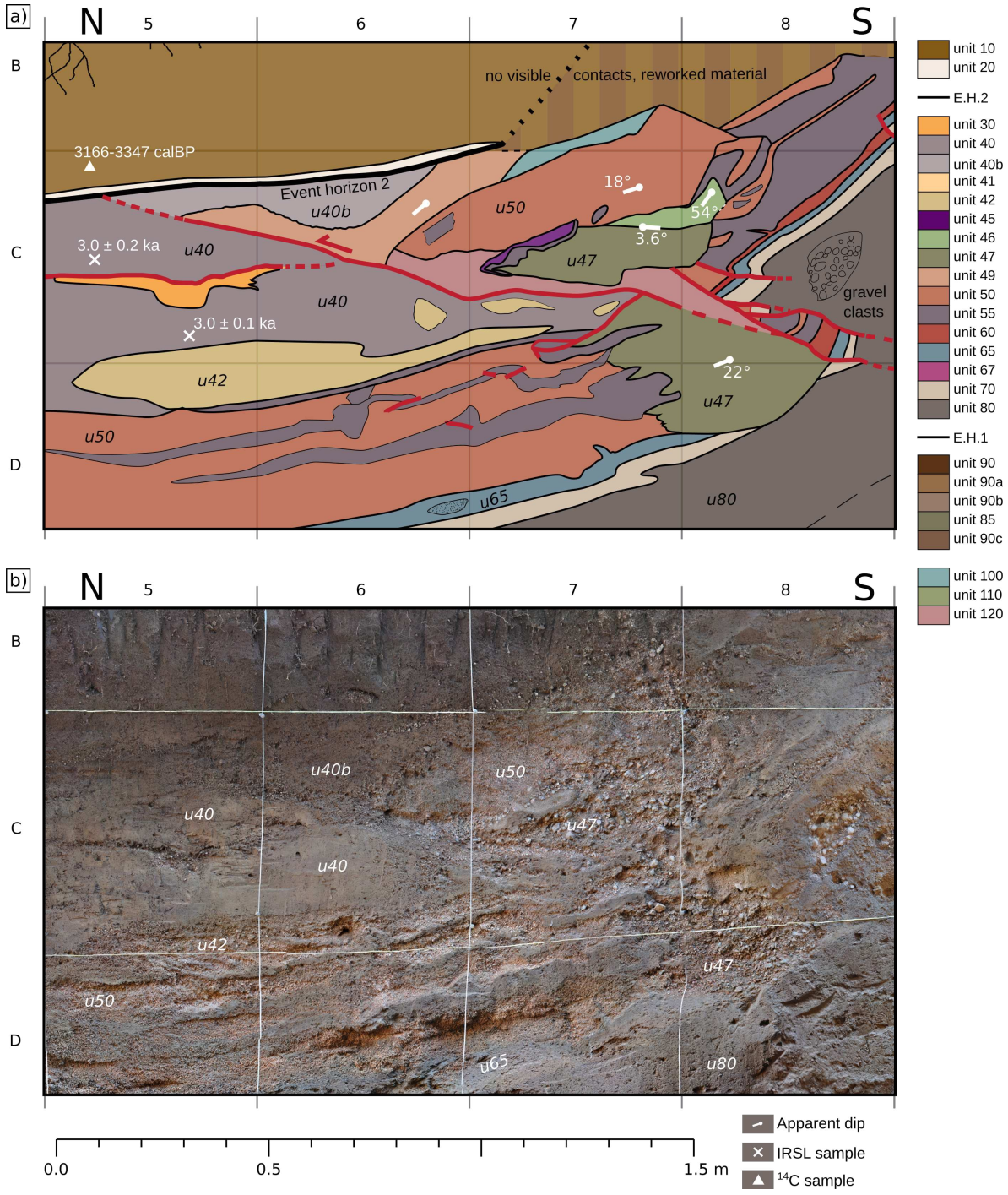


Figure 4.13: Close-up view of the fault zone from Figure 4.12.

Table 4.2: ^{14}C dating results. Zero BP (before present) is defined as 1950 AD. Tbk: Turabulak trench. CKR: Chet-Korumdy-Ridge trench.

Sample	Location	Longitude °E	Latitude °N	Elevation m	Depth cm	Description	Conventional ^{14}C Age yr BP	Calibrated date range (95.4%) cal yr BP
SUU16C05	Tbk	073.4766	42.2029	2422	45	bulk, B layer soil	4300 ±30	4961–4925(9.4%), 4918–4901(2.2%), 4893–4830(83.8%)
SUU16C06	Tbk	073.4766	42.2029	2422	60	bulk, B layer soil	4010 ±30	4567–4561(0.9%), 4531–4418(94.5%)
KGZ15-C02	CKR	073.5589	42.2104	2448	40	charcoal	3040 ±30	3347–3166
KGZ15-C04	CKR	073.5589	42.2104	2448	170	bulk, dark brown clay	7110 ±30	8001–7923(75.1%), 7901–7866(20.3%)
KGZ15-C05	CKR	073.5589	42.2104	2448	150	bulk, dark clay	5260 ±30	6249–6149(12.5%), 6121–6039(31.5%), 6033–5935(51.4%)
KGZ15-C07	CKR	073.5589	42.2104	2448	130	charcoal	4820 ±30	5606–5576 (34.8%), 5548–5476(60.6%)

Table 4.3: Luminescence dating results from the Chet-Korumdy trench. Work carried out by Andrew S. Carr. Uncertainties are standard error. Longitude 073.5589 °E, latitude 42.2104 °N, elevation 2448 m. OD = over-dispersion parameter (*Galbraith et al.*, 1999). The ages for KGZ15-L02 and KGZ15-L03, but not KGZ15-L01, are fading corrected (Section 4.3.2). Total usable aliquots refers to the total number of usable aliquots before outlier removal. The skewness parameter was calculated following *Bailey and Arnold* (2006). Uncertainties on the ages are one sigma.

Sample	Depth m	Total dose rate Gy ka^{-1}	Acceptable aliquots(total analysed)	OD %	Skew in D_e	CAM D_e $pIRIR^{\dagger}_{225}$ Gy	$pIRIR_{225}$ age ka
KGZ15-L01	0.55	8.24±0.32	16(18)	24±4	1.5±0.6	24.6±1.2	3.0±0.2
KGZ15-L02	0.80	8.13±0.30	16(18)	19±3	1.4±0.6	20.1±0.9	3.0±0.1
KGZ15-L03	0.60	7.63±0.30	19(21)	22±3	2.2±0.5	21.1±0.9	3.5±0.2

†following outlier removal.

4.5.2 Turabulak

Further west, another scarp that did not rupture in 1992 is evident at Turabulak (Figure 4.14). The scarp is situated approximately 2.2 km west of the CKR, where a fan deposited by two minor tributaries leaving the Talas Range is interrupted by two small anticlines that warp the fan surface. The eastern anticline is the more prominent of the two, with 50 m of relief and 1.5 km length. Southward-flowing drainage is now diverted eastwards around the anticline, with the drainage channel preserved as a wind gap in the fold crest (Figure 4.14a). The crest of the smaller, western fold is 230 m downslope of the eastern fold and is dissected by two active channels and four wind gaps. I have named this site Turabulak, after the name that Soviet-era topographic maps give the western of the two tributaries that flow into the fan.

As at the CKR site (Section 4.5.1), an uphill-facing, south-up scarp runs across the fan 400 m north of the western fold. The scarp is faintly visible on Pléiades and GoogleEarth imagery and can be traced for 1.2 km before it becomes too faint to follow (Figure 4.14a). It is not visible across the higher, older surface just to the east. In the field the scarp is identifiable by its small elevation change (typically 15–35 cm on my UAV DEM, and up to 62 cm) and a subtle change in surface lithology: cobbles protrude through the hanging wall grass whereas the footwall hosts slightly greener, thicker grass growing in cobble-free soil (Figure 4.14). Topographic profiles through my UAV DEM show that scarp infilling and a rounded hanging wall corner have resulted in a 4-5 m-wide sub-horizontal scarp area between the two sides of offset, planar, $\sim 4°$ sloping alluvial fan (e.g. Figure 4.14e,f).

We excavated a small trench across the scarp at 42.2029°N, 073.4766°E at a point where the footwall has slightly denser vegetation than average and which is recognisable from the aerial imagery shown in Figures 4.14b and 4.14c as a minor abandoned channel. For the purposes of the trench log I defined the ground surface at the trench as horizontal. My trench revealed an alluvial gravel unit made up of well rounded, ∼10 cm

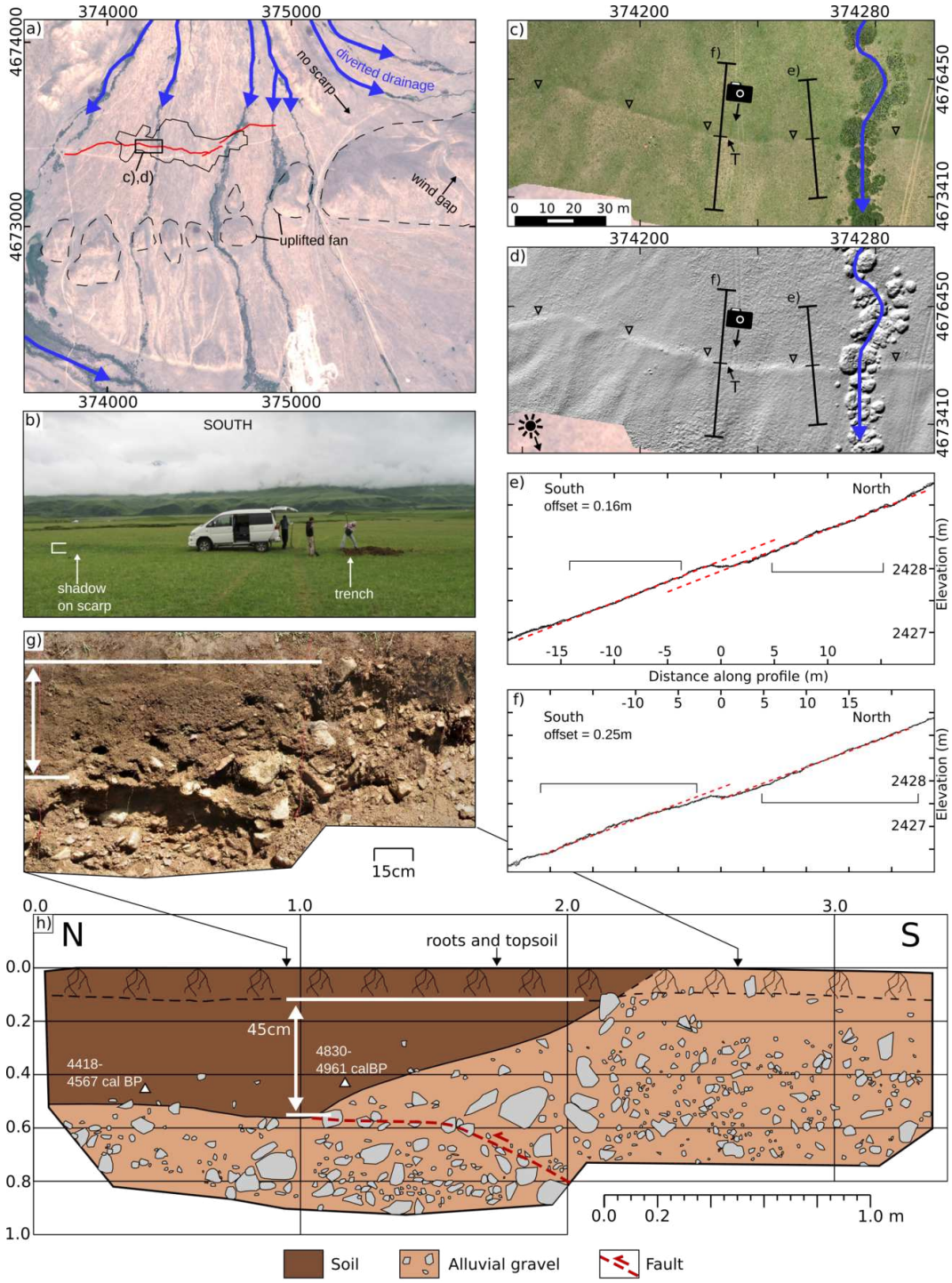


Figure 4.14: a) Pléiades imagery of the Turabulak site, location shown in Figure 4.1. Red line shows the scarp, black solid line marks the extent of my UAV DEM. b) A photograph of the scarp and trench site. The scarp is picked out by a slight shadow running from left to right. c) UAV orthophoto of the scarp, black triangles mark the scarp, T shows trench site, camera shows the viewpoint of panel b). d) Hillshaded 10 cm DEM of the same area. e) A typical topographic profile. The best fit lines are shown in dashed red and the sections of the profile that they were fitted to are marked. f) As e) but for a location across the trench site. g) Photomosaic of the central portion of the east wall of the trench, showing the top of the gravel layer displaced by ∼45 cm and the resulting uphill-facing escarpment partially filled by brown soil. h) Trench log of the east wall. The scale and the location of the white markings are exactly as in panel g).

sized, predominantly granite cobbles in a matrix of coarse sand which contained a small fraction of mud. In the hanging wall (south) the gravel reaches the surface with some thin soil covering, in the footwall the top of the gravel layer is offset 45–55 cm vertically downwards and the scarp is infilled by uniform sandy soil. The 10 cm range in my offset measurement is a consequence of the uncertainty in defining the top of the gravel layer in the hanging wall.

I interpret the trench as showing evidence for a single earthquake that offset the gravel layer, forming the scarp which has since been partially infilled by the sandy soil. The fault is not prominent in the trench gravel but I have tentatively marked it along a convex surface across which there was a contrast in cohesion and which was visible on both walls of the trench (Figure 4.14), its lower section has an apparent dip of 27°, while the upper portion is sub-horizontal and may be the result of collapse of the hanging wall wedge. Taking a fault dip of 30°, and assuming there is no lateral component of slip, the 45–55 cm vertical horizontal offset corresponds to 90–110 cm of slip. Two bulk radiocarbon samples from the base of the soil sediment which postdates the earthquake gave dates of ∼4400–4960 BP (Table 4.2), so it is likely that the earthquake predates 4.4–4.9 ka, but I cannot discount that it is younger than the radiocarbon ages due to inheritance in the radiocarbon. The difference between the two dates can be attributed to inheritance and to the deposition of the soil taking some time.

4.6 Discussion

Our results have confirmed that the ruptures from the 1992 Suusamyr earthquake were fragmented and were short given the magnitude of their offset. I have shown that the western ruptures that had been mapped as 3.4 km in length (*Ghose et al.*, 1997) were even shorter, at 2.0 km, but I have also found that those ruptures in the west were part of a longer, disjointed series of fresh scarps which in total spans almost 12 km where the slip reached, or presumably nearly reached, the surface. At the M41 highway rupture in

the east a large proportion of the slip that would be expected for a M_w 7.2 earthquake based on scaling relationships — at least 3.6±0.1 m — did reach the surface but, even including my new observations, we are left with an unruptured gap of >20 km in the area that experienced some of the strongest shaking and which is directly updip of the plane defined by the aftershocks (*Ghose et al.*, 1997; *Mellors et al.*, 1997).

I cannot rule out the possibility that the two sets of ruptures are the result of two different earthquakes. It is possible that the western surface ruptures are the result of the M_s 6.6 aftershock rather than the mainshock. In that case, we would still have the difficult task of explaining why the sole rupture from the M_w 7.2 mainshock hosted a significant fraction of the slip expected for an earthquake of that magnitude but was only $\leq$ 600 m long. Even for this modern earthquake sequence, because the mainshock and aftershock were so close together in time, we cannot distinguish between their surface ruptures, so we must treat them as one event for the purposes of comparison to the palaeoseismic record.

Based solely on the 1992 ruptures, I could suggest that the earthquake only broke the surface at points where the fault trace runs along the base of bedrock-cored mountains, and that where deformation has migrated away from the range-front, the near-surface fault slip was accommodated in the basin fill via folding. Although that conclusion fits my observations from the most recent event, it does not tally with my observations from prehistoric earthquake ruptures. In Section 4.5 I showed two sites where prehistoric earthquakes have ruptured the surface alongside folds. My trenches through these scarps show no evidence for slip in the 1992 earthquake. The fault tip does, therefore, reach the surface, but reactivation of the breakthrough fault seems to be intermittent.

Figure 4.15 highlights the challenges for interpretation of earthquake histories in areas such as Suusamyr. The fault does not rupture completely new scarps with every earthquake — my results show that the Cholgondysai, Dzhalpaksu and Chet-Korumdy Ridge scarps have all ruptured at least twice — but palaeoseismic investigations at any of the sites individually would reveal different earthquake histories. The scarps are

all shorter than the tens of kilometres subsurface width that is expected of a surface-rupturing earthquake and much shorter than the 50±10 km estimated fault width for the 1992 earthquake. Burial or erosion of scarps certainly contributes to the discontinuity of ruptures, however my observations here indicate that significant discontinuity can be inherent to the tectonic ruptures. Both phenomena are most obvious at the M41 highway rupture where the ruptures crossing the river were eroded within months by the powerful river, but the scarp height distribution I have measured shows real taper to zero within hundreds of metres. Burial and erosion are ubiquitous processes that need to be considered for palaeoseismic studies everywhere; my observations additionally suggest that, like the 1992 ruptures, the prehistoric ruptures were already fragmented at their creation (Sections 4.4.2 and 4.5.2).

The established practice of applying scaling relationships to studies of prehistoric earthquakes presumes that surface ruptures and offsets are representative of fault parameters at depth. Indeed, among reverse-faulting earthquakes there are examples for which the surface expression agrees strongly with the slip at depth, including the 1988 Tennant Creek, Australia (*Bowman*, 1992), 1999 Chi-Chi, Taiwan (*Ji et al.*, 2001; *Lee et al.*, 2003), 2005 Kashmir, Pakistan (*Avouac et al.*, 2006; *Kaneda et al.*, 2008), and 2008 Wenchuan, China (*Lin et al.*, 2009; *Xu et al.*, 2009) earthquakes. However, the scatter in the surface rupture length- and (particularly) displacement-magnitude relationships for reverse faulting earthquakes (*Wells and Coppersmith*, 1994; *Moss and Ross*, 2011) attests to the great range in their behaviour and surface expression.

It is already known that many earthquakes do not produce primary surface rupture (i.e. are blind) (e.g. *Stein and King*, 1984; *Lin and Stein*, 1989; *Stein and Yeats*, 1989; *Lettis et al.*, 1997), and that for a given magnitude, more reverse earthquakes than strike-slip or normal earthquakes fail to produce surface rupture (*Moss and Ross*, 2011). Failure for slip to reach the surface is usually attributed to a portion of the shallow slip being accommodated by folding, or to the majority of the coseismic slip being at depth

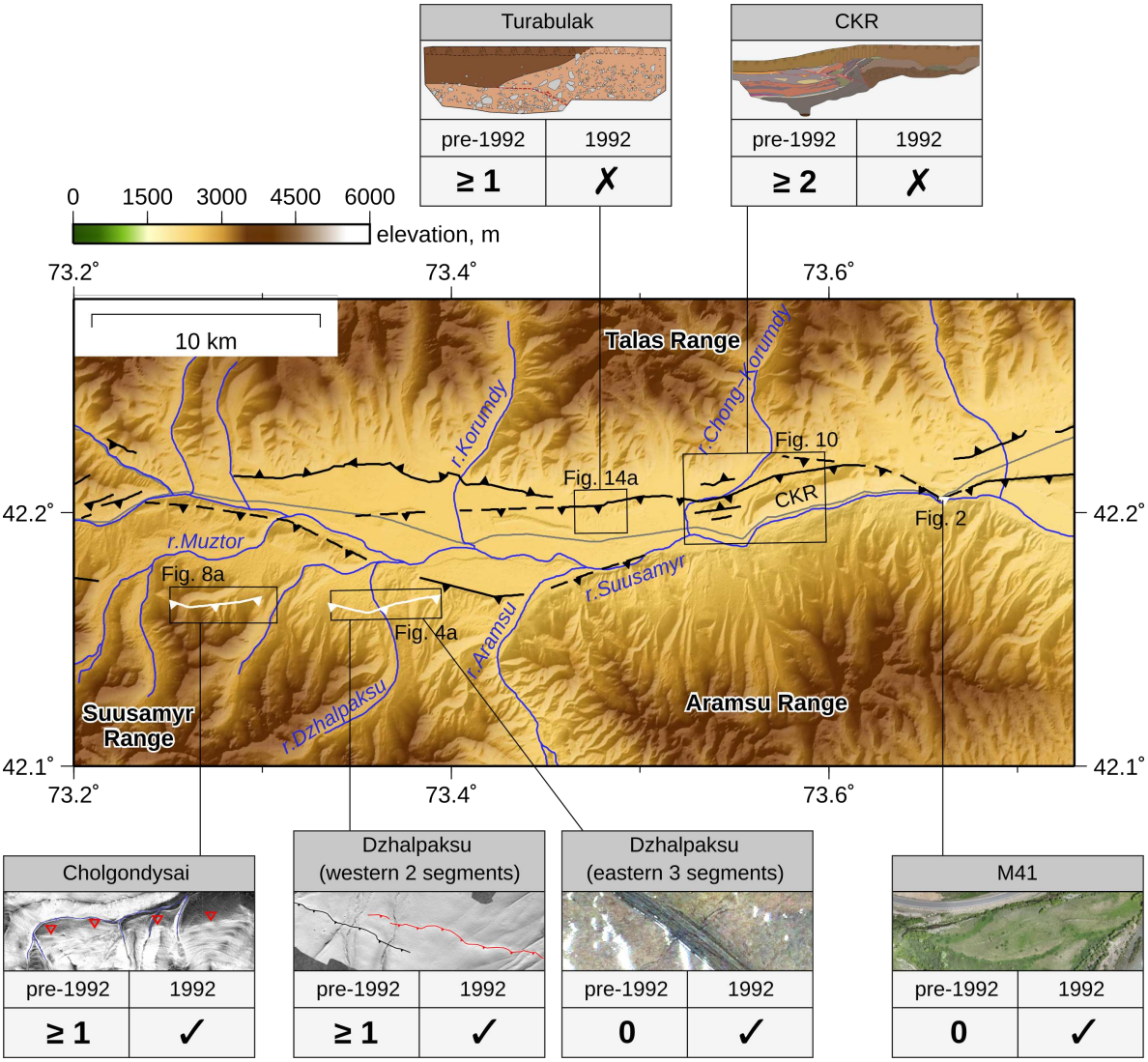


Figure 4.15: Summary of the evidence for surface rupturing earthquakes at each of my sites. The key for the main panel is as in Figure 4.1.

(e.g. *Stein and King*, 1984; *Lin and Stein*, 1989; *Walker et al.*, 2005; *Grandin et al.*, 2015).

There are two scenarios that involve slip partially reaching the surface at ruptures. The first is that an earthquake produces surface breaks of some kind over a long distance but they have smaller average displacement than expected for their moment magnitude. This has been seen for earthquakes such as the 1962 Ipak, Iran (*Ambraseys*, 1963; *Berberian*, 1981) and 2002 Changrueh (Avaj), Iran (*Walker et al.*, 2005) earthquakes, and is compatible with the explanations above. The 1992 Suusamyr earthquake shows the opposite phenomenon, in that the displacement of the surface ruptures is roughly con-

sistent with what is expected from the earthquake's magnitude according to scaling laws (*Thingbaijam et al.*, 2017), but the ruptures are short and separated by a gap that is longer than their total length. Earthquakes that have shown large gaps between segments of surface ruptures are not unheard of. The 1952 Kern County, California, USA earthquake was an oblique earthquake which caused surface ruptures on either side of the San Joaquin Valley but was blind beneath the valley itself (*Buwalda and St. Amand*, 1955; *Bawden*, 2001). The 2005 Dahuiyeh (Zarand), Iran earthquake reached the surface where bedding was planar and sub-parallel to the fault but not where bedding was folded and the bedding was oblique to the rupture plane (*Talebian et al.*, 2006). Neither showed such high displacement-to-length ratios as the eastern segment at Suusamyr.

In both the Kern County and Dahuiyeh cases, structural or lithological controls had an important influence on the pattern of surface rupture, but obtaining information about several earthquakes on the Suusamyr Fault allows us to take our understanding further. The 1992 Suusamyr earthquake had superficially straightforward kinematics — its mechanism is as expected for the region, there is no need to model the seismograms using sub-events and it was a major earthquake that ruptured most or all of the seismogenic layer (*Mellors et al.*, 1997; *Ghose et al.*, 1998; *Sloan et al.*, 2011). As I have discussed, it is plausible that the presence or absence of folds at the near-surface had an influence on the pattern of the 1992 earthquake, but the variability in rupture pattern that I have found between the 1992 and prehistoric earthquakes that I have found shows that there is also an inherent variability. This makes Suusamyr an important example for reverse fault palaeoseismology in general. Although structure could reasonably be expected to be constant over the timescale of several earthquake cycles and to produce similar results, in the Suusamyr case the earthquake record can not be captured without analysis at multiple sites.

4.7 Conclusions

I used satellite imagery, DEMs and field investigations to map and measure surface ruptures from the 1992 Suusamyr earthquake and prehistoric earthquakes on the Suusamyr Fault. There is evidence for a total length of up to 7.6 km of fresh surface ruptures from the 1992 Suusamyr earthquake — a value longer than previously thought but still much shorter than the subsurface rupture length as estimated from the aftershock extent or from scaling relationships given the earthquake's magnitude. The ruptures were discontinuous, with the western 7 km of ruptures being made up of six segments that are spread across 12 km and the eastern, 0.6 km-long rupture segment separated from the western ruptures by a gap of >20 km. At least three of the rupture sections from 1992 were on pre-existing fault scarps, but I have also identified additional active fault scarps that did not rupture in the 1992 earthquake despite being situated in the gap between the 1992 ruptures. By trenching at two sites on those scarps I have compiled a palaeoseismic record for the fault that shows a minimum of three surface-rupturing earthquakes within the past $\sim\geq$8 kyr, but my mapping also shows that the fault scarps are short, discontinuous and reoccupied in an erratic manner. No single section of fault scarp carries a full record of the earthquake history and, although there is abundant evidence for tectonic shortening along the valley, there is no continuous scarp or fold along which single trenches or standard empirical scaling relationships could be applied to recognise the history of $M > 6$ earthquakes.

My results update and add to a valuable example of surface-rupturing earthquakes in the Tien Shan. They also demonstrate that reverse faulting earthquakes can have variability beyond what can be explained by structural geology or near-surface lithology alone, and highlight the importance of investigating as many sites as possible for studies that aim to establish the seismic history of a fault.

Chapter 5

Active Shortening in the Suusamyr Basin, Kyrgyzstan

5.1 Introduction

The relatively rapid rates of shortening, excellent preservation of the landscape, and occurrence of important and recent earthquakes has made the Tien Shan a valuable study area for active intracontinental shortening (*Burbank et al.*, 1999; *Bullen et al.*, 2001; *Sobel et al.*, 2006; *Selander et al.*, 2012; *Campbell et al.*, 2013; *Mackenzie et al.*, 2018). Despite this, the active faults and folds of many parts of it have still not been studied in detail. The M_w7.2 1992 Suusamyr earthquake ruptured the western part of the Suusamyr Basin (*Mellors et al.*, 1997; *Ghose et al.*, 1997; *Bogachkin et al.*, 1997), but the eastern part may still present a seismic hazard and has not been mapped in detail. I have already shown in Chapter 4 that the surface expression of faulting in the Suusamyr Basin is subtle, but that careful analysis of the geomorphology can yield useful information on the location and styles of faulting. That chapter focussed on north-facing surface ruptures in the western part of the basin. In this chapter I map the active fault scarps and folds of the entire basin using high resolution imagery, DEMs and field surveys. Using the results of my mapping and Quaternary dating I then place

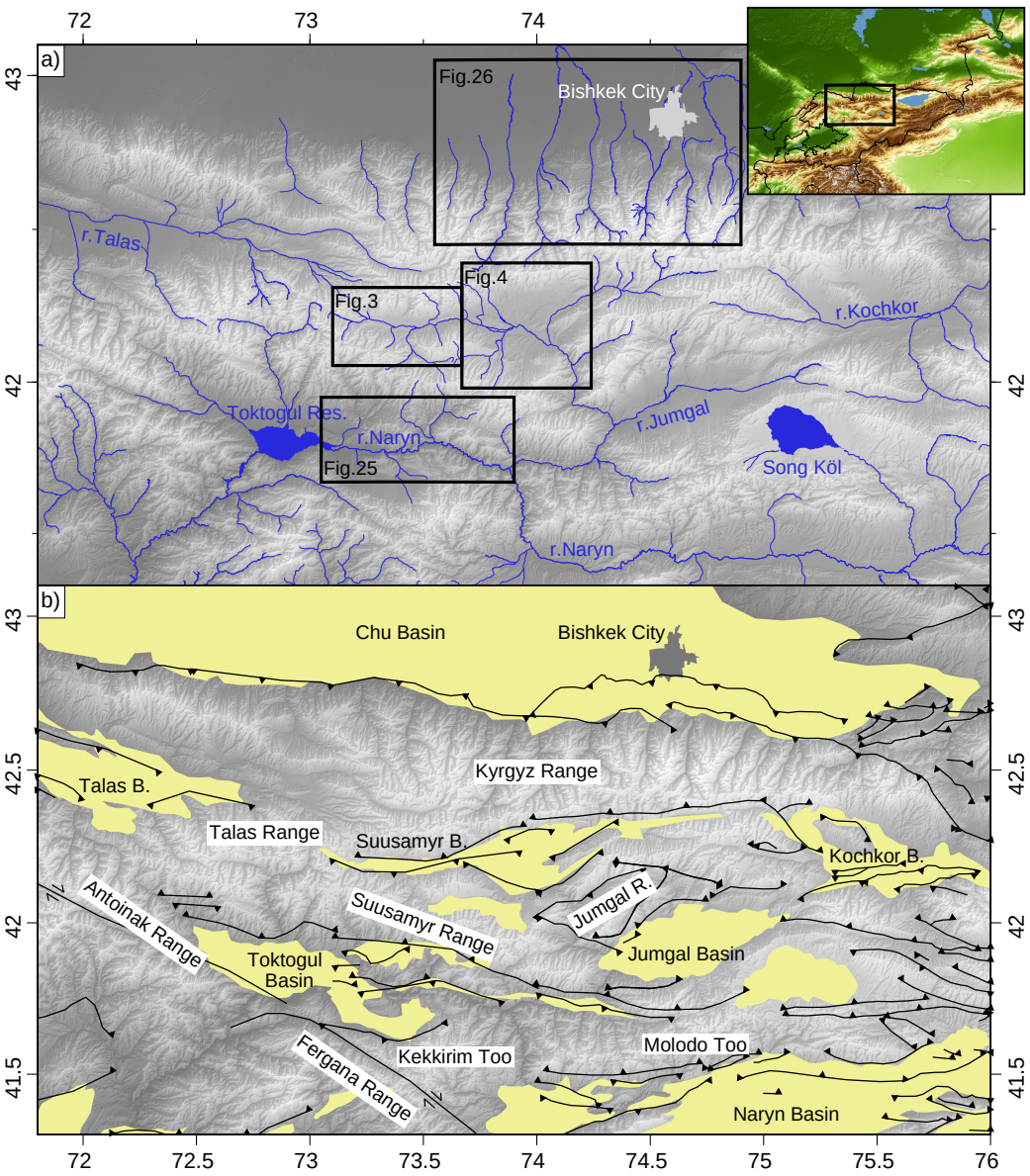


Figure 5.1: a) Drainage and topography of the northwestern Tien Shan. DEM from SRTM, drainage and city outline data are from OpenStreetMap. b) Distribution of faults and basins filled with Cenozoic sediments (*Nikonorov et al.*, 2000) in the northwestern Tien Shan. Fault map based on *Cobbold et al.* (1994); *Thompson et al.* (2002); *Mohadjer et al.* (2016) and my own editing.

constraints on the rates of slip and shortening across the Suusamyr Basin.

Active faults are present throughout the Tien Shan (*Abdrakhmatov et al.*, 2001; *Thompson et al.*, 2002). Quaternary slip rate estimates (e.g. *Thompson et al.*, 2002), geomorphic analyses (*Burbank et al.*, 1999) and the smooth velocity field (*Zubovich et al.*, 2010; *England and Molnar*, 2015) show that deformation takes place pervasively

across the mountain belt; faults within the belt, as well as on its margins, are still active, and the shortening is accommodated across several sub-parallel faults that are active simultaneously. In the western Tien Shan these sub-parallel faults have formed a series of intermontane basins (Figure 5.1). The basins are elongated east–west — approximately parallel to the fault traces and perpendicular to the direction of maximum shortening. They are typically several tens to one or two hundred kilometres long and a few tens of kilometres wide, with over 1 km of relief (*Makarov*, 2012; *Campbell*, 2015). They are filled with Cenozoic sediments (*Nikonorov et al.*, 2000) and are believed to be bounded by relatively steep reverse faults that cut through the seismogenic part of the crust (*Ghose et al.*, 1998; *Park et al.*, 2003; *Goode et al.*, 2011). The development of these intermontane basins has been of some interest as an active example of how intracontinental mountain belts develop (*Burbank et al.*, 1999; *Park et al.*, 2003; *Goode et al.*, 2014).

A common feature of intermontane basins of the Tien Shan is to have active structures within the Cenozoic basin fill that seem to post-date the basin-bounding faults (*Burbank et al.*, 1999; *Thompson et al.*, 2002; *Park et al.*, 2003; *Goode et al.*, 2011). For instance, *Park et al.* (2003) found that the active centre of deformation in the Kochkor Basin (Figure 5.1) has shifted towards the basin interior over time. They compared the results of a magnetotelluric profile to Quaternary shortening estimates to show that an intrabasin thrust, which is connected by a detachment to the basin-margin thrust, now accommodates between one third and all of the total convergence on the southern side of the basin. *Goode et al.* (2014) studied this phenomenon in the Naryn Basin (Figure 5.1) and, based on extrapolating the relative uplift rates of deformed terraces, suggested that the active structures within the interior of the Naryn Basin formed in the past 1 Myr, at least 1–4 Myr later than the mountain ranges surrounding the basin. *Goode et al.* (2011) inquired into the controls on the style of deformation of intermontane basins. They found that in the narrower eastern part of the Naryn Basin (Figure 5.1) deformation takes place on the basin-bounding fault and its splays,

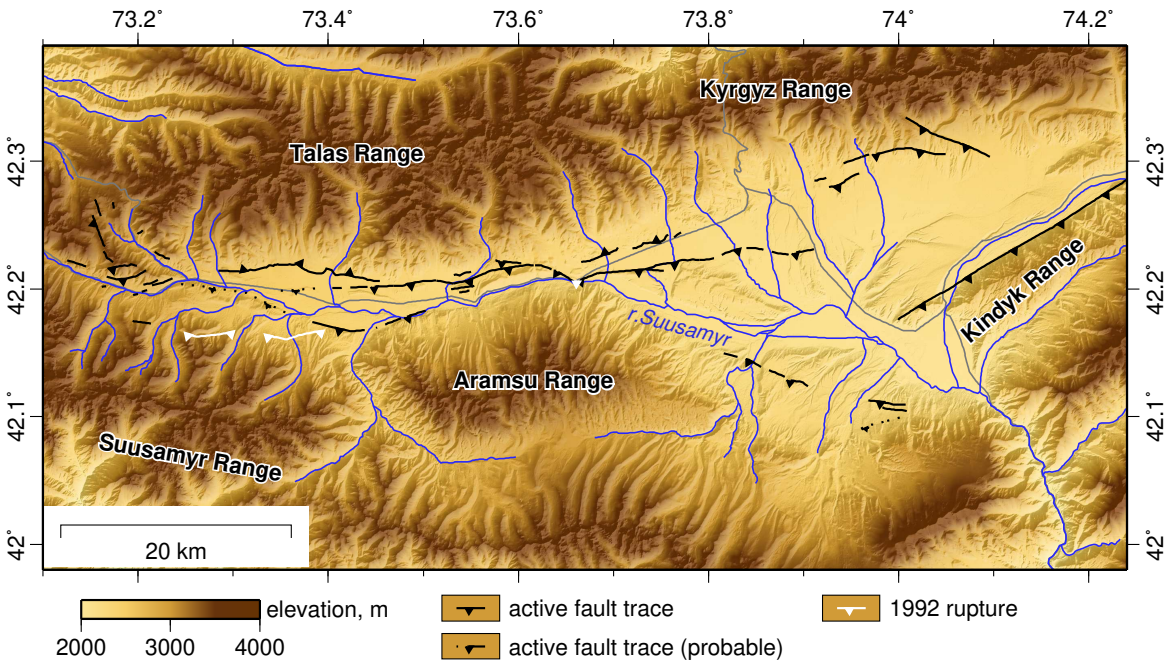


Figure 5.2: A fault map of the Suusamyr Basin, mapping our own. Shaded relief DEM using the AW3D30 DEM (*Takaku et al.*, 2014) illuminated from the SE.

but in the wider western part of the basin deformation has migrated from the basin boundaries into the basin interior. *Goode et al.* (2011) suggest that the difference in style between the parts of the basin with different widths is due to a difference in stress conditions, and therefore favourability of slip, on basin-interior versus basin-bounding faults depending on the overburden on each fault, which is related to the basin width.

Although the development of Tien Shan intermontane basins when considered in north-south cross-section has received some attention, their along-strike development and strain transfer between adjacent basins remain less well understood. The basins are separate, disconnected regions of low topography within the mountain ranges and are arranged slightly offset from each other but as a whole they accommodate a relatively smooth strain field of shortening in the western Tien Shan. The arrangement requires rotation or internal deformation of the ranges between them, but the interbasin ranges are not typically thought to contain major faults (*Thompson et al.*, 2002), so it is not clear how strain is transferred.

The Suusamyr Basin is an intermontane basin in the northwest Tien Shan (Fig-

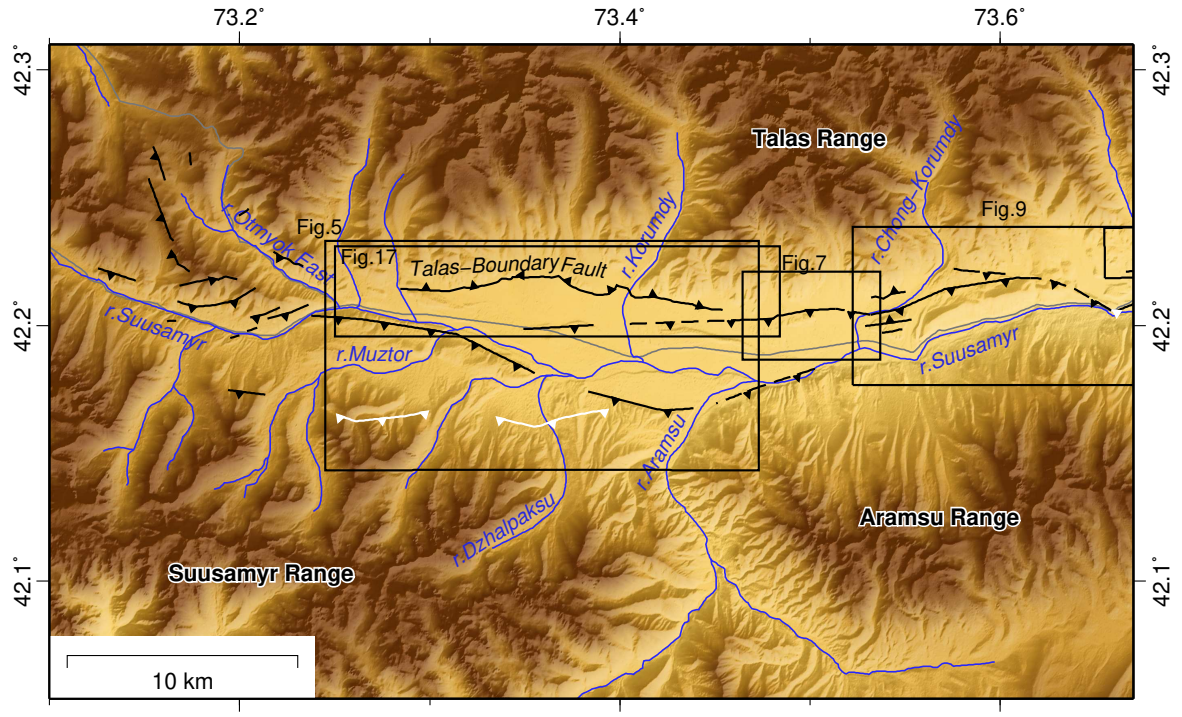


Figure 5.3: Larger map of the western half of the Suusamyr Basin, showing the locations of later figures. Shaded relief DEM using the AW3D30 DEM (*Takaku et al.*, 2014) illuminated from the SE.

ures 5.1 and 5.2)(*Chediya et al.*, 1997) and has been the focus of some research into its tectonics due to the 1992 earthquake (e.g. *Bogachkin et al.*, 1997; *Ghose et al.*, 1998; *Korjenkov et al.*, 1999) but questions remain about the style of faulting, shortening rate, and tectonic development of the basin. The basin is elongated east-west and ∼80 km in length. In its western 35 km the basin has a width of around 4–6 km and is enclosed by the Talas Range to the north and the Suusamyr and Aramsu Ranges to the south (Figure 5.3). In the eastern 45 km of the basin the mountains to the north continue unchanged (although they are referred to there as the Kyrgyz Range) but the southern edge of the basin drops back and the basin widens to up to ∼25 km width (Figure 5.4). The Neogene valley fill is reported to be 800–1100 m in thickness and consist of clays, limestones, sandstones and conglomerates (*Sadybakasov*, 1972; *Korjenkov et al.*, 1999). The surrounding mountain ranges are made up of Paleozoic and Proterozic rocks (*Nikonorov et al.*, 2000). The most prevalent units in the basement

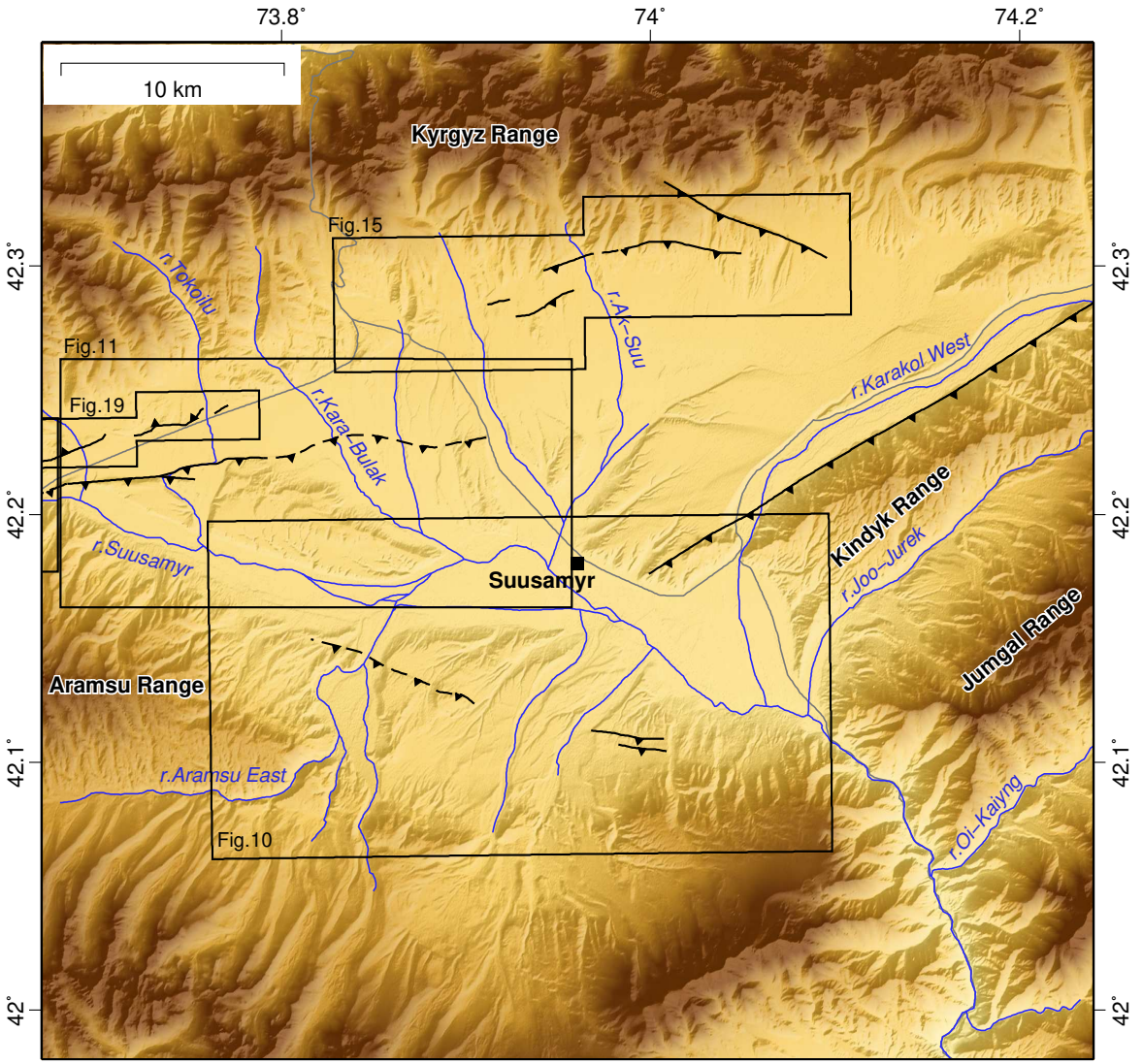


Figure 5.4: Larger map of the eastern half of the Suusamyr Basin, showing the locations of later figures. The distance scale is the same as for Figure 5.3. Shaded relief DEM using the AW3D30 DEM (*Takaku et al.*, 2014) illuminated from the SE.

are made up of intrusives and the remains of volcanic complexes from the Devonian and earlier (*Nikonorov et al.*, 2000).

5.2 Methods

This chapter utilises many of the field and remote mapping techniques that were introduced in Chapter 4. We conducted fieldwork in June 2015 and June 2016, during which we carried out UAV surveys to collect photographs for high-resolution DEMs and dug

pits to collect samples for Quaternary dating. In addition to the freely available images and DEMs, and the Pléiades images and DEMs that are introduced in Chapter 4, I constructed a DEM using three triplets of tristereo imagery acquired by the SPOT-6 and SPOT-7 satellites on 18th October, 1st November and 9th November 2014. The imagery was processed using ERDAS LPS following the method described in Chapter 4 and gridded with a 6 m spacing to make a raster DEM. The SPOT DEM has a larger coverage area than the Pléiades DEM but has lower horizontal resolution (1.5 m resolution of the panchromatic images, as opposed to Pléiades' 0.5 m). Unfortunately there is snow on the high ground in the SPOT images. Although SPOT-6&7 have a bit depth of 12 (i.e. each pixel can take a value from 0 to 4,095) the snow caused the images to have narrow, highly skewed histograms and the non-snow-covered pixels (most of the scene) occupy only a narrow range of values. The narrow histogram resulted in reduced point cloud density and increased noise in the low-lying areas of the DEM, particularly in areas with less prominent features. However, the areas that were snow-covered have excellent point density. Although some interpolation was necessary to make a the 6 m-resolution raster DEM, the interpolated values are not used for any offset measurements, which are all made directly from the pointcloud. The offset measurements and uncertainty estimates were made on swath profiles following the method described in Chapter 4.

Samples of pedogenic carbonate coatings (rinds) on clasts were dated for this study using ^{230}Th/U dating. The dating was carried out by Stacy A. Carolin at the University of Oxford. Pedogenic carbonate is precipitated from supersaturated ground-water percolating through a deposit. The ground water can become supersatutated due to evaporation, freezing, temperature gradients in the soil or other factors, and the pedogenic carbonate typically forms at ∼30–200 cm depth, depending on the climate and site conditions (e.g. *van Calsteren and Thomas*, 2006). ^{230}Th/U dating is based on the fact that uranium is soluble in water, whereas thorium is insoluble at normal surface temperatures. Carbonate precipitated from the water is therefore expected (ideally)

to contain uranium but not thorium initially. ^{234}U decays to ^{230}Th with a half-life of 235.6 kyr, so over time the quantity of ^{230}Th in the carbonate increases. ^{230}Th itself decays with a half-life of 75.4 kyr, so the increase in ^{230}Th concentratoin with time continues until secular equilibrium is reached after ∼350 kyr, at which point the rate of thorium production equals the rate of its decay. For samples younger than 350 kyr, the time elapsed since the formation of the carbonate coating can be estimated by measuring the ^{230}Th present in the sample, relative to ^{234}U and to the 'stable' isotope ^{238}U (e.g. *van Calsteren and Thomas*, 2006).

^{230}Th/U dating has been found to give ages that are compatible with cosmogenic or luminescence dating (*Sharp et al.*, 2003; *Fletcher et al.*, 2010; *Campbell*, 2015) and has already been applied to estimation of fault slip rates (e.g. *Blisniuk and Sharp*, 2003; *Fletcher et al.*, 2010) but there are a number of other factors that must be considered before interpreting the results. Firstly, although the most simple assumption is that the carbonate contained zero thorium initially, in practice the coating will incorporate detrital material that contains thorium (e.g. *van Calsteren and Thomas*, 2006; *Sharp et al.*, 2003). A correction is made for detrital thorium by measuring the sample's concentration of ^{232}Th (which is effectively a stable isotope and must therefore come from the detrital thorium), and using that to estimate the initial concentration of detrital ^{230}Th. In this study the detrital ^{230}Th/^{232}Th atomic ratio is assumed to have the 'bulk earth' value of 0.54×10^{-6}–10.8×10^{-6} (in a uniform distribution). The Donkey software program (written by Andrew Mason at the University of Oxford) was then used to run 10,000 Monte Carlo simulations of age calculations to calculate the average age and age errors for each sample accounting for the detrital thorium.

A second concern is uranium loss due to leaching or dissolution of the carbonate. This often results in porous, opaque or non-lamellar carbonate, therefore samples showing those symptoms are not dated. Thirdly, samples can return dates older than the date of surface stabilisation if they have inherited clast coatings that were already present at the time of a clast's deposition (*Sharp et al.*, 2003; *Campbell*, 2015) . Our samples had

thicker carbonate coatings on the bottom side, as would be expected for coatings that formed in-situ, and we did not see any prominent angular unconformities within the carbonate lamellae of the cut samples that would be indicative of an inherited partial coating(e.g. *Sharp et al.*, 2003). Finally, the 'event' dated by ^{230}Th/U dating is the date of carbonate formation, after which, all being well, the carbonate acts as a closed system (*van Calsteren and Thomas*, 2006). This event is not necessarily at the same time as the date of surface stabilisation, which is the event I would like to date in this study — there is a 'time lag' between surface stabilisation and the precipitation of the first carbonate lamella and, as such, ^{230}Th/U dating gives a minimum age for the surface stabilisation. The time lag varies regionally but where it has been estimated elsewhere it has been found to be $\leq$10 kyr (*Sharp et al.*, 2003; *Blisniuk and Sharp*, 2003; *Fletcher et al.*, 2010).

5.3 Segmented expression of the south-dipping fault

The south-dipping Suusamyr Fault reaches the surface in a set of fault scarps and folds that are highly segmented along strike and in places the active fault trace is situated several kilometres north of the rangefront. In this section I will describe the evidence for each segment, from west to east. The south-vergent fault is discussed separately in a later section (Section 5.4).

5.3.1 The far western part of the Suusamyr Basin

In the western part of the Suusamyr Basin, oppositely-dipping faults reach the surface along the northern and southern sides of the valley (Figure 5.5). On the southern side of the valley the fault has formed the discontinuous line of scarps that ruptured in the 1992 earthquake and was discussed in detail in Chapter 4. The trend of the scarps takes them progressively down the Suusamyr Range hillside as they get further east, and that trend line (i.e. the fault) eventually coincides with a fluvial riser from the Suusamyr

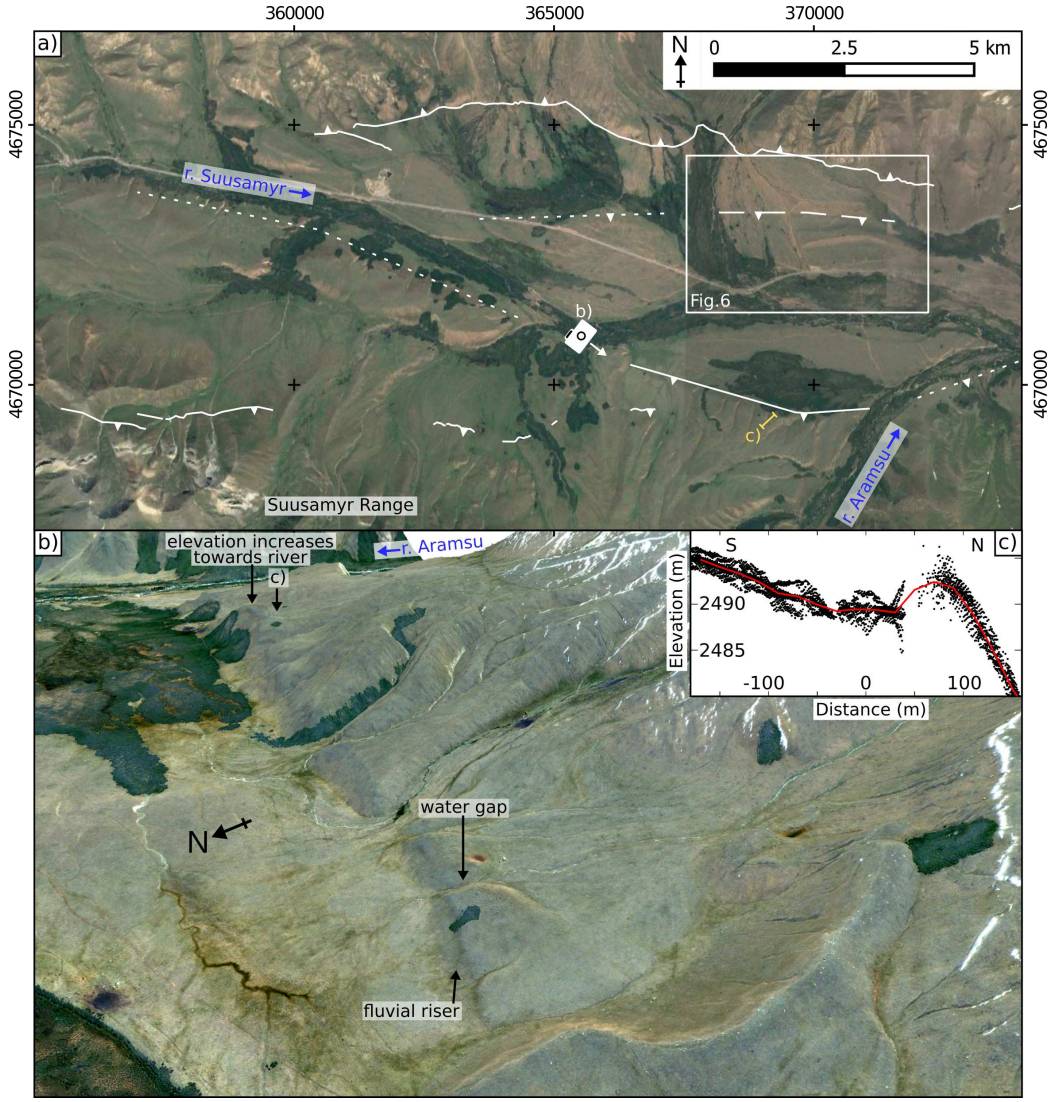


Figure 5.5: a) Fault map of the western part of the Suusamyr Basin. Image from Landsat/Copernicus and copyright Google. Location shown in Figure 5.3. b) 3D perspective view of the fault segment that is coincident with a riser on the southern side of the Suusamyr River. 3x vertical exaggeration. See camera icon in a) for location. c) Topographic profile through the SPOT pointcloud showing the increase in elevation towards the Suusamyr River. Red line shows a smoothed mean. Location marked in yellow on panel a).

River (Figure 5.5a and d). Fluvial landforms partially obscure the tectonic signal here and there is no sign of fresh ruptures along the riser, but the Pléiades DEM shows that parts of the tread above the fluvial riser tilt to the south — i.e. increase in elevation towards the Suusamyr River (Figure 5.5c). An alluvial fan is also funnelled through a water gap between two raised areas behind the riser (Figure 5.5b). These observations suggest that the fault does continue into the section coinciding with the riser. East of

the Aramsu River there are no more clear scarps or folds south of the Suusamyr River, but any fault scarp could have been eroded by the river and that section is therefore shown as dotted in my fault map (Figure 5.5).

In the valley floor north of the Suusamyr Range the tectonic component of topography is again obscured by fluvial processes, but there are signs that there may be a blind fault strand running sub-parallel to the Suusamyr Range rangefront scarps (Figures 5.5a and 5.6). *Korjenkov et al.* (1999) interpreted the area east of the Korumdy River (Figure 5.6) as a wind gap caused by a fault. The Korumdy River should not be confused with the Cong-Korumdy River or Chet-Korumdy Ridge, see Figure 5.3. *Korjenkov et al.* (1999)'s interpretation was based on the fact that a minor stream curves eastwards forming a right angle, rather than following a straighter route that a stream had previously taken and which is now a wind gap (Figure 5.5). However, although changes in river direction can be caused by faulting (e.g. *Keller et al.*, 1998; *Burbank et al.*, 1999; *Benedetti et al.*, 2000), they can also have non-tectonic causes, particularly for a smoothly curved river on an alluvial fan such as this one. Topographic profiles through the Pléiades pointcloud do not show tectonic scarps or clear folding (Figure 5.6). The surface that is elevated highest above the active drainage in this area is a terrace fragment that is too narrow in the north-south (fault-perpendicular) direction to show tectonic deformation clearly (Figure 5.6f). The surfaces that are more extensive, for example within the wind gap, do not show warping in topographic profiles (Figure 5.6e).

A snow-covered Pléiades image in the GoogleEarth archive does however show a scarp (Figure 5.6c). The scarp is located just above the top of the wind gap and is 750–950 m long. I interpret the scarp as tectonic because at least one small riser seems to cross it. Shadowing in the Pléiades image shows that the scarp is north-facing. I was not able to visit this location in the field but given that the scarp is not visible in the topographic profiles, the scarp height is <2 m. A fluvial scarp that is 4 m high is clearly visible in the same profile (Figure 5.6e).

The existence of the scarp shows that there is a fault here on the northern side of the valley floor. Due to the configuration of terrace fragments, the pattern of tectonic uplift and subsidence is not clear, and it is unknown whether there is a fold south of the scarp or this is a fault section without an associated fold.

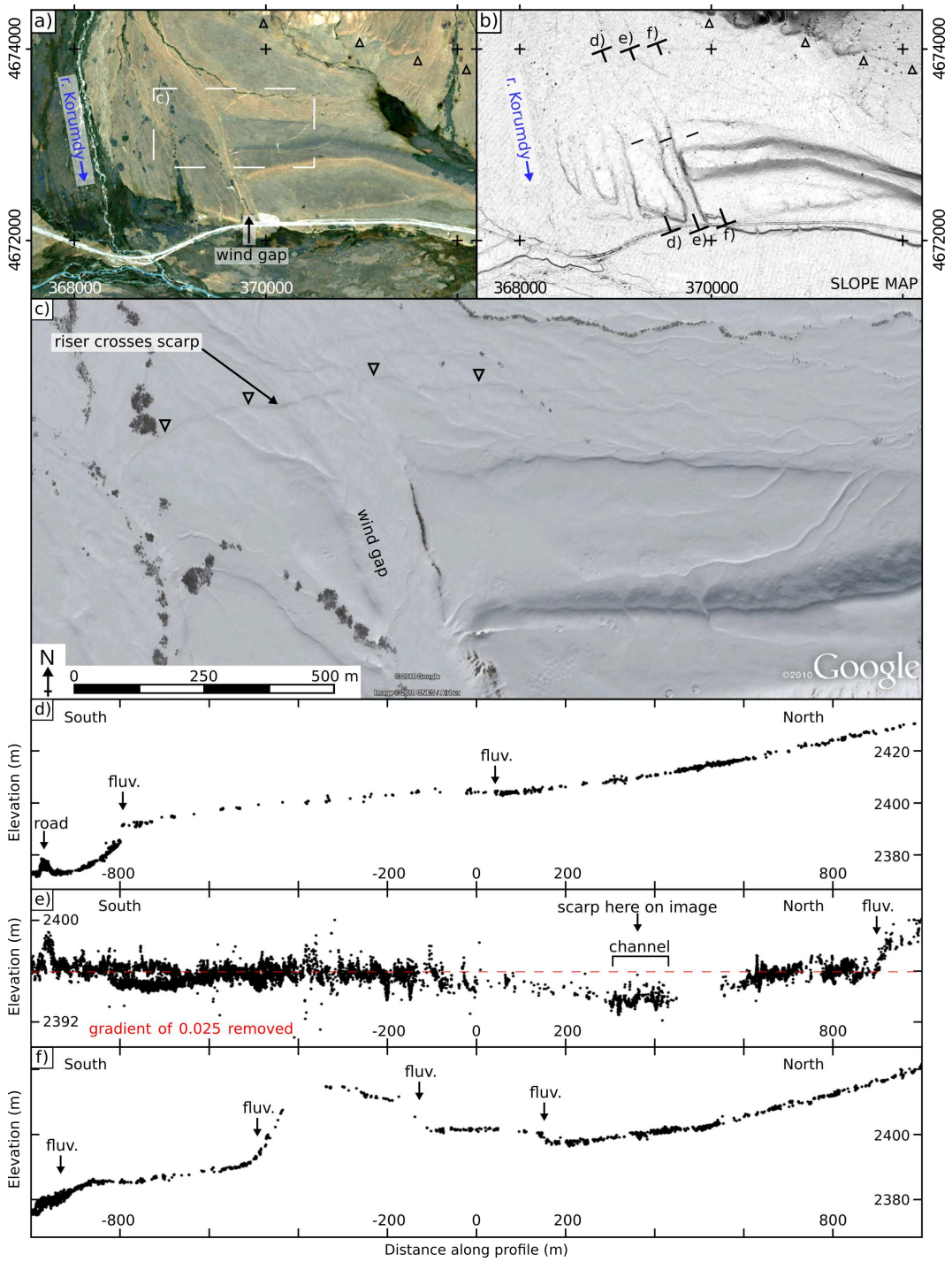


Figure 5.6: a) Pléiades image of the fault strand at the Korumdy River. b) Slope map of the Pléiades DEM for the same area. c) Close-up snow-covered Pléiades image of the top of the wind gap and the small scarp above it. Illumination is from the south. Image dated 9th November 2016 and copyright Google/CNES/Airbus. d)–f) Topographic profiles through my Pléiades pointcloud in the locations shown. Azimuth 339, swath width 40 m. Fluv. = fluvial risers that are visible in imagery. Profile e) has had a gradient of 0.025 removed so that the deviations from a linear slope can be seen, the dashed red line is a guide line showing that there is no measurable displacement across the scarp.

5.3.2 Turabulak

Clear signs of tectonic influence on the topography emerge in the Turabulak area (Figures 5.3 and 5.7). Here we see two raised sections of alluvial fan that are elongated in the east–west direction. Topographic profiles across these features show apparent folding (Figure 5.8). The western part is highly fragmented by several streams passing across it, the visible fragments cover a length of 1200 m. The second part, ∼250 m up-slope from the first and immediately to its east, is more prominent and is clearly visible for 1550–1800 m in length. A scarp runs parallel to the western fold fragments, 400 m to the north of them (Figure 5.7) and was described in Chapter 4, where I showed that it has broken in at least one earthquake, most likely before ∼4.4-4.9 ka. No scarp is visible north of the eastern fold segment, but a 1 km-long straight line of dense vegetation does extend from its northwestern end (marked by three black pointers in Figure 5.7b).

Topographic profiles perpendicular to the line of vegetation reveal up to 6 m deviation from the logarithmic curve of an undeformed fan (Figures 5.8f,g,h). The area is vegetated by low bushes rather than trees, so the 6 m deviation can not be explained solely by the presence of vegetation and I interpret this feature as the continuation of the fault or fold. Given that after a width of approximately 300 m the profile returns to the logarithmic curve, the feature appears to be a fold above a blind fault rather than a scarp, but I note that the topographic cross-section varies along its length (Figures 5.8f,g,h) and may have been modified by non-tectonic processes. The fold ceases to be visible at a riser onto the adjacent fan to its east (Figure 5.8i). That fan is more vegetated, has a larger catchment area and truncates the folded fan and is therefore younger. It is therefore possible that the ending of the visible signs of faulting here does not reflect the underlying fault geometry or slip rate but is due to its surface expression being suppressed on the eastern fan.

As described above, faulting is expressed as three features in the Turabulak area, each 1–1.8 km long: the fragmented western part, the more prominent central part, and the vegetated eastern part. The fact that the small scarp that we trenched only stretches

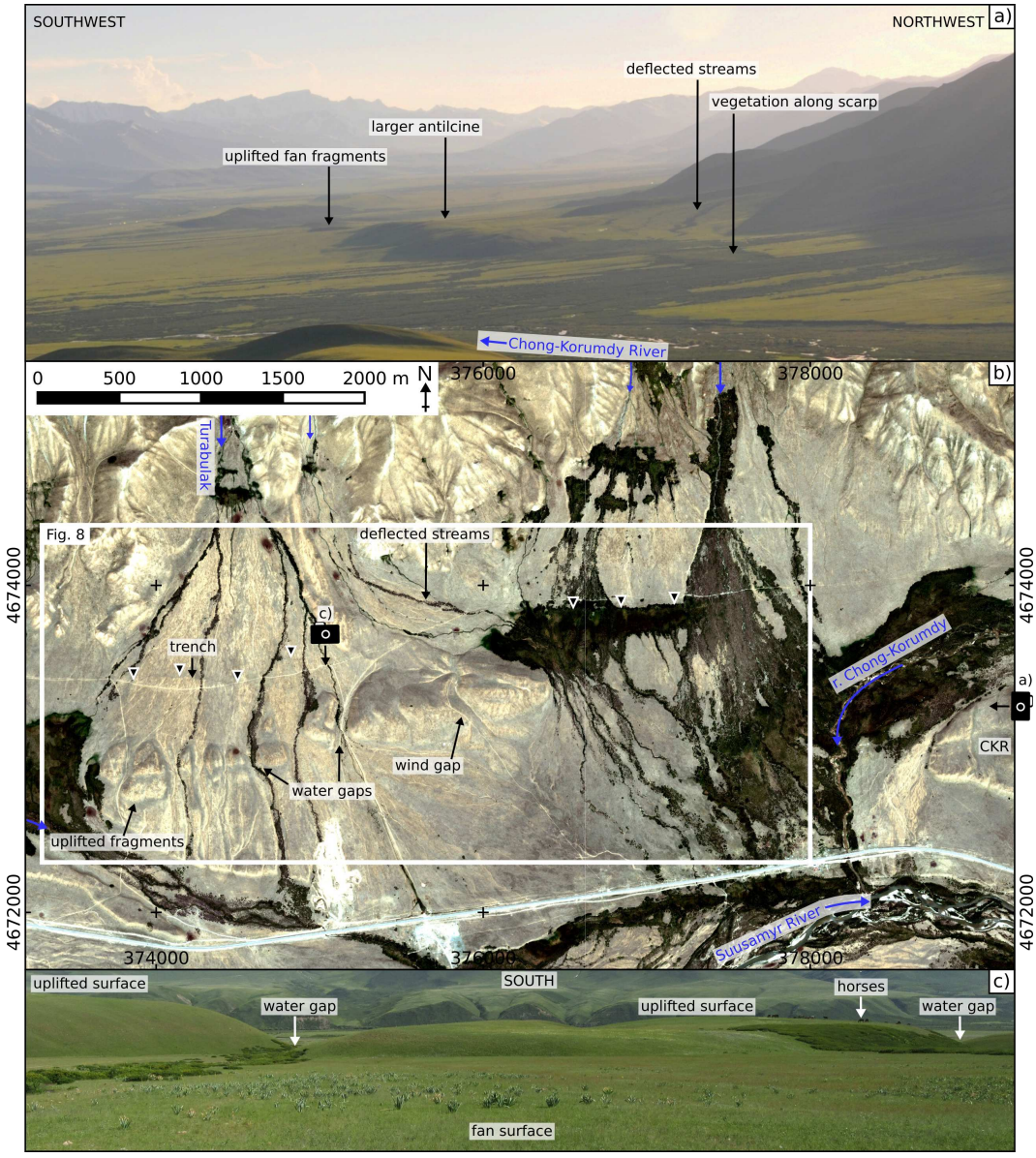


Figure 5.7: The Turabulak area. a) Field photograph looking west from the CKR, as shown on b). b) True-colour Pléiades imagery. c) Field photograph looking south towards the fold fragments. Location shown on panel b).

across the western part and the beginning of the central part indicates that earthquakes do not always rupture as far as the surface across the three parts simultaneously but it is not clear from the information we have whether the sub-surface fault is actually separated into three segments and the three features visible at the surface are three separate folds or whether they are remnants of a single structure.

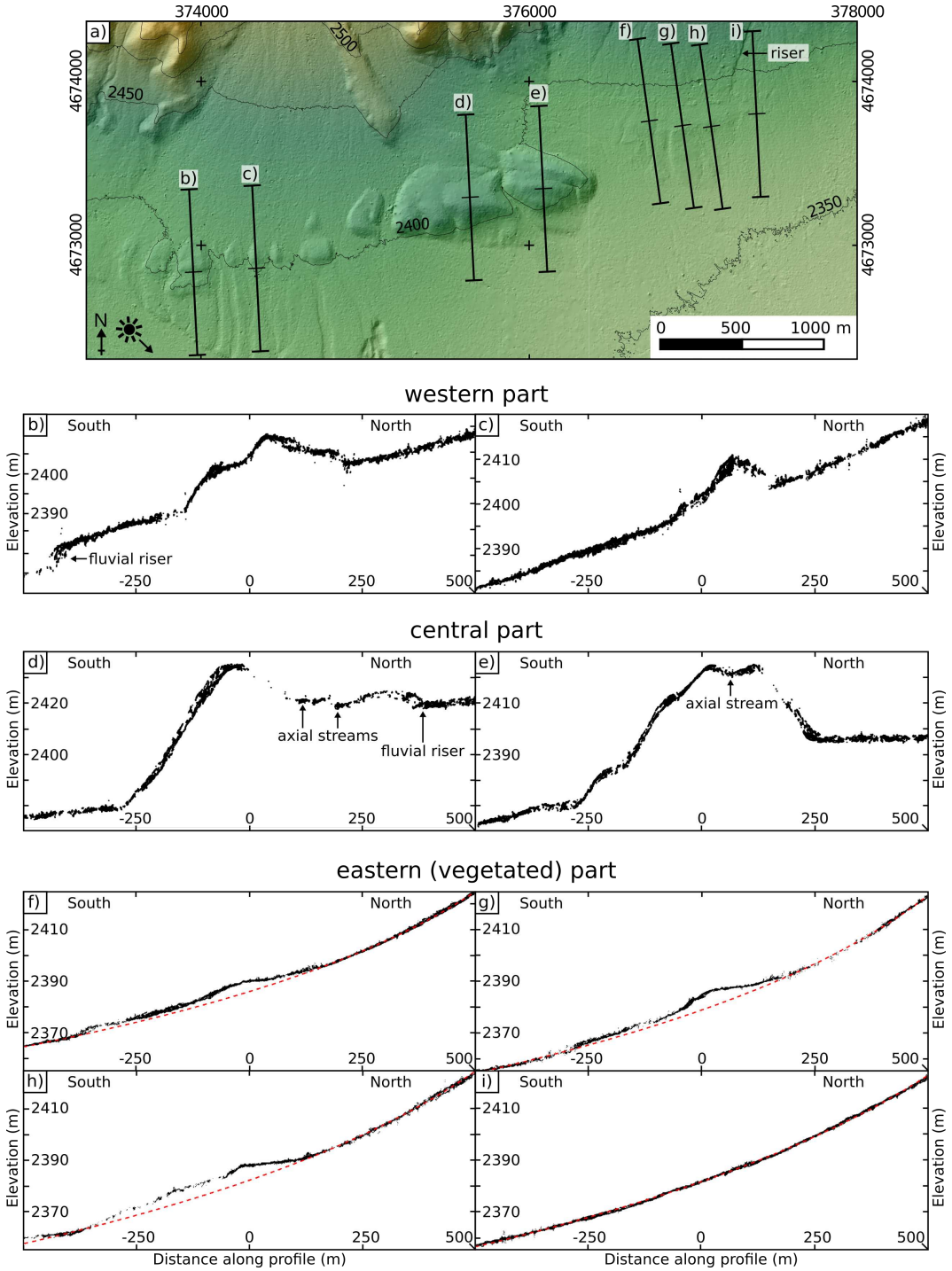


Figure 5.8: Topographic profiles through the Pléiades pointcloud in the Turabulak area. Location shown in Figure 5.7b. a) Hillshaded Pléiades DEM. b)–i) Profiles in the locations indicated. Swath width 40 m. Red dashed lines in f)–i) show logarithmic fits to the undisturbed fans.

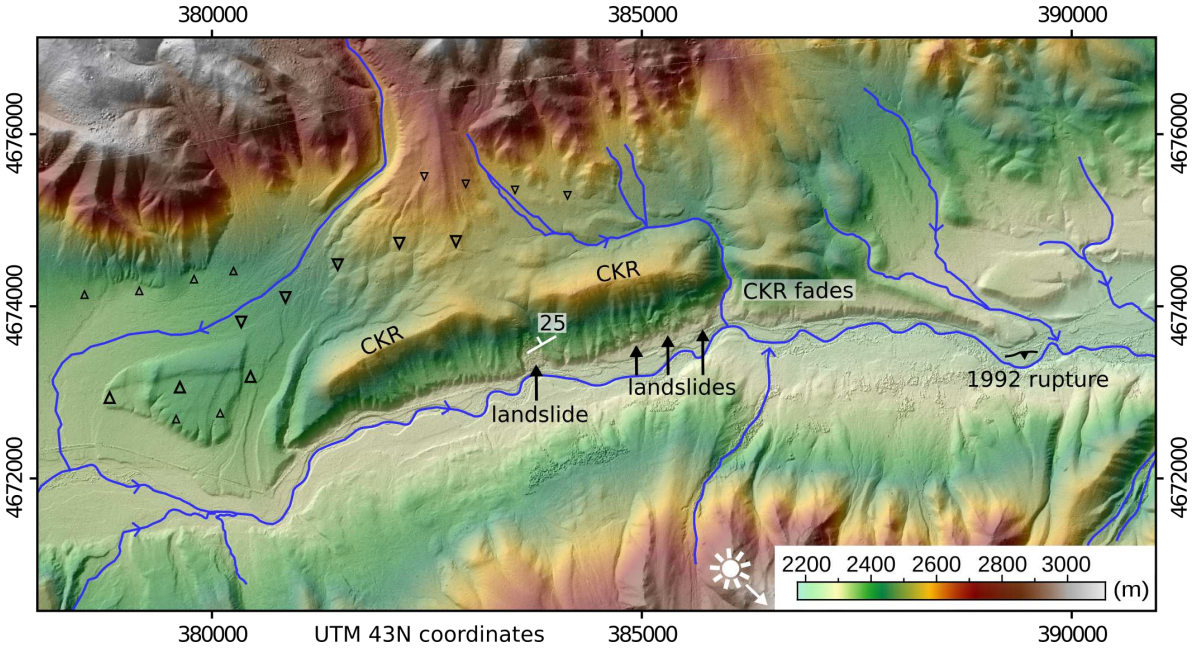


Figure 5.9: Hillshaded Pléiades and SPOT DEMs showing the Chet-Korumdy Ridge (CKR) part of the Suusamyr valley. Open triangles mark scarps.

5.3.3 The Chet Korumdy Ridge

The first expression of the CKR and its associated scarps in the landscape is 1200 m to the east of the eastern end of the vegetated Turabulak fold. As described in Chapter 4, the CKR is part of a growing anticline whose core has been eroded by the Suusamyr River and which has a scarp running alongside it to the north. Much of its southern slope is made up of landslides, demonstrating that the erosion by the river is ongoing (Figure 5.9). The CKR is clear and prominent for most of its length but loses definition towards the east; the ridge tapers out in its eastern three kilometres and there are no prominent scarps alongside it.

5.3.4 The Aramsu East section

East of the end of the CKR and the short M41 highway rupture from 1992, the Aramsu Range begins to taper away and the Suusamyr Basin widens (Figure 5.2, from 73.67°E eastwards). Here the fault splits into separate strands: one strand, which I will refer to as the Aramsu East section, trends to the southeast, and another strand, which I will

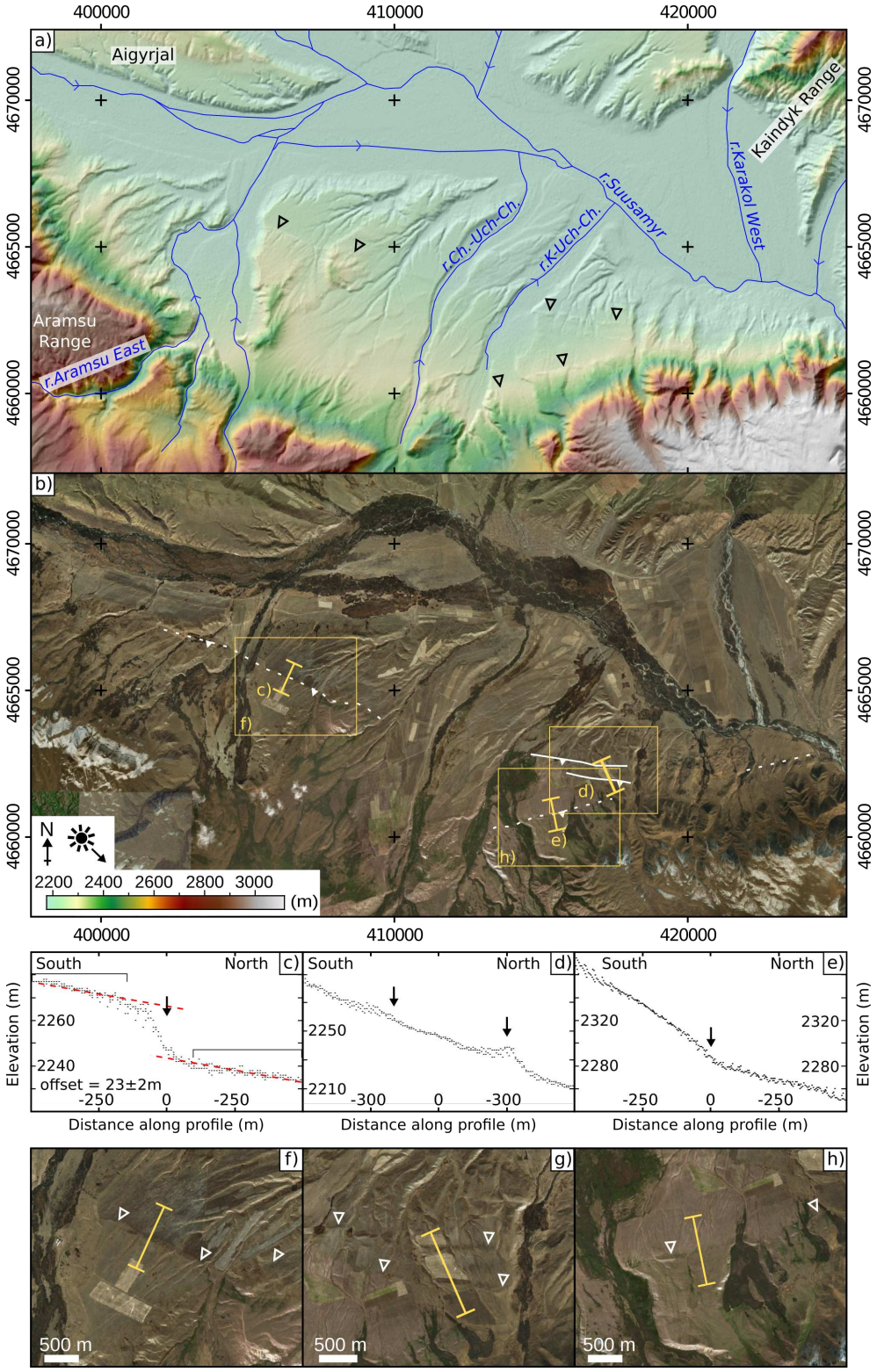


Figure 5.10: a) Hillshaded AW3d30 DEM showing the area of the Aramsu East section of faulting. Ch.-Uch-Ch. = Chong-Uch-Chymchyk stream, K.-Uch-Ch. = Kichi-Uch-Chymchyk stream b) Bing Maps image of the same area (copyright Microsoft), with the scarps marked in white. c)–e) Topographic profiles through the AW3D30 DEM in the locations shown in b). Arrows show where the profile crosses mapped lineaments. Note the different scales for different panels. f)–h) Close-ups of the imagery at the profile locations.

refer to as the Aigyrjal section, cuts across the centre of the valley. We have not found any fault scarps or folds along the 10 km of the northeast edge of the Aramsu Range that is closest to the M41 site. However, there are several lineaments within an area southeast of the Aramsu Range where the Aramsu East River and others have incised into the broad gently sloping basin floor (Figure 5.10). The longest lineament that may be a scarp is 8 km long and straddles the Aramsu East River with a strike of 110°. On the eastern side of the Aramsu East River it is a clearly visible, north-facing escarpment that cuts across the alluvial surface and has a height of ∼23 m (Figure 5.10c and f). Further to the east it runs along the bottom of a higher, more incised area before disappearing. No escarpment is visible within the Aramsu East river valley or west of the river, but there is a drainage channel west of the river that is aligned with the escarpment. It is not clear whether the escarpment is tectonic or fluvial, but its absence on the younger surface in the Aramsu East valley supports the fluvial interpretation, and shows that if it is a fault scarp the fault has not been active since that surface stabilised.

A gap of ∼5 km separates that western escarpment from two other lineaments. They are along strike to the southeast from the 8 km escarpment and located east of the Kichi-Uch-Chymchyk stream (Figure 5.10d and g). The lineaments are sub-parallel to each other and overlapping, striking at 100°, the distance that they cover is 3.5 km. The topographic profile in Figure 5.10d shows that the lineaments are north-facing scarps. Finally, ∼1.2 km to the south of those scarps there is an unusually sharp, linear section of rangefront 4.2 km in length (Figure 5.10e and h). Topographic profiles show a change in slope across this feature rather than a clear fault or fold, and in optical imagery there does seem to be a change in surface roughness across the lineament. These observations suggest that this is a fluvial or lithological boundary rather than a tectonic feature. I therefore classify this as a dotted (highly uncertain) fault section. The rangefront to either side is less sharply defined and does not show active faulting.

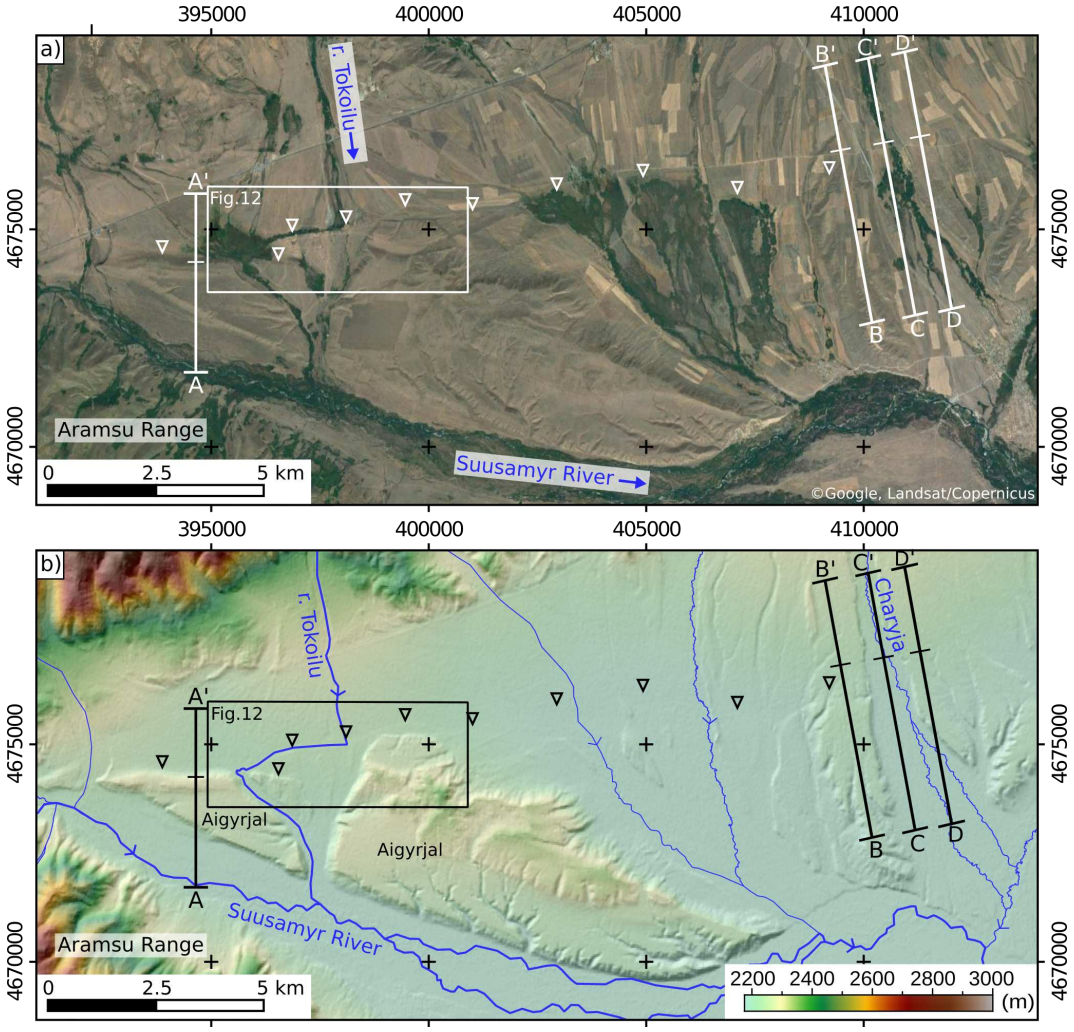


Figure 5.11: a) GoogleEarth image of the Aigyrjal Terraces area and the basin to its east. Open triangles mark the fault. White box shows the area shown in Figure 5.12a. b) Hillshaded AW3D30 DEM of the same area (illumination from 315°).

5.3.5 The Aigyrjal section

The Aigyrjal section is present at the same longitude as the Aramsu East section but runs through the centre of the basin. It has an overall strike of ~085°, making it aligned with the fault in the western part of the basin (Figure 5.4). The segment begins at ~73.68°E (391 000E in UTM43N coordinates) where it runs along the northern side of the Aigyrjal terraces (Figures 5.4 and 5.11).

There is a prominent wind gap through the Aigyrjal terraces where the fault has deflected the Tokoilu River into a right-angle bend (Figures 5.12 and 5.13a). The scarp

in this segment is not a sharp step but a smooth fold tens of metres wide, suggesting that the fault has reached close to the surface but not ruptured it or that the fault scarp has diffused away. On the lowest abandoned terrace level the scarp is ∼2.5–4.5 m in height (Figure 5.12). *Chediya et al.* (1997) and *Korjenkov et al.* (1999) also identified the wind gap and *Korjenkov et al.* (1999) excavated two trenches across the scarp (Figure 5.12). They did not find any ruptures, stratigraphic offsets or extensional fissures, in agreement with the conclusion that the fault is blind here. In their western trench they did find evidence of northwards tilting of beds - the pebble imbrication indicated flow to the south but the beds now dip to the north (*Korjenkov et al.*, 1999). In their eastern trench they found a fine-grained silt to mud unit that thinned out southward which they interpreted as the result of ponding against the scarp. *Korjenkov et al.* (1999) collected samples for infrared stimulated luminescence (IRSL) dating from the ponded sediment and the fan material below it which gave ages of 2100±370 yrs and 3100±710 yrs respectively but which showed a large scatter of equivalent dose values (over-dispersion, (*Galbraith et al.*, 1999)), suggesting non-uniform bleaching and indicating that these ages may be over-estimates. *Korjenkov et al.* (1999) took a sediment sample from the active stream and dated it with the same methods, giving a luminescence age of 560–790 yrs. They cited this as evidence that the residual age of freshly deposited sediments is approximately 500 yrs and therefore estimated that the folding that caused ponding took place approximately 1600–2600 BP.

As well as the low scarp there are two other, much taller, escarpments along the edge of the Aigyrjal terraces east of the wind gap (Figure 5.12f). The escarpments do not continue onto the lower surfaces along-strike from them, suggesting that they are not tectonic scarps. The lower-elevation surface has a sharp riser base and a more diffuse upper corner, suggesting that the bottoms of the escarpment has been shaped more recently than the tops, which would also favour a fluvial rather than tectonic interpretation for their formation. We visited the escarpments in the field and did not see any signs of fresh rupture or sub-scarps within them (Figure 5.13b). Therefore,

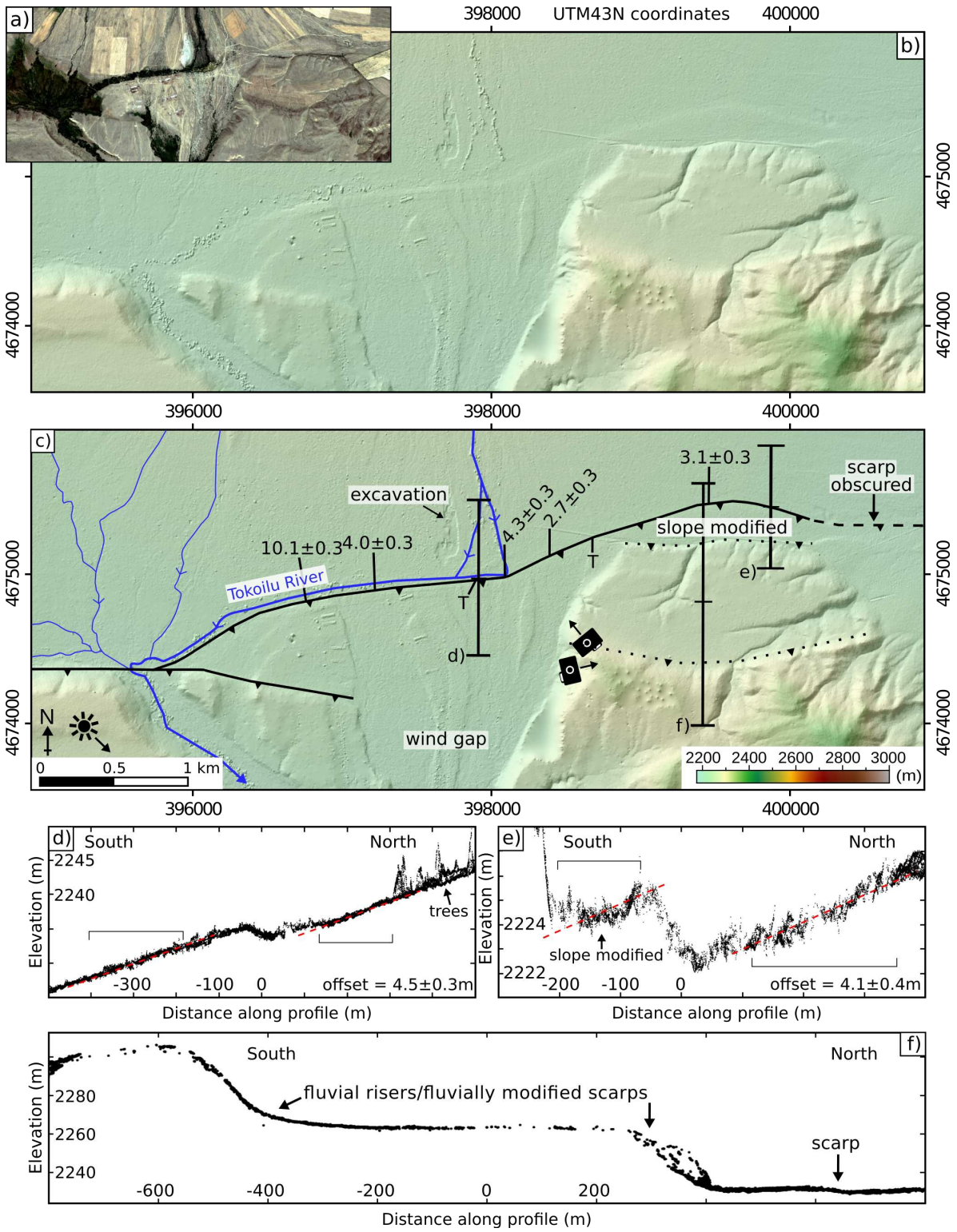


Figure 5.12: a) Pléiades image of the Aigyrjal wind gap. b) Hillshaded Pléiades DEM of the same area. c) Interpretation of the same area showing the deflected Tokoilu river and the fault scarps. T's mark *Korjenkov et al.* (1999)'s trench sites. d), e) & f) Topographic (Pléiades) profiles across the scarp, locations shown in panel c). Camera icons show the viewpoints of Figure 5.13.

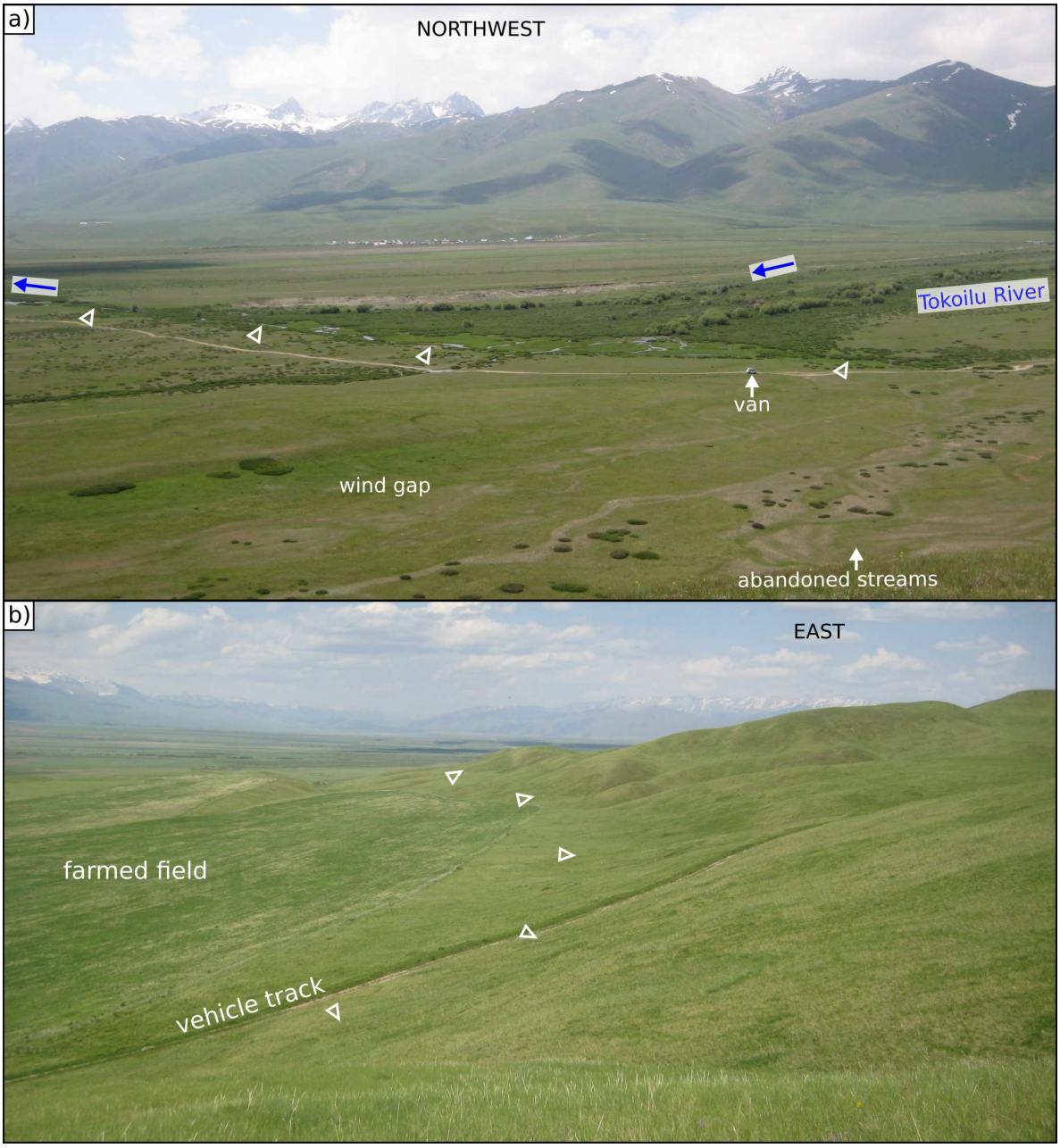


Figure 5.13: Photographs of the Aigyrjal area. Locations shown in Figure 5.12. a) The deflected the Aigyrgal River and its windgap. Scarp marked by open triangles. b) A more diffuse, taller escarpment to the south of the active scarp. The base of the escarpment is shown by open triangles.

although there could have been a tectonic contribution to forming these escarpments, they do not appear to be active currently, and the 2.5–4.5 m high scarp below them seems to be the only active fault strand at this location.

The scarp is visible in the DEM east of the wind gap for 1800 m before being

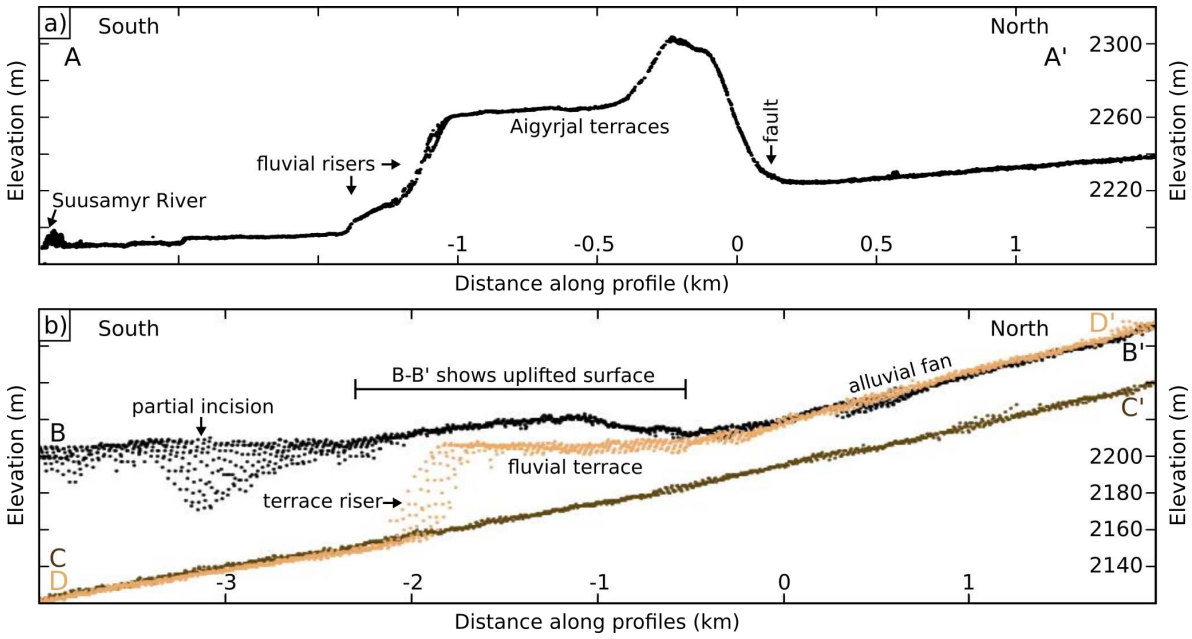


Figure 5.14: a) Topographic profile (Pléiades pointcloud) across part of the Aigyrjal terraces. b) Topographic profiles (AW3D30 DEM) across the eastern end of the Aigyrjal section of the fault. See Figure 5.11 for locations.

obscured by scarp-parallel drainage. The land east of the wind gap is also farmed and the topographic profiles there indicate that the surface slope has been modified, further obscuring any scarp (e.g. Figure 5.12c and e). East of the Aigyrjal terraces there is no topographic scarp but there is a linear change in land cover from farmed alluvial fans to marshy vegetation (Figure 5.11a). The change is along strike of and parallel to the fault so I have mapped it as a continuation of the fault. That interpretation is supported by a topographic profile along the terrace to its east at longitude 73.90°E (410 000E in UTM43N coordinates)(B–B' on Figures 5.11 and 5.14). The profile shows an elevated bump at the transition from sloping fan to sub-horizontal terrace. It has a wavelength of ∼2 km and a height of up to 16 m above the projection of the sub-horizontal terrace. There is no such bump on on profile D–D', which was taken across the same fan and terrace 1.9 km further east (Figures 5.11 and 5.14). Profile C–C' on the surface occupied by the active stream between B–B' and D–D' shows a smooth, undeformed curve (Figure 5.13). I interpret the profiles as showing that a blind fault caused fold growth on the B–B' terrace but that the fault ended before the longitude

of D–D'. The surface that C–C' follows is occupied by the Charyja stream, which is smaller and has a smaller catchment area than the Tokoilu River, so should be expected to erode scarps more slowly than the Tokoilu River. The lack of evidence for faulting in the valley of the Charyja suggests that the section of fault beneath has had a lower recent slip rate than the part of the fault at the Tokoilu wind gap.

5.3.6 The Ak-Suu section

The easternmost section of the Suusamyr Fault within the basin is the Ak-Suu section (Figures 5.3, 5.15 and 5.16). It is situated at the bottom of the Kyrgyz Range and consists of four segments. Two are uphill-facing scarps approximately 3.5 km and 1.5 km in length located between the Charyja and Ak-Suu Rivers (Figure 5.15). A third, ~10 km-long scarp extends from 2.5 km west of the Ak-Suu River to 1.5 km east of the Kara-Sai River (Figure 5.15), and the fourth, easternmost segment is slightly oblique to the others, with a strike of 115°. The easternmost segment is followed by the Kara-Sai River for its upper 2.8 km, then continues for a further 5.5 km. The final 1 km of this 8.3 km-long segment is in a fan, where a linear, swampy vegetated zone is visible but there is no topographic scarp. Except for the final section on the fan, the scarp of the 8.3 km-long eastern segment has a greater height than the western segments but is more diffuse.

We visited the 10 km-long segment at a site immediately east of the Ter-Suu River (Figure 5.16). The scarp cross-cuts local ridges and valleys and has a height of tens of metres across the inactive surfaces (height varies between different surfaces). There is no fresh scarp and the scarp is not visible in or immediately adjacent to the active stream beds, suggesting that this segment has not ruptured within the recent past. We dug two pits at this site, one in the displaced hanging wall surface (Figure 5.16c) and one at the fault in sediments that have ponded against the scarp (Figure 5.16d). The top 60–70 cm of material in the hanging wal pit consisted of soil containing occasional angular pebbles. The soil overlay poorly-sorted gravel of mafic, metasedimentary and granitic

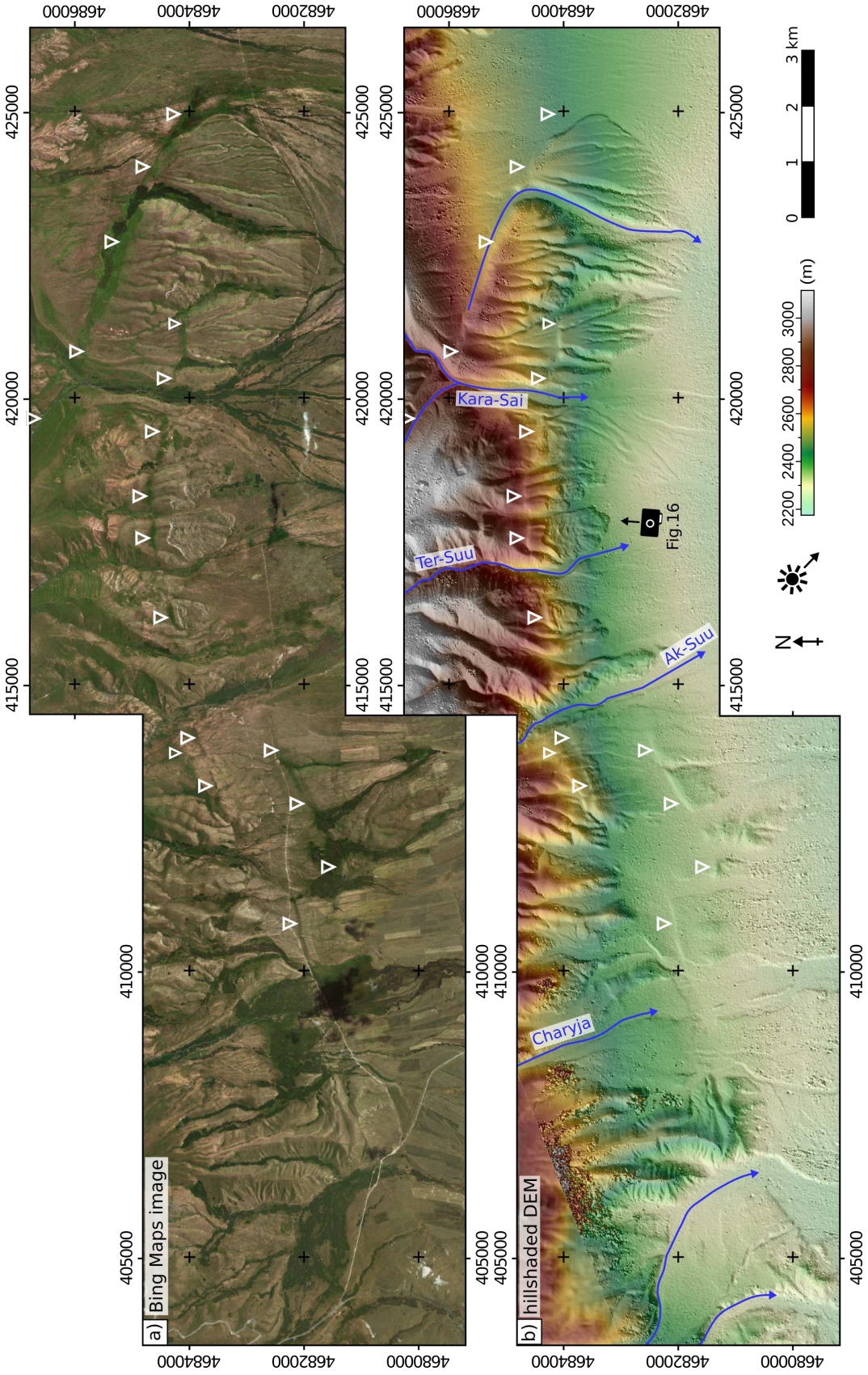


Figure 5.15: a) Bing Maps image of the Ak-Suu fault segment (date listed as May 2010–August 2014), copyright Microsoft and DigitalGlobe. b) Hillshaded SPOT DEM of the same area. Scarps are marked by open triangles.

lithologies, with clasts ranging from millimetres to ∼20 of centimetres in diameter in a matrix of sand and some clay/mud. We did not find any sand lenses that would have been suitable for luminescence dating or and radiocarbon material, therefore were not able to estimate the age of the surface or the fault slip rate. The pit in the ponded sediments exposed ∼25 cm of modern soil and roots above a ∼10 cm-thick black soil layer and a pale brown clay that contained occasional sand grains and pebbles.

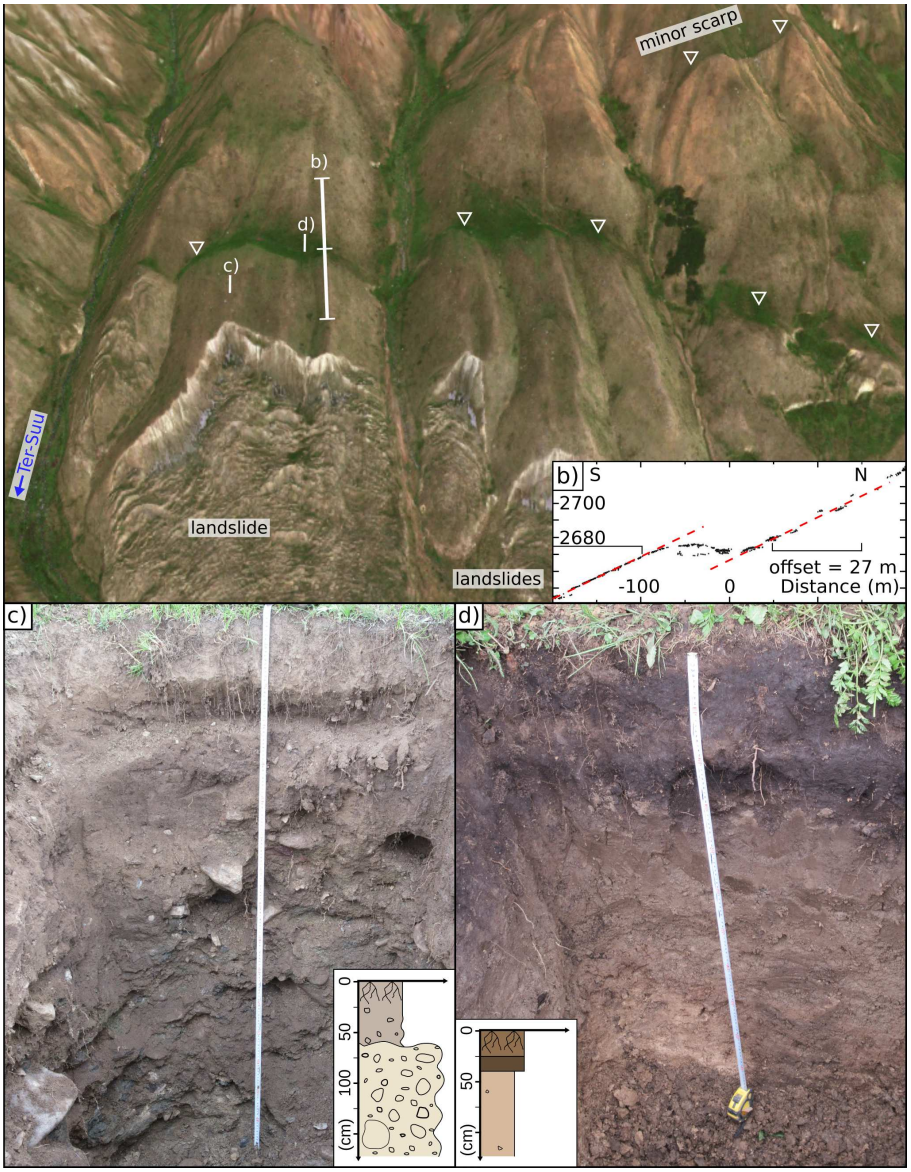


Figure 5.16: a) Perspective view of the Ak-Suu scarp, which is marked by white triangles, at the site where we visited it. Bing Maps image (copyright Microsoft and DigitalGlobe) overlain on the SPOT DEM, 2x vertical exaggeration. b) Topographic profile along a ridge that crosses the scarp. c) Pit excavated on the on the displaced surface which contained soil covering gravel conglomerate. d) Pit excavated in ponded sediments at the scarp, which contained dark soil capped by brown clay with some organic material, pebbles and sand grains.

5.4 The north-dipping fault (Talas-Boundary Fault)

The Talas-Boundary Fault is the Suusamyr Fault's counterpart on the northern side of the Suusamyr Basin (Figure 5.3). It is a reverse fault that dips to the north beneath the Kyrgyz Range and Talas Range. There have been no recorded large earthquakes on the

Talas-Boundary Fault but scarps along it show clear evidence of being active. There are three main sections of the fault that have scarps: the first is a clear, continuous 14 km-long scarp in the western part of the basin (Figures 5.17 and 5.18), the second is a ∼2 km-long section north of the western end of the CKR (Figure 5.9), and the third is an 8 km-long section in the eastern part of the basin, north of the Aigyrjal terraces (Figure 5.19). Unlike the scarps and folds from the Suusamyr Fault, these sections are all along the rangefront, rather than within the valley floor, and are arranged as a single strand.

The 14 km western scarp section has the clearest, most continuous morphology. It runs east–west along the rangefront of the Talas Range (Figures 5.17 and 5.18), cross-cutting several alluvial fans and the drainage, causing streams to have knickpoints incising into the hanging wall. The height of the scarp varies along its length, it is typically ∼2–10 m across the alluvial fans and, based on a qualitative assessment, there appears to be some correlation between scarp height and surface age. The scarp's height and its variation between surfaces of different ages suggest that it is a compound scarp resulting from several earthquakes along the same fault. As the scarp is downhill-facing there are no sites along it that have caused sediment ponding and could be used for the kind of paleoseismic trenching that we carried out on the Suusamyr Fault (Chapter 4). We visited two sections of the scarp in the field at 42.213°N,73.394°E and 42.219°N,73.364°E and found that the surface is a boulder fan with boulders up to 1 m in diameter and was unsuitable for excavation given the tools and time available to us.

The 8 km section of scarp north of Aigyrjal also cross-cuts the local drainage and surface boundaries (Figure 5.19) and has a scarp height that varies along its length.

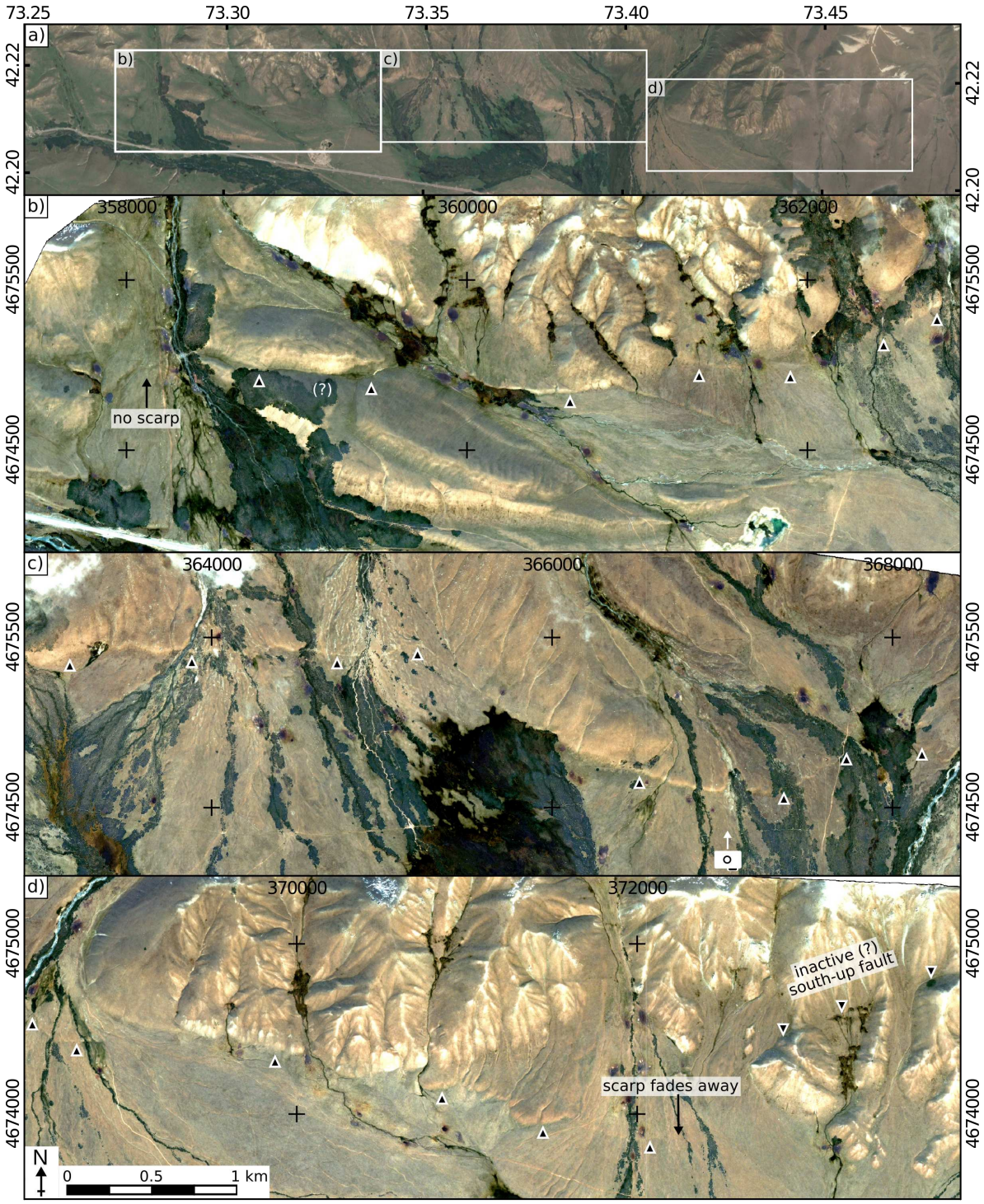


Figure 5.17: a) GoogleEarth image showing the relative positions of the panels below it. Location shown in Figure 5.3. b)-d) Pléiades imagery showing the south-facing scarp along the rangefront of the Talas Range. Camera shows the view point of Figure 5.18. Coordinates in UTM 43N.

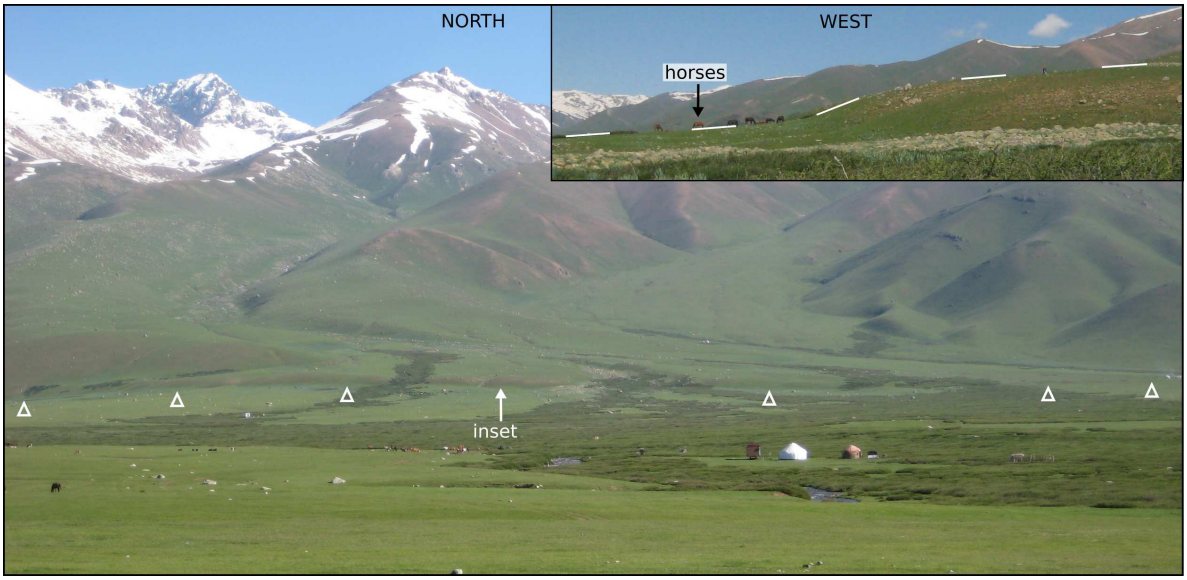


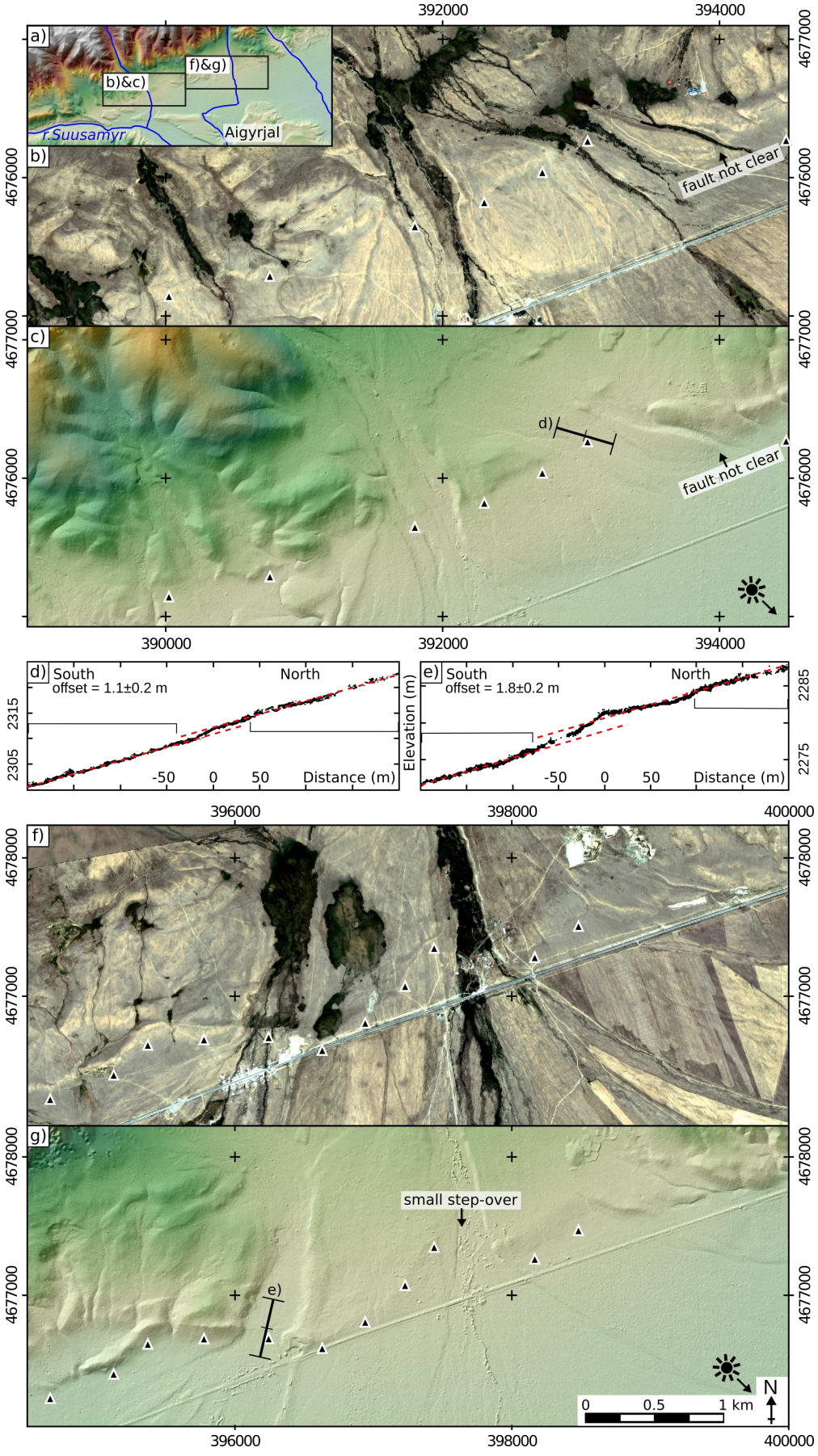
Figure 5.18: Field photographs of the south-facing scarp of the Talas-Boundary Fault. White triangles and dashed line mark the scarp. Location shown on Figure 5.17c.

5.5 The ends of the basin

The Suusamyr Valley is enclosed by mountains at its eastern and western ends. The two ends display different patterns of active faulting — the western end has numerous short scarps cross-cutting the mountains whereas in the eastern basin established faults run parallel to the mountain ranges but do not have fresh scarps.

At the western end of the basin the east–west trending Suusamyr and Talas-Boundary Faults are replaced by a zone of distributed faulting in which there are numerous scarps (Figure 5.21, *Omuraliev and Charimov* (1990)). The scarps are each ≤4 km in length and cross-cut the established landforms (Figure 5.20c). They predominantly trend NE–SW or NW–SE, oblique to the Suusamyr valley.

The scarps on the Andjar Range (between the Suusamyr and Otmyok East Rivers, Figure 5.20a) show little or no deflection across topography, showing that they have a steep dip. The NE–SW trending faults have a south-up sense of displacement, there is no strike-slip component of displacement visible in the satellite imagery but I note that the total displacements on the scarps are small (≤10 m) and therefore the strike-slip component could be difficult to recognise in the drainage channels that cross-cut the


a)
b)&c)
f)&g)
r.Suusamyr
Aigyrjal
b)
fault not clear
c)
d)
fault not clear
392000
394000
4677000
4676000
390000
d)
South
offset = 1.1±0.2 m
North
2315
2305
-50
0
50
Distance (m)
e)
South
offset = 1.8±0.2 m
North
Elevation (m)
2285
2275
396000
398000
400000
f)
4678000
g)
small step-over
e)
0
0.5
1 km
N

scarps, given the natural sinuosity of the channels and the diffusion of the displacement pattern with time. The scarps do not have any open fissures, free faces or other signs of having slipped during the 1992 earthquake and the timing of their slip relative to the faults within the basin is unknown.

The eastern end of the basin is bounded by the Kyrgyz Range to its north and by the Kindyk Range to its south and east (Figures 5.2 and 5.4). The Kindyk Range is a 30 km long, ∼5 km wide, linear, northeast trending mountain range that increases in elevation eastwards, reaching 3444 m. The geological map published by *Nikonorov et al.* (2000) shows a fault running along the northwest rangefront of the Kindyk Range. The southwestern part of the range has an asymmetrical cross-section (Figure 5.21c), with its drainage divide north of the range centre, which suggests that the Kindyk Fault has influenced the topography of the range by uplifting it asymmetrically from the northwest, but there are no scarps or deformed terraces along the Kindyk Fault, which suggests that it has not been active as recently as other faults in the basin. Although the Karakol West River runs parallel to most of the fault and could have eroded any scarps that formed in that section, the conclusion that such no such scarps have been formed is supported by the lack of scarps or terrace deformation along the westernmost section of the fault, which does not have any axial drainage along it (Figure 5.21). There is another fault mapped between the Kindyk and Jumgal Ranges, dipping to the south — the Joo-Jurek Fault (*Korjenkov et al.*, 1999; *Nikonorov et al.*, 2000). The Joo-Jurek Fault does offset geological units (*Nikonorov et al.*, 2000) but does not show signs of being active today: the Jumgal Range behind it would be expected to have asymmetrical topography if there were an active fault dipping below it from one side but instead it has symmetrical topography in cross-section (Figure 5.21c) and there are

Figure 5.19 *(preceding page)*: a) AW3D30 DEM showing the location of the lower panels. b) Pléiades imagery showing the south-facing scarp in the area shown on panel a) along the rangefront of the Kyrgyz Range. c) Pléiades DEM of the same area. d) & e) Topographic profiles across the scarp at two points where it crosses low, young surfaces close to streams. Swath width 20 m through the Pléiades pointcloud. f) & g) As b) and c) for the area shown in panel a).

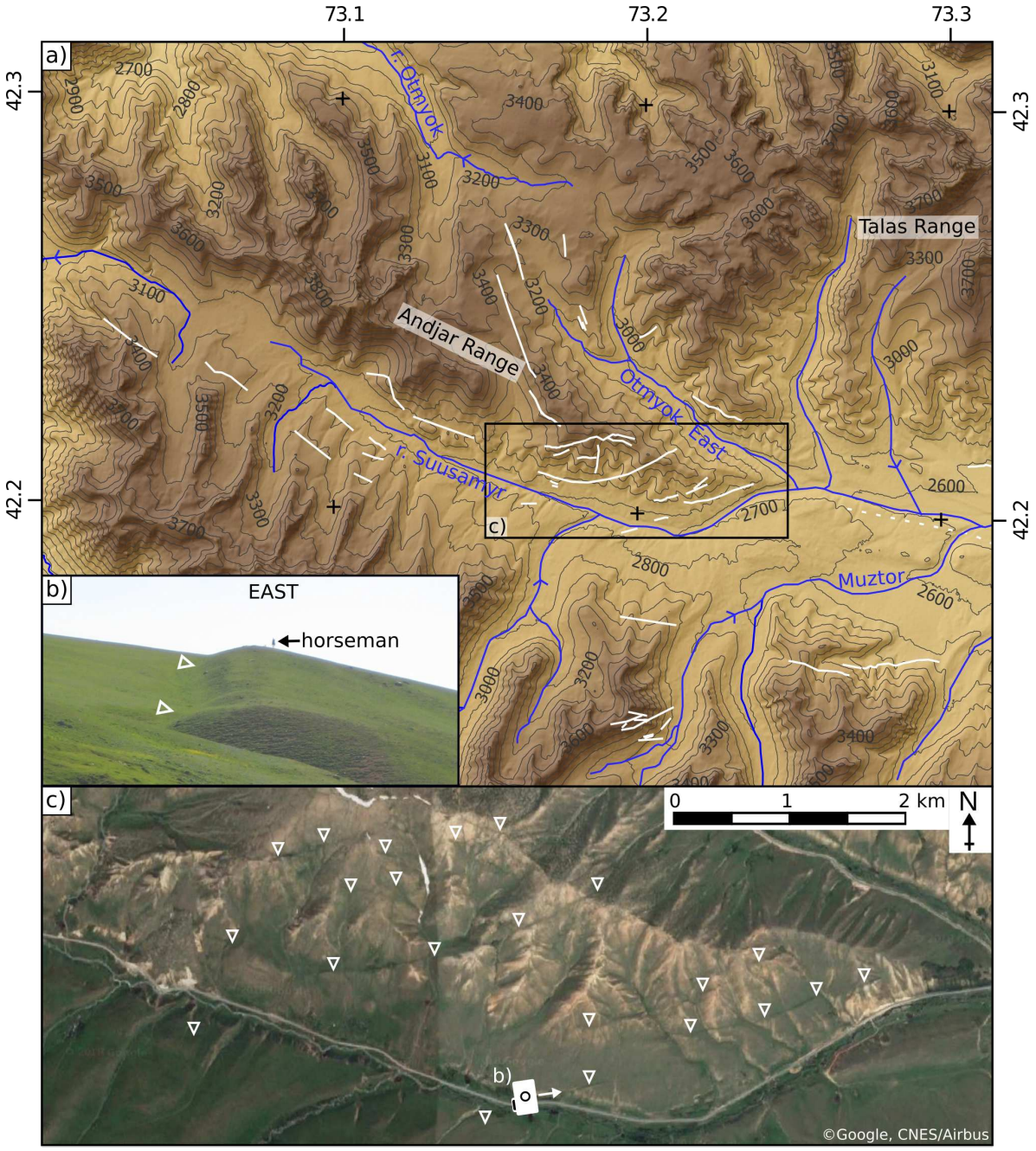


Figure 5.20: a) DEM of the western end of the Suusamyr Basin, with fault scarps marked in white. b) Field photograph of one of the scarps. Man mounted on a horse for scale. c) GoogleEarth satellite image showing some of the more prominent scarps. Scarps are marked by open triangles (not every scarp can be marked by a triangle at this scale, refer to panel a) for more accurate mapping).

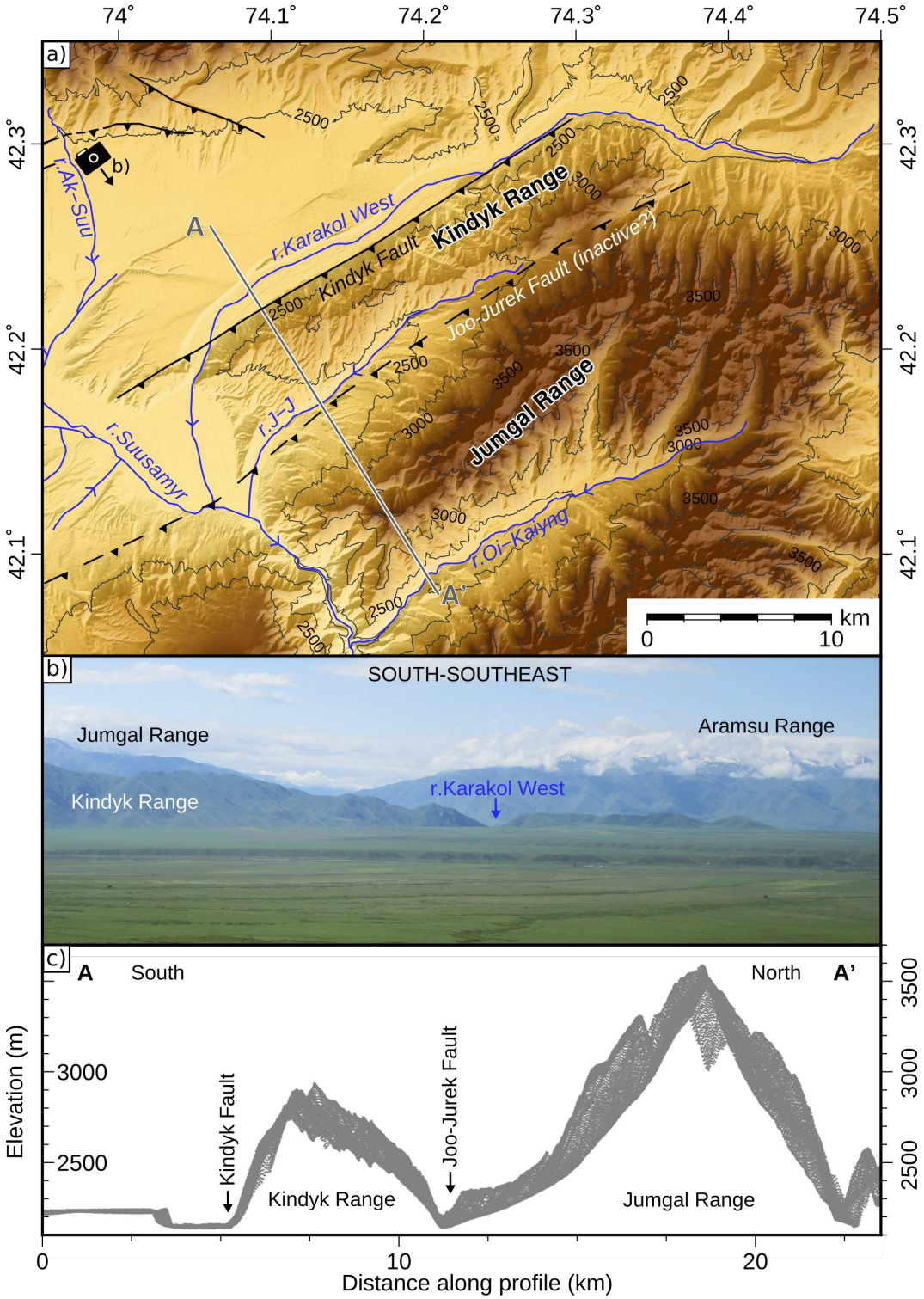


Figure 5.21: The eastern end of the Suusamyr Basin, with active faults marked as black, ticked lines. r.J-J = River Joo-Jurek. b) Field photograph looking south towards the ranges that form the south eastern edge of the Suusamyr Basin. c) Topographic profile through the AW3D30 DEM. Swath width 2 km. Note the asymmetry in the Kindyk Range.

no obvious scarps along the fault. As well as the established faults at the eastern end of the basin not having scarps, unlike at the western end of the basin I have not found any fault scarps within the adjacent ranges.

5.6 Slip rates and shortening rates

To understand the regional significance of the Suusamyr Basin and to take full advantage of the fault maps and measurements it is necessary to have an estimate of the faults' slip rates. The Suusamyr Basin has quite limited opportunities for making slip rate measurements. As I have described in Section 5.4, we did not find any units that would have been suitable for dating at the sites that we visited along the Talas-Boundary Fault. We were unable to obtain any surface ages for the Ak-Suu segment (Section 5.3.6) and potential sites at Turabulak (Section 5.3.2) were rejected because of excessive uncertainties in establishing the original surface morphology. Nonetheless, I have been able to place some constraints on slip and shortening rates using Quaternary dating of offset surfaces and palaeoseismology in the Chet-Korumdy section.

5.6.1 Dating offset Quaternary surfaces

To collect samples for Quaternary dating we dug a pit on one of the terraces at the western end of the CKR that has been abandoned by the Chong-Korumdy River (T7 on Figure 5.22) at 42.19987°N 73.54617°E. The top layer in the pit consisted of fine sandy soil which was mid-brown and showed slight fining upwards but was otherwise homogeneous. At a variable depth of ∼40–55 cm there was a sharp transition to a white, well-developed pedogenic carbonate layer (Figure 5.22b). The transition also approximately corresponded to the contact with a poorly sorted conglomerate. The conglomerate unit was matrix-supported, with sub-rounded clasts that were mostly granitic and up to 10 cm in diameter. The level of carbonate development corresponded to Stage III in the *Gile et al.* (1966) system of description. The unit showed

pervasive white colouration, with small grains as well as larger clasts having carbonate coatings. The layer was not indurated but did contain some nodules in which several small clasts or grains had been bound together by carbonation. Many of the pebbles and cobbles were coated on their undersides with carbonate rinds up to 10 mm thick. As described by *Gile et al.* (1966), these rinds consisted of carbonate with a defined, densely packed fabric that was easily distinguishable from the much thinner, weaker pervasive carbonate. We collected four clasts with thick, lamellar rinds from close to the top of the conglomerate for ^{230}Th/U dating.

Samples from two of the clasts (as01 and as04) were extracted by slicing the clast and rind, then drilling in to the lamella closest to the clast. They returned detritus-corrected ages of $85.9^{+7.6}_{-8.0}$ kyr and $107.5^{+6.9}_{-7.0}$ kyr (Table 5.1). The other two samples (as02 and as05) were extracted by shaving carbonate powder directly off the bottom of the rind after first shaving off the upper lamellae from a patch of the clast. This sampling method resulted in samples that had higher ^{232}Th concentrations (i.e. more detrital contamination) and lower uranium concentrations (Table 5.1) than the driled samples, therefore samples as02 and as05 were not dateable. As explained in Section 5.2, the oldest pedogenic carbonate rind gives a minimum age on the stabilisation of the surface. The ^{230}Th/U dating therefore gives an age of $>107.5^{+6.9}_{-7.0}$ kyr for the stabilisation of T7. As discussed in Section 5.2, at well dated sites the time lag before carbonate precipitation has been found to be $\leq$10 kyr (*Sharp et al.*, 2003; *Blisniuk and Sharp*, 2003; *Fletcher et al.*, 2010), varying geographically. However, because only two rinds have been successfully dated for our site and I do not yet have photographs of the positions of the drill sites on the samples, we should acknowledge a slightly greater uncertainty in the age. I can not rule out that the T7 surface dates to $\sim$125 ka — the date of the Q^2_{II} terrace forming event that has been recognised across the Tien Shan (*Burgette et al.*, 2017).

In an ideal situation I would compare the topography of the tectonically deformed part of T7 with an undeformed section to measure the tectonic deformation. In this

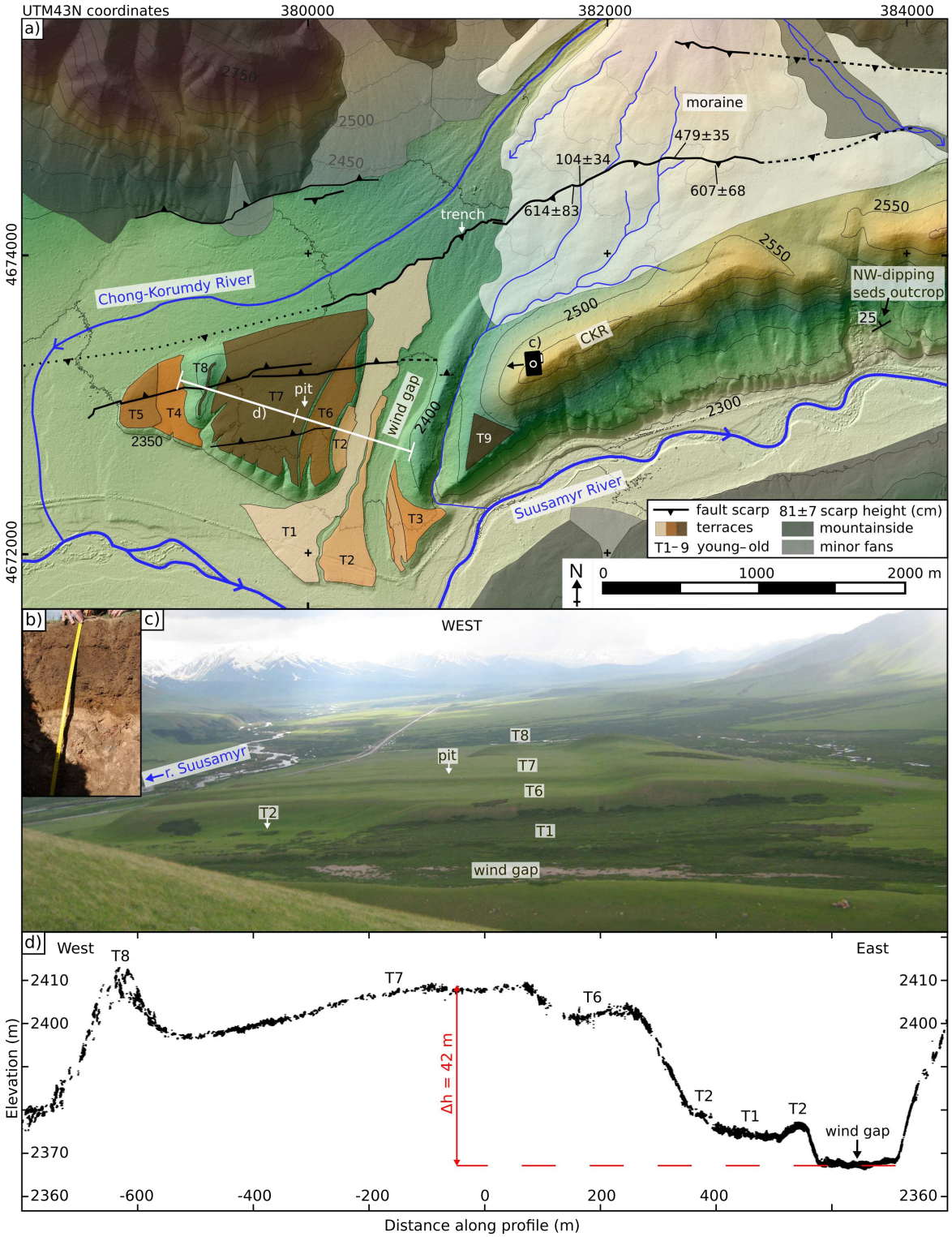


Figure 5.22: a) Map and Pléiades DEM of the western end of the CKR, showing the location of the sampling pit for ^{230}Th/U dating and showing the scarp that crosses the moraine. Scarp height measurements are duplicated from Chapter 4 and are in units of centimetres. b) Photograph of the sampling pit, showing the sandy soil and pedogenic carbonate. c) Field photograph looking west from the CKR, location shown on panel a). d) Topographic profile along the line shown in panel a), showing the 50 m elevation difference between the sampling site and the floor of the wind gap. Profile taken through the Pléiades pointcloud with a swath width 30 m and azimuth 107°.

case that is not possible because T7 has been buried on its north by fluvial sediments from the diverted Chong-Korumdy River and has been eroded from its southern side by the Suusamyr River. Instead, I use the elevation difference between T7 and the floor of the wind gap as a minimum relative uplift, while noting that the wind gap floor itself is likely to have been uplifted somewhat since its formation. The elevation difference is up to 45 m. The 1992 earthquake's fault plane dip of 49–60° (*Mellors et al.*, 1997; *Gómez et al.*, 1997) is consistent with the 55–62° dip of the lowest part of the fault in the trench. I therefore use a fault dip of 55° to convert from uplift rate to a fault slip rate estimate simply. I neglect any near-surface bending of the fault in this estimate.

Taking a surface age of 107.5 kyr, an uplift of 45 m and fault dip of 55° gives a slip rate estimate of 0.5±0.3 mm/yr, with the 60% uncertainty given to allow for the uncertainty in uplift, dip and time lag.

A second Quaternary slip rate constraint can be obtained from the moraine through which the CKR fault scarp passes. This, combined with a displacement estimate for the scarp, would give a direct estimate of the slip rate of the fault itself here. There are no published ages for moraines in the Suusamyr Basin. Although there have been many studies that aimed to date moraines and establish glaciation histories of the Tien Shan (e.g. *Koppes et al.*, 2008; *Zech*, 2012; *Li et al.*, 2014; *Lifton et al.*, 2014; *Blomdin et al.*, 2016), the only glacial stage that can be reliably correlated across the Tien Shan is the one that occurred 15–28 ka during marine isotope stage (MIS) 2 (*Blomdin et al.*, 2016). Moraines dating from that time period are also the youngest large moraines identified other than minor Holocene moraines that are close to present-day glaciers (*Blomdin et al.*, 2016).

Lifton et al. (2014) found that the difference in equilibrium line altitude (ELA) between MIS 2 glaciers and the present-day glaciers is <500 m, and *Blomdin et al.* (2016) report that the lowest elevation moraines from MIS 2 have been found at is 2600 m. At Suusamyr there are now no glaciers but there is ∼1500 m difference in elevation between the moraine we are interested in and the summit of its catchment,

Table 5.1: ^{230}Th/U age data for pedogenic carbonate samples. Errors give 95% confidence level. All isotope ratios are activity ratios.

Sample	Weight (mg)	U (ppm)	^{232}Th (ppm)	^{230}Th/^{232}Th	Measured ^{230}Th/^{238}U	Measured ^{234}U/^{238}U	Rho†	Age (corrected) (kyr)	Initial ^{234}U/^{238}U‡
as01	9.33	7.85	2.06	$7.855^{+0.037}_{-0.035}$	$0.673^{+0.002}_{-0.002}$	$1.142^{+0.004}_{-0.004}$	0.31	$85.9^{+7.6}_{-8.0}$	1.181 ±0.007
as04	9.97	7.26	1.74	$9.719^{+0.053}_{-0.052}$	$0.761^{+0.003}_{-0.002}$	$1.144^{+0.004}_{-0.004}$	0.33	$107.5^{+6.9}_{-7.0}$	1.196 ±0.007
as02	10.16	2.10	3.42	$1.807^{+0.010}_{-0.010}$	$0.964^{+0.005}_{-0.004}$	$1.115^{+0.006}_{-0.006}$	0.25	-	-
as05	10.58	3.26	7.37	$1.395^{+0.008}_{-0.008}$	$1.032^{+0.005}_{-0.005}$	$1.122^{+0.005}_{-0.005}$	0.23	-	-

†Error correlation for ^{230}Th/^{238}U–^{234}U/^{238}U.
‡Back-calculated from the age and the detritus-corrected ^{234}U/^{238}U.

and the base of the moraine is at 2430 m elevation. The moraine crossing the CKR fault is therefore at lower elevation and further below present-day glaciers than the known MIS 2 moraines. The consensus of recent studies of Tien Shan glaciation is that there are still moraines from at least one glaciation predating MIS 2 that was more extensive than the MIS 2 glaciation (*Koppes et al.*, 2008; *Zech*, 2012; *Lifton et al.*, 2014; *Blomdin et al.*, 2016). These observations suggest that an earlier, more extensive glaciation could have been responsible for the CKR moraine. However the Tien Shan moraines with well constrained ages are to the south or east of Suusamyr (see map in *Blomdin et al.*, 2016) and glaciation studies have not focussed on this, northwestern, part of the Tien Shan. It is also recognised that non-climatic effects, and most importantly in this case topography (such as the Chet Korumdy Ridge), can influence the timing and position of moraine deposition (*Barr and Lovell*, 2014), so I cannot be sure that the CKR moraine does not date from MIS 2.

Glaciation(s) that were earlier and more extensive than the MIS 2 glaciation(s) have been dated to different ages at different sites (*Koppes et al.*, 2008; *Zech*, 2012; *Lifton et al.*, 2014; *Blomdin et al.*, 2016). A review by *Blomdin et al.* (2016) concluded that due to the low number of samples and/or the low resolution of the dating, it is not yet possible to robustly identify any single Tien Shan-wide glaciation prior to the MIS 2 glaciation. I conclude that although the CKR moraine might predate MIS 2, the local and regional glaciation records are not developed enough for me to confirm that, or to suggest what the age of the moraine would be if it did predate MIS 2. Therefore the age constraint for the moraine is that it dates to at least 15 ka.

The largest vertical offset that I measured across the scarp in the moraine above the CKR is 6.1±0.8 m (Chapter 4). Assuming a fault dip of 55±6° and assuming that scarp height is equal to fault throw, this corresponds to a slip rate for this fault of ≥0.5±0.1 mm/yr over the past ≥15 kyr.

5.6.2 Slip rate estimate from the earthquake recurrence rate

From the dates and slip magnitudes of past earthquakes it is possible to work out an average slip rate on a trenched fault (e.g *Li et al.*, 2013a; *Landgraf et al.*, 2016; *Wechsler et al.*, 2018). Here I use the results of the paleoseismology at the CKR fault site described in Chapter 4 (location marked in Figure 5.22) to obtain a slip rate estimate that is separate to the two in Section 5.6.1. The maximum scarp height at the trench site and the vertical offset exposed in the trench are approximately 2.5–3.2 m. Assuming a fault dip of 55±6° and that the scarp initially formed 8 ka, this corresponds to an average slip rate of 0.36–0.53 mm/yr. Although this slip rate was obtained from relatively reliable age and offset estimates, as with the other two slip rates, there are caveats associated with it. It is a slip rate averaged over just three earthquakes, only two of which are evident at this site, since we did not see any deformation from the 1992 earthquake in the trench. Given that I have no reason to think that the recurrence interval of earthquakes at this site is constant and, in fact, my dates from Chapter 4 indicate that it is not, caution should be taken before using this as a long-term slip rate estimate.

My three slip rate estimates of 0.5±0.3 mm/yr from T7, ≥0.5±0.1 mm/yr for the fault crossing the moraine, and 0.36–0.53 mm/yr from the trench are in agreement that this section of the fault slips at approximately 0.5 mm/yr. Although each estimate has limitations and uncertainties, it is encouraging that three separate methods give similar results.

As I have shown, a trench in the Suusamyr Basin will not record all of the major earthquakes to have ruptured that part of the fault. The question of whether this along-strike variability in surface rupture offsets for each earthquake is evened out by distributed coseismic deformation, by variation between successive earthquakes, or during the postseismic or interseismic periods is still unanswered (see Appendix A for a report on a preliminary study). Although no other strands of the Suusamyr Fault have been mapped at the longitude of the CKR, some of the shortening may be

accommodated by folding. Therefore, although I have provided slip rate estimates at the fold front they should be considered a minimum estimate of the total slip rate on the Suusamyr Fault.

5.6.3 GPS velocities

The Tien Shan and its surroundings are covered by a network of ∼400 campaign GPS stations and 14 continuously recording stations, velocity measurements from which were published by *Zubovich et al.* (2010). A commonly used strategy for interpreting the displacement pattern around isolated locked faults is to fit the data using an elastic half-space model, either inverting for locking depth, dip and slip rate or fixing some parameters (e.g. *Elliott et al.*, 2008; *Ader et al.*, 2012; *Mackenzie et al.*, 2018). However, the Tien Shan does not contain isolated faults. *England and Molnar* (2015) showed that a model consisting of a linear strain rate with the exception of one sharp step, could be used to fit swath profiles through GPS velocities across the Tien Shan with root-mean-square misfits of around 1 mm/yr. The step is likely to be caused by localised creep across a small number of faults (possibly only one) (*England and Molnar*, 2015; *Mackenzie et al.*, 2018). This implies that, in general, the faults are sufficiently close together for the area they are deforming to appear as a continuum, and therefore for it to be inappropriate to model them as individual faults in an elastic half-space.

Figure 5.23 shows a 160 km-long, 80 km-wide profile through their data perpendicular to the Suusamyr Basin. Rather than being linear, the profile-parallel component of velocity (Figure 5.23b) shows a hyperbolic tangent shape across the basin. The profiles used in *England and Molnar* (2015) used wide swaths that averaged across more than one fault's length, meaning that the position of faults along the profile is not constant within each swath, and could conceivably have led to masking of their individual interseismic loading signals. To check whether it is feasible and likely that the profile in Figure 5.23b does show the pattern of strain accumulation across the Suusamyr and Talas-Boundary Faults I constructed a forward model based upon the configuration of

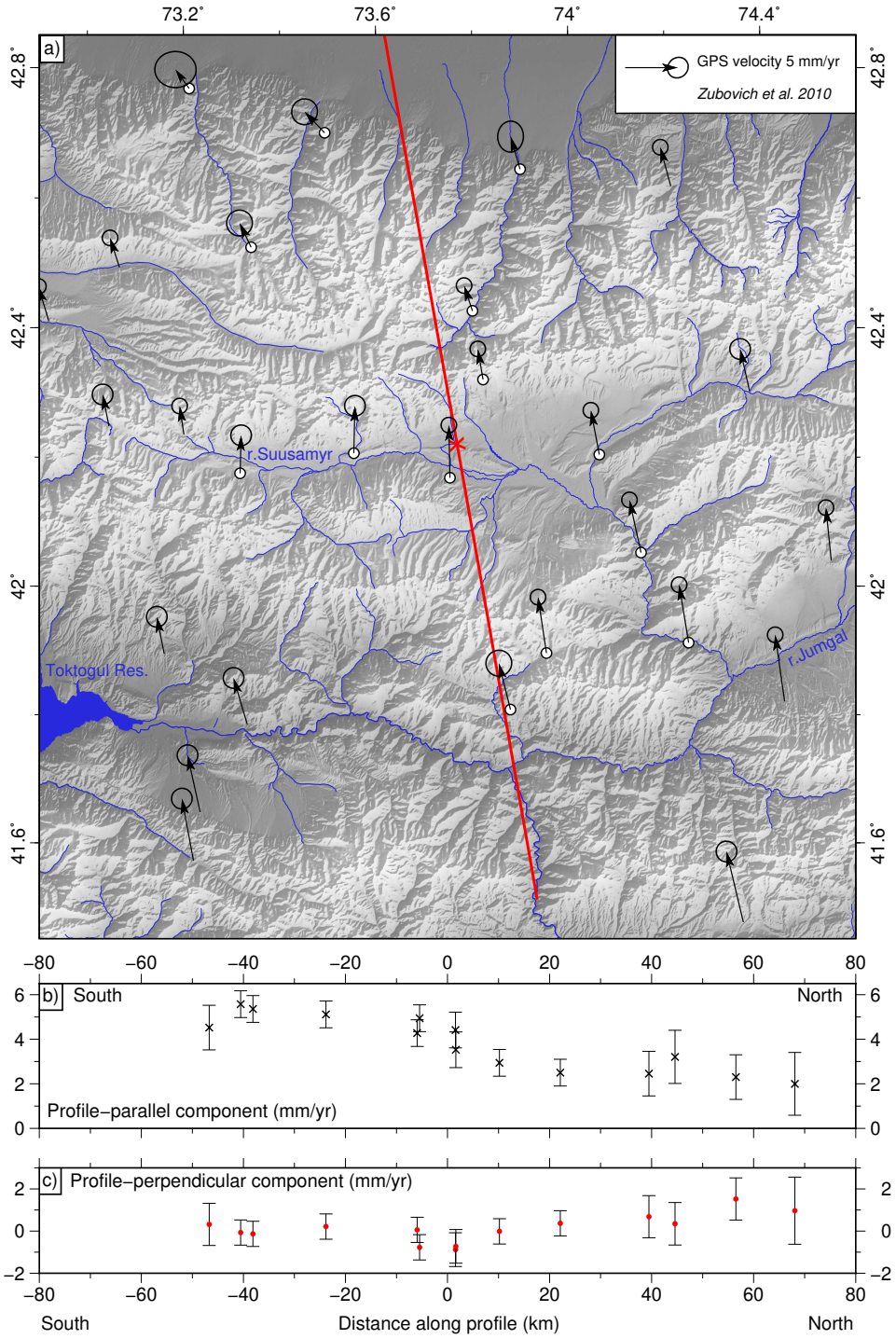


Figure 5.23: a) GPS velocities relative to Eurasia and 95% confidence ellipses (*Zubovich et al.*, 2010). The red line is the profile line for panels b) and c) and the X marks the origin. The stations marked by white dots were used for the profiles. b) The profile-parallel component of velocity, error bars show the 95% confidence interval of each station. The positive direction is northwards (azimuth 350). b) The profile-perpendicular component, positive is to the west (azimuth 260).

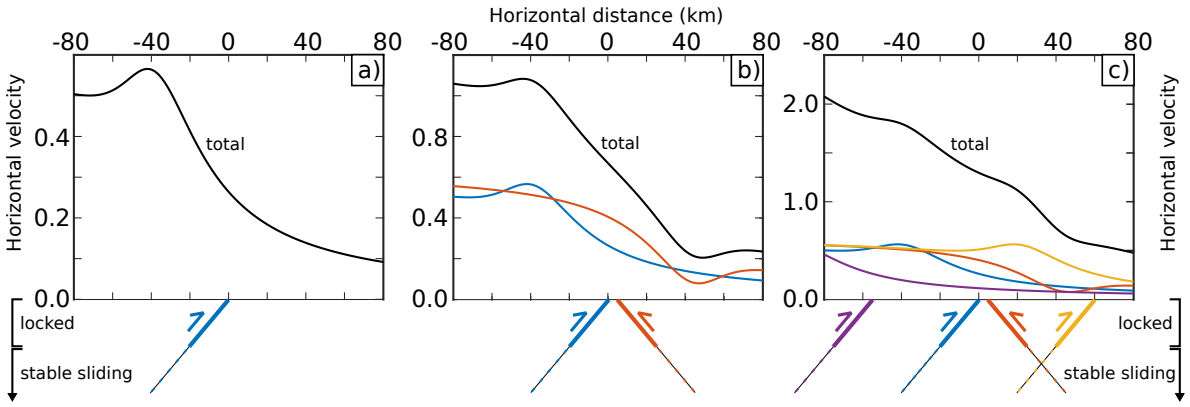


Figure 5.24: Forward models of the horizontal velocity around locked reverse faults. Velocities are shown relative to the far-field in the positive direction (mimicking velocities relative to stable Eurasia) and are given in arbitrary units, where each fault has a slip rate of 1. Black line shows the total for each scenario, coloured lines show the contribution from each fault. a) Single fault. b) Two opposing faults. c) Four faults representing the situation in Figure 5.23b.

known faults that the profile crosses (Figure 5.1). At Suusamyr there are two opposing faults that reach the surface within the basin and there are also active south-dipping faults at the northern rangefront of the Kyrgyz Range ∼60 km to the north, and in the upper Toktogul Basin ∼55 km to the south (Figure 5.1 and Section 5.7). A simple 2D forward model of the horizontal velocity above faults in this configuration is shown in Figure 5.24. The model uses the equations laid out in Section 3.3.1 of *Segall* (2010) and represents faults that are freely sliding at depth and locked above 25 km depth, which is appropriate for the seismogenic thickness in the Tien Shan (*Ghose et al.*, 1998; *Sloan et al.*, 2011). For this illustrative forward model the faults were given dips of 50° and equal slip rates.

The model that takes account of both Suusamyr Basin faults and the faults on either side (Figure 5.24c) shows a velocity profile that is almost linear. Tests using a shallower locking depth of 15 km or using slightly unequal slip rates did not yield materially different results. I conclude that, within reasonable assumptions, the horizontal displacement field across locked Kyrgyz Range rangefront, Talas-Boundary, Suusamyr and upper Toktogul Basin faults would not produce a velocity profile with the short length-scale hyperbolic tangent pattern that can be seen in Figure 5.23b and that the data

cannot be used to estimate a long-term shortening rate across the basin. Postseismic deformation is one possible explanation for the velocity pattern seen around Suusamyr. Thirteen of the fourteen stations in my profile were first measured in May/June 1995, three years after the August 1992 Suusamyr earthquake. The fourteenth, the southernmost station, was first measured in August 1999. The total observation durations are 3.8–11.2 yrs (mean 8.9 yrs). It is possible that postseismic deformation is responsible for the hyperbolic tangent pattern of horizontal velocities across the Suusamyr Basin but that cannot be confirmed without higher spatial or temporal resolution data.

5.7 An active fault in the upper Toktogul Valley

In the western Tien Shan the rangefront faults and the intermontane basins such as Suusamyr, have been the focus of the majority of recent research (e.g. *Burbank et al.*, 1999; *Abdrakhmatov et al.*, 2001; *Thompson et al.*, 2002; *Goode et al.*, 2011; *Patyniak et al.*, 2017). A reason and justification for this is that the faults within and bounding these basins are believed to account for most of the shortening of the Tien Shan — *Thompson et al.* (2002) found that the sum of the geologic shortening rates on eight such faults in their partial transect of the Tien Shan to the east of Suusamyr was indistinguishable from the GPS shortening rate at the 95% confidence level. Nevertheless, many faults that have been active during the Cenozoic have been identified with in the mountainous "blocks" between intermontane basins (e.g. *Cobbold et al.*, 1994; *Thompson et al.*, 2002). An insight into the behaviour of these faults, and the fate of closed basins can be gained from a valley upstream from the Toktogul Basin, the next intermontane basin to the southwest of Suusamyr (Figures 5.1 and 5.25).

The Toktogul Basin has attracted concern because it contains a dammed reservoir which could be a hazard if the dam were damaged in an earthquake (*Simpson et al.*, 1981). The basin is bounded on its western side by the well known Talas–Fergana Fault but it also contains east-west striking reverse faults (e.g. *Cobbold et al.*, 1994). The

region of interest for this study is the valley of the Naryn River, which feeds into the Toktogul Reservoir from the east (Figure 5.25). The Naryn River is several hundred kilometres long and the name "Naryn" is already associated with a basin further south, so I will instead refer to this location as the upper Toktogul Valley. The valley is quite narrow, with a valley bottom typically less than 1.5 km wide and no distinct basin floor, but it does contain a band of Cenozoic sediments (*Nikonorov et al.*, 2000).

Using ∼0.5 m resolution WorldView-2 imagery, we have mapped two sections of active fault scarps along the valley. Beginning 6 km upstream of Kara-Jygach village there is a section of scarps with a length of 3 km, striking ∼80° the northern hillside of the valley (Figure 5.25b). The scarps are almost continuous and sometimes have two or three parallel strands. Shadows and ponding of drainage and scree against the scarps show that they have a south-up sense of displacement. The second, more substantial section of scarps is also on northern side of the valley but further to the east, beginning 25 km upstream of Kara-Jygach. This section has a length of 17 km, a strike of 110° and runs along a geological contact that is clearly visible in satellite imagery (Figure 5.25c). The units to the south of the fault are stratified orange and pale grey sedimentary rocks that seem to trend roughly parallel to the fault. On the basis of the distinctive colour and their location I believe they are Cenozoic basin sediments. As at the first section of scarps, the scarp here has a south-up sense of displacement, is quite continuous except for sections where there appear to have been landslides or scree falls. No significant lateral offset is visible in the available imagery. No fissures or ground cracking such as is seen on images of the 1992 Suusamyr ruptures is visible here but the scarps are still sharply defined and sometimes partially cross small drainage channels (e.g. Figure 5.25e), giving them a 'fresh' appearance. Along most of the scarps the total displacement appears to be small (<10 m), as in Figure 5.25e, but higher-offset sections are preserved in some parts, such as in Figure 5.25d, and I interpret those as cumulative scarps caused by slip in multiple earthquakes.

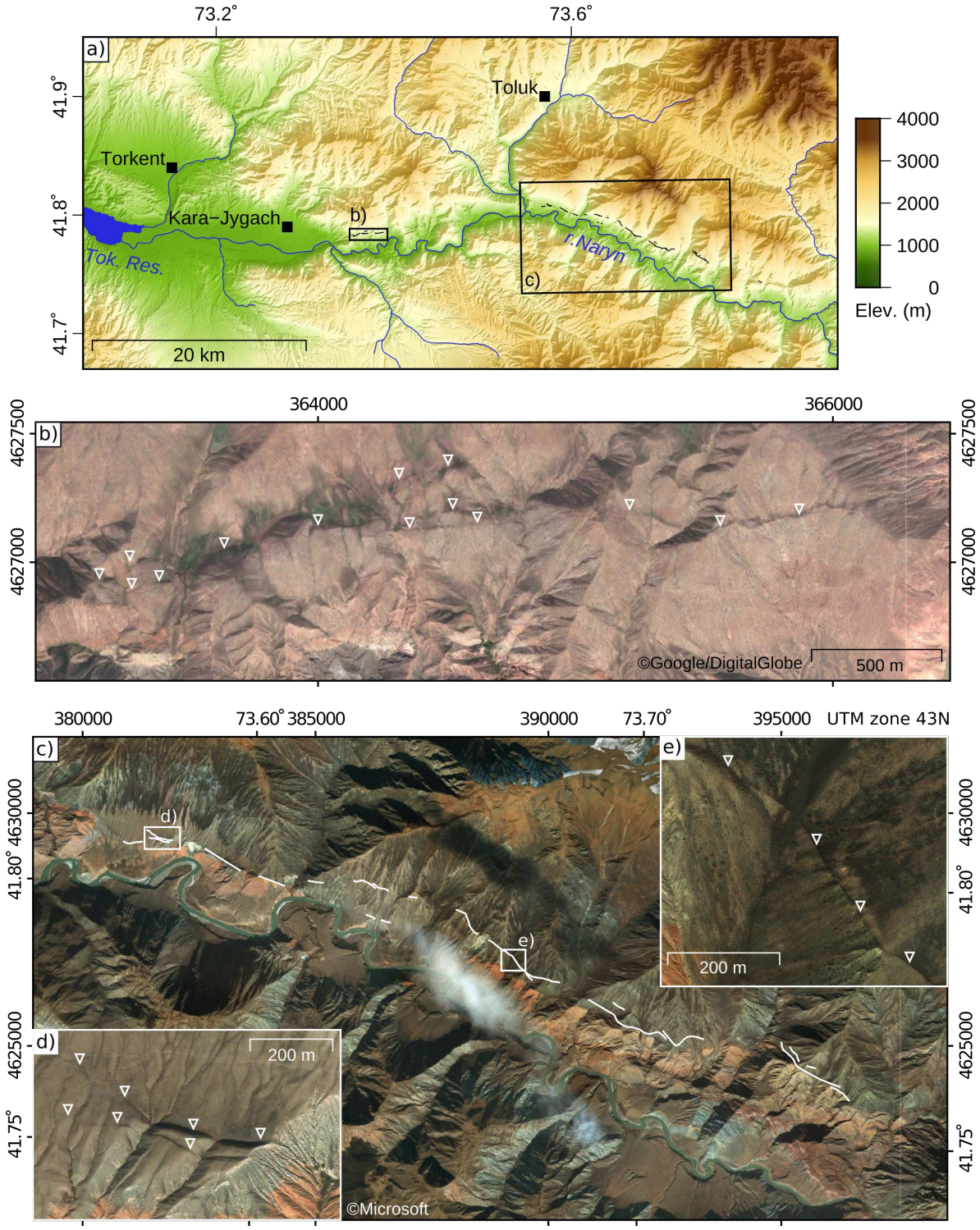


Figure 5.25: a) Topographic map of the Naryn River valley upstream of the Toktogul Reservoir. Location shown on Figure 5.1. AW3D30 DEM illuminated from the NW. b) WorldView-2 image from 5th May 2012 (copyright Google and DigitalGlobe) showing the 3 km long section of scarps in the Naryn River valley upstream of Toktogul. c) WorldView-2 image from 3rd November 2012 (copyright Microsoft and DigitalGlobe) showing the 17 km-long section of scarps further to the east. d) and e) close-up images of the scarp in the regions shown by white boxes.

5.8 Discussion

Putting together my observations at all of the fault sections described in Section 5.3, I have shown that the surface expression of north-vergent shortening is variable, and at the surface the fault appears highly segmented. In the far western part of the basin we see discontinuous fault scarps along the Suusamyr Range and more faulting within the basin floor. The fault has a different morphology in the area north of the Aramsu Range, with the Turabulak and CKR areas having folds and intermittent scarps in front of them. In the wider eastern part of the basin, east of the M41 highway rupture site, we see three fault strands, one close to the southern basin edge (the Aramsu East section), one (the Aigyrjal section) in the centre of the basin and the third (the Ak-Suu section) right on the northern edge of the basin. These three strands generally consist of scarps rather than folds, therefore the fault does reach the surface along them. In total, there is continuous evidence for faulting along the whole length of the basin — a distance of >70 km.

Based on the location evidence from seismology (*Mellors et al.*, 1997) and the surface ruptures (Chapter 4), the 1992 Suusamyr earthquake ruptured the fault beneath the far western, Turabulak and CKR areas, and part of the Aigyrjal section even though they appear as separate segments at the surface. I suggest that these sections at least are connected into a single fault at depth. Therefore, despite its segmented surface appearance, it is likely that the eastern part of the basin is also capable of rupturing in major earthquakes. The scarcity of paleoseismological data and the sparse nature of surface faulting in each earthquake (Chapter 4) prevent me from being able to determine whether any single earthquake has ruptured beneath the entire length of the basin in the past.

My minimum slip rate estimate on the Suusamyr Fault at the CKR of ∼0.5 mm/yr is comparable to the slip rates of ∼0.1 to ∼2.9 mm/yr that *Thompson et al.* (2002) found for eight faults in their transect of the Tien Shan to the east of Suusamyr (centre longitude of their transect approx. 75.5°). This suggests that the distribution style

of shortening at the longitude of Suusamyr is similar to the style in the *Thompson et al.* (2002) area. That area also has qualitatively similar topography to the Suusamyr and Toktogul Basin area in that it has similar elevations and contains intermontane basins (Figure 5.1). This is in contrast to the Kazakh Tien Shan east of Issyk Kul, where *Mackenzie* (2016) (incorporating data from *Cording et al.* (2014)) found slip rates of less than 0.6 mm/yr for four faults, and an exceptional, mostly creeping zone — the Karkara Rangefront Fault and associated structures — with higher slip rate of $\gtrsim$4.3 mm/yr.

Shallow structural complexity such as is seen at Suusamyr might be promoted by the presence of late Cenozoic sediments within the basin due to the rheological properties of the sediments and the absence of an established mature fault within them (*Wesnousky*, 1988; *Dolan and Haravitch*, 2014; *Zinke et al.*, 2014). However, in contrast to the Suusamyr Fault, the Talas-Boundary Fault has a much neater surface trace, forming relatively long continuous scarps along the rangefront, with no signs of it splaying into the valley bottom (Section 5.4). The contrasting surface expression of the two faults in the same basin shows that there are more complicated controls on the surface expression of reverse faults here than only the local stratigraphy.

In the eastern part of the basin there are active, north vergent faults some distance north of the southern rangefront. The most extreme case is the Ak-Suu section which is actually at the northern rangefront, but the Aigyrjal section and, to a lesser extent, the CKR and Turabulak sections show the same phenomenon. As described in Section 5.3.4, there are now relatively few signs of activity along the southern, Aramsu East strand that follows closer to the mountain ranges in the southeast part of the basin. Given that the mountain ranges are the product of tectonic displacements on faults and their positions are controlled by the positions that faults had in the past, these observations suggest that activity has migrated from its established position into the basin interior. The active north-vergent faults are now uplifting the basin floor and are almost co-located with the Talas-Boundary fault (Figures 5.2, 5.9 and 5.11). This suggests that

the Suusamyr Basin is in the process of basin closure. Its western half is already narrower than other intermontane basins, and the Aigyrjal and Ak-Suu fault sections show that closure of the eastern half of the basin is under way. That said, the presence of a scarp that has been produced by multiple earthquakes in the upper Toktogul Valley (Section 5.7) demonstrates that even once basin closure has taken place the faults there can still host earthquakes.

5.8.1 Clustering relationships between faults

A conspicuous aspect of the historic record of earthquakes in Central Asia is that a series of magnitude >6.5 earthquakes hit the northern Tien Shan within a few decades of each other in the late 19th and early 20th centuries. They were the 1885 M6.9 Belovodskoe (*Ignatiev*, 1886; *Kondorskaya et al.*, 1982), 1887 M7.3 Verny (*Hay*, 1888; *Mushketov*, 1890; *Kondorskaya et al.*, 1982), 1889 M8 Chilik (*Mushketov*, 1891; *Krüger et al.*, 2015; *Abdrakhmatov et al.*, 2016), 1911 M8.0 Chon-Kemin(*Bogdanovich et al.*, 1914; *Delvaux et al.*, 2001; *Kulikova and Krüger*, 2015) and 1938 M6.9 Kemino-Chu earthquakes (*Kondorskaya et al.*, 1982). This series of earthquakes forms an apparent 'cluster' in time and space and, as spatiotemporal clustering of earthquakes has been reported in some other parts of the world (e.g. *Grant and Sieh*, 1994; *Berberian and Yeats*, 1999; *Sieh et al.*, 2008; *Lefevre et al.*, 2018), leads to the question of whether clustering is an important characteristic of Tien Shan earthquakes in general.

One of the most complete paleoearthquake histories in the Tien Shan has been compiled for the reverse fault(s) on the other side of the Kyrgyz Range to Suusamyr. The faults dip to the south beneath the Kyrgyz Range and are comprised of the en-echelon Chonkurchak and Shamsi-Tunduk Faults, and the Issyk-Ata Fault to their north (Figure 5.26). Although the Issyk-Ata Fault is separated from the others by up to ∼10 km at the surface (*Thompson*, 2001), *Thompson et al.* (2002) concluded that the Issyk-Ata Fault is a splay from the Chonkurchak–Shamsi-Tunduk fault system, and that the faults meet at depth. The Chonkurchak Fault is the westernmost fault to

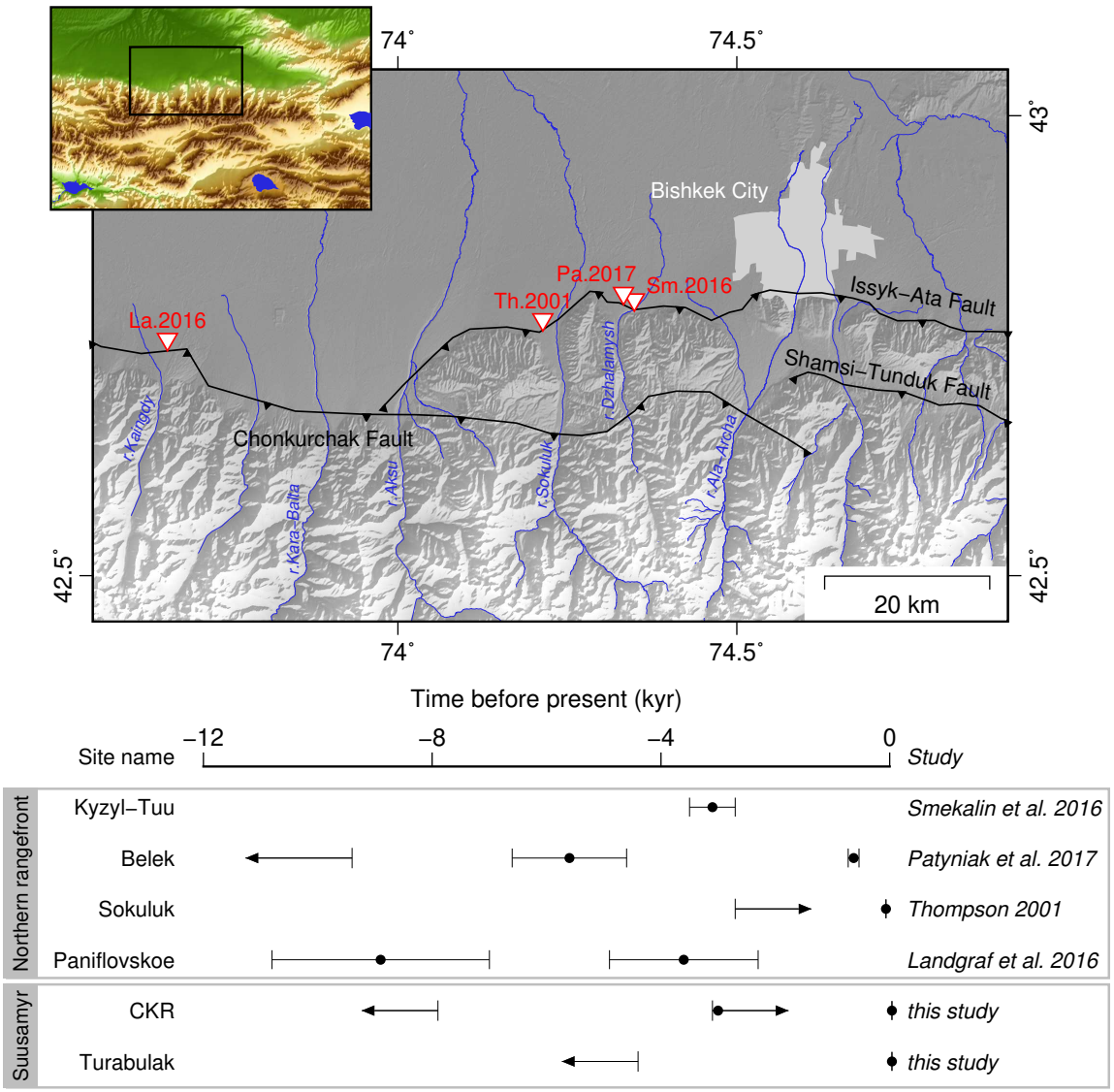


Figure 5.26: Top: Fault map of the northern rangefront of the Kyrgyz Range, showing trench sites from published literature. Location shown in Figure 5.1. Bottom: Timeline showing earthquake dates at the northern Kyrgyz Range sites and at Suusamyr. Dots show the authors' preferred dates for earthquakes. Error bars are one-sigma but note that the probability distributions are not normal distributions. The 1992 Suusamyr earthquake did not break the surface at the CKR or Turabulak sites but is included here because those parts of the fault are believed to have ruptured at depth.

have been involved in the late 19th and early 20th century series of earthquakes, having ruptured in the 1885 Belovodskoe earthquake, and palaeoseismic investigations have been conducted at several sites along it and the Issyk-Ata Fault (site locations shown in Figure 5.26).

Figure 5.26 shows a summary timeline of the paleoseismic results from the Kyrgyz

Range rangefront and Suusamyr sites. At the Sokuluk fan site on the Issyk-Ata Fault (42.767°N,74.214°E) *Thompson* (2001) interpreted terrace offsets as showing evidence for four events since fan formation 13.5–15.7 cal kyr BP. At least three of them were identifiable in a trench dug by *Thompson* (2001); the most recent was the 1885 Belovodskoe event and the penultimate event was dated as <2.3–2.7 cal yr BP. Both *Smekalin et al.* (2016) and (*Patyniak et al.*, 2017) have excavated palaeoseismic trenches at the neighbouring valley mouth, approximately 10 km to the east of *Thompson* (2001)'s site (Figure 5.26). The *Patyniak et al.* (2017) Belek trench was at 42.795°N, 74.333°E, and showed evidence for three paleoearthquakes: one ∼630 ± 95 cal B.P., one at ∼5.6 ± 1.0 cal kyr B.P., and one before 10.5 ± 1.1 cal kyr B.P. *Smekalin et al.* (2016) trenched the same fan at the Kyzyl-Tuu site (exact location unknown, possibly approximately 42.788°N,74.349°E) but reported different results — they found evidence for one paleoearthquake approximately 2721–3500 cal BP (listed as 771–1533 cal BC by *Smekalin et al.* (2016)). *Smekalin et al.* (2016) and *Patyniak et al.* (2017) agree that this section of the fault did not rupture in 1885.

During work on the Chonkurchak Fault, *Landgraf et al.* (2016) excavated three trenches and conducted terrestrial cosmogenic nuclide dating of boulders on the fan at the Paniflovskoe site (42.745°N, 73.660°E)(Figure 5.26). For reference, their site is almost directly north of the M41 highway ruptures from the 1992 Suusamyr earthquake. They found that the most recent event occurred between 1.6–5.8 ka, possibly around 3.6±1.3 ka (as determined using an OxCal model and their preferred, but not definite, interpretation), and the penultimate event between ∼5.8–14.8 ka, possibly around 8.9±1.9 ka (again, the 8.9±1.9 ka estimate was a product of the same OxCal model).

As can be seen from the summary of earthquake dates shown in Figure 5.26, within the uncertainties, it is possible that the Paniflovskoe and CKR sites could have the same earthquake history save for the 1992 event. However, because of the width of the uncertainties, it is also possible that the earthquakes at the two sites were separated by more than a thousand years. The other sites show earthquake histories that are different

to each other, and to the Paniflovskoe and CKR sites. I conclude that the data available do not show any strong evidence for temporal clustering between the northern Kyrgyz Range faults and the Suusamyr Fault, but further work will be necessary to obtain reliable conclusions.

5.9 Summary

I have mapped a series of fault scarps and folds throughout the Suusamyr Basin. The north-vergent Suusamyr Fault is made up of several segments at the surface, some of which are folds and others fault scarps. Several of the segments are slightly misaligned with each other along-strike and in places there is more than one fault strand at the same longitude. There are active fault traces along the southern basin edge and also others in the basin floor many kilometres north of the rangefront. Together though, the segments show faulting along the entire length of the basin.

The south-vergent fault, the Talas-Boundary Fault, is also active but, in contrast to the Suusamyr Fault, it shows ∼10 km-long fault scarps along parts of the basin edge. Beyond the western end of the basin there is a zone containing numerous fault scarps with lengths of <3 km and various orientations that cross-cut the established topography, mostly with a south-up sense of displacement. The eastern edge of the basin, on the other hand, is made up of established faults that do not have fresh scarps. I estimate that the slip rate of the Suusamyr Fault at the western end of its Chet-Korumdy Ridge section to be ∼0.5 mm/yr, but this should be considered a minimum slip rate because some shortening may be accommodated by folding or by any unmapped fault strands. The M_w 7.2 1992 Suusamyr earthquake ruptured the fault beneath several segments in the west of the basin, showing that despite the lack of continuity at the surface, the Suusamyr Fault is capable of producing major earthquakes. The eastern part of the basin is therefore also likely to be capable of producing major earthquakes.

There is now north-vergent active faulting as much as 25 km north of the rangefront,

suggesting that activity has migrated into the basin interior, and leaving <1 km distance between the opposing faults in some places. The Suusamyr Basin therefore appears to be in the process of closure. An example of an already closed basin is given in the upper Toktogul Valley. There I have shown by mapping a fault in the upper Toktogul Valley that even closed basins can still produce earthquakes. More work is now needed to characterise the reverse faults in the Toktogul Basin area. Comparison of the palaeoseismic records of the faults in the Suusamyr Basin and on the opposite side of the Kyrgyz Range shows no convincing evidence for temporal clustering, but the uncertainties in the dates of prehistoric earthquakes mean that some clustering can not be ruled out.

Chapter 6

Concluding remarks

The separate conclusions from my four research chapters have already been given and will not be repeated here but, when viewed as a whole, some broader points can be seen from this thesis.

The three earthquakes that this thesis is centred on are superficially similar. They all took place in parts of the India-Eurasia collision undergoing North–South shortening and their magnitudes, mechanisms and depths are broadly similar. However, they have quite different surface expressions. They each have an aspect that makes the interpretation of their faults from surface observations difficult. I have shown the reasons for this in each case but together these cases show that the reverse fault–geomorphology relationship is highly complicated and that there are significant limitations to what we can learn from surface-based observations, at least given current knowledge. The Wuqia earthquake is a particularly clear example. It took place in a region for which there are geological maps, fault maps, fault slip rates, geological cross-sections and some seismic reflection profiles, yet still the seismogenic fault(s) had not been identified because they were concealed by shallower structures. Chapters 2 and 4 have highlighted that there are particular challenges with timescales similar to or shorter than the 'earthquake cycle'. My approach to understanding the relationship between active faults and their surface expression, and one that I feel still has more to give, has been to study locations

where it is possible put both sides of the story together. This requires sites that have had earthquakes recently and also preserve tectonic geomorphology well over longer timescales. Central Asia, having both recent earthquakes and good preservation, fulfils those requirements.

One impediment to progress in understanding continental reverse faulting earthquakes is a lack of data. In Chapter 4, I looked at the variability in surface ruptures between different earthquakes on a fault. Even aside from the issue of recording multiple earthquakes' ruptures at one fault, it is noticeable that there are only a modest number of continental reverse faulting earthquakes with surface ruptures recorded. The total number appears to be around sixty (53 as of 2011 based on the compilations of *Lettis et al.* (1997) and *Moss and Ross* (2011)). That includes some events whose surface rupture measurements are poorly established, and as I have shown, the listed dimensions for the Suusamyr and Wuqia earthquakes are in need of revision. Once the earthquakes are subdivided by tectonic context (e.g. stable continental region), the set of historical examples that we have to use as the basis of our understanding of reverse fault surface ruptures is far from extensive. Given this situation, any new observations from continental reverse earthquakes are valuable and we should aim to get as much information as possible from each historical earthquake.

Thanks to improvements in observational technology, the most recent earthquakes are the ones that can be characterised best, but Chapters 3 and 4 demonstrate that useful information can still be extracted from 20th century earthquakes. Alongside the Earth Observation data collection boom of the 21st century, data processing and analysis tools have improved. They allowed me to make distance measurements more accurately and at higher resolution than was previously possible and also to map a larger coverage area than was possible at the time of the 1985 and 1992 earthquakes, and therefore conduct targeted fieldwork. 20th century archive datasets combined with 21st century methods and datasets thus have the potential to expand the list of earthquakes whose deformation field and surface ruptures have been measured. Given the limited

occurrence rate of M≥6 earthquakes, the 20th century earthquakes are therefore a valuable resource to earth Scientists.

6.1 Suggestions for future work

The results of this thesis suggest several lines of research that could prove fruitful. On the topic of how each part of the earthquake cycle contributes to the development of topography and geological structure, both Pishan and Suusamyr have potential. Although I measured and modelled the early postseismic deformation from Pishan, the Sentinel-1 satellites have continued to make frequent acquisitions, building up a much longer postseismic record. A study of that longer record that has now accumulated, combined with time series processing methods, might make it possible to identify whether or not the 'shallow' and 'deep' signals that I observed had different time constants. This would produce more information on their mechanisms and the significance of their contribution to the long-term deformation pattern. Such a study could also establish whether there is any uplift of the geological fold over the later postseismic period that I did not observe in the interferograms from the first six months although, as I note in Chapter 2, any such signal is not likely to be large enough to account for all of the fold growth. It could also place a better constraint on the total contribution of postseismic deformation to the long-term strain pattern of the fault and fold system at Pishan.

My work on the 1992 Suusamyr earthquake has focused on its surface ruptures. Ruptures are the easiest component of the deformation to measure and the most important from the perspective of paleoseismology but the questions of if, how and when shallow slip has been accommodated along the parts of the fault without surface ruptures are still open. The absence of signs of post-1992 deformation in the paleoseismic trenches that we dug through prehistoric scarps indicates that there has not been significant localised afterslip or creep on those parts of the fault. Another possibility is more distributed shallow slip. I have shown that there are folds along the parts of the

fault without 1992 ruptures and suggested that the slip could have been accommodated in a distributed manner in those areas but that is not proven. In Appendix A I report on my attempt to derive a coseismic deformation field from DEM differencing. One problem in that project was the poor quality of the pre-earthquake scanned images. Other pre-earthquake images do exist and could be used for DEM differencing or horizontal displacement mapping but the small and possibly diffuse nature of the expected signal, combined with resolution limits of the techniques will probably make it difficult to acquire a satisfactory coseismic displacement field. There are however some post-earthquake SAR data from the ERS and Envisat satellites, beginning in 1998, that could yield a postseismic displacement map. Annual GPS measurements could also be incorporated into that study if the data became available.

Our study on Pishan has joined a fairly small but growing collection of studies that have taken advantage of modern geodetic techniques to study the development of long-term structure through the seismic cycle. The availability of good satellite data across the world's high strain-rate regions and the increasing length of the archive mean that for future earthquakes it should be possible to compare topography or geological structure to displacement routinely, if not with such varied and high-quality datasets as for the Pishan earthquake. More progress on this topic can also be made by applying modern techniques and thinking to historical earthquakes.

Finally, there is a lot still to be learned about the active faults of Central Asia. This project has improved our knowledge of the faults in three particular locations but even the basic parameters of slip rate and earthquake history are not well known for many others. Given the seismic hazard that the faults in the region could pose, further work on Central Asian faults and earthquakes will be needed for a long time to come.

Bibliography

Abdrakhmatov, K., R. Weldon, S. Thompson, D. Burbank, C. Rubin, M. Miller, and P. Molnar (2001), Onset, style and current rate of shortening in the central Tien Shan (Kyrgyzstan), *Russ. Geol. Geophys*, *42*, 1502–1526. 1.2, 1.2, 3.2.1, 5.1, 5.7

Abdrakhmatov, K. E., R. T. Walker, G. E. Campbell, A. S. Carr, A. Elliott, C. Hillemann, J. Hollingsworth, A. Landgraf, D. Mackenzie, A. Mukambayev, M. Rizza, and R. A. Sloan (2016), Multisegment rupture in the 11 July 1889 Chilik earthquake (Mw 8.0-8.3), Kazakh Tien Shan, interpreted from remote sensing, field survey, and paleoseismic trenching, *Journal of Geophysical Research: Solid Earth*, *121*(6), 4615–4640, doi:10.1002/2015JB012763. 1.2, 4.1, 4.3.2, 4.5.1, 5.8.1

Abdrakhmatov, K. Y., S. A. Aldazhanov, B. H. Hager, M. W. Hamburger, T. A. Herring, K. B. Kalabaev, V. I. Makarov, P. Molnar, S. V. Panasyuk, M. T. Prilepin, R. E. Reilinger, I. S. Sadybakasov, B. J. Souter, Y. A. Trapeznikov, V. Y. Tsurkov, and A. V. Zubovich (1996), Relatively recent construction of the Tien Shan inferred from GPS measurements of present-day crustal deformation rates, *Nature*, *384*(6608), 450–453, doi:10.1038/384450a0. 1.2

Ader, T., J.-P. Avouac, J. LiuZeng, H. LyonCaen, L. Bollinger, J. Galetzka, J. Genrich, M. Thomas, K. Chanard, S. N. Sapkota, S. Rajaure, P. Shrestha, L. Ding, and M. Flouzat (2012), Convergence rate across the Nepal Himalaya and interseismic coupling on the Main Himalayan Thrust: Implications for seismic hazard, *Journal of Geophysical Research: Solid Earth*, *117*(B4), doi:10.1029/2011JB009071. 5.6.3

Ainscoe, E., J. Elliott, A. Copley, T. Craig, T. Li, B. Parsons, and R. Walker (2017), Blind Thrusting, Surface Folding, and the Development of Geological Structure in the Mw 6.3 2015 Pishan (China) Earthquake, *Journal of Geophysical Research: Solid Earth*, *122*(11), 9359–9382, doi:10.1002/2017JB014268. 1.4, 2.3.1, 2.5

Ainscoe, E. A., K. E. Abdrakhmatov, S. Baikulov, A. S. Carr, A. J. Elliott, C. Grützner, and R. T. Walker (2019), Variability in surface rupture between successive earthquakes on the Suusamyr Fault, Kyrgyz Tien Shan: implications for palaeoseismology, *Geophysical Journal International*, *216*(1), 703–725, doi:10.1093/gji/ggy457. 1.4

Aitken, M. J. (1985), *Thermoluminescence dating*, Studies in archaeological science, Academic Press. B

Akoğlu, A. M., S. Jónsson, T. Wang, Z. Çakır, U. Dogan, S. Ergintav, B. Osmanoğlu, G. Feng, C. Zabcı, A. Özdemir, and O. Emre (2018), Evidence for Tear Faulting from New Constraints of the 23 October 2011 Mw 7.1 Van, Turkey, Earthquake Based on

InSAR, GPS, Coastal Uplift, and Field ObservationsEvidence for Tear Faulting from New Constraints of the 2011 Van, Turkey, Earthquake, *Bulletin of the Seismological Society of America*, *108*(4), 1929–1946, doi:10.1785/0120170314. 1.1

Allen, M. B., and S. J. Vincent (1997), Fault reactivation in the Junggar region, northwest China: the role of basement structures during Mesozoic-Cenozoic compression, *Journal of the Geological Society*, *154*(1), 151–155, doi:10.1144/gsjgs.154.1.0151. 3.6

Allmendinger, R. W. (1998), Inverse and forward numerical modeling of trishear fault-propagation folds, *Tectonics*, *17*(4), 640–656, doi:10.1029/98TC01907. 1.1

Ambraseys, N. (2009), *Earthquakes in the mediterranean and middle east: A multidisciplinary study of seismicity up to 1900*, Cambridge University Press, Cambridge, doi:10.1017/CBO9781139195430. 1.1

Ambraseys, N. N. (1963), The Buyin-Zara (Iran) earthquake of September, 1962 a field report, *Bulletin of the Seismological Society of America*, *53*(4), 705–740. 4.6

Ambraseys, N. N. (2001), Reassessment of earthquakes, 1900-1999, in the Eastern Mediterranean and the Middle East, *Geophysical Journal International*, *145*(2), 471–485, doi:10.1046/j.0956-540x.2001.01396.x. 3.3

Amos, C. B., D. W. Burbank, D. C. Nobes, and S. A. L. Read (2007), Geomorphic constraints on listric thrust faulting: Implications for active deformation in the Mackenzie Basin, South Island, New Zealand, *Journal of Geophysical Research: Solid Earth*, *112*(B3), B03S11, doi:10.1029/2006JB004291. 1.1, 2.7.1

Anderson, J. G., G. P. Biasi, and S. G. Wesnousky (2017), Fault Scaling Relationships Depend on the Average Fault Slip Rate, *Bulletin of the Seismological Society of America*, *107*(6), 2561–2577, doi:10.1785/0120160361. 4.1

Arnold, L. J., R. M. Bailey, and G. E. Tucker (2007), Statistical treatment of fluvial dose distributions from southern Colorado arroyo deposits, *Quaternary Geochronology*, *2*(1), 162–167, doi:10.1016/j.quageo.2006.05.003. 4.3.2

Arrowsmith, J. R., and M. R. Strecker (1999), Seismotectonic range-front segmentation and mountain-belt growth in the Pamir-Alai region, Kyrgyzstan (India-Eurasia collision zone), *GSA Bulletin*, *111*(11), 1665–1683, doi:10.1130/0016-7606(1999)111<1665:SRFSAM>2.3.CO;2. 1.2

Avşar, U., A. Hubert-Ferrari, M. D. Batist, and N. Fagel (2014), A 3400year lacustrine paleoseismic record from the North Anatolian Fault, Turkey: Implications for bimodal recurrence behavior, *Geophysical Research Letters*, *41*(2), 377–384, doi:10.1002/2013GL058221. 1.1

Avouac, J.-P. (2015), From Geodetic Imaging of Seismic and Aseismic Fault Slip to Dynamic Modeling of the Seismic Cycle, *Annual Review of Earth and Planetary Sciences*, *43*(1), 233–271, doi:10.1146/annurev-earth-060614-105302. 2.6.3

Avouac, J.-P., and G. Peltzer (1993), Active tectonics in southern Xinjiang, China: Analysis of terrace riser and normal fault scarp degradation along the Hotan-Qira Fault System, *Journal of Geophysical Research: Solid Earth*, *98*(B12), 21,773–21,807, doi:10.1029/93JB02172. 2.1, 2.2

Avouac, J.-P., F. Ayoub, S. Leprince, O. Konca, and D. Helmberger (2006), The 2005, Mw 7.6 Kashmir earthquake: Sub-pixel correlation of ASTER images and seismic waveforms analysis, *Earth and Planetary Science Letters*, *249*(3-4), 514–528, doi:dx. 3.5, 4.6

Ayoub, F., S. Leprince, R. Binet, K. W. Lewis, O. Aharonson, and J. P. Avouac (2008), Influence of camera distortions on satellite image registration and change detection applications, in *IGARSS 2008 - 2008 IEEE International Geoscience and Remote Sensing Symposium*, vol. 2, pp. II–1072–II–1075, doi:10.1109/IGARSS.2008.4779184. 3.5

Ayoub, F., S. Leprince, and J.-P. Avouac (2009), Co-registration and correlation of aerial photographs for ground deformation measurements, *ISPRS Journal of Photogrammetry and Remote Sensing*, *64*(6), 551–560, doi:10.1016/j.isprsjprs.2009.03.005. 3.5

Bailey, R. M., and L. J. Arnold (2006), Statistical modelling of single grain quartz De distributions and an assessment of procedures for estimating burial dose, *Quaternary Science Reviews*, *25*(19), 2475–2502, doi:10.1016/j.quascirev.2005.09.012. 4.3

Bally, A., I.-M. Chou, R. Clayton, H. Eugster, S. M. Kidwell, L. Meckel, R. Ryder, A. B. Watts, and A. Wilson (1986), Notes on sedimentary basins in China; report of the American Sedimentary Basins Delegation to the People's Republic of China, *USGS Numbered Series 86-327*, U.S. Geological Survey,. 3.2.1

Bande, A., E. R. Sobel, A. Mikolaichuk, A. Schmidt, and D. F. Stockli (2017a), Exhumation history of the western Kyrgyz Tien Shan: implications for intramontane basin formation., *Tectonics*, *36*(1), 163–180, doi:10.1002/2016TC004284. 1.2

Bande, A., E. R. Sobel, A. Mikolaichuk, and V. T. Acosta (2017b), Talas-Fergana Fault Cenozoic timing of deformation and its relation to Pamir indentation, *Geological Society, London, Special Publications*, *427*(1), 295–311, doi:10.1144/SP427.1. 1.2, 3.6

Barnhart, W. D., and R. B. Lohman (2013), Characterizing and estimating noise in InSAR and InSAR time series with MODIS, *Geochemistry, Geophysics, Geosystems*, *14*(10), 4121–4132, doi:10.1002/ggge.20258. 2.6.1

Barnhart, W. D., C. M. J. Brengman, S. Li, and K. E. Peterson (2018), Ramp-flat basement structures of the Zagros Mountains inferred from co-seismic slip and afterslip of the 2017 Mw7.3 Darbandikhan, Iran/Iraq earthquake, *Earth and Planetary Science Letters*, *496*, 96–107, doi:10.1016/j.epsl.2018.05.036. 3.6

Barr, I. D., and H. Lovell (2014), A review of topographic controls on moraine distribution, *Geomorphology*, *226*, 44–64, doi:10.1016/j.geomorph.2014.07.030. 5.6.1

Bawden, G. W. (2001), Source parameters for the 1952 Kern County earthquake, California: A joint inversion of leveling and triangulation observations, *Journal of Geophysical Research: Solid Earth*, *106*(B1), 771–785, doi:10.1029/2000JB900315. 4.6

Bekaert, D. P. S., R. J. Walters, T. J. Wright, A. J. Hooper, and D. J. Parker (2015a), Statistical comparison of InSAR tropospheric correction techniques, *Remote Sensing of Environment*, *170*, 40–47, doi:10.1016/j.rse.2015.08.035. 2.6.1

Bekaert, D. P. S., A. Hooper, and T. J. Wright (2015b), A spatially variable power law tropospheric correction technique for InSAR data, *Journal of Geophysical Research: Solid Earth*, *120*(2), 1345–1356, doi:10.1002/2014JB011558. 2.6.1

Benedetti, L., P. Tapponnier, G. King, B. Meyer, and I. Manighetti (2000), Growth folding and active thrusting in the Montello region, Veneto, northern Italy, *Journal of Geophysical Research: Solid Earth*, *105*(B1), 739–766. 2.7.1, 5.3.1

Berberian, M. (1979), Evaluation of the instrumental and relocated epicentres of Iranian earthquakes, *Geophysical Journal of the Royal Astronomical Society*, *58*(3), 625–630, doi:10.1111/j.1365-246X.1979.tb04798.x. 3.3

Berberian, M. (1981), Active faulting and tectonics of Iran, *Zagros-Hindu Kush-Himalaya Geodynamic Evolution*, *3*, 33–69. 4.6

Berberian, M., and R. S. Yeats (1999), Patterns of historical earthquake rupture in the Iranian Plateau, *Bulletin of the Seismological Society of America*, *89*(1), 120–139. 5.8.1

Berberian, M., J. A. Jackson, M. Qorashi, M. Talebian, M. Khatib, and K. Priestley (2000), The 1994 Sefidabeh earthquakes in eastern Iran: blind thrusting and bedding-plane slip on a growing anticline, and active tectonics of the Sistan suture zone, *Geophysical Journal International*, *142*(2), 283–299, doi:10.1046/j.1365-246x.2000.00158.x. 3.5

Bernard, S., J.-P. Avouac, S. Dominguez, and M. Simoes (2007), Kinematics of fault-related folding derived from a sandbox experiment, *Journal of Geophysical Research: Solid Earth*, *112*(B3), B03S12, doi:10.1029/2005JB004149. 2.7.1

Biasi, G. P., and R. J. Weldon (2006), Estimating Surface Rupture Length and Magnitude of Paleoearthquakes from Point Measurements of Rupture Displacement, *Bulletin of the Seismological Society of America*, *96*(5), 1612–1623, doi:10.1785/0120040172. 4.1

Bindi, D., K. Abdrakhmatov, S. Parolai, M. Mucciarelli, G. Grünthal, A. Ischuk, N. Mikhailova, and J. Zschau (2012), Seismic hazard assessment in Central Asia: Outcomes from a site approach, *Soil Dynamics and Earthquake Engineering*, *37*, 84–91, doi:10.1016/j.soildyn.2012.01.016. 4.1

Bird, P. (2003), An updated digital model of plate boundaries, *Geochemistry, Geophysics, Geosystems*, *4*(3), doi:10.1029/2001GC000252. 1.1

Blayney, T., Y. Najman, G. DupontNivet, A. Carter, I. Millar, E. Garzanti, E. R. Sobel, M. Rittner, S. And, Z. Guo, and G. Vezzoli (2016), Indentation of the Pamirs with respect to the northern margin of Tibet: Constraints from the Tarim basin sedimentary record, *Tectonics*, *35*(10), 2345–2369, doi:10.1002/2016TC004222. 1.2

Blisniuk, P., and W. Sharp (2003), Rates of late Quaternary normal faulting in central Tibet from U-series dating of pedogenic carbonate in displaced fluvial gravel deposits, *Earth and Planetary Science Letters*, *215*(1-2), 169–186, doi:10.1016/S0012-821X(03)00374-1. 5.2, 5.6.1

Blomdin, R., A. Stroeven, J. Harbor, N. Lifton, J. Heyman, N. Gribenski, D. Petrakov, M. Caffee, M. Ivanov, C. Httestrand, I. Rogozhina, and R. Usubaliev (2016), Evaluating the timing of former glacier expansions in the Tian Shan: A key step towards robust spatial correlations, *Quaternary Science Reviews*, *153*, 78–96, doi:10.1016/j.quascirev.2016.07.029. 5.6.1

Blong, R. J., and R. Gillespie (1978), Fluvially transported charcoal gives erroneous 14c ages for recent deposits, *Nature*, *271*(5647), 739–741, doi:10.1038/271739a0. 4.3.2

Bogachkin, B., A. Korzhenkov, E. Mamyrov, Y. Nechaev, M. Omuraliev, A. Petrosyan, K. Pletnev, E. Rogozhin, and T. Charimov (1997), The structure of the 1992 Susamyr earthquake source based on its geological and seismological manifestations, *Izvestiya - Physics of the Solid Earth*, *33*(11), 867–882. 4.2, 4.4, 4.4.2, 4.4.2, 5.1, 5.1

Bogdanovich, K. I., I. M. Kark, B. Y. Korolkov, and D. I. Mushketov (1914), Earthquake in Northern District of Tien Shan, 22 December 1910 (4 January 1911), *Communications of the Geological Community, St Petersburg, Russia*. 1.2, 5.8.1

Bosboom, R., A. Houben, G. Dupont-Nivet, H. Brinkhuis, G. Villa, O. Mandic, M. Stoica, W. Krijgsman, Z. Guo, and C. Li (2011), Late Eocene sea retreat from the Tarim Basin (West China) linked to Asian aridification and Mediterranean Tethys., *Palaeogeography, Palaeoclimatology, Palaeoecology*, *299*, 385–398, doi:10.1016/j.palaeo.2010.11.019. 3.2.1, 3.2.1, 3.2

Bott, M. H. P. (1959), The Mechanics of Oblique Slip Faulting, *Geological Magazine*, *96*(2), 109–117, doi:10.1017/S0016756800059987. 1.1

Bouilhol, P., O. Jagoutz, J. M. Hanchar, and F. O. Dudas (2013), Dating the IndiaEurasia collision through arc magmatic records, *Earth and Planetary Science Letters*, *366*, 163–175, doi:10.1016/j.epsl.2013.01.023. 1.2

Bowman, J. R. (1992), The 1988 Tennant Creek, northern territory, earthquakes: A synthesis, *Australian Journal of Earth Sciences*, *39*(5), 651–669, doi:10.1080/08120099208728056. 4.6

Brandenburg, J. P. (2013), Trishear for curved faults, *Journal of Structural Geology*, *53*, 80–94, doi:10.1016/j.jsg.2013.04.006. 1.1

Bronk Ramsey, C. (2009), Bayesian Analysis of Radiocarbon Dates, *Radiocarbon*, *51*(1), 337–360, doi:10.1017/S0033822200033865. 4.3.2

Brunet, M.-F., E. R. Sobel, and T. McCann (2017), Geological evolution of Central Asian Basins and the western Tien Shan Range, *Geological Society, London, Special Publications*, *427*, SP427.17, doi:10.1144/SP427.17. 1.2

Bufe, A., D. P. S. Bekaert, E. Hussain, B. Bookhagen, D. W. Burbank, J. A. Thompson Jobe, J. Chen, T. Li, L. Liu, and W. Gan (2017), Temporal changes in rock uplift rates of folds in the foreland of the Tian Shan and the Pamir from geodetic and geologic data, *Geophysical Research Letters*, *44*(21), 10,977–10,987, doi:10.1002/2017GL073627. 3.2.3, 3.3, 3.6

Bullen, M., D. Burbank, and J. Garver (2003), Building the Northern Tien Shan: Integrated thermal, structural, and topographic constraints, *Journal of Geology*, *111*(2), 149–165, doi:10.1086/345840. 1.2

Bullen, M. E., D. W. Burbank, J. I. Garver, and K. Y. Abdrakhmatov (2001), Late Cenozoic tectonic evolution of the northwestern Tien Shan: New age estimates for the initiation of mountain building, *Geological Society of America Bulletin*, *113*(12), 1544–1559, doi:10.1130/0016-7606(2001)113<1544:LCTEOT>2.0.CO;2. 1.2, 5.1

Burbank, D., J. McLean, M. Bullen, K. Abdrakhmatov, and M. Miller (1999), Partitioning of intermontane basins by thrust-related folding, Tien Shan, Kyrgyzstan, *Basin Research*, *11*(1), 75–92, doi:10.1046/j.1365-2117.1999.00086.x. 1.2, 2.1, 5.1, 5.1, 5.3.1, 5.7

Burbank, D. W., and R. S. Anderson (2011), *Tectonic Geomorphology, Second Edition*, John Wiley & Sons, doi: 10.1002/9781444345063. 1.1, 1.3, 1.2, 2.7.1

Burgette, R. J., R. J. Weldon II, K. Y. Abdrakhmatov, C. Ormukov, L. A. Owen, and S. C. Thompson (2017), Timing and process of river and lake terrace formation in the Kyrgyz Tien Shan, *Quaternary Science Reviews*, *159*, 15–34, doi:10.1016/j.quascirev.2017.01.003. 5.6.1

Burtman, V., and P. Molnar (1993), Geological and geophysical evidence for deep subduction of continental crust beneath the Pamir, *Special Paper of the Geological society of America*, *281, ISBN 0-8137-2281-0*, doi:10.1130/SPE281-p1. 1.2, 1.2, 3.1, 3.3, 3.1, 3.2, 3.3, 3.6, 3.13, 3.6

Burtman, V. S. (2013), The geodynamics of the Pamir-Punjab syntaxis, *Geotectonics*, *47*(1), 31–51, doi:10.1134/S0016852113010020. 1.2

Buwalda, J. P., and P. St. Amand (1955), Geological effects of the Arvin-Tehachapi earthquake, in Oakeshott, G.B., ed., earthquakes in Kern County California during 1952, *California Div Mines Bull.*, *171*, 41–56. 4.6

Buylaert, J. P., A. S. Murray, K. J. Thomsen, and M. Jain (2009), Testing the potential of an elevated temperature IRSL signal from K-feldspar, *Radiation Measurements*, *44*(5), 560–565, doi:10.1016/j.radmeas.2009.02.007. 4.3.2

Campbell, G. (2015), Active tectonics of the Tien Shan, Central Asia, Ph.D., University of Cambridge. 5.1, 5.2

Campbell, G. E., R. T. Walker, K. Abdrakhmatov, J. Schwenninger, J. Jackson, J. R. Elliott, and A. Copley (2013), The Dzhungarian fault: Late Quaternary tectonics and slip rate of a major right-lateral strike-slip fault in the northern Tien Shan region, *Journal of Geophysical Research: Solid Earth*, *118*(10), 5681–5698, doi:10.1002/jgrb.50367. 5.1

Casana, J., and J. Cothren (2008), Stereo analysis, DEM extraction and orthorectification of CORONA satellite imagery: archaeological applications from the Near East, *Antiquity*, *82*(317), 732–749, doi:10.1017/S0003598X00097349. 3.5

Cattin, R., P. Briole, H. Lyon-Caen, P. Bernard, and P. Pinettes (1999), Effects of superficial layers on coseismic displacements for a dip-slip fault and geophysical implications, *Geophysical Journal International*, *137*(1), 149–158, doi:10.1046/j.1365-246x.1999.00779.x. 2.4.1

Chediya, O. K. (1986), *Morfostruktury i noveishii tektogenez Tyan'-Shanya (Morfostructures and Neotectonics of the Tien Shan)*, Ilim, Frunze, Kyrgyzstan. 1.2

Chediya, O. K., G. Mikhel, and V. Mikhaylyov (1997), On rates of Holocene tectonic movements and an attempt to determine the duration of seismic calms in the central Tien Shan (in Russian), *Echo of Science. Proc. Nat. Acad. Sci. Kyrgyz Republic*, (1), 13–17. 4.5.1, 5.1, 5.3.5

Chen, H., F. Zhang, X. Cheng, L. Liao, J. Luo, J. Shi, B. Wang, C. Yang, and L. Chen (2010), The deformation features and basin-range coupling structure in the northeastern Pamir tectonic belt, *Scientia Geologica Sinica*, *45*, 102–112. 3.2.1, 3.3, 3.2.2

Chen, J., K. Scharer, D. Burbank, R. Heermance, and C.-S. Wang (2005), Quaternary detachment folding of the Mingyaole anticline, southwestern Tian Shan, *Dizhen Dizhi*, *27*, 530–547. 3.2.2, 3.2.3

Chen, J., R. Heermance, D. Burbank, K. M. Scharer, J. Miao, and C. Wang (2007), Quantification of growth and lateral propagation of the Kashi anticline, southwest Chinese Tian Shan, *J. Geophys. Res*, *112*, doi:10.1029/2006JB004345. 3.2.1

Chen, Y., V. Courtillot, J.-P. Cogné, J. Besse, Z. Yang, and R. Enkin (1993), The configuration of Asia prior to the collision of India: Cretaceous paleomagnetic constraints, *Journal of Geophysical Research: Solid Earth*, *98*(B12), 21,927–21,941, doi:10.1029/93JB02075. 1.2

Cheng, X., Z. Huang, H. Chen, Z. Du, K. Li, and J. Shi (2012), Fault characteristics and division of tectonic units of the thrust belt in the front of the West Kunlun Mountains, *Acta Petrologica Sinica*, *28*, 2591–2601. 3.2.2

Cheng, X., H. Chen, X. Lin, S. Yang, S. Chen, F. Zhang, K. Li, and Z. Liu (2016), Deformation geometry and timing of theWupoer thrust belt in the NE Pamir and its tectonic implications, *Frontiers of Earth Science*, *10*(4), 751–760, doi:10.1007/s11707-016-0606-z. 3.2.1, 3.3, 3.2.2

Chester, J. S., and F. M. Chester (1990), Fault-propagation folds above thrusts with constant dip, *Journal of Structural Geology*, *12*(7), 903–910, doi:10.1016/0191-8141(90)90063-5. 1.1

Cobbold, P., E. Sadybakasov, and J. Thomas (1994), Cenozoic transpression and basin development, Kyrghyz Tienshan, Central Asia, in *Geodynamic Evolution of Sedimentary Basins, International Symposium. ed. F. Roure et al.*, p. 457, Moscow. 5.1, 5.7

Copley, A. (2014), Postseismic afterslip 30 years after the 1978 Tabas-e-Golshan (Iran) earthquake: observations and implications for the geological evolution of thrust belts, *Geophysical Journal International*, *197*(2), 665–679, doi:10.1093/gji/ggu023. 2.7.1, 2.7.1, 3.5, 3.6

Copley, A., and R. Jolivet (2016), Fault rheology in an aseismic fold-thrust belt (Shahdad, eastern Iran), *Journal of Geophysical Research: Solid Earth*, p. 2015JB012431, doi:10.1002/2015JB012431. 1.1

Copley, A., and K. Reynolds (2014), Imaging topographic growth by long-lived postseismic afterslip at Sefidabeh, east Iran, *Tectonics*, *33*(3), 330–345, doi:10.1002/2013TC003462. 1.1, 2.7.1, 2.7.1, 3.5, 3.6

Copley, A., E. Karasozen, B. Oveisi, J. R. Elliott, S. Samsonov, and E. Nissen (2015), Seismogenic faulting of the sedimentary sequence and laterally variable material properties in the Zagros Mountains (Iran) revealed by the August 2014 Murmuri (E. Dehloran) earthquake sequence, *Geophysical Journal International*, *203*(2), 1436–1459, doi:10.1093/gji/ggv365. 2.6.1

Cording, A., R. Hetzel, M. Kober, and J. Kley (2014), 10be exposure dating of river terraces at the southern mountain front of the Dzungarian Alatau (SE Kazakhstan) reveals rate of thrust faulting over the past ˜ 400 ka, *Quaternary Research*, *81*(1), 168–178, doi:10.1016/j.yqres.2013.10.016. 5.8

Cowgill, E., R. D. Gold, C. Xuanhua, W. Xiao-Feng, J. R. Arrowsmith, and J. Southon (2009), Low Quaternary slip rate reconciles geodetic and geologic rates along the Altyn Tagh fault, northwestern Tibet, *Geology*, *37*(7), 647–650, doi:10.1130/G25623A.1. 1.1

Daëron, M., J.-P. Avouac, and J. Charreau (2007), Modeling the shortening history of a fault tip fold using structural and geomorphic records of deformation, *Journal of Geophysical Research: Solid Earth*, *112*(B3), doi:10.1029/2006JB004460. 2.1, 2.7.1

Davies, J., and A. Kent (2017), *The Red Atlas*, University of Chicago Press, Chicago, USA. A.2

De Zan, F., and A. Monti Guarnieri (2006), TOPSAR: Terrain Observation by Progressive Scans, *IEEE Transactions on Geoscience and Remote Sensing*, *44*(9), 2352–2360, doi:10.1109/TGRS.2006.873853. 2.3.1

DeCelles, P. G., P. Kapp, G. E. Gehrels, and L. Ding (2014), Paleocene-Eocene foreland basin evolution in the Himalaya of southern Tibet and Nepal: Implications for the age of initial India-Asia collision, *Tectonics*, *33*(5), 824–849, doi:10.1002/2014TC003522. 1.2

Deev, E. V., I. V. Turova, A. M. Korzhenkov, D. V. Luzhansky, A. S. Gladkov, M. V. Rodkin, S. V. Abdieva, J. V. Maeika, E. A. Rogozhin, A. B. Fortuna, A. M. Muraliev, T. A. Charimov, and A. S. Yudakhin (2016), Paleoseismological and archaeoseismological data from the western AlabashKonurolen intramontane basin (southern Lake Issyk Kul area, Kyrgyzstan), *Russian Geology and Geophysics*, *57*(7), 1090–1098, doi:10.1016/j.rgg.2016.06.008. 4.1, 4.5.1

Delvaux, D., K. Abdrakhmatov, I. N Lemzin, and A. Strom (2001), Landslides and surface breaks of the 1911 Ms 8.2 Kemin earthquake, Kyrgyzstan, *Russian Geology and Geophysics*, *42*, 1583–1592. 1.2, 5.8.1

Dewey, J. F., and K. C. A. Burke (1973), Tibetan, Variscan, and Precambrian Basement Reactivation: Products of Continental Collision, *The Journal of Geology*, *81*(6), 683–692. 1.2

D'Lemos, R. S., D. I. Schofield, R. E. Holdsworth, and T. R. King (1997), Deep crustal and local rheological controls on the siting and reactivation of fault and shear zones, northeastern Newfoundland, *Journal of the Geological Society*, *154*(1), 117–121, doi:10.1144/gsjgs.154.1.0117. 3.6

Dolan, J. F., and B. D. Haravitch (2014), How well do surface slip measurements track slip at depth in large strike-slip earthquakes? The importance of fault structural maturity in controlling on-fault slip versus off-fault surface deformation, *Earth and Planetary Science Letters*, *388*, 38–47, doi:10.1016/j.epsl.2013.11.043. 5.8

Dupont-Nivet, G., P. C. Lippert, V. Hinsbergen, D. J.j, M. J. M. Meijers, and P. Kapp (2010), Palaeolatitude and age of the IndoAsia collision: palaeomagnetic constraints, *Geophysical Journal International*, *182*(3), 1189–1198, doi:10.1111/j.1365-246X.2010.04697.x. 1.2

Ekström, G., M. Nettles, and A. M. Dziewoski (2012), The global CMT project 20042010: Centroid-moment tensors for 13,017 earthquakes, *Physics of the Earth and Planetary Interiors*, *200201*, 1–9, doi:10.1016/j.pepi.2012.04.002. 1.1, 1.6, 3.3

Elliott, J., A. Copley, R. Holley, K. Scharer, and B. Parsons (2013), The 2011 Mw 7.1 Van (Eastern Turkey) earthquake, *Journal of Geophysical Research: Solid Earth*, *118*(4), 1619–1637, doi:10.1002/jgrb.50117. 1.1

Elliott, J. R., J. Biggs, B. Parsons, and T. J. Wright (2008), InSAR slip rate determination on the Altyn Tagh Fault, northern Tibet, in the presence of topographically correlated atmospheric delays, *Geophysical Research Letters*, *35*(12), doi:10.1029/2008GL033659. 2.6.1, 5.6.3

Elliott, J. R., E. A. Bergman, A. C. Copley, A. R. Ghods, E. K. Nissen, B. Oveisi, M. Tatar, R. J. Walters, and F. Yamini-Fard (2015), The 2013 Mw 6.2 Khaki-Shonbe

(Iran) Earthquake: Insights into seismic and aseismic shortening of the Zagros sedimentary cover, *Earth and Space Science*, *2*(11), 435–471, doi:10.1002/2015EA000098. 2.7.1, 3.6, 3.6

Elliott, J. R., R. Jolivet, P. J. Gonzlez, J.-P. Avouac, J. Hollingsworth, M. P. Searle, and V. L. Stevens (2016), Himalayan megathrust geometry and relation to topography revealed by the Gorkha earthquake, *Nature Geoscience*, *9*(2), 174–180, doi:10.1038/ngeo2623. 2.7.1

Engdahl, E. R., R. v. d. Hilst, and R. Buland (1998), Global teleseismic earthquake relocation with improved travel times and procedures for depth determination, *Bulletin of the Seismological Society of America*, *88*(3), 722–743. 3.3

England, P., and G. Houseman (1985), Role of lithospheric strength heterogeneities in the tectonics of Tibet and neighbouring regions, *Nature*, *315*(6017), 297, doi:10.1038/315297a0. 1.2

England, P., and P. Molnar (2005), Late Quaternary to decadal velocity fields in Asia, *Journal of Geophysical Research: Solid Earth*, *110*(B12), B12,401, doi:10.1029/2004JB003541. 1.2, 2.2

England, P., and P. Molnar (2015), Rheology of the lithosphere beneath the central and western Tien Shan, *Journal of Geophysical Research: Solid Earth*, *120*(5), 3803–3823, doi:10.1002/2014JB011733. 5.1, 5.6.3, 5.6.3

Erslev, E. (1991), Trishear fault-propagation folding, *Geology*, *19*(6), 617–620, doi:10.1130/0091-7613(1991)019<0617:TFPF>2.3.CO;2. 1.1, 2.1

Falcon, N. L. (1969), Problems of the relationship between surface structure and deep displacements illustrated by the Zagros Range, *Geological Society, London, Special Publications*, *3*(1), 9–21, doi:10.1144/GSL.SP.1969.003.01.02. 1.1, 3.6

Fan, G., J. F. Ni, and T. C. Wallace (1994), Active tectonics of the Pamirs and Karakorum, *Journal of Geophysical Research: Solid Earth*, *99*(B4), 7131–7160, doi:10.1029/93JB02970. 1.2, 3.3, 3.1, 3.2, 3.3

Farr, T. G., P. A. Rosen, E. Caro, R. Crippen, R. Duren, S. Hensley, M. Kobrick, M. Paller, E. Rodriguez, L. Roth, D. Seal, S. Shaffer, J. Shimada, J. Umland, M. Werner, M. Oskin, D. Burbank, and D. Alsdorf (2007), The Shuttle Radar Topography Mission, *Reviews of Geophysics*, *45*(2), doi:10.1029/2005RG000183. 4.3.1

Feng, X., Z. Yang, C.-Q. Luan, D. Yu, D. Kou, and Y. Zhang (1986), The Wuqia earthquake of Xinjiang, *Earthquake Research in China*, *2*(1), 56–60. 3.1, 3.3, 3.3, 3.6, 3.4, 3.5, 3.4, 3.6

Feng, Z.-Y., C.-Q. Luan, J. Li, and Y. Zhang (1988), The deformation zone of Wuqia earthquake of M = 7.4 in 1985, *Seismology & Geology*, *10*(2), 39–45. 3.3, 3.4, 3.4, 3.5, 3.4

Field, E. H., R. J. Arrowsmith, G. P. Biasi, P. Bird, T. E. Dawson, K. R. Felzer, D. D. Jackson, K. M. Johnson, T. H. Jordan, C. Madden, A. J. Michael, K. R. Milner, M. T. Page, T. Parsons, P. M. Powers, B. E. Shaw, W. R. Thatcher, R. J. Weldon, and Y. Zeng (2014), Uniform California Earthquake Rupture Forecast, Version 3 (UCERF3)The TimeIndependent Model, *Bulletin of the Seismological Society of America*, *104*(3), 1122–1180, doi:10.1785/0120130164. 4.1

Fielding, E. J., P. R. Lundgren, T. Taymaz, S. YolsalÇevikbilen, and S. E. Owen (2013), FaultSlip Source Models for the 2011 M 7.1 Van Earthquake in Turkey from SAR Interferometry, Pixel Offset Tracking, GPS, and Seismic Waveform Analysis, *Seismological Research Letters*, *84*(4), 579–593, doi:10.1785/0220120164. 1.1

Fletcher, K. E. K., W. D. Sharp, K. J. Kendrick, W. M. Behr, K. W. Hudnut, and T. C. Hanks (2010), 230th/U dating of a late Pleistocene alluvial fan along the southern San Andreas fault, *GSA Bulletin*, *122*(9-10), 1347–1359, doi:10.1130/B30018.1. 5.2, 5.6.1

Floyd, M. A., R. J. Walters, J. R. Elliott, G. J. Funning, J. L. Svarc, J. R. Murray, A. J. Hooper, Y. Larsen, P. Marinkovic, R. Bürgmann, I. A. Johanson, and T. J. Wright (2016), Spatial variations in fault friction related to lithology from rupture and afterslip of the 2014 South Napa, California, earthquake, *Geophysical Research Letters*, *43*(13), 6808–6816, doi:10.1002/2016GL069428. 3.5, 3.6

Freed, A. M. (2007), Afterslip (and only afterslip) following the 2004 Parkfield, California, earthquake, *Geophysical Research Letters*, *34*(6), doi:10.1029/2006GL029155. 3.5

Funning, G. J., B. Parsons, T. J. Wright, J. A. Jackson, and E. J. Fielding (2005), Surface displacements and source parameters of the 2003 Bam (Iran) earthquake from Envisat advanced synthetic aperture radar imagery, *Journal of Geophysical Research: Solid Earth*, *110*(B9), doi:10.1029/2004JB003338. 2.3.1, 2.3.1

Galbraith, R. F., R. G. Roberts, G. M. Laslett, H. Yoshida, and J. M. Olley (1999), Optical Dating of Single and Multiple Grains of Quartz from Jinmium Rock Shelter, Northern Australia: Part I, Experimental Design and Statistical Models, *Archaeometry*, *41*(2), 339–364, doi:10.1111/j.1475-4754.1999.tb00987.x. 4.3.2, 4.3, 5.3.5

Ge, W.-P., P. Molnar, Z.-K. Shen, and Q. Li (2015), Present-day crustal thinning in the southern and northern Tibetan Plateau revealed by GPS measurements, *Geophysical Research Letters*, *42*(13), 5227–5235, doi:10.1002/2015GL064347. 2.2

Ghose, S., R. J. Mellors, A. M. Korjenkov, M. W. Hamburger, T. L. Pavlis, G. L. Pavlis, M. Omuraliev, E. Mamyrov, and A. R. Muraliev (1997), The Ms = 7.3 1992 Suusamyr, Kyrgyzstan, earthquake in the Tien Shan: 2. Aftershock focal mechanisms and surface deformation, *Bulletin of the Seismological Society of America*, *87*(1), 23–38. 4.1, 4.2, 4.4, 4.4.1, 4.4.1, 4.4.2, 4.6, 4.4.2, 4.5.1, 4.6, 5.1

Ghose, S., M. Hamburger, and C. Ammon (1998), Source parameters of moderate-sized earthquakes in the Tien Shan, central Asia from regional moment tensor inversion, *Geophysical Research Letters*, *25*(16), 3181–3184. 1.2, 1.2, 4.2, 4.6, 5.1, 5.1, 5.6.3

Gile, L. H., F. F. Peterson, and R. B. Grossman (1966), Morphological and genetic consequences of carbonate accumulation in desert soils, *Soil Science*, *101*(5), 347. 5.6.1

Gold, R. D., E. Cowgill, J. R. Arrowsmith, and A. M. Friedrich (2017), Pulsed strain release on the Altyn Tagh fault, northwest China, *Earth and Planetary Science Letters*, *459*, 291–300, doi:10.1016/j.epsl.2016.11.024. 1.1

Goldfinger, C., Y. Ikeda, R. Yeats, and J. Ren (2013), Superquakes and Supercycles, *Seismological Research Letters*, *84*, 24, doi:10.1785/0220110135. 1.1

Goldstein, R. M., and C. L. Werner (1998), Radar interferogram filtering for geophysical applications, *Geophysical Research Letters*, *25*(21), 4035–4038, doi:10.1029/1998GL900033. 2.3.1

Gómez, J. M., B. Bukchin, R. Madariaga, E. A. Rogozhin, and B. Bogachkin (1997), Rupture process of the 19 August 1992 Susamyr, Kyrgyzstan, earthquake, *Journal of Seismology*, *1*(3), 219–235, doi:10.1023/A:1009780226399. 4.1, 4.2, 4.4.1, 5.6.1

Goode, J. K., D. W. Burbank, and B. Bookhagen (2011), Basin width control of faulting in the Naryn Basin, south-central Kyrgyzstan, *Tectonics*, *30*(6), doi:10.1029/2011TC002910. 5.1, 5.7

Goode, J. K., D. W. Burbank, and C. Ormukov (2014), Pliocene-Pleistocene initiation, style, and sequencing of deformation in the central Tien Shan, *Tectonics*, *33*(4), 464–484, doi:10.1002/2013TC003394. 5.1

Gourmelen, N., and F. Amelung (2005), Postseismic Mantle Relaxation in the Central Nevada Seismic Belt, *Science*, *310*(5753), 1473–1476, doi:10.1126/science.1119798. 3.5

Grandin, R., M. Vallée, C. Satriano, R. Lacassin, Y. Klinger, M. Simoes, and L. Bollinger (2015), Rupture process of the Mw = 7.9 2015 Gorkha earthquake (Nepal): Insights into Himalayan megathrust segmentation, *Geophysical Research Letters*, *42*(20), 8373–8382, doi:10.1002/2015GL066044. 4.6

Grant, L., and K. Sieh (1994), Paleoseismic evidence of clustered earthquakes on the San Andreas Fault in the Carrizo Plain, California, *Journal of Geophysical Research*, *99*(B4), 6819–6841, doi:10.1029/94JB00125. 1.1, 5.8.1

Grützner, C., E. Carson, R. T. Walker, E. J. Rhodes, A. Mukambayev, D. Mackenzie, J. R. Elliott, G. Campbell, and K. Abdrakhmatov (2017), Assessing the activity of faults in continental interiors: Palaeoseismic insights from SE Kazakhstan, *Earth and Planetary Science Letters*, *459*, 93–104, doi:10.1016/j.epsl.2016.11.025. 4.1, 4.5.1

Guérin, G., N. Mercier, and G. Adamiec (2011), Dose-rate conversion factors: Update, *Ancient TL*, *29*, 5–8. B

Guidoboni, E., A. Comastri, D. Mariotti, C. Ciuccarelli, and M. G. Bianchi (2012), Ancient and Medieval Earthquakes in the Area of LAquila (Northwestern Abruzzo,

Central Italy), A.D. 11500: A Critical Revision of the Historical and Archaeological DataAncient and Medieval Earthquakes in the Area of LAquila (Central Italy), A.D. 11500, *Bulletin of the Seismological Society of America*, *102*(4), 1600–1617, doi:10.1785/0120110173. 1.1

Guilbaud, C., M. Simoes, L. Barrier, A. Laborde, J. Van der Woerd, H. Li, P. Tapponnier, T. Coudroy, and A. Murray (2017), Kinematics of active deformation across the Western Kunlun mountain range (Xinjiang, China), and potential seismic hazards within the southern Tarim Basin., *Journal of Geophysical Research: Solid Earth*, p. 2017JB014069, doi:10.1002/2017JB014069. 2.5.2, 2.4

Hay, M. B. (1888), The Earthquakes of May and June, 1887, in the Verny (Vernoe) District, Russian Turkestan, and Their Consequences, *Proceedings of the Royal Geographical Society and Monthly Record of Geography*, *10*(10), 638–646, doi:10.2307/1800851. 1.2, 5.8.1

He, P., Q. Wang, K. Ding, M. Wang, X. Qiao, J. Li, Y. Wen, C. Xu, S. Yang, and R. Zou (2016), Source model of the 2015 Mw 6.4 Pishan earthquake constrained by InSAR and GPS: insight into blind rupture in the western Kunlun Shan, *Geophysical Research Letters*, pp. 1511–1519, doi:10.1002/2015GL067140. **??**, 2.3.1, 2.3.1

Heermance, R. V., J. Chen, D. W. Burbank, and C. Wang (2007), Chronology and tectonic controls of Late Tertiary deposition in the southwestern Tian Shan foreland, NW China, *Basin Research*, *19*(4), 599–632, doi:10.1111/j.1365-2117.2007.00339.x. 3.2.1, 3.2, 3.2.1

Heermance, R. V., J. Chen, D. W. Burbank, and J. Miao (2008), Temporal constraints and pulsed Late Cenozoic deformation during the structural disruption of the active Kashi foreland, northwest China, *Tectonics*, *27*(6), TC6012, doi:10.1029/2007TC002226. 2.4, 3.1, 3.2.1, 3.2.1, 3.3, 3.2.2, 3.2.2, 3.2.3

Helmstetter, A., and B. E. Shaw (2009), Afterslip and aftershocks in the rate-and-state friction law, *Journal of Geophysical Research: Solid Earth*, *114*(B1), B01,308, doi:10.1029/2007JB005077. 2.6.3

Hemphill-Haley, M. A., and R. J. Weldon (1999), Estimating prehistoric earthquake magnitude from point measurements of surface rupture, *Bulletin of the Seismological Society of America*, *89*(5), 1264–1279. 4.1

Hendrix, M. S., T. A. Dumitru, and S. A. Graham (1994), Late Oligocene-early Miocene unroofing in the Chinese Tian Shan: An early effect of the India-Asia collision, *Geology*, *22*(6), 487–490, doi:10.1130/0091-7613(1994)022<0487:LOEMUI>2.3.CO;2. 1.2

Hollingsworth, J., S. Leprince, F. Ayoub, and J.-P. Avouac (2012), Deformation during the 19751984 Krafla rifting crisis, NE Iceland, measured from historical optical imagery, *Journal of Geophysical Research: Solid Earth*, *117*(B11), B11,407, doi:10.1029/2012JB009140. 3.5

Hollingsworth, J., S. Leprince, F. Ayoub, and J.-P. Avouac (2013), New constraints on dike injection and fault slip during the 19751984 Krafla rift crisis, NE Iceland, *Journal*

of Geophysical Research: Solid Earth, *118*(7), 3707–3727, doi:10.1002/jgrb.50223. A.1

Holt, W. E., and T. C. Wallace (1987), A procedure for the joint inversion of regional and teleseismic long-period body waves, *Geophysical Research Letters*, *14*(9), 903–906, doi:10.1029/GL014i009p00903. 3.3

Homza, T. X., and W. K. Wallace (1995), Geometric and kinematic models for detachment folds with fixed and variable detachment depths, *Journal of Structural Geology*, *17*(4), 575–588, doi:10.1016/0191-8141(94)00077-D. 1.1, 2.1

Honda, R., and K. Yomogida (2003), Effects of a soft surface layer on near-fault static and dynamic displacements, *Geophysical Journal International*, *154*(2), 441–462, doi:10.1046/j.1365-246X.2003.02014.x. 2.4.1

Howarth, J. D., S. J. Fitzsimons, R. J. Norris, R. Langridge, and M. J. Vandergoes (2016), A 2000 yr rupture history for the Alpine fault derived from Lake Ellery, South Island, New Zealand, *Geological Society of America Bulletin*, *128*(3-4), 627–643, doi:10.1130/B31300.1. 1.1

Hu, B. (1992), Petroleum geology and prospects of the Tarim (Talimu) Basin, China, *Giant oil and gas fields of the decade 1978-1988, AAPG Memoir*, pp. 493–510, doi:10.1306/M54555C31. 3.2.1, 3.2.1

Hu, X., E. Garzanti, T. Moore, and I. Raffi (2015), Direct stratigraphic dating of India-Asia collision onset at the Selandian (middle Paleocene, 59 1 Ma), *Geology*, *43*(10), 859–862, doi:10.1130/G36872.1. 1.2

Hu, Y. (1982), Late Tertiary foraminifera of the Tarim basin and their geological significance, *Chinese Science Bulletin*, *27*(15), 938–941. 3.2.1

Hubbard, J., J. H. Shaw, J. Dolan, T. L. Pratt, L. McAuliffe, and T. K. Rockwell (2014), Structure and Seismic Hazard of the Ventura Avenue Anticline and Ventura Fault, California: Prospect for Large, Multisegment Ruptures in the Western Transverse Ranges, *Bulletin of the Seismological Society of America*, doi:10.1785/0120130125. 2.7.1

Huntley, D., and M. Baril (1997), The K content of the K-feldspars being in measured in optical and thermoluminescence dating, *Ancient TL*, *15*, 11–13. B

Huntley, D., and R. Hancock (2001), The Rb contents of the K-feldspar grains being measured in optical dating, *Ancient TL*, *19*, 43–46. B

Huntley, D. J., and M. Lamothe (2001), Ubiquity of anomalous fading in K-feldspars and the measurement and correction for it in optical dating, *Canadian Journal of Earth Sciences*, *38*(7), 1093–1106, doi:10.1139/e01-013. 4.3.2

Ignatiev, I. (1886), Earthquakes in Tomak district in 1885 (in Russian), *Isvestia Russ. Geogr. Soc.*, *22*, 1–14. 5.8.1

Ischuk, A., R. Bendick, A. Rybin, P. Molnar, S. F. Khan, S. Kuzikov, S. Mohadjer, U. Saydullaev, Z. Ilyasova, G. Schelochkov, and A. V. Zubovich (2013), Kinematics of the Pamir and Hindu Kush regions from GPS geodesy, *Journal of Geophysical Research: Solid Earth*, *118*(5), 2408–2416, doi:10.1002/jgrb.50185. 1.2

Jackson, J., and D. McKenzie (1988), The relationship between plate motions and seismic moment tensors, and the rates of active deformation in the Mediterranean and Middle East, *Geophysical Journal International*, *93*(1), 45–73, doi:10.1111/j.1365-246X.1988.tb01387.x. 1.1

James, M. R., and S. Robson (2014), Mitigating systematic error in topographic models derived from UAV and ground-based image networks, *Earth Surface Processes and Landforms*, *39*(10), 1413–1420, doi:10.1002/esp.3609. 4.3.1, A.2

Jamison, W. R. (1987), Geometric analysis of fold development in overthrust terranes, *Journal of Structural Geology*, *9*(2), 207–219, doi:10.1016/0191-8141(87)90026-5. 1.1

Jay, C. N., L. M. Flesch, and R. O. Bendick (2017), Kinematics and dynamics of the Pamir, Central Asia: Quantifying surface deformation and force balance in an intra-continental subduction zone, *Journal of Geophysical Research: Solid Earth*, *122*(6), 4741–4762, doi:10.1002/2017JB014177. 1.2

Ji, C., D. V. Helmberger, T.-R. A. Song, K.-F. Ma, and D. J. Wald (2001), Slip distribution and tectonic implication of the 1999 Chi-Chi, Taiwan, Earthquake, *Geophysical Research Letters*, *28*(23), 4379–4382, doi:10.1029/2001GL013225. 4.6

Jiang, X., Z.-X. Li, and H. Li (2013), Uplift of the West Kunlun Range, northern Tibetan Plateau, dominated by brittle thickening of the upper crust, *Geology*, *41*(4), 439–442, doi:10.1130/G33890.1. 2.2

Jiang, X.-D., and Z.-X. Li (2014), Seismic reflection data support episodic and simultaneous growth of the Tibetan Plateau since 25 Myr, *Nature Communications*, *5*, 5453, doi:10.1038/ncomms6453. 2.2, 2.7.2

Johanson, I. A., E. J. Fielding, F. Rolandone, and R. Bürgmann (2006), Coseismic and Postseismic Slip of the 2004 Parkfield Earthquake from Space-Geodetic Data, *Bulletin of the Seismological Society of America*, *96*(4B), S269–S282, doi:10.1785/0120050818. 3.6

Jolivet, R., C. Lasserre, M.-P. Doin, S. Guillaso, G. Peltzer, R. Dailu, J. Sun, Z.-K. Shen, and X. Xu (2012), Shallow creep on the Haiyuan Fault (Gansu, China) revealed by SAR Interferometry, *Journal of Geophysical Research: Solid Earth*, *117*(B6), B06,401, doi:10.1029/2011JB008732. 1.1

Jónsson, S., P. Segall, R. Pedersen, and G. Björnsson (2003), Post-earthquake ground movements correlated to pore-pressure transients, *Nature*, *424*(6945), 179–183, doi:10.1038/nature01776. 2.6.2

Kalmetieva, Z., A. Mikolaichuk, B. Moldobekov, A. Meleshko, M. Jantaev, A. Zubovich, and H.-B. Havenith (2009), *Atlas of Earthquakes in Kyrgyzstan*. 1.2, 4.1

Kaneda, H., T. Nakata, H. Tsutsumi, H. Kondo, N. Sugito, Y. Awata, S. S. Akhtar, A. Majid, W. Khattak, A. A. Awan, R. S. Yeats, A. Hussain, M. Ashraf, S. G. Wesnousky, and A. B. Kausar (2008), Surface Rupture of the 2005 Kashmir, Pakistan, Earthquake and Its Active Tectonic ImplicationsSurface Rupture of the 2005 Kashmir, Pakistan, Earthquake and Its Active Tectonic Implications, *Bulletin of the Seismological Society of America*, *98*(2), 521–557, doi:10.1785/0120070073. 4.6

Kao, H., R. Gao, R.-J. Rau, D. Shi, R.-Y. Chen, Y. Guan, and F. T. Wu (2001), Seismic image of the Tarim basin and its collision with Tibet, *Geology*, *29*(7), 575–578, doi:10.1130/0091-7613(2001)029<0575:SIOTTB>2.0.CO;2. 2.2

Keller, E. A., R. L. Zepeda, T. K. Rockwell, T. L. Ku, and W. S. Dinklage (1998), Active tectonics at Wheeler Ridge, southern San Joaquin Valley, California, *Geological Society of America Bulletin*, *110*(3), 298–310, doi:10.1130/0016-7606(1998)110<0298:ATAWRS>2.3.CO;2. 5.3.1

King, G. C. P., R. S. Stein, and J. Lin (1994), Static stress changes and the triggering of earthquakes, *Bulletin of the Seismological Society of America*, *84*(3), 935–953. 3.6

Kondorskaya, N. V., N. V. Shebalin, Y. A. Khrometskaya, and A. D. Gvishiani (1982), *New catalog of strong earthquakes in the USSR from ancient times through 1977; translated by World Data Center A for Solid Earth Geophysics*, Boulder, Colorado. 1.2, 3.1, 4.1, 5.8.1

Koppes, M., A. R. Gillespie, R. M. Burke, S. C. Thompson, and J. Stone (2008), Late quaternary glaciation in the Kyrgyz Tien Shan, *Quaternary Science Reviews*, *27*(7-8), 846–866. 5.6.1

Korjenkov, A., D. Bowman, K. Haselton, and N. Porat (1999), Recent drainage diversions under thrusting conditions in the Suusamyr Valley, the Tien Shan Range, Kyrgyzstan, *Israel Journal of Earth Sciences*, *48*(2), 63–79. 4.5.1, 5.1, 5.3.1, 5.3.5, 5.12, 5.5

Kostrov, V. (1974), Seismic moment and energy of earthquakes, and seismic flow of rock, *Physics of the Solid Earth*, *1*, 13–21. 1.1

Kreemer, C., G. Blewitt, and E. C. Klein (2014), A geodetic plate motion and Global Strain Rate Model, *Geochemistry, Geophysics, Geosystems*, *15*(10), 3849–3889, doi:10.1002/2014GC005407. 1.2, 1.5

Krüger, F., G. Kulikova, and A. Landgraf (2015), Instrumental magnitude constraints for the 11 July 1889, Chilik earthquake, *Geological Society, London, Special Publications*, *432*, SP432.8, doi:10.1144/SP432.8. 1.2, 4.1, 5.8.1

Kulikova, G., and F. Krüger (2015), Source process of the 1911 M8.0 Chon-Kemin earthquake: investigation results by analogue seismic records, *Geophysical Journal International*, *201*(3), 1891–1911, doi:10.1093/gji/ggv091. 1.2, 4.1, 5.8.1

Kulikova, G., and F. Krüger (2017), Historical seismogram reproductions for the source parameters determination of the 1902, Atushi (Kashgar) earthquake, *Journal of Seismology*, *21*(6), 1577–1597, doi:10.1007/s10950-017-9683-z. 3.1, 4.1

Landgraf, A., O. Zielke, J. R. Arrowsmith, P. Ballato, M. R. Strecker, T. F. Schildgen, A. M. Friedrich, and S. H. Tabatabaei (2013), Differentiating simple and composite tectonic landscapes using numerical fault slip modeling with an example from the south central Alborz Mountains, Iran, *Journal of Geophysical Research: Earth Surface*, *118*(3), 1792–1805, doi:10.1002/jgrf.20109. 1.1

Landgraf, A., A. Dzhumabaeva, K. E. Abdrakhmatov, M. R. Strecker, E. A. Macaulay, J. Arrowsmith, H. Sudhaus, F. Preusser, G. Rugel, and S. Merchel (2016), Repeated large-magnitude earthquakes in a tectonically active, low-strain continental interior: The northern Tien Shan, Kyrgyzstan, *Journal of Geophysical Research: Solid Earth*, *121*(5), 2015JB012,714, doi:10.1002/2015JB012714. 1.2, 4.1, 4.5.1, 5.6.2, 5.8.1

Le Béon, M., J. Suppe, M. K. Jaiswal, Y.-G. Chen, and M. E. Ustaszewski (2014), Deciphering cumulative fault slip vectors from fold scarps: Relationships between long-term and coseismic deformations in central Western Taiwan, *Journal of Geophysical Research: Solid Earth*, *119*(7), 2013JB010,794, doi:10.1002/2013JB010794. 2.7.1, 2.7.1

Lee, W. H. K., F. T. Wu, and C. Jacobsen (1976), A catalog of historical earthquakes in China compiled from recent Chinese publications, *Bulletin of the Seismological Society of America*, *66*(6), 2003–2016. 1.1

Lee, W. H. K., F. T. Wu, and S. C. Wang (1978), A catalog of instrumentally determined earthquakes in China (magnitude greater than 6) compiled from various sources, *Bulletin of the Seismological Society of America*, *62*(2), 383–398. 1.1, 2.2

Lee, Y.-H., M.-L. Hsieh, S.-D. Lu, T.-S. Shih, W.-Y. Wu, Y. Sugiyama, T. Azuma, and Y. Kariya (2003), Slip vectors of the surface rupture of the 1999 Chi-Chi earthquake, western Taiwan, *Journal of Structural Geology*, *25*(11), 1917–1931, doi:10.1016/S0191-8141(03)00039-7. 4.6

Lefevre, M., Y. Klinger, M. Al-Qaryouti, M. Le Béon, and K. Moumani (2018), Slip deficit and temporal clustering along the Dead Sea fault from paleoseismological investigations, *Scientific Reports*, *8*(1), 4511, doi:10.1038/s41598-018-22627-9. 5.8.1

Leonard, M. (2010), Earthquake Fault Scaling: Self-Consistent Relating of Rupture Length, Width, Average Displacement, and Moment ReleaseEarthquake Fault Scaling: Self-Consistent Relating of Rupture Length, Width, Average Displacement, *Bulletin of the Seismological Society of America*, *100*(5A), 1971–1988, doi:10.1785/0120090189. 4.1

Leprince, S., S. Barbot, F. Ayoub, and J.-P. Avouac (2007a), Automatic and Precise Orthorectification, Coregistration, and Subpixel Correlation of Satellite Images, Application to Ground Deformation Measurements, *IEEE Transactions on Geoscience and Remote Sensing*, *45*(6), 1529–1558, doi:10.1109/TGRS.2006.888937. 3.5

Leprince, S., F. Ayoub, Y. Klinger, and J. P. Avouac (2007b), Co-Registration of Optically Sensed Images and Correlation (COSI-Corr): an operational methodology for ground deformation measurements, in *2007 IEEE International Geoscience and Remote Sensing Symposium*, pp. 1943–1946, doi:10.1109/IGARSS.2007.4423207. 3.5

Leprince, S., K. W. Hudnut, S. O. Akciz, A. Hinojosa-Corona, and J. M. Fletcher (2011), Surface rupture and slip variation induced by the 2010 El Mayor-Cucapah earthquake, Baja California, quantified using COSI-Corr analysis on pre- and post-earthquake LiDAR acquisitions, *AGU Fall Meeting Abstracts*, *41*, EP41A–0596. A.2.2

Lettis, W. R., D. L. Wells, and J. N. Baldwin (1997), Empirical observations regarding reverse earthquakes, blind thrust faults, and quaternary deformation: Are blind thrust faults truly blind?, *Bulletin of the Seismological Society of America*, *87*(5), 1171–1198. 4.6, 6

Li, A., Y. Ran, L. Xu, and H. Liu (2013a), Paleoseismic study of the east Kalpintage fault in southwest Tianshan based on deformation of alluvial fans and 10be dating, *Natural Hazards*, *68*(2), 1075–1087, doi:10.1007/s11069-013-0675-1. 5.6.2

Li, H., J. Van der Woerd, Z. Sun, J. Si, P. Tapponnier, J. Pan, D. Liu, and M.-L. Chevalier (2012a), Co-seismic and cumulative offsets of the recent earthquakes along the Karakax left-lateral strike-slip fault in western Tibet, *Gondwana Research*, *21*(1), 64–87, doi:10.1016/j.gr.2011.07.025. 2.2

Li, T., J. Chen, J. A. Thompson, D. W. Burbank, and W. Xiao (2012b), Equivalency of geologic and geodetic rates in contractional orogens: New insights from the Pamir Frontal Thrust, *Geophysical Research Letters*, *39*(15), L15,305, doi:10.1029/2012GL051782. 3.2.2, 3.2.3, 3.2.3, 3.3

Li, T., J. Chen, J. A. Thompson, D. W. Burbank, and X. Yang (2013b), Quantification of three-dimensional folding using fluvial terraces: A case study from the Mushi anticline, northern margin of the Chinese Pamir, *Journal of Geophysical Research: Solid Earth*, *118*(8), 4628–4647, doi:10.1002/jgrb.50316. 3.1, 3.2.1, 3.4, 3.2.2, 3.2.3

Li, T., J. Chen, J. A. Thompson, D. W. Burbank, and X. Yang (2015), Active flexural-slip faulting: A study from the Pamir-Tian Shan convergent zone, NW China, *Journal of Geophysical Research: Solid Earth*, *120*(6), 2014JB011,632, doi:10.1002/2014JB011632. 3.2

Li, T., J. Chen, L. Fang, Z. Chen, J. A. Thompson, and C. Jia (2016), The 2015 Mw 6.4 Pishan Earthquake: Seismic Hazards of an Active Blind Wedge Thrust System at the Western Kunlun Range Front, Northwest Tibetan Plateau, *Seismological Research Letters*, *87*(3), 601–608, doi:10.1785/0220150205. 2.3.1, 2.3.1, 2.4, 2.4, 2.8, 2.5.1, 2.5.1, 2.7.2, 2.8

Li, Y., G. Liu, Y. Chen, Y. Li, J. Harbor, A. P. Stroeven, M. Caffee, M. Zhang, C. Li, and Z. Cui (2014), Timing and extent of Quaternary glaciations in the Tianger Range, eastern Tian Shan, China, investigated using 10be surface exposure dating, *Quaternary Science Reviews*, *98*, 7–23, doi:10.1016/j.quascirev.2014.05.009. 5.6.1

Lifton, N., C. Beel, C. Hättestrand, C. Kassab, I. Rogozhina, R. Heermance, M. Oskin, D. Burbank, R. Blomdin, N. Gribenski, M. Caffee, B. M. Goehring, J. Heyman, M. Ivanov, Y. Li, Y. Li, D. Petrakov, R. Usubaliev, A. T. Codilean, Y. Chen, J. Harbor, and A. P. Stroeven (2014), Constraints on the late Quaternary glacial history of the Inylchek and Sary-Dzaz valleys from in situ cosmogenic

10be and 26al, eastern Kyrgyz Tian Shan, *Quaternary Science Reviews*, *101*, 77–90, doi:10.1016/j.quascirev.2014.06.032. 5.6.1

Lin, A., Z. Ren, D. Jia, and X. Wu (2009), Co-seismic thrusting rupture and slip distribution produced by the 2008 Mw 7.9 Wenchuan earthquake, China, *Tectonophysics*, *471*(3), 203–215, doi:10.1016/j.tecto.2009.02.014. 4.6

Lin, J., and R. Stein (1989), Coseismic folding, earthquake recurrence, and the 1987 source mechanism at Whittier Narrows, Los Angeles basin, California, *Journal of Geophysical Research*, *94*(B7), 9614–9632. 4.6

Lin, J., and R. S. Stein (2004), Stress triggering in thrust and subduction earthquakes and stress interaction between the southern San Andreas and nearby thrust and strike-slip faults, *Journal of Geophysical Research: Solid Earth*, *109*(B2), doi:10.1029/2003JB002607. 3.6

Liu, Y., C. Xu, Z. Li, Y. Wen, J. Chen, and Z. Li (2016), Time-Dependent Afterslip of the 2009 Mw 6.3 Dachaidan Earthquake (China) and Viscosity beneath the Qaidam Basin Inferred from Postseismic Deformation Observations, *Remote Sensing*, *8*(8), 649, doi:10.3390/rs8080649. 2.6.3

Lu, R., X. Xu, D. He, B. Liu, X. Tan, and X. Wang (2016), Co-seismic and blind fault of the 2015 Pishan Mw 6.5 earthquake: implications for the sedimentary- tectonic framework of the western Kunlun Mountains, northern Tibetan Plateau, *Tectonics*, pp. 956–964, doi:10.1002/2015TC004053. 2.3.1, 2.4

Lyon-Caen, H., and P. Molnar (1984), Gravity anomalies and the structure of western Tibet and the Southern Tarim Basin, *Geophysical Research Letters*, *11*(12), 1251–1254, doi:10.1029/GL011i012p01251. 2.2

Lyzenga, G. A., W. R. Panero, and A. Donnellan (2000), Influence of anelastic surface layers on postseismic thrust fault deformation, *Journal of Geophysical Research: Solid Earth*, *105*(B2), 3151–3157, doi:10.1029/1999JB900269. 2.6.2, 2.6.3, 2.7.1

Mackenzie, D. (2016), Active shortening in the Alpine-Himalayan belt, Ph.D., University of Oxford. 5.8

Mackenzie, D., and A. Elliott (2017), Untangling tectonic slip from the potentially misleading effects of landform geometry, *Geosphere*, *13*(4), 1310–1328, doi:10.1130/GES01386.1. 4.3.3, 4.4.2

Mackenzie, D., J. R. Elliott, E. Altunel, R. T. Walker, Y. C. Kurban, J.-L. Schwenninger, and B. Parsons (2016), Seismotectonics and rupture process of the MW 7.1 2011 Van reverse-faulting earthquake, Eastern Turkey, and implications for hazard in regions of distributed shortening, *Geophysical Journal International*, pp. 501–524, doi:10.1093/gji/ggw158. 1.1, 1.4, 2.7.1, 2.7.1, 3.6

Mackenzie, D., R. Walker, K. Abdrakhmatov, G. Campbell, A. Carr, C. Gruetzner, A. Mukambayev, and M. Rizza (2018), A creeping intracontinental thrust fault: past and present slip-rates on the Northern edge of the Tien Shan, Kazakhstan, *Geophysical Journal International*, *215*(2), 1148–1170, doi:10.1093/gji/ggy339. 5.1, 5.6.3

Mai, P. M., and G. C. Beroza (2000), Source Scaling Properties from Finite-Fault-Rupture Models, *Bulletin of the Seismological Society of America*, *90*(3), 604–615, doi:10.1785/0119990126. 4.1

Makarov, V. I. (1977), *New tectonic structures of the Central Tien Shan*, Order of the Red Banner Geology Institute, Akad. Sci., Moscov. 1.2

Makarov, V. I. (2012), Compositional, structural, and geodynamic controls of the evolution of inter- and intramontane basins of the Tien Shan, *Russian Geology and Geophysics*, *53*(4), 367–375, doi:10.1016/j.rgg.2012.03.001. 5.1

Marone, C. J., C. H. Scholtz, and R. Bilham (1991), On the mechanics of earthquake afterslip, *Journal of Geophysical Research: Solid Earth*, *96*(B5), 8441–8452, doi:10.1029/91JB00275. 2.6.3

Matte, P., P. Tapponnier, N. Arnaud, L. Bourjot, J. P. Avouac, P. Vidal, L. Qing, P. Yusheng, and W. Yi (1996), Tectonics of Western Tibet, between the Tarim and the Indus, *Earth and Planetary Science Letters*, *142*(34), 311–330, doi:10.1016/0012-821X(96)00086-6. 2.2, 2.5.1

McAuliffe, L. J., J. F. Dolan, E. J. Rhodes, J. Hubbard, J. H. Shaw, and T. L. Pratt (2015), Paleoseismologic evidence for large-magnitude (Mw 7.5-8.0) earthquakes on the Ventura blind thrust fault: Implications for multifault ruptures in the Transverse Ranges of southern California, *Geosphere*, *11*(5), 1629–1650, doi:10.1130/GES01123.1. 3.5

McCaffrey, R., and G. A. Abers (1988), SYN3: A program for inversion of teleseismic body waveforms on microcomputers, *Air Force Geophys. Lab. Tech. Rep. AFGL-TR-0099, Hanscomb Air Force Base, Mass.* 3.3

McCalpin, J. P. (2009), *Paleoseismology*, vol. 95, 2 ed., Academic Press, google-Books-ID: RxxEfNPU6ksC. 1.1

Medialdea, A., K. J. Thomsen, A. S. Murray, and G. Benito (2014), Reliability of equivalent-dose determination and age-models in the OSL dating of historical and modern palaeoflood sediments, *Quaternary Geochronology*, *22*, 11–24, doi:10.1016/j.quageo.2014.01.004. 4.3.2

Mejdahl, V. (1979), Thermoluminescence Dating: Beta-Dose Attenuation in Quartz Grains, *Archaeometry*, *21*(1), 61–72, doi:10.1111/j.1475-4754.1979.tb00241.x. B

Mellors, R. J., F. L. Vernon, G. L. Pavlis, G. A. Abers, M. W. Hamburger, S. Ghose, and B. Iliasov (1997), The Ms = 7.3 1992 Suusamyr, Kyrgyzstan, earthquake: 1. Constraints on fault geometry and source parameters based on aftershocks and body-wave modeling, *Bulletin of the Seismological Society of America*, *87*(1), 11–22. 4.1, 4.2, 4.4.1, 4.6, 4.6, 5.1, 5.6.1, 5.8

Melnick, D. (2016), Rise of the central Andean coast by earthquakes straddling the Moho, *Nature Geoscience*, *9*(5), 401–407, doi:10.1038/ngeo2683. 1.1, 2.7.1

Middleton, T. A., R. T. Walker, B. Parsons, Q. Lei, Y. Zhou, and Z. Ren (2015), A major, intraplate, normal-faulting earthquake: the 1739 Yinchuan event in northern China, *Journal of Geophysical Research: Solid Earth*, p. 2015JB012355, doi:10.1002/2015JB012355. 4.3.1

Milliner, C. W. D., J. F. Dolan, J. Hollingsworth, S. Leprince, and F. Ayoub (2016), Comparison of coseismic near-field and off-fault surface deformation patterns of the 1992 Mw 7.3 Landers and 1999 Mw 7.1 Hector Mine earthquakes: Implications for controls on the distribution of surface strain, *Geophysical Research Letters*, *43*(19), 2016GL069,841, doi:10.1002/2016GL069841. 3.5

Miyazaki, S., P. Segall, J. Fukuda, and T. Kato (2004), Space time distribution of afterslip following the 2003 Tokachi-oki earthquake: Implications for variations in fault zone frictional properties, *Geophysical Research Letters*, *31*(6), L06,623, doi:10.1029/2003GL019410. 2.6.3

Mohadjer, S., T. A. Ehlers, R. Bendick, K. Stübner, and T. Strube (2016), A Quaternary fault database for central Asia, *Nat. Hazards Earth Syst. Sci.*, *16*(2), 529–542, doi:10.5194/nhess-16-529-2016. 5.1

Molnar, P. (1979), Earthquake recurrence intervals and plate tectonics, *Bulletin of the Seismological Society of America*, *69*(1), 115–133. 1.1

Molnar, P., and P. Tapponnier (1975), Cenozoic tectonics of Asia: Effects of a continental collision, *Science*, *189*(4201), 419–426, doi:10.1126/science.189.4201.419. 1.2

Molnar, P., and P. Tapponnier (1978), Active tectonics of Tibet, *Journal of Geophysical Research: Solid Earth*, *83*(B11), 5361–5375, doi:10.1029/JB083iB11p05361. 2.2

Molnar, P., and P. Tapponnier (1981), A possible dependence of tectonic strength on the age of the crust in Asia, *Earth and Planetary Science Letters*, *52*(1), 107–114, doi:10.1016/0012-821X(81)90213-2. 1.2

Molnar, P., E. T. Brown, B. C. Burchfiel, Q. Deng, X. Feng, J. Li, G. M. Raisbeck, J. Shi, W. Zhangming, F. Yiou, and H. You (1994), Quaternary Climate Change and the Formation of River Terraces across Growing Anticlines on the North Flank of the Tien Shan, China, *The Journal of Geology*, *102*(5), 583–602, doi:10.1086/629700. 2.5.1

Moss, R. E. S., and Z. E. Ross (2011), Probabilistic Fault Displacement Hazard Analysis for Reverse Faults, *Bulletin of the Seismological Society of America*, *101*(4), 1542–1553, doi:10.1785/0120100248. 4.6, 6

Murray, A. S., and A. G. Wintle (2000), Luminescence dating of quartz using an improved single-aliquot regenerative-dose protocol, *Radiation Measurements*, *32*(1), 57–73, doi:10.1016/S1350-4487(99)00253-X. 4.3.2

Mushketov, I. (1890), Le tremblement de terre de Verny, 28 Mai (9 Juin) 1887, *Memoires du Comite Geologique,*, *X(1)*. 1.2, 5.8.1

Mushketov, I. V. (1891), Materials for investigation of earthquakes in Russia, *Annex to the 27th volume of tidings of the Imperial Russian Geographical Society*, *1*, 64. 1.2, 5.8.1

Najman, Y., E. Appel, M. Boudagher-Fadel, P. Bown, A. Carter, E. Garzanti, L. Godin, J. Han, U. Liebke, G. Oliver, R. Parrish, and G. Vezzoli (2010), Timing of India-Asia collision: Geological, biostratigraphic, and palaeomagnetic constraints, *Journal of Geophysical Research: Solid Earth*, *115*(B12), B12,416, doi:10.1029/2010JB007673. 1.2

Neil, E. A., and G. Houseman (1997), Geodynamics of the Tarim Basin and the Tian Shan in central Asia, *Tectonics*, *16*, 571–584, doi:10.1029/97TC01413. 1.2

Nikonorov, V., J. Karaev, F. Borisov, T. Zamaletdinov, T. Larina, V. Tolsky, T. Nogaev, and N. Polovinskaja (2000), Mineral Resources Map of Kyrgyz Republic. 5.1, 5.1, 5.5, 5.7

Nissen, E., M. Ghorashi, J. Jackson, B. Parsons, and M. Talebian (2007), The 2005 Qeshm Island earthquake (Iran)-a link between buried reverse faulting and surface folding in the Zagros Simply Folded Belt?, *Geophysical Journal International*, *171*(1), 326–338, doi:10.1111/j.1365-246X.2007.03514.x. 2.1

Nissen, E., F. Yamini-Fard, M. Tatar, A. Gholamzadeh, E. Bergman, J. R. Elliott, J. A. Jackson, and B. Parsons (2010), The vertical separation of mainshock rupture and microseismicity at Qeshm island in the Zagros fold-and-thrust belt, Iran, *Earth and Planetary Science Letters*, *296*(3), 181–194, doi:10.1016/j.epsl.2010.04.049. 3.6

Nissen, E., J. Jackson, S. Jahani, and M. Tatar (2014a), Zagros phantom earthquakes reassessedThe interplay of seismicity and deep salt flow in the Simply Folded Belt?, *Journal of Geophysical Research: Solid Earth*, *119*(4), 3561–3583, doi:10.1002/2013JB010796. 3.6

Nissen, E., T. Maruyama, J. Ramon Arrowsmith, J. R. Elliott, A. K. Krishnan, M. E. Oskin, and S. Saripalli (2014b), Coseismic fault zone deformation revealed with differential lidar: Examples from Japanese Mw 7 intraplate earthquakes, *Earth and Planetary Science Letters*, *405*, 244–256, doi:10.1016/j.epsl.2014.08.031. A.1

Okada, Y. (1985), Surface deformation due to shear and tensile faults in a half-space, *Bulletin of the Seismological Society of America*, *75*(4), 1135–1154. 2.3.1

Olley, J., G. Caitcheon, and A. Murray (1998), The distribution of apparent dose as determined by Optically Stimulated Luminescence in small aliquots of fluvial quartz: Implications for dating young sediments, *Quaternary Science Reviews*, *17*(11), 1033–1040, doi:10.1016/S0277-3791(97)00090-5. 4.3.2

Omuraliev, M. O., and T. A. Charimov (1990), Seismic deformations and seismic hazards in the western part of northern Kyrgyzia (in Russian), *Proceedings of the Kyrgyz Academy of Sciences*, *4*, 83–88. 5.5

Oskin, M. E., J. R. Arrowsmith, A. H. Corona, A. J. Elliott, J. M. Fletcher, E. J. Fielding, P. O. Gold, J. J. G. Garcia, K. W. Hudnut, J. Liu-Zeng, and O. J. Teran (2012), Near-Field Deformation from the El MayorCucapah Earthquake Revealed by Differential LIDAR, *Science*, *335*(6069), 702–705, doi:10.1126/science.1213778. A.1

Park, S. K., S. C. Thompson, A. Rybin, Vladimir Batalev, and Robert Bielinski (2003), Structural constraints in neotectonic studies of thrust faults from the magnetotelluric method, Kochkor Basin, Kyrgyz Republic, *Tectonics*, *22*(2), doi:10.1029/2001TC001318. 5.1

Patyniak, M., A. Landgraf, A. Dzhumabaeva, K. E. Abdrakhmatov, S. Rosenwinkel, O. Korup, F. Preusser, J. Fohlmeister, J. R. Arrowsmith, and M. R. Strecker (2017), Paleoseismic Record of Three Holocene Earthquakes Rupturing the IssykAta Fault near Bishkek, North KyrgyzstanPaleoseismic Record of Three Holocene Earthquakes Rupturing the IssykAta Fault near Bishkek, *Bulletin of the Seismological Society of America*, *107*(6), 2721–2737, doi:10.1785/0120170083. 4.1, 4.5.1, 5.7, 5.8.1

Petersen, M. D., M. P. Moschetti, P. M. Powers, C. S. Mueller, K. M. Haller, A. D. Frankel, Y. Zeng, S. Rezaeian, S. C. Harmsen, O. S. Boyd, N. Field, R. Chen, K. S. Rukstales, N. Luco, R. L. Wheeler, R. A. Williams, and A. H. Olsen (2015), The 2014 United States National Seismic Hazard Model, *Earthquake Spectra*, *31*(S1), S1–S30, doi:10.1193/120814EQS210M. 4.1

Phillips, R. J., R. R. Parrish, and M. P. Searle (2004), Age constraints on ductile deformation and long-term slip rates along the Karakoram fault zone, Ladakh, *Earth and Planetary Science Letters*, *226*(3-4), 305–319, doi:10.1016/j.epsl.2004.07.037. 1.1

Poisson, B., and J. Avouac (2004), Holocene Hydrological Changes Inferred from Alluvial Stream Entrenchment in North Tian Shan (Northwestern China), *The Journal of Geology*, *112*(2), 231–249, doi:10.1086/381659. 2.5.1

Prescott, J. R., and J. T. Hutton (1994), Cosmic ray contributions to dose rates for luminescence and ESR dating: Large depths and long-term time variations, *Radiation Measurements*, *23*(2), 497–500, doi:10.1016/1350-4487(94)90086-8. B

Qiao, X., P. Yu, Z. Nie, J. Li, X. Wang, S. I. Kuzikov, Q. Wang, and S. Yang (2017), The Crustal Deformation Revealed by GPS and InSAR in the Northwest Corner of the Tarim Basin, Northwestern China, *Pure and Applied Geophysics*, *174*(3), 1405–1423, doi:10.1007/s00024-017-1473-6. 3.6

Qiusheng, L., G. Rui, L. Deyuan, L. Jingwei, F. Jingyi, Z. Zhiying, L. Wen, L. Yingkang, Y. Quanren, and L. Dexing (2002), Tarim underthrust beneath western Kunlun: evidence from wide-angle seismic sounding, *Journal of Asian Earth Sciences*, *20*(3), 247–253, doi:10.1016/S1367-9120(01)00057-8. 2.2

Readhead, M. (2002), Absorbed dose fraction for 87rb beta particles, *Ancient TL*, *20*, 25–29. B

Reigber, C., G. W. Michel, R. Galas, D. Angermann, J. Klotz, J. Y. Chen, A. Papschev, R. Arslanov, V. E. Tzurkov, and M. C. Ishanov (2001), New space geodetic

constraints on the distribution of deformation in Central Asia, *Earth and Planetary Science Letters*, *191*(12), 157–165, doi:10.1016/S0012-821X(01)00414-9. 1.2

Reimer, P. J., E. Bard, A. Bayliss, J. W. Beck, P. G. Blackwell, C. B. Ramsey, C. E. Buck, H. Cheng, R. L. Edwards, M. Friedrich, P. M. Grootes, T. P. Guilderson, H. Haflidason, I. Hajdas, C. Hatté, T. J. Heaton, D. L. Hoffmann, A. G. Hogg, K. A. Hughen, K. F. Kaiser, B. Kromer, S. W. Manning, M. Niu, R. W. Reimer, D. A. Richards, E. M. Scott, J. R. Southon, R. A. Staff, C. S. M. Turney, and J. v. d. Plicht (2013), IntCal13 and Marine13 Radiocarbon Age Calibration Curves 0-50,000 Years cal BP, *Radiocarbon*, *55*(4), 1869–1887. 4.3.2

RIA Novosti (2011), Tashkentskoe zemletryasenie (1966 g.). Spravka, *RIA Novosti, 26.04.2011, online edition, https://ria.ru/20110426/368030901.html*. 1.2

Rockwell, T. K., E. A. Keller, and G. R. Dembroff (1988), Quaternary rate of folding of the Ventura Avenue anticline, western Transverse Ranges, southern California, *Geological Society of America Bulletin*, *100*(6), 850–858, doi:10.1130/0016-7606(1988)100<0850:QROFOT>2.3.CO;2. 2.7.1

Roering, J. J., M. L. Cooke, and D. D. Pollard (1997), Why blind thrust faults do not propagate to the Earth's surface: Numerical modeling of coseismic deformation associated with thrust-related anticlines, *Journal of Geophysical Research: Solid Earth*, *102*(B6), 11,901–11,912, doi:10.1029/97JB00680. 1.1

Rosen, P., C. Werner, E. Fielding, S. Hensley, S. Buckley, and P. Vincent (1998), Aseismic creep along the San Andreas Fault northwest of Parkfield, CA measured by radar interferometry, *Geophysical Research Letters*, *25*(6), 825–828, doi:10.1029/98GL50495. 1.1

Roustaei, M., E. Nissen, M. Abbassi, A. Gholamzadeh, M. Ghorashi, M. Tatar, F. Yamini-Fard, E. Bergman, J. Jackson, and B. Parsons (2010), The 2006 March 25 Fin earthquakes (Iran)insights into the vertical extents of faulting in the Zagros Simply Folded Belt, *Geophysical Journal International*, *181*(3), 1275–1291, doi:10.1111/j.1365-246X.2010.04601.x. 3.6

Sadybakasov, I. (1972), *Neotectonics of the central Tien Shan (in Russian)*, Ilim., Frinze (Bishkek). 5.1

Saillard, M., L. Audin, B. Rousset, J.-P. Avouac, M. Chlieh, S. R. Hall, L. Husson, and D. L. Farber (2017), From the seismic cycle to long-term deformation: linking seismic coupling and Quaternary coastal geomorphology along the Andean megathrust, *Tectonics*, *36*(2), 241–256, doi:10.1002/2016TC004156. 2.7.1

Savage, J. C., and R. O. Burford (1973), Geodetic determination of relative plate motion in central California, *Journal of Geophysical Research*, *78*(5), 832–845, doi:10.1029/JB078i005p00832. 1.1

Scharer, K. M., D. W. Burbank, J. Chen, R. J. Weldon, C. Rubin, R. Zhao, and J. Shen (2004), Detachment folding in the Southwestern Tian ShanTarim foreland, China: shortening estimates and rates, *Journal of Structural Geology*, *26*(11), 2119–2137, doi:10.1016/j.jsg.2004.02.016. 3.2, 3.2.1, 3.4, 3.2.2, 3.2.2

Scharer, K. M., D. W. Burbank, J. Chen, and R. J. Weldon (2006), Kinematic models of fluvial terraces over active detachment folds: Constraints on the growth mechanism of the Kashi-Atushi fold system, Chinese Tian Shan, *GSA Bulletin*, *118*(7-8), 1006–1021, doi:10.1130/B25835.1. 3.2.2

Scheiber, R., and A. Moreira (2000), Coregistration of interferometric SAR images using spectral diversity, *IEEE Transactions on Geoscience and Remote Sensing*, *38*(5), 2179–2191, doi:10.1109/36.868876. 2.3.1

Schiffer, M. B. (1986), Radiocarbon dating and the old wood problem: The case of the Hohokam chronology, *Journal of Archaeological Science*, *13*(1), 13–30, doi:10.1016/0305-4403(86)90024-5. 4.3.2

Scholz, C. H. (2002), *The mechanics of earthquakes and faulting*, 2nd ed. ed., Cambridge University Press, Cambridge. 1.1

Schurr, B., Ratschbacher Lothar, Sippl Christian, Gloaguen Richard, Yuan Xiaohui, and Mechie James (2014), Seismotectonics of the Pamir, *Tectonics*, *33*(8), 1501–1518, doi:10.1002/2014TC003576. 1.2

Scott, C. P., and R. B. Lohman (2016), Sensitivity of earthquake source inversions to atmospheric noise and corrections of InSAR data, *Journal of Geophysical Research: Solid Earth*, *121*(5), 2016JB012,969, doi:10.1002/2016JB012969. 2.3.1

Segall, P. (2010), *Earthquake and Volcano Deformation*, Princeton University Press. 5.6.3

Selander, J., M. Oskin, C. Ormukov, and K. Abdrakhmatov (2012), Inherited strike-slip faults as an origin for basement-cored uplifts: Example of the Kungey and Zailiskey ranges, northern Tian Shan, *Tectonics*, *31*(4), TC4026, doi:10.1029/2011TC003002. 3.6, 5.1

Sevara, C. (2016), Capturing the Past for the Future: an Evaluation of the Effect of Geometric Scan Deformities on the Performance of Aerial Archival Media in Image-based Modelling Environments, *Archaeological Prospection*, *23*(4), 325–334, doi:10.1002/arp.1539. A.2

Sharp, W. D., K. R. Ludwig, O. A. Chadwick, R. Amundson, and L. L. Glaser (2003), Dating fluvial terraces by 230th/U on pedogenic carbonate, Wind River Basin, Wyoming, *Quaternary Research*, *59*(2), 139–150, doi:10.1016/S0033-5894(03)00003-6. 5.2, 5.6.1

Shaw, J. H., A. Plesch, J. F. Dolan, T. L. Pratt, and P. Fiore (2002), Puente Hills Blind-Thrust System, Los Angeles, California, *Bulletin of the Seismological Society of America*, *92*(8), 2946–2960, doi:10.1785/0120010291. 2.7.1

Shen, Z.-K., M. Wang, Y. Li, D. D. Jackson, A. Yin, D. Dong, and P. Fang (2001), Crustal deformation along the Altyn Tagh fault system, western China, from GPS, *Journal of Geophysical Research: Solid Earth*, *106*(B12), 30,607–30,621, doi:10.1029/2001JB000349. 1.2

Sibson, R. H. (1985), A note on fault reactivation, *Journal of Structural Geology*, *7*(6), 751–754, doi:10.1016/0191-8141(85)90150-6. 1.1

Sieh, K., D. H. Natawidjaja, A. J. Meltzner, C.-C. Shen, H. Cheng, K.-S. Li, B. W. Suwargadi, J. Galetzka, B. Philibosian, and R. L. Edwards (2008), Earthquake Supercycles Inferred from Sea-Level Changes Recorded in the Corals of West Sumatra, *Science*, *322*(5908), 1674–1678, doi:10.1126/science.1163589. 5.8.1

Simpson, D. W., M. W. Hamburger, V. D. Pavlov, and I. L. Nersesov (1981), Tectonics and seismicity of the Toktogul Reservoir Region, Kirgizia, USSR, *Journal of Geophysical Research: Solid Earth*, *86*(B1), 345–358, doi:10.1029/JB086iB01p00345. 5.7

Sims, J. (1973), Earthquake-induced structures in sediments of Van Norman Lake, San Fernando, California, *Science*, *182*(4108), 161–163, doi:10.1126/science.182.4108.161. 1.1

Sloan, R. A., J. A. Jackson, D. McKenzie, and K. Priestley (2011), Earthquake depth distributions in central Asia, and their relations with lithosphere thickness, shortening and extension, *Geophysical Journal International*, *185*(1), 1–29, doi:10.1111/j.1365-246X.2010.04882.x. 3.6, 3.6, 3.15, 4.6, 5.6.3

Smekalin, O. P., V. S. Imaev, A. M. Korzhenkov, and A. V. Chipizubov (2016), Paleoseismological investigations in the pleistoseismal zone of the 1885 Belovodskoe earthquake, North Tien Shan, *Seismic Instruments*, *52*(4), 279–289, doi:10.3103/S0747923916040083. 5.8.1

Sobel, E. R., and T. A. Dumitru (1997), Thrusting and exhumation around the margins of the western Tarim basin during the India-Asia collision, *Journal of Geophysical Research: Solid Earth*, *102*(B3), 5043–5063, doi:10.1029/96JB03267. 1.2

Sobel, E. R., M. Oskin, D. Burbank, and A. Mikolaichuk (2006), Exhumation of basement-cored uplifts: Example of the Kyrgyz Range quantified with apatite fission track thermochronology, *Tectonics*, *25*(2), TC2008, doi:10.1029/2005TC001809. 5.1

Sobel, E. R., L. M. Schoenbohm, J. Chen, R. Thiede, D. F. Stockli, M. Sudo, and M. R. Strecker (2011), Late MiocenePliocene deceleration of dextral slip between Pamir and Tarim: Implications for Pamir orogenesis, *Earth and Planetary Science Letters*, *304*(3), 369–378, doi:10.1016/j.epsl.2011.02.012. 3.2.3

Sobel, E. R., J. Chen, L. M. Schoenbohm, R. Thiede, D. F. Stockli, M. Sudo, and M. R. Strecker (2013), Oceanic-style subduction controls late Cenozoic deformation of the Northern Pamir orogen, *Earth and Planetary Science Letters*, *363*, 204–218, doi:10.1016/j.epsl.2012.12.009. 1.2

Stein, R., and G. King (1984), Seismic potential revealed by surface folding: 1983 Coalinga, California, earthquake, *Science*, *224*(4648), 869–872. 2.1, 4.6

Stein, R. S., and G. Ekström (1992), Seismicity and geometry of a 110-km-long blind thrust fault 2. Synthesis of the 19821985 California Earthquake Sequence, *Journal of Geophysical Research: Solid Earth*, *97*(B4), 4865–4883, doi:10.1029/91JB02847. 2.7.1, 2.7.1

Stein, R. S., and R. S. Yeats (1989), Hidden Earthquakes, *Scientific American*, *260*(6), 48–59. 4.6

Stein, S., and A. M. Friedrich (2014), How much can we clear the crystal ball?, *Astronomy & Geophysics*, *55*(2), 2.11–2.17, doi:10.1093/astrogeo/atu076. 1.1

Stirling, M., T. Goded, K. Berryman, and N. Litchfield (2013), Selection of earthquake scaling relationships for seismic-hazard analysis, *Bulletin of the Seismological Society of America*, *103*(6), 2993–3011, doi:10.1785/0120130052. 4.1

Storchak, D. A., D. D. Giacomo, I. Bondr, E. R. Engdahl, J. Harris, W. H. K. Lee, A. Villaseor, and P. Bormann (2013), Public Release of the ISCGEM Global Instrumental Earthquake Catalogue (19002009), *Seismological Research Letters*, *84*(5), 810–815, doi:10.1785/0220130034. 3.1

Strecker, M. R., W. Frisch, M. W. Hamburger, L. Ratschbacher, S. Semiletkin, A. Zamoruyev, and N. Sturchio (1995), Quaternary deformation in the Eastern Pamirs, Tadzhikistan and Kyrgyzstan, *Tectonics*, *14*(5), 1061–1079, doi:10.1029/95TC00927. 1.2

Sun, J., Z.-K. Shen, T. Li, and J. Chen (2016), Thrust faulting and 3d ground deformation of the 3 July 2015 Mw 6.4 Pishan, China earthquake from Sentinel-1a radar interferometry, *Tectonophysics*, *683*, 77–85, doi:10.1016/j.tecto.2016.05.051. 2.3.1

Suppe, J. (1983), Geometry and kinematics of fault-bend folding., *American Journal of Science*, *283*(7), 684–721. 1.1, 2.1

Suppe, J., and D. Medwedeff (1990), Geometry and kinematics of fault-propagation folding, *Eclogae Geologicae Helvetiae*, *83*(3), 409–454. 1.1, 2.1, 2.7.1

Sykes, L. R. (1978), Intraplate seismicity, reactivation of preexisting zones of weakness, alkaline magmatism, and other tectonism postdating continental fragmentation, *Reviews of Geophysics*, *16*(4), 621–688, doi:10.1029/RG016i004p00621. 1.1

Takaku, J., T. Tadono, and K. Tsutsui (2014), Generation of high resolution global DSM from ALOS PRISM, pp. 243–248, doi:10.5194/isprsarchives-XL-4-243-2014. 4.3.1, 5.2, 5.3, 5.4

Talebian, M., J. Biggs, M. Bolourchi, A. Copley, A. Ghassemi, M. Ghorashi, J. Hollingsworth, J. Jackson, E. Nissen, B. Oveisi, B. Parsons, K. Priestley, and A. Saiidi (2006), The Dahuiyeh (Zarand) earthquake of 2005 February 22 in central Iran: reactivation of an intramountain reverse fault, *Geophysical Journal International*, *164*(1), 137–148, doi:10.1111/j.1365-246X.2005.02839.x. 4.6

Talebian, M., A. C. Copley, M. Fattahi, M. Ghoraishi, J. A. Jackson, H. Nazari, R. A. Sloan, and R. T. Walker (2016), Active faulting within a megacity: the geometry and slip rate of the Pardisan thrust in central Tehran, Iran, *Geophysical Journal International*, p. ggw347, doi:10.1093/gji/ggw347. 2.1

Tapponnier, P., and P. Molnar (1976), Slip-line field theory and large-scale continental tectonics, *Nature*, *264*(5584), 319–324, doi:10.1038/264319a0. 1.2

Taylor, M., and A. Yin (2009), Active structures of the Himalayan-Tibetan orogen and their relationships to earthquake distribution, contemporary strain field, and Cenozoic volcanism, *Geosphere*, *5*(3), 199–214, doi:10.1130/GES00217.1. 2.1

Thatcher, W. (2009), How the Continents Deform: The Evidence From Tectonic Geodesy, *Annual Review of Earth and Planetary Sciences*, *37*(1), 237–262, doi:10.1146/annurev.earth.031208.100035. 1.1

Thingbaijam, K. K. S., P. M. Mai, and K. Goda (2017), New Empirical Earthquake SourceScaling Laws, *Bulletin of the Seismological Society of America*, *107*(5), 2225–2246, doi:10.1785/0120170017. 4.1, 4.6

Thomas, M. Y., J.-P. Avouac, J. Champenois, J.-C. Lee, and L.-C. Kuo (2014), Spatiotemporal evolution of seismic and aseismic slip on the Longitudinal Valley Fault, Taiwan, *Journal of Geophysical Research: Solid Earth*, *119*(6), 5114–5139, doi:10.1002/2013JB010603. 2.6.3

Thompson, J. A., D. W. Burbank, T. Li, J. Chen, and B. Bookhagen (2015), Late Miocene northward propagation of the northeast Pamir thrust system, northwest China, *Tectonics*, *34*(3), 2014TC003,690, doi:10.1002/2014TC003690. 3.2.3

Thompson, J. A., J. Chen, H. Yang, T. Li, B. Bookhagen, and D. Burbank (2018), Coarse- versus fine-grain quartz OSL and cosmogenic 10be dating of deformed fluvial terraces on the northeast Pamir margin, northwest China, *Quaternary Geochronology*, *46*, 1–15, doi:10.1016/j.quageo.2018.01.002. 3.2.3, 3.7, 3.6, 3.9

Thompson, S. C. (2001), Active tectonics in the central Tien Shan, Kyrgyz Republic, Thesis. 5.8.1, 5.8.1

Thompson, S. C., R. J. Weldon, C. M. Rubin, K. Abdrakhmatov, P. Molnar, and G. W. Berger (2002), Late Quaternary slip rates across the central Tien Shan, Kyrgyzstan, central Asia, *Journal of Geophysical Research: Solid Earth*, *107*(B9), 2203, doi:10.1029/2001JB000596. 1.2, 1.2, 4.1, 4.3.3, 5.1, 5.1, 5.7, 5.8, 5.8.1

Thompson Jobe, J. A., T. Li, J. Chen, D. W. Burbank, and A. Bufe (2017), Quaternary tectonic evolution of the PamirTian Shan convergence zone, Northwest China, *Tectonics*, *36*(12), 2748–2776, doi:10.1002/2017TC004541. 3.2.1, 3.3, 3.2.2, 3.2.3

Thomsen, K. J., A. S. Murray, M. Jain, and L. Btter-Jensen (2008), Laboratory fading rates of various luminescence signals from feldspar-rich sediment extracts, *Radiation Measurements*, *43*(9), 1474–1486, doi:10.1016/j.radmeas.2008.06.002. 4.3.2

Toda, S., R. S. Stein, K. RichardsDinger, and S. B. Bozkurt (2005), Forecasting the evolution of seismicity in southern California: Animations built on earthquake stress transfer, *Journal of Geophysical Research: Solid Earth*, *110*(B5), doi:10.1029/2004JB003415. 3.6

USGS (2017), http://earthquake.usgs.gov/earthquakes/eventpage/iscgem888031, *Earthquake Hazards Program Earthquake Catalog*. 2.2

van Calsteren, P., and L. Thomas (2006), Uranium-series dating applications in natural environmental science, *Earth-Science Reviews*, *75*(1), 155–175, doi:10.1016/j.earscirev.2005.09.001. 5.2

Vilotte, J. P., M. Daignieres, R. Madariaga, and O. C. Zienkiewicz (1984), The role of a heterogeneous inclusion during continental collision, *Physics of the Earth and Planetary Interiors*, *36*(3), 236–259, doi:10.1016/0031-9201(84)90049-9. 1.2

Walker, R. T., E. Bergman, J. Jackson, M. Ghorashi, and M. Talebian (2005), The 2002 June 22 Changureh (Avaj) earthquake in Qazvin province, northwest Iran: epicentral relocation, source parameters, surface deformation and geomorphology, *Geophysical Journal International*, *160*(2), 707–720, doi:10.1111/j.1365-246X.2005.02516.x. 4.6

Walker, R. T., M. M. Khatib, A. Bahroudi, A. Rodés, C. Schnabel, M. Fattahi, M. Talebian, and E. Bergman (2015), Co-seismic, geomorphic, and geologic fold growth associated with the 1978 Tabas-e-Golshan earthquake fault in eastern Iran, *Geomorphology*, *237*, 98–118, doi:10.1016/j.geomorph.2013.02.016. 2.5.1

Wang, C., X. Cheng, H. Chen, W. Ding, X. Lin, L. Wu, K. Li, J. Shi, and Y. Li (2016), The effect of foreland palaeo-uplift on deformation mechanism in the Wupoer fold-and-thrust belt, NE Pamir: Constraints from analogue modelling, *Journal of Geodynamics*, *100*, 115–129, doi:10.1016/j.jog.2016.03.001. 3.2.1, 3.2.2

Wang, J. (2004), Historical earthquake investigation and research in China, *Annals of Geophysics*, *47*(2-3). 1.1

Wang, L.-N., Z.-G. Zhao, and Z.-G. Wang (1987), Long period source parameters of the Wuqia, Xinjiang earthquake of August 23, 1985 - Results from inversion of the records of the IDA network, *Acta Seismologica Sinica*, *9*(1), 108–111. 3.3, 3.1, 3.3

Wang, R., F. L. Martın, and F. Roth (2003), Computation of deformation induced by earthquakes in a multi-layered elastic crustFORTRAN programs EDGRN/EDCMP, *Computers & Geosciences*, *29*(2), 195–207, doi:10.1016/S0098-3004(02)00111-5. 2.4.1

Webb, L. E., and C. L. Johnson (2006), Tertiary strike-slip faulting in southeastern Mongolia and implications for Asian tectonics, *Earth and Planetary Science Letters*, *241*(1), 323–335, doi:10.1016/j.epsl.2005.10.033. 3.6

Wechsler, N., T. K. Rockwell, and Y. Klinger (2018), Variable slip-rate and slip-per-event on a plate boundary fault: The Dead Sea fault in northern Israel, *Tectonophysics*, *722*(Supplement C), 210–226, doi:10.1016/j.tecto.2017.10.017. 5.6.2

Wedmore, L. N. J., L. C. Gregory, K. J. W. McCaffrey, M. Wilkinson, and R. J. Walters (2017), High resolution shallow co-seismic and post-seismic slip from the 2016 central Italy earthquake sequence captured using terrestrial laser scanning, structure from motion and low-cost near-field GNSS, *AGU Fall Meeting Abstracts*, *43*. 3.6

Wei, H.-H., Q.-R. Meng, L. Ding, and Z.-Y. Li (2013), Tertiary evolution of the western Tarim basin, northwest China: A tectono-sedimentary response to northward indentation of the Pamir salient, *Tectonics*, *32*(3), 558–575, doi:10.1002/tect.20046. 2.1, 2.2, 3.2.1, 3.2.1, 3.2, 3.6, 3.15

Weldon, R., K. Scharer, T. Fumal, and G. Biasi (2004), Wrightwood and the earthquake cycle: What a long recurrence record tells us about how faults work, *GSA Today*, *14*(9), 4–10, doi:10.1130/1052-5173(2004)014<4:WATECW>2.0CO;2. 1.1

Wells, D., and K. Coppersmith (1994), New empirical relationships among magnitude, rupture length, rupture width, rupture area, and surface displacement, *Bulletin of the Seismological Society of America*, *84*(4), 974–1002. 3.6, 4.1, 4.6

Wen, Y., C. Xu, Y. Liu, and G. Jiang (2016), Deformation and Source Parameters of the 2015 Mw 6.5 Earthquake in Pishan, Western China, from Sentinel-1a and ALOS-2 Data, *Remote Sensing*, *8*(2), 134, doi:10.3390/rs8020134. **??**, 2.3.1, 2.3.1

Wesnousky, S. G. (1988), Seismological and structural evolution of strike-slip faults, *Nature*, *335*(6188), 340–343, doi:10.1038/335340a0. 5.8

Westoby, M. J., J. Brasington, N. F. Glasser, M. J. Hambrey, and J. M. Reynolds (2012), Structure-from-Motion photogrammetry: A low-cost, effective tool for geoscience applications, *Geomorphology*, *179*, 300–314, doi:10.1016/j.geomorph.2012.08.021. 4.3.1

Weston, J., E. R. Engdahl, J. Harris, D. Di Giacomo, and D. A. Storchak (2018), ISC-EHB: reconstruction of a robust earthquake data set, *Geophysical Journal International*, *214*(1), 474–484, doi:10.1093/gji/ggy155. 3.3

Whipple, K. X., M. Shirzaei, K. V. Hodges, and J. Ramon Arrowsmith (2016), Active shortening within the Himalayan orogenic wedge implied by the 2015 Gorkha earthquake, *Nature Geoscience*, *9*(9), 711–716, doi:10.1038/ngeo2797. 2.7.1

Wickham, J. (1995), Fault displacement-gradient folds and the structure at Lost Hills, California (U.S.A.), *Journal of Structural Geology*, *17*(9), 1293–1302, doi:10.1016/0191-8141(95)00029-D. 1.1, 2.7.1

Wittlinger, G., J. Vergne, P. Tapponnier, V. Farra, G. Poupinet, M. Jiang, H. Su, G. Herquel, and A. Paul (2004), Teleseismic imaging of subducting lithosphere and Moho offsets beneath western Tibet, *Earth and Planetary Science Letters*, *221*(14), 117–130, doi:10.1016/S0012-821X(03)00723-4. 2.2

Wright, T., B. Parsons, J. Jackson, M. Haynes, E. Fielding, P. England, and P. Clarke (1999), Source parameters of the 1 October 1995 Dinar (Turkey) earthquake from SAR interferometry and seismic bodywave modelling, *Earth and Planetary Science Letters*, *172*(12), 23–37, doi:10.1016/S0012-821X(99)00186-7. 2.3.1

Wright, T., B. Parsons, and E. Fielding (2001), Measurement of interseismic strain accumulation across the North Anatolian Fault by satellite radar interferometry, *Geophysical Research Letters*, *28*(10), 2117–2120, doi:10.1029/2000GL012850. 1.1

Wright, T. J., Z. Lu, and C. Wicks (2003), Source model for the Mw 6.7, 23 October 2002, Nenana Mountain Earthquake (Alaska) from InSAR, *Geophysical Research Letters*, *30*(18), doi:10.1029/2003GL018014. 2.3.1

Wright, T. J., Z. Lu, and C. Wicks (2004), Constraining the Slip Distribution and Fault Geometry of the Mw 7.9, 3 November 2002, Denali Fault Earthquake with Interferometric Synthetic Aperture Radar and Global Positioning System Data, *Bulletin of the Seismological Society of America*, *94*(6B), S175–S189, doi:10.1785/0120040623. 2.3.1

Wright, T. J., J. R. Elliott, H. Wang, and I. Ryder (2013), Earthquake cycle deformation and the Moho: Implications for the rheology of continental lithosphere, *Tectonophysics*, *609*, 504–523, doi:10.1016/j.tecto.2013.07.029. 2.6.2

Xu, X., X. Wen, G. Yu, G. Chen, Y. Klinger, J. Hubbard, and J. Shaw (2009), Coseismic reverse- and oblique-slip surface faulting generated by the 2008 Mw 7.9 Wenchuan earthquake, China, *Geology*, *37*(6), 515–518, doi:10.1130/G25462A.1. 4.6

Xu, Y., S. W. Roecker, R. Wei, W. Zhang, and B. Wei (2006), Analysis of Seismic Activity in the Crust from Earthquake Relocation in the Central Tien Shan, *Bulletin of the Seismological Society of America*, *96*(2), 737–744, doi:10.1785/0120030220. 3.6, 3.15

Yan, D.-P., Y.-B. Xu, Z.-B. Dong, L. Qiu, S. Zhang, and M. Wells (2016), Fault-related fold styles and progressions in fold-thrust belts: Insights from sandbox modeling, *Journal of Geophysical Research: Solid Earth*, *121*(3), 2015JB012,397, doi:10.1002/2015JB012397. 1.2

Yashchenko, V. (1990), Topographic survey of the USSR completed at a scale of 1:25,000, *Mapping Sciences and Remote Sensing*, *27*(1), 3–8, doi:10.1080/07493878.1990.10641783. A.2

Yielding, G., J. A. Jackson, G. C. P. King, H. Sinvhal, C. Vita-Finzi, and R. M. Wood (1981), Relations between surface deformation, fault geometry, seismicity, and rupture characteristics during the El Asnam (Algeria) earthquake of 10 October 1980, *Earth and Planetary Science Letters*, *56*, 287–304, doi:10.1016/0012-821X(81)90135-7. 3.5

Yin, A., S. Nie, P. Craig, T. M. Harrison, F. J. Ryerson, Q. Xianglin, and Y. Geng (1998), Late Cenozoic tectonic evolution of the southern Chinese Tian Shan, *Tectonics*, *17*(1), 1–27, doi:10.1029/97TC03140. 1.2

Youngs, R. R., W. J. Arabasz, R. E. Anderson, A. R. Ramelli, J. P. Ake, D. B. Slemmons, J. P. McCalpin, D. I. Doser, C. J. Fridrich, F. H. Swan, A. M. Rogers, J. C. Yount, L. W. Anderson, K. D. Smith, R. L. Bruhn, P. L. K. Knuepfer, R. B. Smith, C. M. dePolo, D. W. OLeary, K. J. Coppersmith, S. K. Pezzopane, D. P. Schwartz,

J. W. Whitney, S. S. Olig, and G. R. Toro (2003), A Methodology for Probabilistic Fault Displacement Hazard Analysis (PFDHA), *Earthquake Spectra*, *19*(1), 191–219, doi:10.1193/1.1542891. 4.1

Zech, R. (2012), A late Pleistocene glacial chronology from the Kitschi-Kurumdu Valley, Tien Shan (Kyrgyzstan), based on 10be surface exposure dating, *Quaternary Research*, *77*(2), 281–288, doi:10.1016/j.yqres.2011.11.008. 5.6.1

Zhang, G., X. Shan, Y. Zhang, E. Hetland, C. Qu, and G. Feng (2016), Blind thrust rupture of the 2015 Mw 6.4 Pishan earthquake in the Northwest Tibetan Plateau by joint inversion of InSAR and seismic data, *Journal of Asian Earth Sciences*, *132*, 118–128, doi:10.1016/j.jseaes.2016.10.005. 2.3.1

Zheng, G., H. Wang, T. J. Wright, Y. Lou, R. Zhang, W. Zhang, C. Shi, J. Huang, and N. Wei (2017), Crustal deformation in the India-Eurasia collision zone from 25 years of GPS measurements, *Journal of Geophysical Research: Solid Earth*, p. 2017JB014465, doi:10.1002/2017JB014465. 1.1, 1.6

Zheng, H., C. M. Powell, Z. An, J. Zhou, and G. Dong (2000), Pliocene uplift of the northern Tibetan Plateau, *Geology*, *28*(8), 715–718, doi:10.1130/0091-7613(2000)28<715:PUOTNT>2.0.CO;2. 2.8

Zhou, Y., J. R. Elliott, B. Parsons, and R. T. Walker (2015a), The 2013 Balochistan earthquake: An extraordinary or completely ordinary event?, *Geophysical Research Letters*, *42*(15), 6236–6243, doi:10.1002/2015GL065096. 2.1

Zhou, Y., B. Parsons, J. R. Elliott, I. Barisin, and R. T. Walker (2015b), Assessing the ability of Pleiades stereo imagery to determine height changes in earthquakes: a case study for the El Mayor-Cucapah epicentral area, *Journal of Geophysical Research: Solid Earth*, p. 2015JB012358, doi:10.1002/2015JB012358. 4.3.1, A.1

Zhou, Y., R. T. Walker, J. Hollingsworth, M. Talebian, X. Song, and B. Parsons (2016), Coseismic and postseismic displacements from the 1978 Mw 7.3 Tabas-e-Golshan earthquake in eastern Iran, *Earth and Planetary Science Letters*, *452*, 185–196, doi:10.1016/j.epsl.2016.07.038. 2.7.1, 3.5, A.1

Zinke, R., J. Hollingsworth, and J. F. Dolan (2014), Surface slip and off-fault deformation patterns in the 2013 MW 7.7 Balochistan, Pakistan earthquake: Implications for controls on the distribution of near-surface coseismic slip, *Geochemistry, Geophysics, Geosystems*, *15*(12), 5034–5050, doi:10.1002/2014GC005538. 5.8

Zohar, M., A. Salamon, and R. Rubin (2016), Reappraised list of historical earthquakes that affected Israel and its close surroundings, *Journal of Seismology*, *20*(3), 971–985, doi:10.1007/s10950-016-9575-7. 1.1

Zubovich, A., T. Schöne, S. Metzger, O. Mosienko, S. Mukhamediev, A. Sharshebaev, and C. Zech (2016), Tectonic interaction between the Pamir and Tien Shan observed by GPS, *Tectonics*, p. 2015TC004055, doi:10.1002/2015TC004055. 1.2

Zubovich, A. V., X.-q. Wang, Y. G. Scherba, G. G. Schelochkov, R. Reilinger, C. Reigber, O. I. Mosienko, P. Molnar, W. Michajljow, V. I. Makarov, J. Li, S. I. Kuzikov, T. A. Herring, M. W. Hamburger, B. H. Hager, Y.-m. Dang, V. D. Bragin, and R. T. Beisenbaev (2010), GPS velocity field for the Tien Shan and surrounding regions, *Tectonics*, *29*(6), TC6014, doi:10.1029/2010TC002772. 1.2, 3.1, 3.2, 3.2.3, 4.1, 5.1, 5.6.3, 5.23

Appendix A

DEM Differencing for the Suusamyr Earthquake

A.1 Introduction

Although I have established the distribution of surface ruptures from the 1992 earthquake well, the question of the relationship between the rupture pattern and the sub-surface distribution of slip is unresolved. Either the discontinuity of the surface ruptures really was caused by an irregular sub-surface slip distribution, or the slip pattern was smooth but shallow slip was accommodated by off-fault processes in the gaps between surface ruptures, such as by folding.

In this section of work I tried to construct a map of the vertical displacements in the Suusamyr valley during the coseismic and postseismic periods. My aims were to better establish the top depth of slip along the fault during the earthquake and the distribution of the slip. Given that the discontinuous 1992 scarps span ∼35 km length (Chapter 4) and that several metres of slip reached some ruptures, it seems likely that slip reached within 1–2 km of the surface for much of the length of the fault, and particularly in the area between the sets of surface ruptures. If the slip was accommodated by folding in the sections with no surface rupture then there should also be a correlation between the

coseismic surface displacements and the pattern of folding that I have identified from the geomorphology — short wavelength uplift associated with fold growth should be seen. Alternatively, if coseismic vertical displacements are visible around the surface ruptures but not between them, that would suggest that the discontinuity of the surface ruptures really was caused by an irregular sub-surface slip distribution for the earthquake.

My strategy was to compute elevation differences between a pre-earthquake DEM and a recent DEM, which should yield a map of displacements during the intervening time period. This has been successfully applied to large tectonic events using LiDAR (*Oskin et al.*, 2012; *Nissen et al.*, 2014b), satellite DEMs (*Zhou et al.*, 2015b) and aerial photos (*Hollingsworth et al.*, 2013; *Zhou et al.*, 2016).

A.2 Aerial photographs and processing

I obtained 874 scans of black and white aerial photographs of the Suusamyr region (e.g. Figure A.1), covering squares K-43-63 and K-43-64 of the CSK-42 coordinate system. The photographs are the result of systematic mapping surveys conducted by the Soviet Union during the second half of the twentieth century (e.g. *Yashchenko*, 1990; *Davies and Kent*, 2017), but unfortunately their metadata are not available. The dates of acquisition are unknown, as are the specifications of the camera.

The images were scanned from hard copies as 8-bit RGB images at 300 dpi and supplied in jpg format. Although the photographs do have fiducual marks which locate the principal point of the camera I do not know the focal length of the camera and therefore cannot use standard photogrammetric software to correct for the camera distortions. I therefore opted to take advantage of the large number of photographs and their overlapping ground footprints to process the photos using Structure from Motion (SfM), implemented using the Agisoft Photoscan Pro (v1.3.4) software, the advantage of SfM being that the the algorithm includes solving for the camera's internal geometry. 369 images covering our area of interest were used in the model.

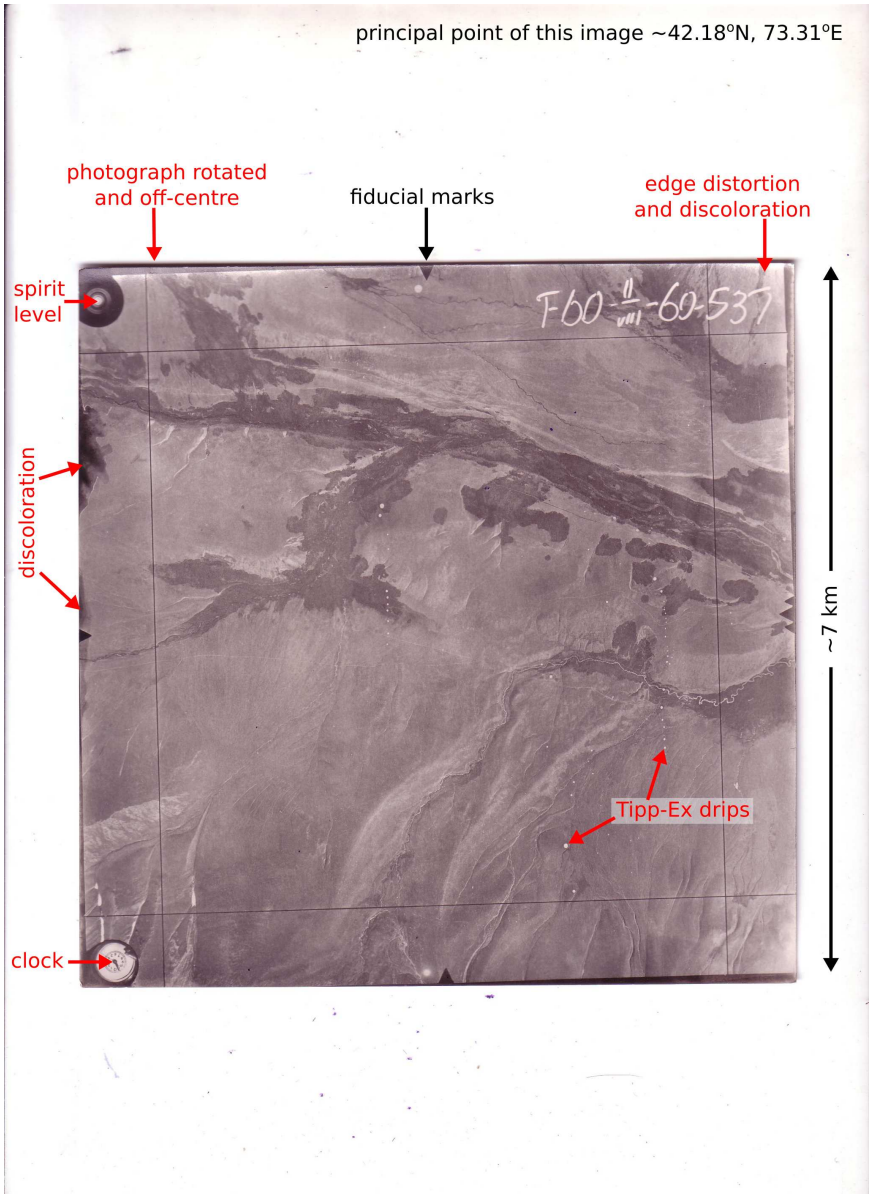


Figure A.1: A typical aerial photograph of the Suusamyr valley.

The scanned images have several characteristics that are non-optimal for DEM generation. Agisoft Photoscan was designed for use with modern digital photos and therefore assumes that the entire image is filled by the photograph, that the principal point is at the same location (in image coordinates) in every image and that the lens coordinate system does not rotate with respect to the image coordinate system. In our images the photographs are smaller than the scanned area, imperfectly centred and often rotated by several degrees, meaning none of the three assumptions above are true. Scanning and

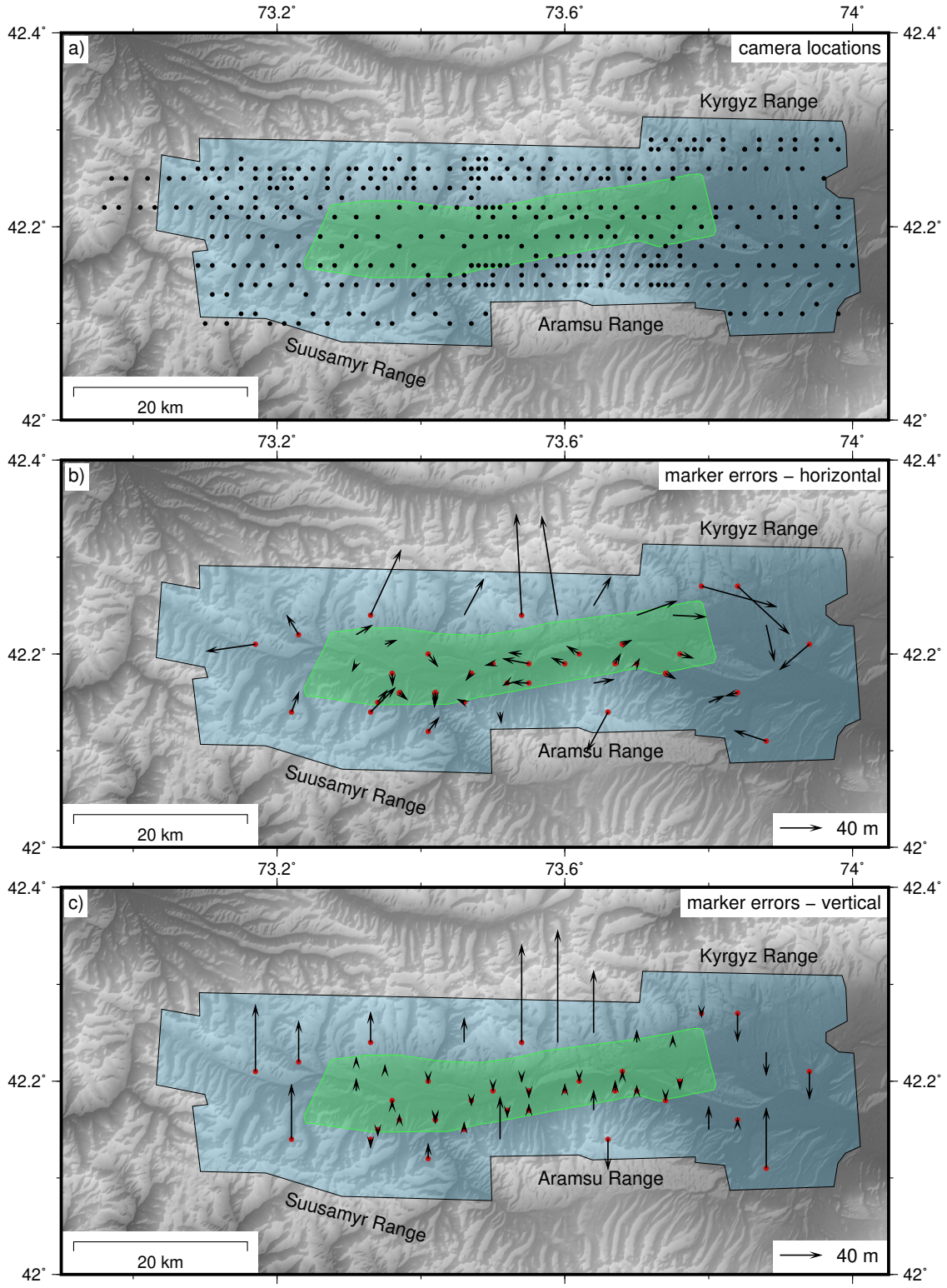


Figure A.2: An overview of the survey setup. Blue overlay shows the extent of the Agisoft pointcloud. Green overlay shows the extent of the Pléiades DEM and the difference map. a) Dots show the locations that each photograph was taken from. b) Arrows show horizontal errors for the ground control and check points (i.e. estimated position minus true position). Ground control points are marked with a red dot. Points within the green polygon were assigned 10/20 m accuracy (high weighting in georeferencing) and points outside were assigned only 50 m accuracy (low weighting). c) As b) but for vertical errors.

the earlier hard copy making process both add their own different geometric distortions which complicate the relationship between image coordinates and ground coordinates (e.g. *Sevara*, 2016). Furthermore, the viewing geometry of the aerial surveys is quite uniform: the reconstructed camera locations in Photoscan show that the flights were flown in roughly straight east-west lines (Figure A.2), successive lines were flown at only slightly different altitudes, with a typical flying altitude of 4 km above the ground, and the viewing angle was always close to nadir. This uniform viewing geometry gives poor constraint on the camera's radial distortion coefficients and is therefore susceptible to the 'bowl effect' — survey-scale doming errors in the model (*James and Robson*, 2014).

A.2.1 Airphoto processing workflow

My workflow for the aerial photograph SfM processing is shown in Figure A.3 and has been designed to account as well as possible for the issues described in Section A.2. First, the white background, spirit level and clock must be manually masked on each image to ensure that the software does not attempt to use them for point matching. The images show signs of their age, including fading of the corners and edges, discolouration, pen markings and scratches (Figure A.1), so the worst of the areas affected by these issues were masked out.

Before alignment I placed a total of 4 tie points (which had no geographic location information), and 32 control points on the images (Figure A.2b and c). I identified the locations of the control points using the Pléiades data where possible and using alternative imagery and JAXA's AW3D30 DEM for points outside the Pléiades region. The control points were weighted by assigning an "accuracy" to each, most Pléiades points were assigned 10 m accuracy, lower quality Pléiades points were assigned 20 m accuracy and points located using other datasets were assigned 50 m accuracy. For the sparse pointcloud generation step ("align photos") it was necessary to use a fixed camera model; allowing a free camera model resulted in a pointcloud with fractionally smaller reprojection errors but with dramatic vertical exaggeration. The vertical exaggeration

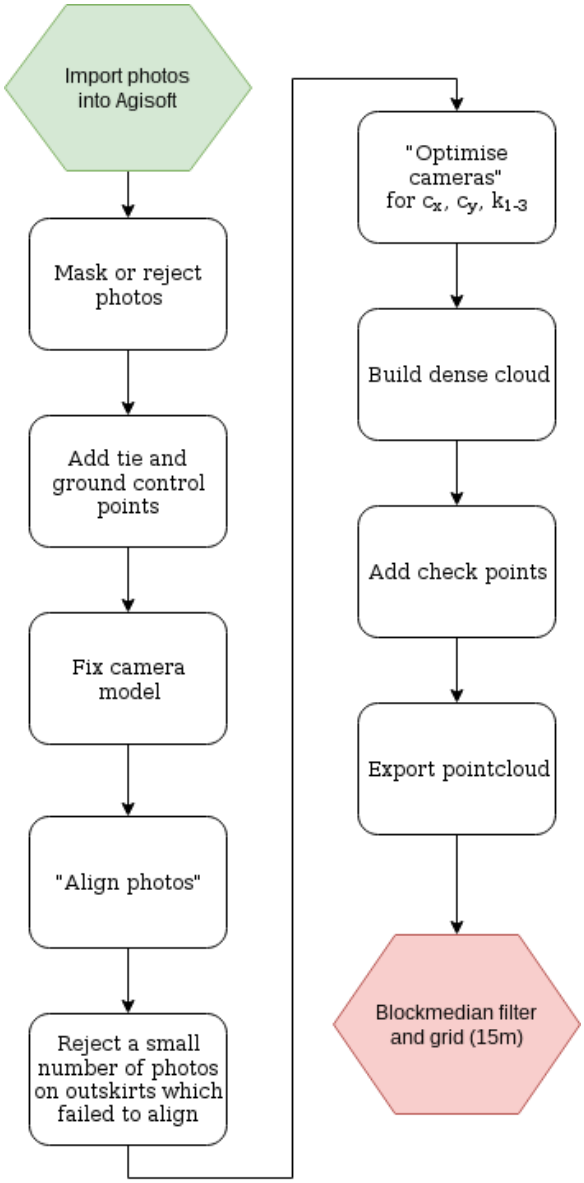


Figure A.3: The workflow for producing the airphoto DEM.

and the estimated flying altitude are controlled by the focal length. I used trial and error to find that a 1200 pixel (4 inch) focal length gave the best fit to my control points, and I used that value along with zero tangential and radial distortion as our fixed camera model.

The resulting sparse cloud had a doming error which I corrected using the "optimize cameras" tool to solve for principal point coordinates and three radial distortion coefficients. As discussed above, the scanning and hard copy processes mean that the

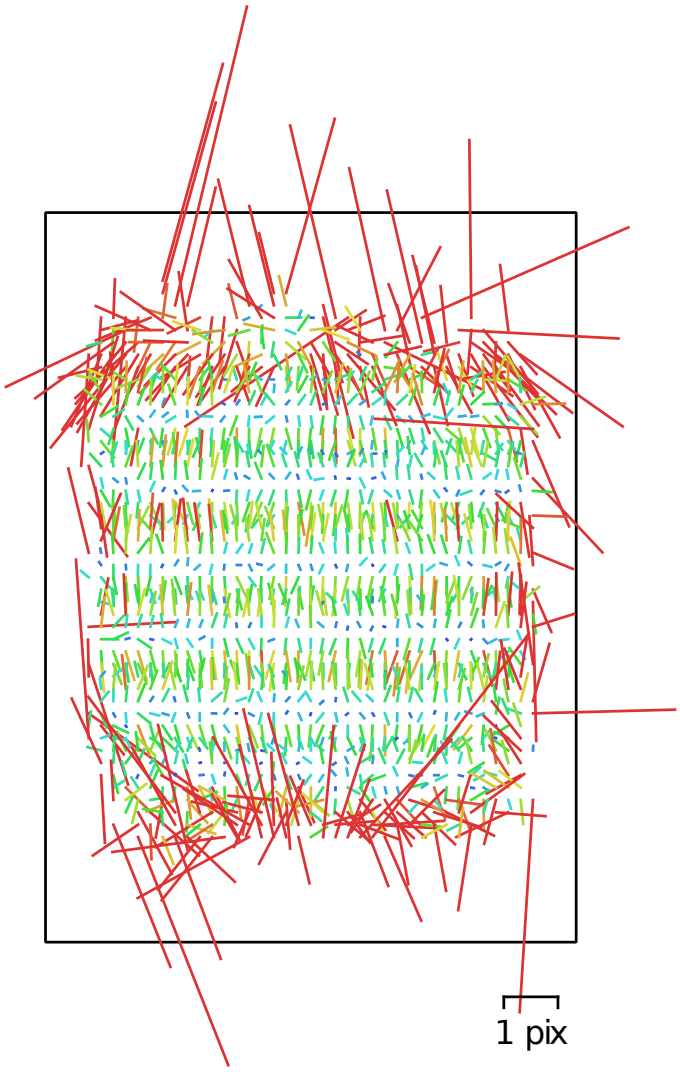


Figure A.4: The black rectangle represents the image frame. Coloured bars represent reprojection error vectors for the pixels in the corresponding location, averaged across every image. White areas are masked out on every photo, the edges of the photo are masked out on most images so the red bars at the top and bottom of the image only represent a few points. Systematic, horizontal stripes are clear. These are the result of geometric distortions in the scanning.

tool is unlikely to have recovered accurate values for the original camera's principal point or radial distortion and this step was only used as an empirical correction of the point cloud geometry. After the correction I built the dense cloud using half-resolution photos ("high" quality setting), filtered the pointcloud using a 15 m blockmedian filter and gridded the result using GMT's "surface" command.

My final pointcloud had a final RMS error of 43.5 m for the control points and 52.5

m RMS error for 13 check points added after processing. The points within the Pléiades area generally have lower error than those outside it (Figure A.2). A visualisation of the success of the camera calibration is given by the image residuals plot (Figure A.4). Image residual plots show maps of reprojection error vectors averaged across the same multiple-pixel area in every image. For an ideal project the vectors would be small and not systematic. The plot for this project shows repeated horizontal stripes across the image frame, I attribute this to geometric distortion of the scanner and conclude that our camera calibration is satisfactory, since radial and tangential distortions are far less prominent than the scanning distortion.

A.2.2 DEM differencing

The DEM differencing itself is straightforward for this project. The same methods were used to filter and grid both pointclouds and the grids were made with identical extents and resolution. The pointclouds are sufficiently dense that the great majority of the 15×15 m grid cells did contain points. The difference map is then made by a simple subtraction of one grid from the other. By using this method I avoid aliasing or downsampling artefacts. There was no need for additional coregistration because the airphoto pointcloud was already georeferenced with reference to the Pléiades dataset thanks to the control points.

This initial DEM differencing does not take into account coseismic horizontal displacements. Horizontal displacement of an area with non-zero slope leads to an apparent vertical displacement (e.g. *Leprince et al.*, 2011): if a planar slope dipping at an angle θ is displaced horizontally by x m, then the apparent vertical displacement is equal to $x.tan(\theta)$. The result of horizontal displacement is the same as coregistration error, therefore if the DEM differencing result shows signs of local coregistration error in locations with steep slopes and which are likely to have experienced horizontal displacement then further analysis must be made before interpreting the result.

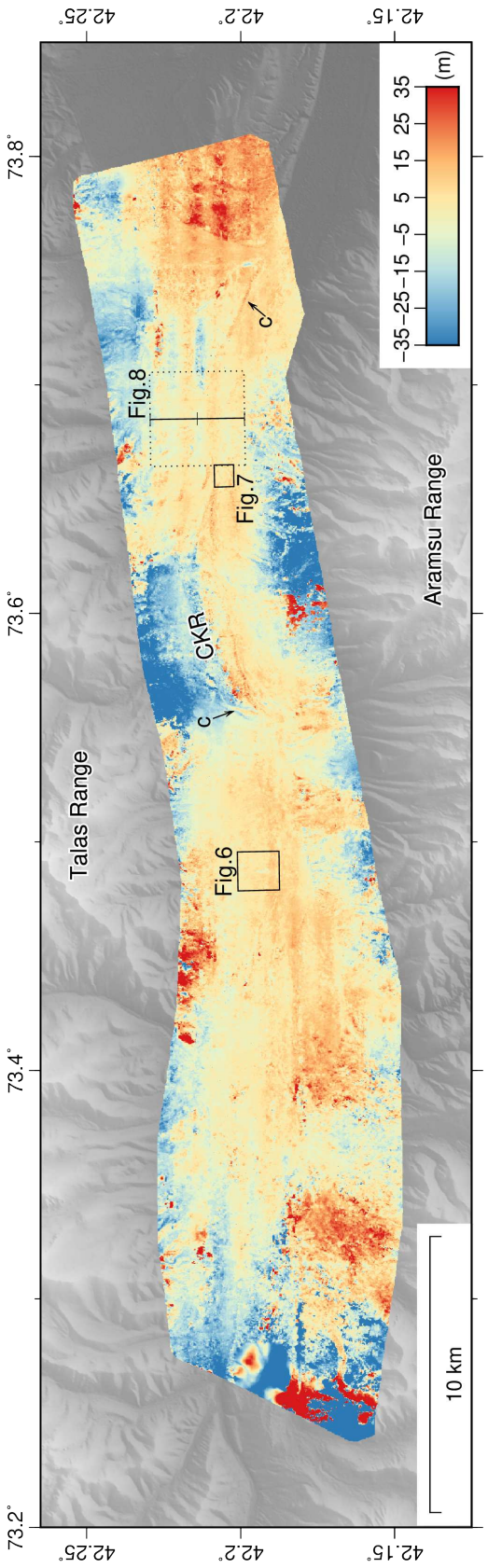


Figure A.5: The DEM difference result. Negative values indicate subsidence. Points marked 'c' are examples of coregistration error.

A.3 Differencing results

The result is shown in Figure A.5. It does accurately portray some short-wavelength height changes: excavations at 42.192°N,73.487°E (Figure A.6) and 42.215°N,73.672°E are clearly visible in the difference map and their location and shape are accurately depicted, and the M41 Highway site of 1992 surface rupture shows a short wavelength height change of ∼3 m (the same as the present-day scarp height) with a location and strike matching the scarp (Figure A.7). Although some short wavelength height changes are visible in the difference map, the overall quality of the result is not high enough to show the distribution of coseismic vertical displacements. Short-wavelength noise is particularly problematic in the southwest of the area, where there is a sparser coverage of aerial photographs (Figure A.2a). A wave artefact is prominent across much of the difference map. It has a ∼10 m amplitude and ∼1 km wavelength (Figure A.8). I saw no waves in a DEM difference map between the Pléiades and AW3D30 DEMs and the wavelength and orientation of the artefact match the scanning artefact shown by Figure A.4, so I conclude that the artefact comes from the airphoto DEM and is a result of the geometric distortions in the scanning.

Localised coregistration errors can be seen, for example at points marked 'c' in Figure A.5, but they are not consistent across the map, so coregistration is not the main problem in this case. The coregistration errors also do not consistently have the sense that would be expected if they were caused by real coseismic horizontal displacements. Signals with a half-wavelength of ∼2–5 km are the most prominent and more problematic signals in the DEM difference result, especially around the higher-elevation edges of the difference map. They are likely to arise from imperfect (exterior) camera orientation during the SfM bundle adjustment and probably result from the poor scanning quality, poor photo quality, poor camera model treatment and large number of images.

Now that I have estimated the camera focal length, a more targeted study using fewer images could be conducted in ERDAS Imagine or similar software which has

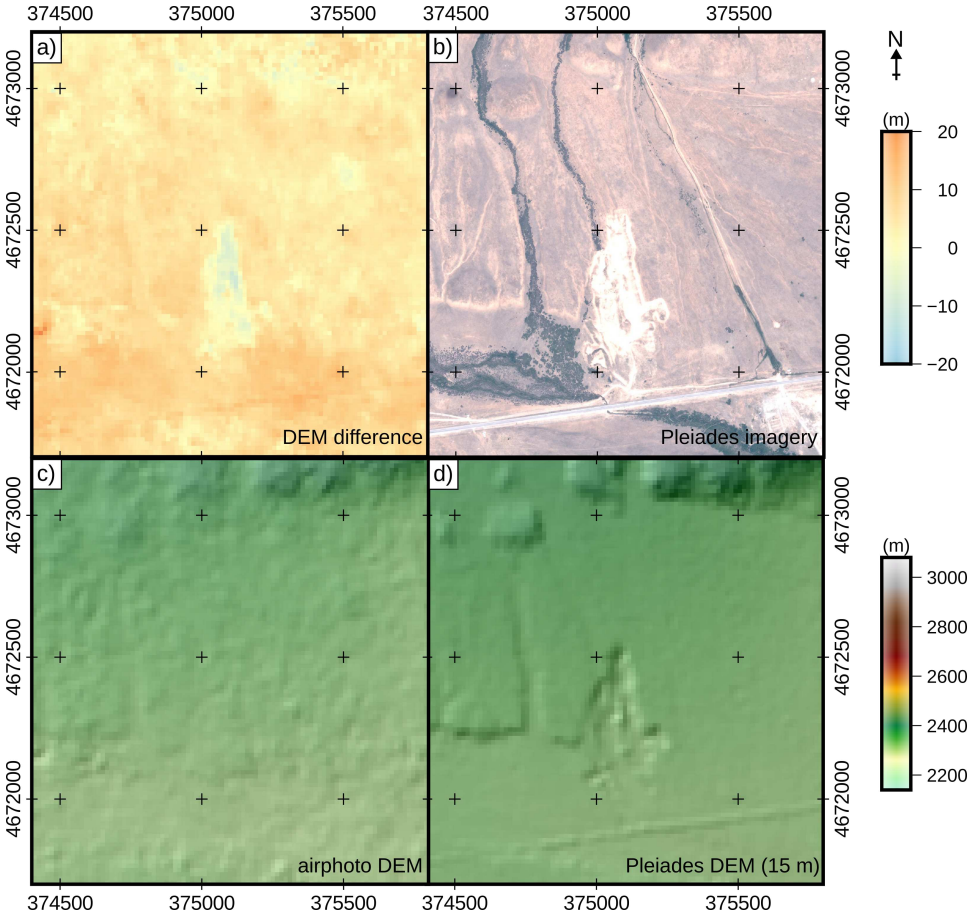


Figure A.6: An excavation successfully identified in the DEM difference map. a) DEM difference showing the excavated area with ∼10 m elevation difference with respect to the surrounding area. Colour scale is as in Figures A.7 and A.5. b) The same area in Pléiades imagery, the excavation is bright white and its location and shape correlate well with the blue-yellow shape in a). c) Hillshaded airphoto DEM of the area. d) Hillshaded Pléiades DEM gridded to 15 m. Coordinates in UTM 43N.

better capability for using the fiducial marks on photographs and might have more effective photogrammetric algorithms in this case. I have not opted to attempt that because the scanning artefact and photo quality would still be hindrances in any software, and because it would not be feasible to cover such a large ground area using alternative software, so it would still not be possible to meet my goal of measuring vertical displacements along the length of the Suusamyr earthquake. Declassified KH-9 images are available. They avoid many of the drawbacks of the aerial photographs: each covers a large area, the focal length and principal point are known, and they were scanned on a photogrammetric scanner. The images could be used to generate a DEM in the

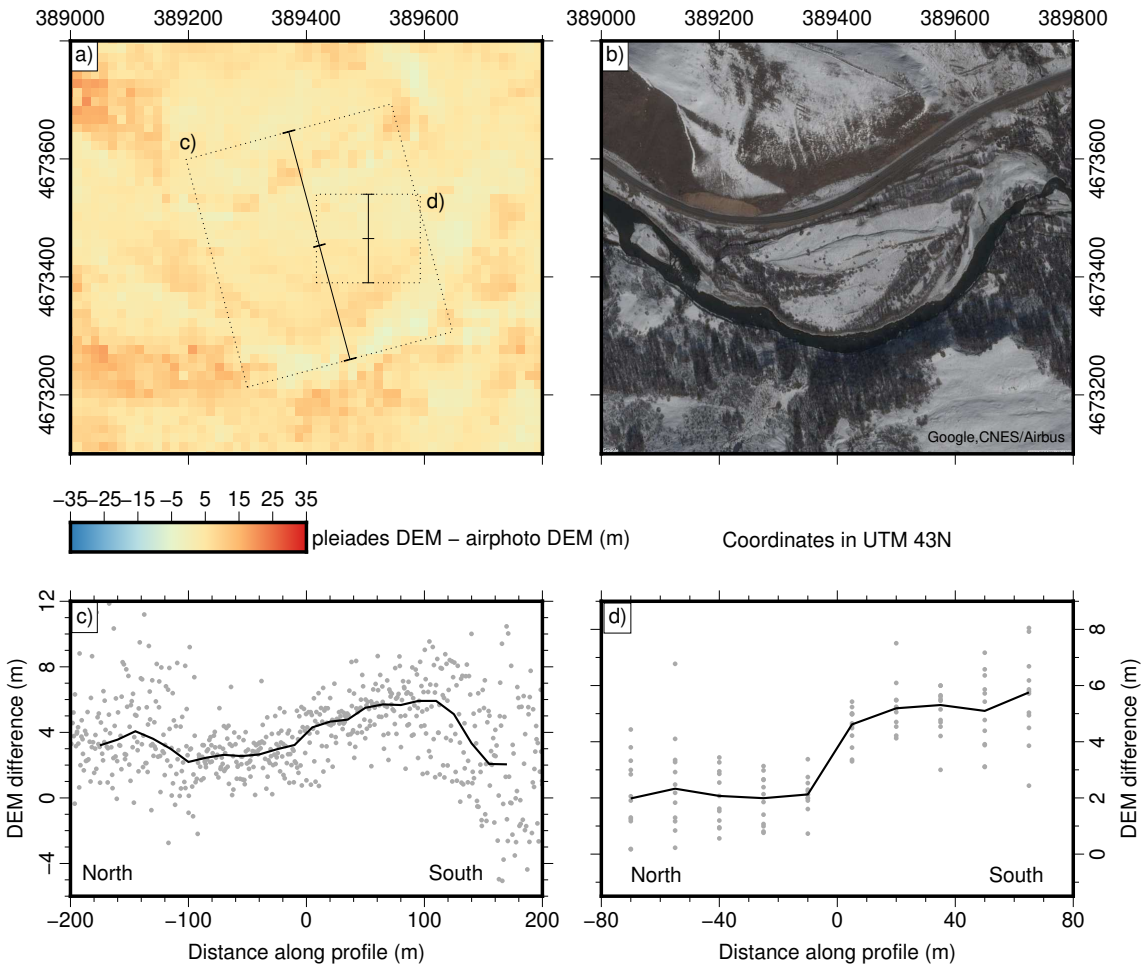


Figure A.7: The differencing results at the site of the 1992 M41 highway ruptures. a) DEM difference. b) Optical imagery of the same area from GoogleEarth. c) and d) Profiles through the difference map, centred on the scarp. Black lines show the median. The profiles each show ∼3 m displacement across the scarp. This area has almost zero slope, so it is clear that the signal is not due to horizontal offset.

future but they were not a priority for this thesis because their spatial resolution is several times worse than that of the aerial photos, so attempting to map the earthquake's height change using them would be ambitious.

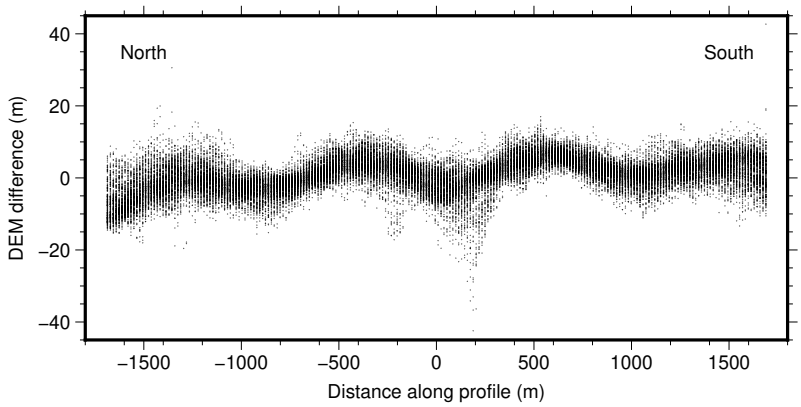


Figure A.8: A swath profile through the difference map showing waves with ∼1 km wavelength and ∼10 m amplitude. Location shown on Figure A.5.

A.4 Conclusions

I used DEM differencing to create an elevation change map for the 1992 Suusamyr earthquake and the following 23 years. The result was accurate for some sub-kilometre sized sites, including two excavations and a surface rupture, but much of the map was dominated by artefacts. The poor quality result was due to a lack of metadata, the large number of photos needed to cover the region of interest and scanning distortions, among other factors. I do not know of any other processing method or dataset currently available that is likely to produce a result that is accurate to the required level (<5 m) over the whole length of the fault. The relationship between slip distribution and rupture pattern therefore remains unsolved.

Appendix B

Further details on the luminescence dating methodology

The environmental dose rates of the samples were estimated as follows. The total uranium, thorium and potassium contents of the samples were determined from sub-samples of the sampling tubes using inductively-coupled plasma mass spectrometry, carried out at the University of Leicester. Elemental concentrations were converted to dose rates using the conversion factors of (*Guérin et al.*, 2011), with appropriate adjustment for grain size (*Mejdahl*, 1979; *Readhead*, 2002) and sample water content (*Aitken*, 1985). Dose rates for internal K and Rb were based on the assumption of K-feldspar grain K and Rb concentrations of 12.5±0.5% and 400±100 ppm respectively (*Huntley and Baril*, 1997; *Huntley and Hancock*, 2001). It was assumed that the as-measured water content was appropriate, and a 2% (absolute) uncertainty in water content was propagated into the final dose rate uncertainties. It is assumed that the dose rate remained constant for the duration of burial. Cosmic dose rates were determined following *Prescott and Hutton* (1994) and were based on the current sample burial depth. Details of the various calculated dose rate components are shown in Table B.1.

Table B.1: Details of the sample dose rate determinations. Elemental concentrations were obtained using ICP-MS , with associated relative uncertainties (derived from replicate measurements using this method) of 10% assigned to U and Th and 5% assigned to K. These were propogated to the final dose rate determination along with an (absolute) water content uncertainty of ±2%. The measured grain size range was size range 212-250 μm.

Sample	Water	Depth	U	Th	K	Beta (ext)	Beta (int)	Gamma	Total Cosmic	Total dose rate
	%	m	ppm	ppm	%	mGy a^{-1}	mGy a^{-1}	mGy a^{-1}	mGy a^{-1}	Gy ka^{-1}
KGZ15-L01	10.3	0.55	13.7	28.8	3.1	3659±227	986±68	3287±209	310±16	8.24±0.32
KGZ15-L02	8.2	0.80	11.4	25.9	3.5	3739±228	986±68	3104±188	300±15	8.13±0.30
KGZ15-L03	14.4	0.60	13.3	25.8	3.0	3362±209	986±68	2973±188	308±15	7.63±0.30

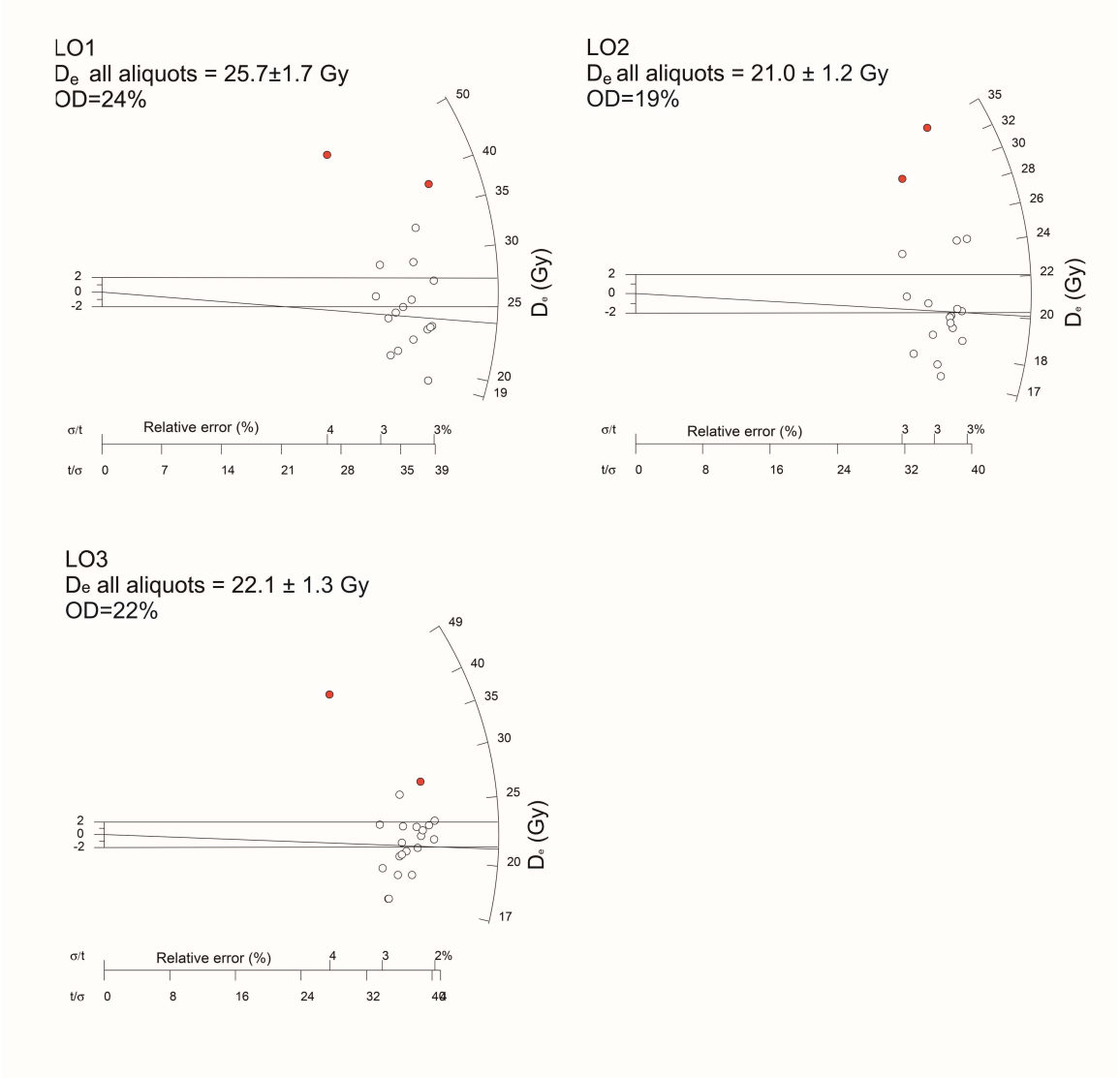


Figure B.1: Radial plots showing the distribution in equivalent doses for the $pIRIR_{225}$ analysis of the samples LO1-LO3. The plots show all measured aliquots and are centred (2 horizontal bars) on the Central Age D_e for all alliquots. The identified outlier aliquots are shown in red and the resulting mean D_e following their removal (Table 4.3) is shown with the additional marker line. The central age mean and overdispersion parameter for all measured aliquots are also shown.